KU LEUVEN

Arenberg Doctoral School

Faculty of Engineering Technology

Aerosol Jet Printing of Fibrillar Collagens for the Replication of Dense Collagenous Tissues

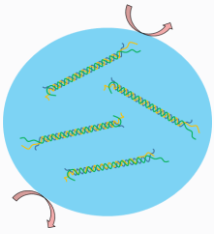

Rory Laurence David Gibney

Supervisor (s):

Prof. Dr. Eleonora Ferraris

Prof. Dr. Jennifer Patterson

Members of the Examination Committee:

Prof. Dr. Veerle Bloemen

Prof. Dr. Hans Van Oosterwyck

Dr. Bjorn Vergauwen

Prof. Dr. Adrian Ranga

Prof. Dr. Lorenzo Moroni

(Maastricht University, Netherlands)

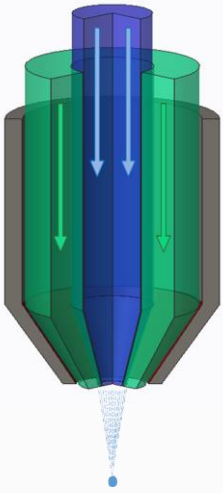

Aerosol Jet Printing of Fibrillar Collagens for the Replication of Dense Collagenous Tissues

Rory Laurence David GIBNEY

Supervisor(s):

Prof. Dr. Eleonora Ferraris

Prof. Dr. Jennifer Patterson

Members of the Examination Committee:

Prof. Dr. Veerle Bloemen

Prof. Dr. Hans Van Oosterwyck

Dr. Bjorn Vergauwen

Prof. Dr. Adrian Ranga

Prof. Dr. Lorenzo Moroni

(Maastricht University, Netherlands)

Dissertation presented in partial fulfilment of the requirements for the degree of Doctor of Engineering Technology (PhD)

June 2022

© 2022 Rory Gibney

Uitgegeven in eigen beheer, Rory Gibney, 24 Headfort Park, Kells, Co. Meath, A82 X6D0, Ireland

Alle rechten voorbehouden. Niets uit deze uitgave mag worden vermenigvuldigd en/of openbaar gemaakt worden door middel van druk, fotokopie, microfilm, elektronisch of op welke andere wijze ook zonder voorafgaandelijke schriftelijke toestemming van de uitgever.

All rights reserved. No part of the publication may be reproduced in any form by print, photoprint, microfilm, electronic or any other means without written permission from the publisher.

Acknowledgements

I would like to thank the members of the examination committee for taking the time to review my manuscript and for contributing to the peer-review process. To Prof. Veerle Bloemen, thank you for providing insight into the cell culture experiments, though they didn't come to fruition they provided a valuable learning experience that could aid another PhD student in future cell culture of aerosol jet printed collagen. To Prof. Hans van Oosterwyck, thank you for always providing valuable insights and encouragement during meetings. To Dr. Bjorn Vergauwen thank you for offering challenging questions and insights regarding collagen structure and characterization. To Prof. Adrian Ranga, Prof. Greet Van den Berghe, and Prof. Lorenzo Moroni, thank you for taking part in and presiding over these defences.

I would like to acknowledge the funding bodies which made this work possible the FWO (Fonds voor Wetenschappelijk Onderzoek – Vlaanderen) and VLAIO (Vlaanderen Agentschap Innoveren & Ondernemen), and I would like to thank everyone involved in securing those funds Prof. Eleonora Ferraris, Dr. Jennifer Patterson, Dr. Nadia Zakaria, and Prof. Carina Koppens.

This PhD was particularly challenging at times and would not have been completed without the support of many people both professional support from researchers at KU Leuven, and briefly researchers at NUI Galway, but particularly the emotional support from my girlfriend Steffi, my friends, and my family.

I would like to thank my supervisor Dr. Eleonora Ferraris and the present and former members of the Additive Manufacturing Lab research group namely Frederik Vogeler, Olivier Degryse, Miriam Seiti, Akash Verma, Loren De Vogelaer, and Jie Zhang. I would also like to thank my fellow PhD candidates, the postdoctoral researchers and the technical team at SBE particularly Hannah Agten, and Jenny Peeters. I would like to thank Kimberly Crevits for being very

facilitating to my use of Fiber lab. At many times over the course of this PhD I found myself dependent upon people's good will to measure my samples, or grant me access and training to valuable equipment, with that in mind I would also like to thank Dr. Nada Savić and Prof. Tatjana Vogt, Dr. Clio Deferm, Dr. Julian Steele, and Dr. Lily Karamanou.

I would like to thank Dr. Dimitrios Zeugolis for hosting me for my secondment in REMODEL (NUI Galway), for providing valuable feedback, and for facilitating such an open and welcoming research group. Additionally, I would like to thank all the PhD candidates and postdocs in REMODEL and Curam who helped me in extracting and characterizing collagens and allowed me to come crashing into their social lives in Galway, particularly Eugenia, Nacho, Meletios, Hector, João, Mehmet, Alex, and Gabriele.

I would like to thank Dr. Jennifer Patterson and all the members of Pattersonium Biomaterials, Abhi, Susanna, Alex, Laurien, Soultan, Taíla, Laurens, Burak, Christian, Ricardo, and Jasper. Although the group was not long-lived it gave me a grounding in aspects of tissue engineering research, and I think we will always be immortalized as the coolest group at the mad scientist-themed MTM Departementsfeest in 2017.

I would like to thank all present members and alumni of the Earls of Leuven Gaelic football team. It has been an absolute pleasure to be part of the establishment of this institution of Gaelic heritage in Leuven. Al, you quickly established an highly inclusive and diverse base for me upon settling in Leuven, like you have for so many, and from which the type of friendships that will last a lifetime have sprouted. I owe the Earls so much for the social support I received during this PhD, and there would be no Earls without you, Al. I would also like to call out some O.G. Earls for their friendship during this PhD Jarno, Jacko, Freddie, Alice, Jannick, Ciara, Ferghal, Rossa, and Kaan, and a special shout-out to my Earls academic counsel Karl Duffy & Daire Cott, and my Earls soul counsellor Juan Carlos Tinjaca.

To Steffi, one of the most comforting parts of this PhD was the knowledge that after long hours in the lab you would be there in

person or online to talk to me, cheer me up if needed, and be silly with me. You taught me the importance of setting goals and rewarding yourself with breaks, and I thank you for dragging me out of the apartment or out of the hole in which I put myself, and for being a role model to me. I would also like to thank the Bombeeck-de Jonge clan, Gillian, Steven, Sophie, Jackson, and Georgke. Gillian and Steven, thank you for the support, the chats, the hesprolletjes, the stoofvlees, the forelmoussse, and of course, the maatjes.

Anois, cúpla focail as gaeilge a mo chlann. A Mhaim is a Dhaid, go raibh míle maith agaibh as ucht do tacaíocht agus do spreagadh chun a bheith díograiseach, macánta, agus cineálta. Daz agus Eva, tharraing sibh suas mé mar bhur dtionscadalín agus mhúnlaigh sibh m'aigne go dtí m'aigne seo. Daz, go raibh maith agat as ucht an blas. Eva, go raibh maith agat as ucht an treoir. Stiofáin, go raibh maith agat as ucht a bheith mo dheartháir mór agus sin é. Níl. Go raibh maith agat Stiofáin as ucht do dílseacht. Agus ba mhaith liom buíochas a ghahail le Wayne agus Sarah, agus leis an chéad ghlúin eile Jonah, Luca, Odhran, and Éilidh.

Finally I would like to thank the city of Leuven. Five years ago I fell in love with a city like never before, and wherever I go I will always remember the sun shining through the steeple of Sint-Geertruikerk, the summer concerts, the bells of Sint-Pieterskerk playing pop songs, the various festivals and red carpet on Bondgonotenlaan, swallows calling on summer evenings and the sound of countless bikes crossing cobbled streets.

Abstract

Bioprinting, or the use of additive manufacturing techniques to produce scaffolds for tissue engineering, has recently been established as a useful tool in tissue engineering and regenerative medicine. However, a major limitation of bioprinting has been the mechanical properties of the printed constructs. While there are many tissues where this may not be treated as a priority, mechanical strength is a particularly important property for any construct aiming to replicate connective tissues, such as the cornea and cartilage. The strength of these tissues is often attributed to the overwhelming presence of the fibrillar collagens in their extracellular matrix, the long uninterrupted triple helix secondary structure of the fibrillar collagens, and the ability of these triple helices to align and assemble into densely packed fibrils. While fibrillar collagens, particularly collagen type I, have been bioprinted using some bioprinting techniques, the mechanical properties of the resultant constructs are typically very weak. The overall intent of this dissertation is to perform a fundamental study on aerosol jet printing of fibrillar collagens and develop it as a method for generating mechanically strong collagen hydrogels.

Aerosol jet® printing is a relatively recent electronic printing technology developed to print electronics onto a wider variety of surfaces than possible using pre-existing electronic printing technologies. It achieves its enhanced deposition characteristics by accelerating aerosol droplets of the ink towards the substrate while confined in a coaxial flow of dry gas. This allows the aerosol ink droplets to continue their intended path for a greater distance thereby allowing deposition onto rough substrates. The aerosol ink droplets also dry out remarkably quickly due to the high surface-area-to-volume ratio of an aerosol droplet. This method of drying out the ink is particularly attractive to collagen printing since it allows a relatively dilute solution to be processed into highly concentrated collagen scaffolds with a lower risk of thermal

denaturation, and without the use of toxic solvents. However, by transitioning straight from solution to solid in this way, it is unlikely for collagen fibrils to assemble. In order to generate an aerosol, it is also necessary to exert high shear forces on the bulk solution to produce the tiny aerosol droplets. Hence, before exalting aerosol jet printing as a method to print collagen it is necessary to establish whether the printed material is stable, and whether the shear forces of aerosolization damage the collagen structure.

Aerosol jet printing was investigated as a method to produce mechanically strong collagen scaffolds using one recombinant collagen (recombinant human collagen type III, RHCIII), and two animal-derived collagens; bovine Achilles' tendon-derived collagen type I, and porcine articular cartilage-derived collagen type II. The accuracy and stability of aerosol jet printed collagen was investigated via microscope examination of printed scaffolds. The effect of the shear forces of aerosolization on the structure of each collagen used was determined by sodium dodecyl sulphate-polyacrylamide gel electrophoresis (SDS-PAGE), circular dichroism (CD) spectroscopy, and in one case Fourier transform infra-red (FTIR) spectroscopy. The mechanical properties of the printed collagen scaffolds were measured via ferrule-topped nanoindentation. The structural properties of the aerosol jet printed collagen scaffolds were investigated via swelling ratio measurements and scanning electron microscopy (SEM).

Samenvatting

Bioprinten, of het gebruik van additieve fabricagetechnieken om scaffolds voor weefselmanipulatie te produceren, is recent vastgesteld als een nuttig hulpmiddel in weefselmanipulatie en regeneratieve geneeskunde. Aanzienlijke beperkingen van bioprinten zijn echter de mechanische eigenschappen van de geprinte constructies. Hoewel er veel weefsels zijn waar dit niet als een prioriteit wordt behandeld, is mechanische sterkte een bijzonder belangrijke eigenschap voor elk construct dat gericht is op het nabootsen van bindweefsel, zoals het hoornvlies en kraakbeen. De sterkte van deze weefsels wordt vaak toegeschreven aan de prominente aanwezigheid van de fibrillaire collagenen in hun extracellulaire matrix, de lange ononderbroken secundaire structuur van de drievoudige helix van de fibrillaire collagenen, en het vermogen van deze drievoudige helixen om uit te lijnen en samen te voegen tot dicht opeengepakte fibrillen. Hoewel fibrillaire collagenen, in het bijzonder collageen type I, gebioprint zijn met behulp van enkele bioprinttechnieken, zijn de mechanische eigenschappen van de resulterende constructies doorgaans erg zwak. De algemene bedoeling van dit proefschrift is om een fundamentele studie uit te voeren naar aerosol-jetprinten van fibrillaire collagenen en deze te ontwikkelen als een methode voor het genereren van mechanisch sterke collageen hydrogels.

Aerosol-jetprinten is een relatief recente elektronische printtechnologie die is ontwikkeld om elektronica op een grotere verscheidenheid aan oppervlakken te printen dan mogelijk is met behulp van reeds bestaande elektronische printtechnologieën. Het bereikt verbeterde afzettingseigenschappen door aërosoldruppels van de inkt naar het substraat te versnellen, gevat in een coaxiale stroom van droog gas. Hierdoor kunnen de aërosol-inktdruppels hun beoogde pad over een grotere afstand voortzetten, waardoor afzetting op ruwe substraten mogelijk wordt. De aerosol-inktdruppels drogen bovendien opmerkelijk snel uit door de hoge

oppervlakte-volumeverhouding van een aerosoldruppel. Deze methode om de inkt uit te drogen is bijzonder interessant voor collageenprinten, omdat het een relatief verdunde oplossing mogelijk maakt om te worden verwerkt tot hooggeconcentreerde collageensteigers met een lager risico op thermische denaturatie en zonder het gebruik van giftige oplosmiddelen. Door op deze manier rechtstreeks van oplossing naar vaste stof over te gaan, is het echter onwaarschijnlijk dat collageenfibrillen zich samenvoegen. Om een aerosol te genereren, is het ook nodig om hoge afschuifkrachten op de bulkoplossing uit te oefenen om de kleine aerosoldruppeltjes te produceren. Daarom is het, vooraleer aerosol-jetprinten als een methode voor het printen van collageen wordt voorgesteld, noodzakelijk om vast te stellen of het geprinte materiaal stabiel is en of de afschuifkrachten van aerosolisatie de collageenstructuur beschadigen.

Aerosol-jetprinten werd onderzocht als een methode voor de productie van mechanisch sterke collageensteigers met behulp van één recombinant collageen (recombinant menselijk collageen type III, RHCIII) en twee van dieren afkomstige collagenen; collageen type I afkomstig uit achillespezen van runderen, en collageen type II afkomstig uit gewrichtskraakbeen van varkens. De nauwkeurigheid en stabiliteit van met aerosol geprint collageen werd onderzocht via microscooponderzoek van geprinte steigers. Het effect van de afschuikrachten van aerosolisatie op de structuur van elk gebruikt collageen werd bepaald door natriumdodecylsulfaat-polyacrylamidegelelektroforese (SDS-PAGE), circulair dichroïsme (CD) spectroscopie en in één geval Fourier-transformatie infrarood (FTIR) spectroscopie. De mechanische eigenschappen van de geprinte collageensteigers werden gemeten via nano-indentatie met een ferrule-top. De structurele eigenschappen van de aerosol-jetgeprinte collageensteigers werden onderzocht via metingen van de zwelverhouding en scanning-elektronenmicroscopie (SEM).

Abbreviations

2PP	2-photon polymerization
ACI	autologous chondrocyte implantation
AJP	aerosol jet printing
BSS	biosynthetic stromal substitute
CAM	cell adhesion molecules
CD	circular dichroism
DALK	deep anterior lamellar keratoplasty
DBB	Droplet based bioprinting
DLP	digital light processing
DM	Descemet's membrane
DMEK	Descemet's membrane endothelial keratoplasty
DNA	deoxyribonucleic acid
EBB	Extrusion based bioprinting
ECM	extracellular matrix
EDC	(1-ethyl-3-(3-dimethylaminopropyl) carbodiimide),
EMA	European medicines agency
FACIT	fibril associated collagens with interruptions
FDA	Food and drug administration
FECD	Fuch's endothelial corneal dystrophy
GAG	glycosaminoglycans
H&E	hematoxylin & eosin
HCEC	human corneal epithelial cells
HSP	heat shock protein
LAFT	laser-assisted forward transfer
LBB	Light based bioprinting
LGDW	laser-guidance direct writing
LIFT	laser-induced forward transfer
LK	lamellar keratoplasty
LO	lysyl oxidase
MACI	matrix-induced autologous chondrocyte implant
MES	2-(N-morpholino)ethanesulfonic acid
MEW	melt electrowriting
MFC	mass flow controllers

MSC	mesenchymal stem cell
NHS	N-hydroxysuccinimide
OA	osteoarthritis
OCT	optical coherence tomography
PBS	phosphate buffered saline
PEG	polyethylene glycol
PTM	post-translational modification
RGD	arginine (R), glycine (G), aspartate (D); tripeptide motif
RHCI	recombinant human collagen type I
RHCIII	recombinant human collagen type III
SDS-PAGE	sodium dodecyl sulphate-polyacrylamide gel electrophoresis
SEM	scanning electron microscopy
STL	stereolithography
TCP	tissue culture plastic
TE	tissue engineering
TEM	transmission electron microscopy
TERM	tissue engineering and regenerative medicine
UA	ultrasonic atomizer
VEGF	vascular endothelial growth factor
WHO	world health organization

Table of Contents

Acknowledgements 3
Abstract 6
Samenvatting 8
Abbreviations 10
Table of Figures 17
1 General Introduction 20
1.1 Tissue Engineering 20
1.1.1 The Extracellular Matrix (ECM) 23
1.1.2 Biomaterials 25
1.2 Collagen 26
1.2.1 Collagen Families 27
1.2.2 Collagen Synthesis 28
1.2.3 Collagen Sources 33
1.2.4 Collagen crosslinking 39
1.3 Biofabrication, Bioprinting & 3D Printing Biomaterials 42
1.3.1 Extrusion-Based Bioprinting (EBB) 44
1.3.2 Droplet-Based Bioprinting (DBB) 46
1.3.3 Light-Based Bioprinting (LBB) 47
1.3.4 Multi-Modal Bioprinting 49
1.3.5 Aerosol Jet® Printing 50
1.4 The Cornea 53
1.4.1 The Anatomy of the Cornea 53
1.4.2 Corneal Injury, Pathologies, and Dystrophies 59

1.4.3 Visual Impairment, treatments, and surgical techniques 61
1.5 Cartilage 68
1.5.1 Composition and anatomy of articular cartilage ...68
1.5.2 Cartilage injury and pathologies 70
1.5.3 Cartilage mechanical behaviour....71
1.5.4 Cartilage tissue engineering....72
1.6 Research Hypothesis and Objectives 75
1.6.1 General Aim 75
1.6.2 Specific Objectives 77
1.6.3 Organization of the Thesis 78
2 The fundamentals of aerosol jet printing collagen and methods development....80
2.1 Introduction 80
2.1.1 An Introduction to aerosol jet printing....80
2.1.2 Aerosol jet printing, why haven't I heard of it?!....83
2.1.3 AJP as a bioprinting method for collagen 85
2.2 Materials and methods....87
2.2.1 Materials 87
2.2.2 Collagen extractions....87
2.2.3 AJP print program development and sample production 89
2.2.4 AJP scaffold stabilization....91
2.2.5 Differential Scanning Calorimetry (DSC) 93
2.2.6 Attenuated Total Reflectance Fourier-Transform Infra-red (ATR-FTIR) 94
2.2.7 Nanoindentation....95

2.3 Results 99
2.3.1 Collagen extractions 99
2.3.2 AJP print program 99
2.3.3 AJP scaffold stabilisation 101
2.3.4 DSC 103
2.3.5 FTIR 104
2.3.6 Nanoindentation 105
2.4 Discussion 106
2.5 Conclusion 110
3 High resolution bioprinting of recombinant human collagen type III for corneal tissue engineering 111
3.1 Abstract 111
3.2 Introduction 112
3.3 Materials & Methods 116
3.3.1 Materials 116
3.3.2 Production of AJP RHCIII samples 116
3.3.3 Optical Characterization 118
3.3.4 Physical characterization 119
3.3.5 Viscosity 121
3.3.6 SDS-PAGE 121
3.3.7 CD Spectroscopy 122
3.4 Results 122
3.4.1 AJP RHCIII sample production 122
3.4.2 Optical Characterization 123
3.4.3 Physical characterization 124
3.4.4 Viscosity 125

3.4.5 CD Spectroscopy 126
3.4.6 SDS-PAGE 126
3.5 Discussion 128
3.6 Conclusion 133
4 Bioprinting of collagen type I and II via aerosol jet printing for the replication of dense collagenous tissues 134
4.1 Abstract 134
4.2 Introduction 135
4.3 Materials and methods 139
4.3.1 Ink preparation 139
4.3.2 Aerosol jet printing of collagen type I and II 139
4.3.3 Post print processing of aerosol jet printed collagen type I and II 141
4.3.4 Viscosity 142
4.3.5 SDS-PAGE 142
4.3.6 Circular Dichroism 143
4.3.7 Nanoindentation 144
4.3.8 Swelling Ratio 145
4.3.9 Scanning Electron Microscopy (SEM) 145
4.3.10 Statistical Analysis 145
4.4 Results 146
4.4.1 AJP of collagen type I and II 146
4.4.2 Viscosity 146
4.4.3 SDS-PAGE 147
4.4.4 CD spectroscopy 148
4.4.5 Aerosol jet printing of collagen type I and II 149

4.4.6 Post print processing of aerosol jet printed collagen type I and II 149
4.4.7 Nanoindentation 150
4.4.8 Swelling ratio 151
4.4.9 SEM 151
4.5 Discussion 152
4.6 Conclusion 157
5 Concluding remarks and where the future lies for aerosol jet printing collagen 158
6 Appendices 165
6.1 Nanoindentation – Load-v-indentation graphs 165
6.2 Glycerol as a stabilizing agent 166
6.3 Preliminary Cell Culture on Aersol Jet Printed Collagen Type I and II 167
6.4 MATLAB® Code 170
6.4.1 Multi-layered circular sample toolpath generator 170
Bibliography 175
7 Curriculum Vitae 207
List of Publications 208

Table of Figures

Figure 1-1. Paradigm of tissue engineering illustration.....28

Figure 1-2. An illustration of interactions between a cell and the extracellular matrix. 31

Figure 1-3. (i) The Gly-X-Y sequence of the alpha chains (ii) post translational modifications, and (iii) a procollagen molecule.....35

Figure 1-4. The structural hierarchy of the major fibrillar collagens. 39

Figure 1-5. Reaction schematic for EDC/NHS crosslinking. 48

Figure 1-6. Illustration of some concepts of cell culture and bioprinting.....51

Figure 1-7. Extrusion bioprinting, and melt electrowriting 53

Figure 1-8. Droplet based bioprinting methods: (i) inkjet, and (ii) Microvalve printing. 54

Figure 1-9**.** Examples of light-based bioprinting methods: (i) LIFT, and (ii) Stereolithography. 56

Figure 1-10. A simplified view of an aerosol jet printer. 58

Figure 1-11: Diagram of the human eye and the cornea.....61

Figure 1-12**.** Treatments for corneal dystrophies 70

Figure 1-13. Optical Coherence Tomography (OCT) of the anterior cornea at 12, 24, 36, and 48 months post implantation for a BSS implant 73

Figure 1-14. Histology sections of adult bovine cartilage stained for (A) sulphated GAG content using Safarin O, (B) collagen and cells using H&E stain, and (C) a schematic of the cartilage zones. 77

Figure 2-1. A diagram of the aerosolization and deposition phases of aerosol jet printing. 89

Figure 2-2. (A) The Optomec® AJ300 aerosol jet printer at KU Leuven Campus De Nayer, (B) a view inside the AJ300, (C) the IDS Nanojet, and (D) the Gartner hype cycle 91

Figure 2-3. The scheme of the print program with even-numbered layers (2nd, 4th, ..) at 90° to the previous layer and odd-number layers rotated by the "angle of rotation" 97

Figure 2-4. SDS-PAGE gels of extracted (A) collagen type I, and (B) collagen type II. 106

Figure 2-5. (A) A print preview of a MATLAB-generated print program,and (B) the resultant 1 mm diameter sample after printing showing similar superficial patterning. 108

Figure 2-6. Image of aerosol jet printed collagen 108

Figure 2-7. AJP collagen stablization rating system. 109

Figure 2-8. DSC thermograms of aerosol jet printed RHCIII with acidic (non-fibrillar) and neutral (fibrillar) non-printed controls.....111

Figure 2-9. The average FTIR spectra negative controls, positive controls, and printed samples for collagen type I and II, and RHCIII.. 112

Figure 2-10. The average effective elastic moduli measured for (A) the non-crosslinked sample sets, and (B) EDC:NHS crosslinked collagen type II sample set. 113

Figure 3-1. (A) A crosslinked 7 mm sample swollen in PBS held on a corneal scalpel; (B) print lines in the centre of a sample (C) a failed sample, and (D) the transmission spectra of 7 mm samples measured. 131

Figure 3-2. (a) The indentation profile used in the study, (b) an indentation curve, (c) The average effective E of each sample from 25 indentations, and (d) An effective E map of a sample.....132

Figure 3-3. SEM images of 4.5 mm AJP RHCIII samples at the edges where they were torn apart. 133

Figure 3-4. CD spectra of untreated RHCIII and 2-hour sonicated RHCIII showing the characteristic collagen CD ellipticity.....134

Figure 3-5. SDS-PAGE gels of ultrasonically atomized RHCIII. ...135

Figure 4-1 A 6 mg/ml collagen type II 5.25 mm diameter sample after being removed from its print substrate post neutralization. .149

Figure 4-2. The dynamic viscosity of untreated collagen solutions and the same solutions after a 5-minute treatment with ultrasonic atomization in an aerosol jet printer. 155

Figure 4-3. Silver stained SDS-PAGE gels for detecting degradation of collagen of collagen type I (a) and collagen type II (b) from exposure to ultrasonic atomization 156

Figure 4-4. CD spectra of (a)collagen type I sonicated non-atomized, (b) collagen type I ultrasonically atomized, (c) collagen type II sonicated non-atomized, and (d) collagen type II ultrasonically atomized. 157

Figure 4-5. The average elastic modulus of each sample group measured by nanoindentation using a Hertzian model. 158

Figure 4-6. The average swelling ratio of each sample group ...159

Figure 4-7. SEM images of cross-sections from each sample group. 160

Figure 6-1. Examples of inaccurate, or bad indentations. 174

Figure 6-2 SDS-PAGE of collagen type I inks with and without glycerol after exposure to ultrasonic atomization 175

Figure 6-3. A H&E stained collagen type II 5.25 mm sample after 3 days of culture with 50,000 hPCs.....177

1 General Introduction

Parts adapted from:

Gibney, Rory; Ferraris, Eleonora; (2021) An Introduction to Tissue Engineering and Bio-printing; In: Arras, Peter & Luengo, David (Eds.) *Teaching and Subjects on Bio-medical Engineering: Approaches and Experiences from the BIOART-Project*, Ch. 24 p.286-301

Gibney, Rory; Ferraris, Eleonora; (2021) Bio-fabrication of Corneal Substitutes; In: Arras, Peter & Luengo, David (Eds.) *Teaching and Subjects on Bio-medical Engineering: Approaches and Experiences from the BIOART-Project*, Ch. 25 p. 302-316

"Bioprinting of collagen type I and II via aerosol jet printing for the replication of dense collagenous tissues"; Gibney, Rory; Ferraris, Eleonora; Frontiers in Bioengineering and Biotechnology 2021, 9:786945

1.1 Tissue Engineering

Tissue engineering (TE) is a relatively new form of engineering first described by R. Langer and J.P. Vacanti as 'an interdisciplinary field that applies the principles of engineering and life sciences towards the development of biological substitutes that restore, maintain, or improve biological tissue function or a whole organ' [1].The paradigm of TE is that of a circular process, illustrated in Figure 1-1, where i) a biopsy is taken from a patient and cells isolated, ii) those cells are then expanded in culture, iii) the cells are seeded onto a scaffold with signals, iv) the scaffold and cells are cultured until they mature into a tissue, and v) the tissue is implanted into the original patient [2]. The idea being to replace, regenerate, or re-store a patient's failing organ, or pathological

tissue using the patient's own cells, negating the need for donors, transplants, and the associated immunosuppressive drugs. As with any such illustration it can be guilty of simplifying the field and in such a quickly evolving field it is vulnerable to losing relevance, but the major points are still communicated. Some aspects of TERM such as the scaffold free cell therapies, of cell free regenerative medicine are excluded though these are not part of the scope of this thesis. Step 3 of the paradigm in Figure 1-1 illustrates the "three pillars of tissue engineering" where a scaffold, cells, and bioactive molecules are combined to develop a tissue, which has become the field of Biofabrication and is the main focus of this thesis [3].

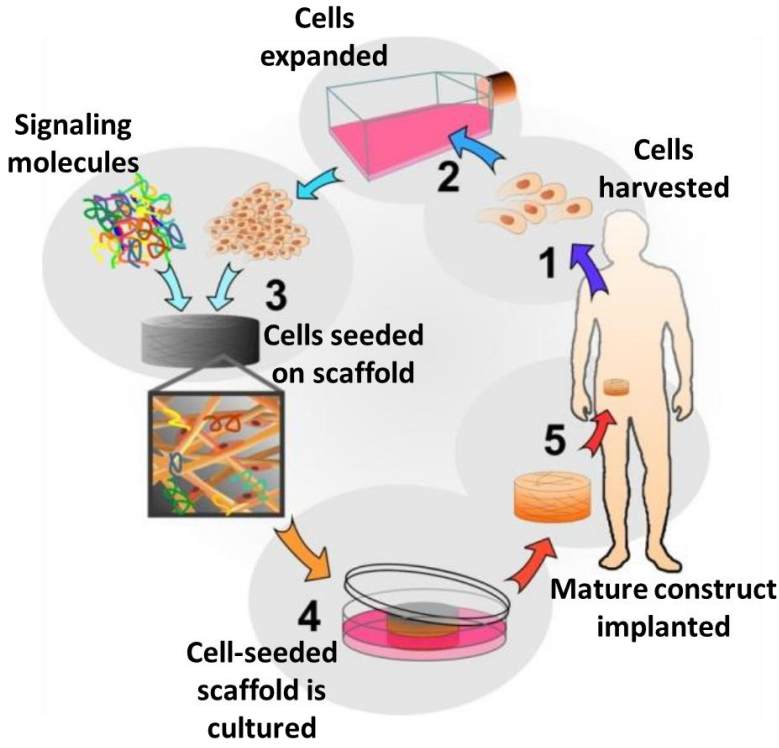

Figure 1-1. Paradigm of tissue engineering illustrating: 1, the explant of cells, 2, the expansion of those cells in culture, 3, cells are seeded on a scaffold in the presence of signalling molecules (growth factors, hormones, proteins, or even mechanical stimuli), 4 culture of the construct to tissue maturation, and 5, implantation of the mature tissue construct. Adapted from [2].

The cells typically used in TE are stem cells which can be differentiated into many different cell types using chemical and physical cues such as growth factors, and mechanical stimulation, respectively. Stem cells come in different potencies (capacity for differentiation and proliferation), the most potent also being the most controversial, embryonic stem cells, however multipotent adult stem cells, such as mesenchymal stem cells (MSCs), are the most commonly used stem cells in TE, though they don't escape controversy [4,5]. Once the cells are isolated from a patient, they are expanded in a tissue culture vessel containing culture medium. The vessel can be a tissue culture flask as depicted in step 2 of Figure 1-1, or a petri dish, whilst the medium is a liquid, buffered at a suitable pH, and containing the necessary ions, and nutrients to sustain the cells. Under these conditions, cells are expected to adhere to a surface of the culture vessel and grow in a monolayer until they reach a desired level of "confluence"; the amount of available surface that is covered with adherent cells. The cells are then harvested using trypsin, an enzyme that metabolises the proteins secreted by cells to attach to the vessel and each other, and re-suspended in fresh media. The re-suspended cells can then be counted, and subsequently used. Although this is a proven method for expanding cells, it is limited in two dimensions with cells only capable of re-producing in monolayers; thus, making it an inefficient and difficult way to generate 3-dimensional tissue.

A TE scaffold, put simply, should resemble a sponge; it is highly porous to allow media to access all volumes in the scaffold, and it has a high surface area to volume ratio [6]. Most human cells (apart from hematopoietic cells) require a suitable substrate so that they can attach and begin interactions, otherwise the cells become rounded and inactive (quiescent), though this is normal morphology for some cell types such as chondrocytes. At the scale of a cell, the perimeter of pores of a sponge-like TE scaffold can provide a continuous 2-dimensional substrate to which it can attach. Once attached to a TE scaffold the cells can then proliferate, differentiate and begin making their own matrix to take the place of the TE scaffold which should degrade slowly. One way of achieving this

sponge-like morphology is through the use of a class of materials called hydrogels. Hydrogels are made of a polymer network swollen with water, an everyday example being the dessert, jelly, which is made of a gelatin swollen in water. Although on the surface jelly does not appear very sponge-like, on the microscale and nanoscale it is filled with pores. The porous, heavily hydrated polymer network of hydrogels is a useful as mimic of the extracellular matrix (ECM) for tissue engineering. However, there are many other ways of creating porous scaffolds, such as gas foaming, salt-leaching, and biofabrication strategies such as bioprinting and electrospinning.

1.1.1 The Extracellular Matrix (ECM)

In order to understand cell attachment, it is necessary to understand how cells interact with their extracellular matrix (ECM). The ECM is the non-cellular component of tissues; a network of proteins, glycoproteins, proteoglycans, and polysaccharides that gives all tissue its physical shape and present biochemical and biomechanical cues to cells present in the tissue [7]. The composition of the ECM is specific to each tissue but some common components are the protein, collagen, and the glycoprotein, fibronectin [8]. Cells interact with their surrounding ECM through proteins in the cell membrane (cell adhesion molecules, CAMs, such as integrins) attaching to complementary sites in the ECM components, as seen in Figure 1-2 [9]. The complementary sites are usually in the form of short amino acid sequences, such as RGD, which is naturally present in fibronectin. TE scaffolds often use extracted ECM components, or synthetic 'motifs' (synthetic short peptide sequences similar to RGD), to exploit their capacity for cell attachment, or modify artificial polymers, such as PEG, with RGD or similar peptides to increase their capacity for cell attachment [10]. Other methods to improve cell attachment include increasing the hydrophilicity (or wettability) of a surface which is carried out on the plastic used to culture cells, TCP (tissue culture plastic), or coating a scaffold with in a thin layer of a biopolymer such as collagen [11].

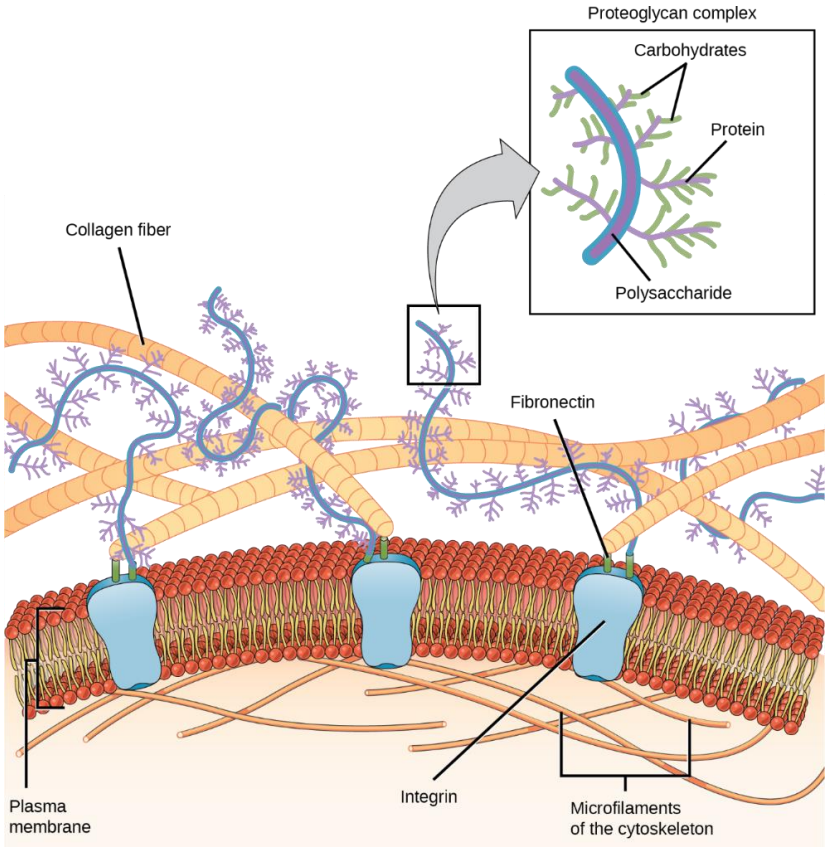

Figure 1-2. An illustration of interactions between a cell and the extracellular matrix. The cell membrane (plasma membrane) is made of a phospholipid bilayer with integral proteins, integrins mediating the interaction of the plasma membrane with proteins such as collagen, and proteoglycans. Attachment is often through glycoprotein, fibronectin. [12] *©2017 Rice University*

Once cells have attached to a scaffold then regulatory signals are often used to influence their behaviour. These signals can be in the form of chemicals added to the cell culture media (growth factors, biomolecules), mechanical stimuli, or electrical ward 2015 Growth factors are the most common signals. Growth factors are polypeptides or proteins (mostly) that are recognised by cells at their surface and induce intracellular signalling pathways that regulate the cell behaviour and development. For instance, vascular endothelial growth factor (VEGF) can stimulate vasculogenesis (the production of blood vessels) by vascular endothelial cells through inducing their

proliferation and promoting cell migration [13]. Vasculogenesis is one of the major challenges facing TE as it approaches questions of scalability, as capillaries need to be generated to deliver oxygen to the centre of scaffolds. Mechanical stimuli can also to direct the lineage of some stem cells, such as mesenchymal stem cells [14]. Electrical stimuli has been shown to enhance the differentiation and maturation of neurons and cardiomyocytes, respectively [15],[16]. This combination of cells, a scaffold, and signals illustrated in Step 3 of the paradigm in Figure 1-1, is often referred to as the "three pillars of tissue engineering" [3]. When a level of automation is included through bioprinting, electrospinning, or bioassembly, this is considered biofabrication. The level of automation in biofabrication has expanded relatively quickly from being employed solely for the manufacture of a scaffold, to being employed for scaffold fabrication, cell deposition, and fabrication of an encapsulating bio-reactor [17].

1.1.2 Biomaterials

The term biomaterial is used to refer to a wide range of materials including synthetic polymers, ceramics, and metals, along with biologically-derived materials, their unifying quality is that they are used to replace, restore, or regenerate tissue. However, the definition of a biomaterial is quite a contentious issue. A comprehensive and widely-accepted leading opinion paper on the definition of biomaterials was published by David F. Williams in 2009 [18]. The biomaterials used to build TE scaffolds must possess certain qualities, among which are that they must be biocompatible, and biodegradable [19]. For a material to be defined as biocompatible, the material, its metabolites and any leachates from production, must not be toxic to cells. Biodegradation is necessary so that the construct can slowly degrade and be absorbed by the recipient whilst cells in the construct, or recruited by the construct, replace the biomaterial with their own matrix. As stated previously, cell attachment is necessary for cells to remain active, hence cells should be able to attach to a biomaterial for it to be considered effective for use in TE. This is relatively straightforward for ECM-derived

biomaterials such as collagen and fibronectin since they possess CAMs, however, many biomaterials do not inherently possess CAMs. For these biomaterials the potential for cell attachment can be increased by, as mentioned earlier, increasing the hydrophilicity of their surface. Better still, they can be functionalised with CAMs such as the peptide sequence RGD [11].

1.2 Collagen

Collagens are a family of extracellular matrix proteins found in all metazoan ECM from sponges to humans. The first member of the collagen family (a collagen type IV variant) is thought to have evolved over 700 million years ago in the last common ancestor between metazoa, choanoflagellates and filasterean, and is regarded by some as having facilitated multicellularity [20]. From this first member of the collagen family the other members are thought to have evolved, which currently rests at 28 different collagens in mammals [21]. All collagens possess a characteristic right-handed triple helix structure which is assembled by three polypeptide chains, called α-chains, with left-handed polyproline structures. The α-chains may be identical, homotrimeric collagen type II & III, or a mix of two or more genetically distinct α chains, heterotrimeric collagen type I. The α chains have several domains, the most common being the collagenous domains which contain repeated Gly-X-Y amino acid sequences (shown in Figure 1-3) that lead to the formation of the triple helix, however these sequences are not unique to collagen and hence other proteins may be determined to be collagen-like or to have a collagen-like domain, such as the complement protein C1q or synthetic collagen-like peptides [22]. The X and Y positions in the Gly-X-Y collagenous domains are frequently filled by proline and hydroxyproline respectively, with hydroxyproline is so rare in non-collagen proteins that it serves as a proxy for measuring collagen content [23]. The collagenous domains of different collagens vary in length, accounting for up to 96% of the protein structure in collagen type I and just 10% in collagen type XII [24]. These domains may also contain interruptions to the Gly-X-Y sequence, where glycine is not in its expected location, as in collagen type IV which has around 20 of interruptions in its collagenous domains [25]. These characteristics

and the 42 genetically distinct genes by which the α chains are encoded, discern the different collagen types from each other.

The nomenclature of collagen appears to be in order of discovery with the use of roman numerals first used to distinguish collagen type II, and then to distinguish what had been known as collagen, collagen type I, and thereafter being used to describe newly discovered collagens. The nomenclature of α chains is αn(N), where n is a number between 1 and 6 and N is the roman numeral of the associated collagen type; the n does not reflect on any similarities between the α chains in different collagen types, i.e. the α-1(I) chain is the no more similar to the α-1(IV) chain than it is to the α-2(I) or α-2(IV) chain [26].

1.2.1 Collagen Families

The collagen family is divided into sub-families based common traits, such as the fibrillar collagens, the basement membrane collagens, and the fibril-associated collagens with interruptions (FACITs). The fibrillar collagens are the most common collagens, and are of the most interest to this work exploring dense collagenous tissues such as the corneal stroma, and articular cartilage. The properties one typically associates with collagen are mostly the properties of the fibrillar collagens, and henceforth the term collagen is used to refer to fibrillar collagens unless stated otherwise. The structure of the fibrillar collagens is dominated by a long collagenous domain. They assemble into fibrils with light and dark patches (cross-striation) giving rise to a unique banded pattern every 64-67nm, dependent on the collagen type, though this can also vary due to the SEM/TEM preparation method [27,28]. The fibrillar collagens consist of collagen type I, II, III, V, XI, XXIV, and XXVII. Collagen types I, II, and III, are often referred to as the major fibrillar collagens due to their abundance, whereas collagens type XXIV and XXVII are outliers within the fibrillar collagens because they have a much shorter collagenous domain and have some interruptions [28,29]. Basement membranes collagens (collagen type IV, VII, XXVIII) form meshed fibrillar networks that act as a substrate for cells in many tissues, such as Descemet's Membrane in the cornea which

acts as a substrate for the corneal endothelium. FACITs do not form fibrils, but associate themselves with fibrils, often with a collagenous domain attached to the outside of a collagen fibril and separate domain sticking out, believed to facilitate interactions between the fibrils and proteoglycans [29,30]. Other sub-families of collagens include the beaded filament collagens, the transmembrane collagens, and short-chain collagens which are discussed in the following collagen review articles and books [20,24,27,28].

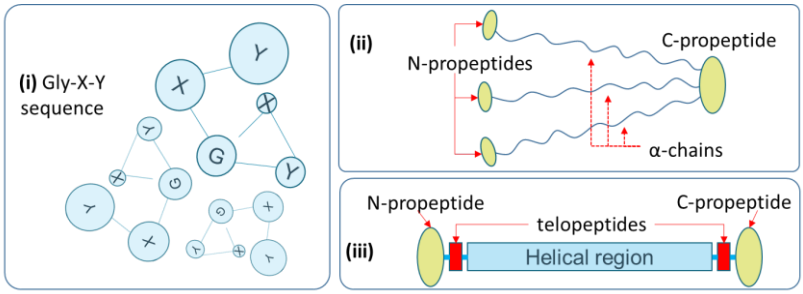

Figure 1-3. (i) The Gly-X-Y sequence of the alpha chains with only glycine occupying the inside of the helix due to stoichiometry. (ii) PTMs occur before the alpha chains become interweaved into a triple-helix but may still occur after the association of their C-propeptides. (iii) The triple helix formation results in a procollagen molecule with propeptides, and short telopeptides at either end of the collagenous domain.

1.2.2 Collagen Synthesis

All fibrillar collagens are synthesized in the form of a soluble precursor known as a procollagen which is essentially a collagen molecule with globular N- and C- terminus propeptides attached, as seen in Figure 1-3. The procollagen propeptides are formed by the assembly of propeptides in each collagen α-chain that makes a collagen molecule and they play vital roles in collagen synthesis [31]. The C- terminal propeptide plays a particularly important role during collagen synthesis. The amino acid sequence of the C-propeptides is highly conserved among the different procollagen α-chains of the fibrillar collagens apart from a sequence of 15 amino acids which allow the relevant α-chains from each collagen type to recognise each other, thereby preventing α-chains from different collagens associating with each other, and thereby allowing cells to simultaneously produce different collagens [32]. Once the C-propeptides from 3 procollagen α-chains recognise each other, they

form a trimer with free floating α-chains as seen in Figure 1-3. From there the α-chains begin folding in the C to N direction to form a triple helix, though this is not the case for some transmembrane collagens [27,33]. Alpha chains have also been shown to associate and form triple helices in propeptide-free recombinant collagen [34]. Hence, the triple helix initiation by propeptide may not be essential to triple-helix formation but it appears essential to the simultaneous production of multiple collagens [35]. Before the formation of the triple helix a number of post-translational modifications (PTM) are carried out on the α chains. One of the more prevalent PTMs is the hydroxylation of proline residues in the Y-position (of the Gly-X-Y amino acid sequence) into 4-hydroxyproline by prolyl 4-hydroxylase, which is essential to the stability of the collagen triple-helix [36]. Hydroxyproline accounts for 90-150 residues per 1000 in collagen (depending on the collagen type) which is all formed by proline hydroxylation [37]. A far less common PTM is the hydroxylation of proline residues in the X-position by prolyl 3-hydroxylase into 3-hydroxyproline, which occurs in just a few collagens, predominantly in type IV, but also in some other collagens at a rate of a 1-6 residues per 1000 [38].

As mentioned previously, 4-hydroxyproline is believed to stabilise the collagen triple helix, however, there is less consensus over the function of 3-hydroxproline [39]. Yet, the evidence suggests that 3-hydroxyproline is vital since it is conserved in collagens throughout the animal kingdom and in humans the absence of 3-hydroxyproline has been attributed to recessive osteogenesis imperfecta [38]. Other PTMs include the hydroxylation of lysine residues, and the glycosylation of lysine and hydroxylysine residues, respectively, which are key to native crosslinking [40]. The formation of the triple helix renders the residues inaccessible to the PTM enzymes, and hence no PTMs are performed once the triple-helix is formed [24]. The folding of the triple helix in a procollagen molecule is unstable at physiological temperatures. Hence molecules, such as the procollagen-specific chaperone molecule heat-shock protein 47 (HSP47), associate with the procollagen molecule during and after triple helix formation in the endoplasmic reticulum to prevent

denaturation. It has been shown to take over 20 HSP47 molecules to stabilise a single procollagen molecule at physiological temperature, and that a disruption to the HSP47 encoding gene is lethal to embryonic development in knockout mice [41,42]. “Collagen trafficking” describes the transit of procollagen molecules with the help of HSP47, other chaperones and vacuoles from the endoplasmic reticulum, to the Golgi apparatus, and eventually the plasma membrane [43]. During, and after, collagen trafficking, the procollagen propeptides are cleaved by proteinases at different times depending on the propeptide and the collagen type [31]. Propeptide cleavage leaves a mature collagen molecule (a tropocollagen) with a long collagenous domain with short telopeptides on both termini which can then proceed to fibrillogenesis. However, collagen type III with its N-propeptide still attached (pNcollagen type III) is regularly found in some fibrils with it believed to play a role in regulating fibril diameter through steric hindrance or another unknown mechanism [44]. It is necessary to distinguish fibrillogenesis in vivo and in vitro as though the process is similar the stimuli are different in each case.

1.2.2.1 Collagen fibrillogenesis in vivo and in vitro

Fibrillogenesis is the process by which mature collagen molecules, tropocollagen, achieve a higher state of entropy by forming superhelical self-assembles that internalise the hydrophobic regions of different collagen molecules, whilst hydrophilic parts interact with each other and ions in solution [45]. This is driven by the fact that tropocollagen is unstable under physiological conditions, but there are also several other stimuli and actors involved in fibrillogenesis *in vivo*. In the superhelical self-assemblies, fibrils, collagen molecules assemble adjacent to each other staggered by around a quarter length of the molecule, first forming an intermediary superhelical structures, microfibrils, so that it remains stable, before eventually forming a larger superhelical structure, a fibril, similar to the 2-dimensional representation seen in Figure 1-4 [33,46]. The characteristic D-banded pattern of collagen fibrils seen in Figure 1-4 arises from this molecular packing model, with alignment of systemic repeats of the 0.46 D gap and 0.54 D

overlap accounting for the light and dark patches, respectively. “D” is the period of this pattern, and is often measured to be 64-67 nm in length using transmission electron microscopy, with variations arising from the preparation method.

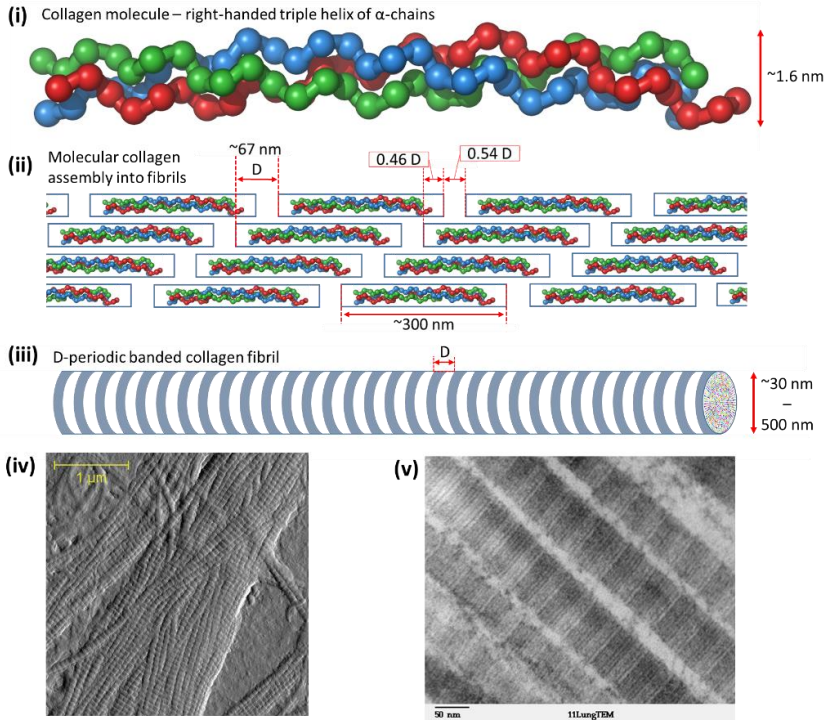

Figure 1-4. The structural hierarchy of the major fibrillar collagens, (i) illustrates the assembly of three left-handed helical α-chains into a right-handed triple helix of around 300nm in length, (ii) a schematic of collagen fibrillogenesis showing the stacking of collagen molecules side-by-side and end-to-end, (iii) the resultant a D-banded collagen fibril from fibrillogenesis. Microscopy images of collagen fibrils: (iv) AFM of collagen fibrils made in vitro by osteoblasts [53]*, and (v) TEM of collagen fibrils in lung tissue banded collagen (scale bar: 50 nm).*

The graphical representation in Figure 1-4 is similar to what is normally used to describe collagen fibril molecular packing in most literature, but the 3D molecular packing of a microfibril, first described in 2006, treats the molecules less as parallel straight rods and more similar to a single fibre woven into a thread [47]. This model, revealed with electron density mapping also showed that the microfibrils interdigitate with other microfibrils with the molecular

interaction occurring in the telopeptides. There is also evidence that 3-hydroxproline residues align in microfibrils, suggesting that their enigmatic role could be related to fibrillogenesis [38,48].

The location for in vivo fibrillogenesis is still debated, with evidence for it occurring in multiple locations outside the cell, in vacuoles within the plasma membrane, and in Golgi-to-plasma membrane carriers (fibripositors) [43,49]. However, in contrast to the thermodynamically driven self-assembly of collagen molecules into fibrils by themselves in vitro, in vivo fibrillogenesis has been shown to require the presence of fibronectin, integrins and collagen type V, at least in the case of collagen type I [50]. It is suggested that integrins and fibronectin combine to provide and temporary surface from which fibrils can grow with collagen type V acting as a nucleator for collagen type I fibrils, and possibly similarly with collagen type XI acting as a nucleator for collagen type II fibrils [50–52]. This would explain why collagen fibrils formed in vivo are heterotypic, and might partially explain why it is difficult to replicate the mechanical strength of native fibrils with fibrils formed in vitro.

In vitro fibrillogenesis is mainly controlled by pH, ionic strength, and temperature, other influencing factors include the collagen concentration, ion species, surfactants, and saccharides present, and the presence/absence of telopeptides [54,55]. It is thermodynamically driven process; collagen at an acidic pH is far below its isoelectric point (pI) inducing individual collagen molecules to have a surface charge and allowing them to distribute evenly in the solution. Raising the pH using an alkali brings the collagen closer to its pI, and the addition of salts (buffers), particularly phosphate salts lowers the pI to the point where the electrostatic forces can no longer overcome aggregation [56,57]. The collagen molecules then precipitate and aggregate staggered side-by-side same as in vivo. Native type fibrils with characteristic D-banding begin to form within the pH range of 5.0 – 8.5, ionic strength between 0.1 and 0.8 [54], and temperatures from 4°C to 37°C [58]. However, unlike fibrils formed in vivo, fibrils formed in vitro can lack the characteristic D-banding, usually in conditions that are unfavourable for fibrillogenesis [54,59]. Experimenting with the various influences of

fibrillogenesis can elucidate different fibrillar architectures, in terms of fibril length, thickness, mechanical properties and polydispersity. The presence of divalent phosphate ions have shown to have a major influence on collagen precipitation with some reporting the formation of salt bridges within fibrils between positively charged amino acid residues [60]. There is a close relationship between time and temperature in respect to fibril formation, with lower incubation temperatures requiring much longer incubation times; at least 15 hours at 4°C compared to around 30 minutes or more at 37°C [58]. This is further reflected in the fibril morphology and stiffness with fibrils formed at lower temperatures often thicker, shorter and stiffer than their counterparts at 37°C or room temperature [58]. In terms of mechanical properties, telocollagen forms far stronger fibrils than atelocollagen, likely due to it being a closer mimic of in vivo fibrillogenesis, and it at least allows the possibility of intermolecular interdigitation of telopeptides, similar to that mentioned in vivo.

1.2.3 Collagen Sources

With collagens present in all metazoa, and the genes responsible for all collagens known, there are many conceivable sources of collagen but the most common sources of fibrillar collagens are from animals, from cells in vitro, and from genetically modified organisms.

1.2.3.1 Animal-Derived Collagens

When sourcing from animals, it is important to find an accessible collagen rich tissue from which the relevant collagen can be extracted, hence the hides or tendons of commercially farmed animals (pigs, sheep, and cows) are commonly used to extract collagen type I, whilst collagen type II is sourced from their cartilage. Some waste products of food processing, such as fish scales can also be used as a collagen source, however the thermal properties of fish scale collagen varies significantly depending on species and only a few reported species have thermal properties similar to mammalian collagens [61]. Arguably the most common animal-derived collagen has been rat-tail collagen type I due to the ease of its extraction due

to its high purity, and the availability of rat tails in a biomedical lab [28]. Once a highly collagenous animal tissue is sourced there are two usual methods of extraction, acid solubilisation and pepsin-solubilisation. Acid solubilisation attempts to disrupt collagen fibrils by lowering ionic strength of the solution below collagen's pI so that collagen molecules can swell and separate. This results in collagen with intact telopeptides (telocollagen) in solution, however the many intermolecular lysyl oxidase crosslinks present between the telopeptides are not affected by the acid. Hence a lot of collagen remains in the form of insoluble supramolecular assemblies held together by crosslinks, and in soluble small dimers, and trimers of molecular collagen. The insoluble collagen and insoluble contaminants are usually removed by centrifugation. Once the collagen is in solution the salt precipitation method is used to separate the collagen from other contaminants. This method adds salt, usually NaCl, in an effort to raise the ionic strength of the solution to the pI of collagen, thereby inducing the precipitation of fibrils. Once the fibrils precipitate, they float on the surface of the solution and can be collected using a sieve. The fibrils can then be washed and re-solubilised to achieve a collagen solution of a relatively high purity. Centrifugation can be used to remove remaining contaminants, and the salt precipitation can be repeated to improve the purity. Pepsin-solubilisation is similar to acid-solubilisation with the addition of a pepsin-digestion step. Pepsin is an enzyme found in most mammalian stomach linings, hence it has a peak activity at a pH close to that of the mammalian stomach ~pH 2. It metabolises most protein structures except for triple helices. When used to extract collagen, the process is quite similar to acid-solubilisation with the added step of a pepsin digestion. During the pepsin digestion, pepsin cleaves most of the non-collagenous telopeptides, yielding atelocollagen, meaning that most intermolecular crosslinks are removed and resulting in a higher yield of soluble collagen compared to acid-solubilisation alone. However, atelocollagen forms weaker fibrils and weaker collagen hydrogels.

Animal-derived collagens have been used in biomedical implants for quite some time from decellularized xenografts that are

predominantly made of collagen like the Artefact® vascular graft (bovine carotid artery)[62], to devices that are made from extracted animal derived collagens, such as Collacote®, a collagen sponge for wound dressing. However, the possibility for interspecies disease transmission and allergic or immune reactions can make animal derived collagens less desirable [63], hence collagen is also sourced from humans. The most common source of human collagen is the placenta/amniotic membrane, from which several collagens can be extracted namely collagen type I, III, and IV, however these may still illicit an immune response. Another frequent concern over extracted collagens is batch-to-batch variability which may be addressed by rigorous extraction protocols, but it remains difficult to rule out variations in the source tissue.

1.2.3.2 Collagens produced in vitro

Cultured mammalian cells can be induced to produce collagen, particularly neo-natal fibroblasts for collagen type I and chondrocytes for collagen type II. This is highly useful for the production of human collagens which are necessary for research but that are naturally hard to come by due to the huge ethical and moral implications of using human tissue as a source of materials. Since the cultured cells possess the various enzymes and chaperones for collagen synthesis, there is also less of a concern over the hydroxylation and/or glycosylation of proline and lysine residues in the synthesized collagen compared to recombinant collagens. However, in vitro production of collagen is dependent on the 2D culture system of culturing cell which requires a lot of resources and is not a very efficient method of production. Collagen type I produced by neo-natal fibroblasts is commercially available from a number of large producers such as Sigma Aldrich (C2249), and Advanced Biomatrix (VitroCol®) and has been used in a number of publications [64,65]. However, likely due to their high cost, these collagens produced *in vitro* are more often used for dilute collagen coatings to improve attachment rather than as scaffold materials.

1.2.3.3 Recombinant Collagens

Recombinant proteins are produced by inserting the relevant gene for the desired protein into a host organism, resulting in a purer product in contrast to extracted proteins and the capability to experiment with the amino acid sequence through gene modification. Recombinant collagens have received growing interest due to these capabilities and due to the elimination of the possible risks associated with the use of animal-derived collagens in humans (disease transmission, allergens, pathogens, immunogenicity) [63]. The host organism selected for recombinant proteins is usually a single-celled organism that is well studied and is easily grown in large quantities, usually within a bioreactor rather than the 2D culture flask system. Both prokaryotes (E. coli [35]) and eukaryotes (pichia pastoris [66]) have been used to produce various recombinant collagens, however some multi-celled organisms have also been used to produce recombinant collagens, such as tobacco plants [67]. These single-celled microorganisms lack the environment, various enzymes and other proteins that facilitate collagen production and perform the post-translational modifications (PTMs, aforementioned in 1.2.2) that are carried out in metazoan collagen synthesis. PTMs are very important for collagen stability, fibril mechanics and a number of forms of osteogenesis imperfecta (OI) are associated with incomplete PTMs [68]. Thus, recombinant collagen production requires the insertion of several genes alongside the genes for the relevant collagen.

The first reported case of recombinant collagen production with levels of 4-hydroproline residues close to that of human collagen was achieved by the co-expression of prolyl 4-hydroxylase alongside α1(III) (the α-chain of collagen type III) in yeast (pichia pastoris) [66]. However, it contained no hydroxylysine residues, and no telopeptides, due to the use of pepsin to process procollagen(III) into RHCIII [35]. 3-hydroxyproline is not known to occur mammalian collagen type III, so the possible complications arising from its absence associated with other fibrillar collagens were avoided [38]. The co-expression of HSP47 did not seem to be necessary despite its importance to collagen synthesis in vivo outlined earlier in 1.2.2. This

could potentially be due to the lower temperature of the production, 30°C, and the presence of glycerol in the culture media, which is known to increase the thermal stability of collagen [69,70]. An international patent was lodged in 1997 by Fibrogen®(US) and the Academy of Finland on this expression system [71]. The same expression system was also applied to the production of other fibrillar collagens, a homotrimeric version of collagen type I, and collagen type II, though these resulted in lower yields [72,73]. The production technique was later commercialised and the culture was moved from a shaker-flask system to fermentation vessels where higher cell densities and higher expression levels could be achieved [74]. Although there is no published data on the RHCIII yields, the same system was optimised to give yields of up to 500 mg homotrimeric collagen type I per litre of culture, and given earlier results, RHCIII yields would be expected to be higher [74]. A surprising finding of their studies was that the co-expression of prolyl 4-hydroxylase and proα-chains increased the half-life of prolyl hydroxylase from around ~50 minutes with no proα-chains to ~12.5 hours when expressed with proα1(III) [72]. This effect of increasing the prolyl 4-hydroxylase half-life was less pronounced for proα1(I) and proα1(II), which was likely a major contributor to their reported lower levels of hydroxylation and lower yields [73]. Fibrogen's RHCIII has been investigated in the form of a hydrogel for corneal tissue engineering/regeneration, and seemed to succeed in a 4-year proof-of-concept clinical trial with 10 patients [75].

Further mimesis of collagen PTMs was achieved in Nicotiana tabacum(tobacco plants) by co-expressing human prolyl 4-hydroxylases (α and β) and lysyl 3-hydroxylase with α1(I) and α2(I) leading to recombinant human collagen type I [67]. This led to efficient proline hydroxylation, and efficient hydroxylation and glycosylation of lysine residues by lysyl 3-hydroxylase. Ficin was used for propeptide cleavage, and it would be expected that this enzyme would also cleave the telopeptides, but this was not explicitly stated. The collagen was extracted from the tobacco plants by harvesting the leaves with approximately 200mg of collagen produced per kilogram of tobacco leaves [67]. This has developed commercial

operations becoming Collplant Ltd. and has recently been investigated as an injectable hydrogel for tissue repair [76,77]. PTMs have also been replicated in E. coli using prolyl and lysyl hydroxylases encoded by the giant virus, Mimi-virus. Rutschmann et al. achieved levels of prolyl and lysyl hydroxylation in recombinant human collagen type III similar to that of native human collagen type III, however, in contrast to the previous examples they produced telocollagen by excluding the propeptide gene sequences [35]. The exclusion of the propeptide sequences did not appear to affect the assembly of the triple helix or the solubility of the collagen produced. Circular dichroism and enzymatic digestion were used to exhibit the triple-helical nature of the collagen produced. The yield of RHCIII produced by E. coli was reported to be up to 90 mg per litre of culture, which though impressive, does put it far behind that of Fibrogen, albeit with a closer replication of native collagen type III. It is not known whether recombinant collagen production in E. coli has advanced into commercial operations.

1.2.3.3.1 Recombinant Collagens Economic Viability

A common limiting factor to the uptake of recombinant collagens has been their cost [78]. Most recombinant proteins cost a few hundred euros for a few micrograms of the protein. The efficiency of Fibrogen's method RHCIII dramatically changed this trend with 100 mg costing $315 in 2014, but by 2016 Fibrogen had ceased distribution of their RHCIII. Similarly, Collplant, initially distributed their RHCI through Sigma Aldrich with 15 mg costing €230 but this was discontinued in 2017/2018 due to it having no economic viability. Collplant pursued the use of their material to develop of medical devices, such as those highlighted earlier, in collaboration with pharmaceutical companies, such as AbbVie Inc [79]. with whom they recently struck a deal to give AbbVie exclusive access to their RHCI . A similar motive could be behind Fibrogen's decision to cease supply of RHCIII. Upon realising Fibrogen's departure from distribution in 2016, a procurement procedure was initiated in this project to find the most feasible replacement supplier. The new suppliers had much higher prices but eventually MyBioSource Inc. (San Diego, USA) was found to be the most feasible supplier; 10 mg

cost €329. However, by 2020 MyBioSource also ceased distribution along with all other RHCIII distributors considered in 2016 apart from Abcam, who then discontinued RHCIII in the new year. Though there are a few producers of recombinant human collagen type III using other expression systems (wheat germ, E. coli), none are at prices that could be considered feasible for use in bioprinting. It is not clear whether there are any companies currently distributing RHCIII using Fibrogen's pichia pastoris expression system.

1.2.4 Collagen crosslinking

Crosslinking is a method by which intramolecular and intermolecular covalent bonds are introduced to further stabilise the collagen triple helix and fibril assemblies both in vivo, and in vitro.

1.2.4.1 In vivo crosslinking

Most crosslinking in vivo occurs due to the action of the enzyme lysyl oxidase (LO). Lysyl oxidase converts the carboxylic group in the side chains of selected lysine and hydroxylysine to an aldehyde [80]. Due to the tight winding of the triple helix, the non-collagenous telopeptides are a preferable substrate for LO. Intramolecular bonds are formed via aldol condensation reaction between the aldehyde forms of lysine and hydroxylysine between the telopeptides of alpha chains within the same collagen molecule. Intermolecular bonds form during fibrillogenesis via the same aldol condensation reaction but either end to end between aligned telopeptides or between the telopeptide of one collagen molecule and the triple helix of the adjacent quarter-staggered collagen molecule. Sugar mediating crosslinking causes the stiffening of many collagenous tissues with aging and has also been associated with the increased brown pigmentation of these tissues with age. It has been attributed to the low turnover rate of collagen and the accumulation of reducing sugars leading to glycation of the collagen with prolonged exposure and the formation of advanced glycation end products (AGEs). The base level of reducing sugars, glucose and ribose, is a risk factor of the formation of AGEs which puts patients with diabetes-related hyperglycaemia at an increased risk[81].

1.2.4.2 In vitro crosslinking

In vitro crosslinking is often performed on collagen gels to increase their stability and mechanical strength, these may be physical, chemical, enzymatic or photo-reactive crosslinks. Crosslinking with lysyl oxidase cannot be replicated in vitro [82]. Fibrillogenesis is often referred to as a form of physical crosslinking, although no covalent bonds are formed. Most chemical crosslinks occur between a free carboxylic group usually on aspartic acid or glutamic acid residues, and the free-amine group of a lysine or 4-hydroxylysine residue, the resultant bond may incorporate a residue of the crosslinking agent, or it can result in a "zero-length" crosslink [28,83]. Some of the most common crosslinking agents are the aldehydes, and the carbodiimides. Glutaraldehyde is the most commonly used aldehyde and is a potent crosslinking agent of collagen hence its use in tissue fixing agent, however it is associated with cytotoxic effects [84]. The cytotoxic effects may be due to unreacted glutaraldehyde which is difficult to completely eliminate, or due to the degradation products from residual glutaraldehyde in the resultant crosslink [85]. EDC (1-ethyl-3-(3-dimethylaminopropyl) carbodiimide), usually in the form of a hydrochloride, is the most commonly used carbodiimide. Carbodiimides result in "zero-length" crosslinks, i.e. through a series of substitution reactions they lead to the formation of peptide bonds with no residual carbodiimide in the resultant molecule [83]. This is done through the formation of a transient adduct between EDC and the carboxyl group of one protein, an O-acylisourea derivative, which then undergoes a substitution reaction with free-amine group of a lysine or hydroxylysine on another protein. However, the O-acylisourea intermediate is quickly hydrolysed in aqueous solutions, hence EDC is often used with NHS (N-hydroxysuccinimide) which reacts with the unstable O-acylisourea intermediate to form a more stable amine-reactive NHS ester which will form a peptide bond with another protein [83]. After crosslinking the construct must be extensively washed, often with buffer such as 1XPBS containing glycine, to react with and remove any residual EDC which is cytotoxic. The EDC-NHS method of crosslinking is also highly useful for protein synthesis and

modification. Other crosslinking agents include plant-derived crosslinking agents such as genipin, and 4-star poly(ethylene glycol) ether tetra succinimidyl glutarate [86].

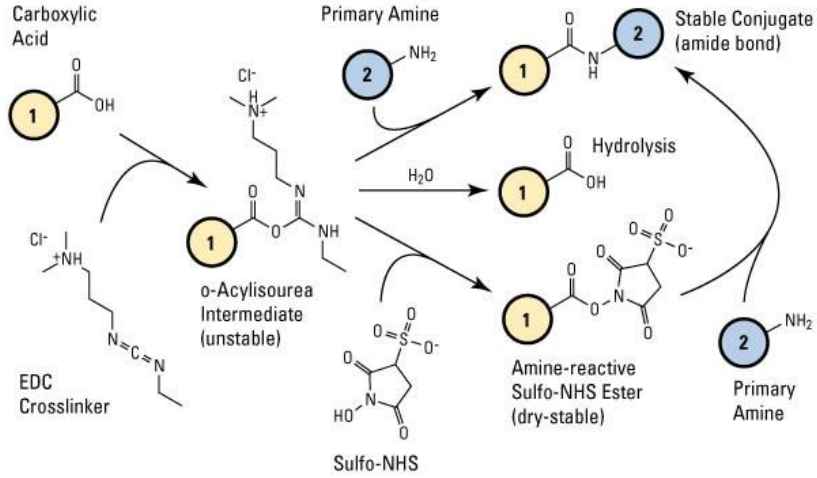

Figure 1-5. Reaction schematic for EDC/NHS crosslinking illustrating the formation of the O-acylisourea derivative, and how it can react with NHS to lead to a more stable amine-reactive molecule, thereby preventing the hydrolysis of the O-acylisourea derivative [87].

1.3 Biofabrication, Bioprinting & 3D Printing Biomaterials

The term biofabrication first appeared in published literature in 1985 in reference to the regeneration of the ocular surface using collagen gels [88], since then it has been used loosely to describe TE processes but also the fabrication of materials by living organisms [89–91]. However, efforts have been made within TE community define the term and related terminology. Biofabrication has had a dedicated journal since 2009 and an international society, the ISBF, since 2010 which has been the most credible source for these definitions. In 2016 the ISBF published a paper in the Biofabrication journal which aimed to clearly define biofabrication terminology. It defined biofabrication as "*the automated generation of biologically functional products with structural organization from living cells, bioactive molecules, biomaterials, cell aggregates such as micro-tissues, or hybrid cell-material constructs, through bioprinting or bioassembly and subsequent tissue maturation processes*" [92]. The terminology used in biofabrication has been given particular importance due to the fast growth of the biofabrication field with researchers from different backgrounds, and the ability of some biofabrication techniques, such as bioprinting, to gain attention in the media and capture the public's imagination which presents ethical challenges for researchers [93]. Bioprinting is a branch of biofabrication defined as the automated deposition of living and non-living materials in a prescribed geometry for the production of bioengineered structures [93]. However, there has been some confusion in the field regarding this definition, with many assuming that the term bioprinting could only be applied to the deposition of cells, but this has never been the consensus within the biofabrication community. According to the community, bioprinting has always included approaches where material to which cells easily attach (fibronectin, collagen, antibodies) are deposited and later cultured with cells to facilitate cell patterning [94]. Then in 2009, the definition of bioprinting was expanded to include the deposition of non-living materials (i.e. synthetic polymers and inorganic material) for the purpose of biofabrication [95].

The way in which cells are incorporated into a bioprinted structure varies, from simply seeding cells onto a scaffold, to bioprinting cells or cell spheroids of a single cell type, to the precise deposition of specific cell types in specific patterns to illicit the maturation of a particular tissue. Should an ink contain cells, it is referred to as a bioink, whereas an ink containing a hydrogel/hydrogel-precursor intended to be printed alongside a bioink, or for cell seeding is referred to as a biomaterial ink [96]. Conventional inkjet printers were used as the first bioprinters. Robert J. Klebe performed the first case of bioprinting, or 'cytoscribing' in 1988 by filling the inkjet cartridges of two HP printers with a fibronectin solution, and a solution containing monoclonal antibodies, thereby creating a substrate to which cells could specifically attach in subsequent culture [97]. The first cell printing was performed by Boland & Wilson in 2003 using the firmware and parts from a HP660C inkjet printer but with a modified dispensing system to allow the use of wider nozzles through which large mammalian cells could pass [98]. Since then, the field of bioprinting has expanded at a remarkable pace with several printing technologies, each of which have their own particular advantages and drawbacks. Bioprinting technologies can usually classified as one of the following: extrusion-based bioprinting (EBB), droplet-based bioprinting (DBB), and laser-based bioprinting (LBB) [99]. More recently, there has been the development of multi-modal printers which integrate different types of print-heads and printing technologies into one system to fulfil multiple needs.

Similar to regular 3D printing, bioprinting frequently makes use of different inks for different purposes within the same print. A sacrificial ink is an ink that may be used to support in voids within a scaffold and prevent the surrounding material from collapsing into the void. The sacrificial ink can then be removed afterwards usually using a solvent or conditions, to which only the sacrificial ink is vulnerable. A cell carrier ink, is a bioink that contains cells, but may not have sufficient matrix materials to support itself or an entire scaffold. These are often used where the biomaterial used as the main structural component of the scaffold cannot be printed with

cells; thermoplastics such as polycaprolactone. Printing methods have also been developed where the whole scaffold is printed within a support bath made of a thixotropic hydrogel/hydrogel suspension.

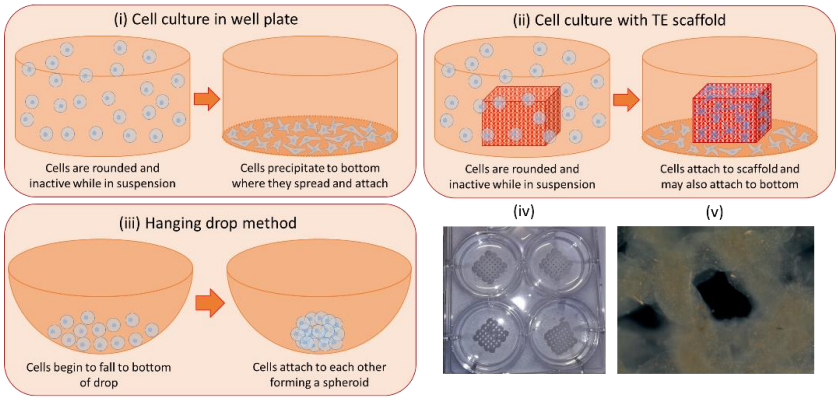

Figure 1-6. Illustration of some concepts of cell culture and bioprinting. (i) cells precipitate out of suspension when left in a well plate and attach to the bottom, (ii) when cells are incubated with a suitable TE scaffold the cells attach to the scaffold, (iii) the hanging drop method for forming cell spheroids. (iv) An example of bioprinted scaffolds for TE, and (v) a microscope image of an acellular TE scaffold.

Cell aggregates are structures composed of cells loosely bound to each other, typically by ECM biopolymers secreted by the cells. A monolayer of cells grown in a tissue culture vessel can be broken up into aggregates by harvesting them without the use of ECM degrading enzymes, like trypsin. However, using this method the aggregates are randomly sized. A popular method for producing more consistent spheroid-shaped cell aggregates (cell spheroids) is the hanging drop method illustrated in Figure 1-6 [100]. The cell spheroids are formed by pipetting a cell suspension, in small amounts with an estimated number of cells, on to a petri dish which is then inverted. Gravity allows the cells to settle out of suspension and form a cluster at the bottom of the droplet, away from the TCP. The cells, without a substrate for attachment, attach to each other and begin forming some matrix resulting in a cell spheroid.

1.3.1 Extrusion-Based Bioprinting (EBB)

EBB is the most common type of bioprinting due to the simplicity of its design. EBB typically loads an ink, usually a hydrogel/hydrogel-

precursor, into a syringe, which is then extruded through a nozzle by applying a force by mechanical or pneumatic means, as seen in Figure 1-7.

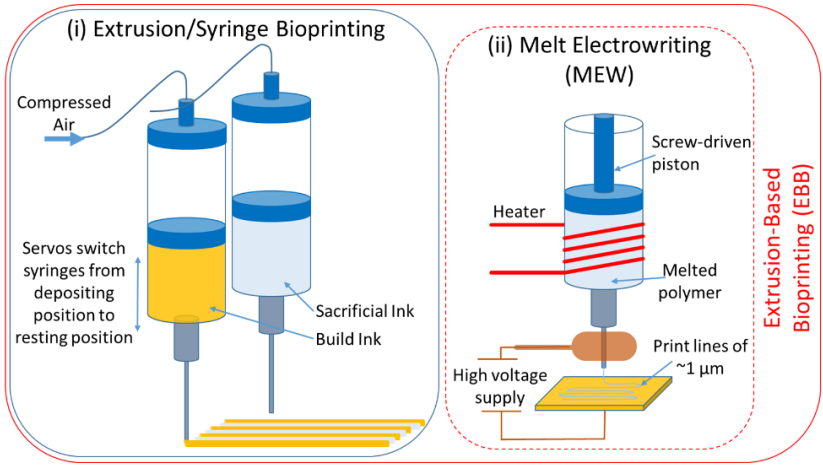

Figure 1-7. (i) Extrusion bioprinting usually involves more than one printhead, with a build ink which will form the end-construct, a sacrificial ink, which is removed after printing, and a cell carrier ink. (ii) Melt electrowriting involves melting a polymer and extruding it through a nozzle attached to the anode of a high voltage power supply, and the build platform attached to the cathode, leading to extruded filaments as small as 1 µm in diameter.

EBB constructs usually fit into a 6, 12, or 24 well wellplate. Print accuracy is totally dependent on the user identifying the suitable print parameters for the rheology of their ink; print parameters such as: extrusion pressure/speed, and print speed. The ink must have some means by which it can transition from being a fluid with suitable viscosity for extrusion, to hydrogel with sufficient viscoelasticity to support its shape and provide support for proceeding layers. A quicker transition is also advantageous, as it reduces print time. This transition can cause the geometry of the printed material to change as new bonds being formed, or chemical structural changes can cause contraction of the material. Therefore, print fidelity is just as important as print accuracy. This is relatively straightforward for some hydrogels like gelatine which exhibits thermogelation, alginate which quickly transitions from a solution to a crosslinked gel in the presence of divalent ions (ionic crosslinking), or cellulose nanocrystal hydrogels which exhibit severe shear-

thinning. The combination of two or more of these materials also leads to the development of composite inks, which can achieve improved print quality along with enhanced bioactivity/cell survival or other characteristics (e.g., higher stiffness). For instance, Wu et al. made a bioink containing human corneal epithelial cells (HCECs) that exploited the thermogelation of gelatin, alginate's ionic crosslinking for stability, and collagen for bioactivity in order to provide a better mimic of native ECM [101]. There has also been widespread use of composite inks in bone tissue engineering such as the "3-3-3" ink by Cidonio et al. which is comprised of 3% laponite, 3% alginate, and 3% methylcellulose resulting in an ink with high printability and high bioactivity [102]. The results achieved with composite inks has improved EBB's performance when compared to DBB and LBB methods which generally have better print accuracy, and print fidelity. EBB methods are also more frequently used for the deposition cell aggregates compared to their DBB, and LBB counterparts, as the aggregates are often too large for most DBB and LBB methods. The simplicity of the EBB design allows EBB printers to have multiple printheads so that several inks can be used such as a cell-carrier ink, a build ink and a sacrificial ink as seen in Figure 1-7 (i).

1.3.2 Droplet-Based Bioprinting (DBB)

The inkjet printers used in the first cases of bioprinting are DBB methods. They use thermal, acoustic, or mechanical systems to eject droplets of an ink on to a substrate. Inkjet printers have continued their development in cell printing. However, they struggle to produce scalable TE scaffolds due to a number of limitations. Inkjet printers can only print inks in a limited viscosity range (<15 mPa.s), and work properly with cell densities $<1\times 10^6$ cells/ml. In addition, they cannot be used to print cell aggregates [103]. They are also known to be prone to blockages, particularly with increasing print time due to cells or particulates settling out of suspension within the ink reservoir [104]. However, inkjet printers have been used alongside other printers and have been incorporated into some multi-modal bioprinters. DBB can also be used effectively to deposit

a binder solution onto some form of polymer pre-cursor or inorganic material, for example, Inzana et al. used a collagen solution in phosphoric acid to bind calcium phosphate powder in bone tissue engineering, where a collagen solution in phosphoric acid was used to bind calcium phosphate powder [105]. Other DBB techniques include microvalve-bioprinting, drop-on-demand bioprinting, and acoustic droplet ejection.

The Bioscaffolder 3.2 utilises an inkjet printhead to aspirate cell suspensions from a 96 well plate and deposit them on the build plate, along with multiple EBB print-heads for the deposition of more structurally relevant materials i.e., hydrogel, polymer (PCL) inks, and sacrificial materials. In this way, an inkjet printhead can print many different types of cells during the same print which is particularly attractive for the manufacturer of biosensors and organ-on-chip microfluidic devices [106].

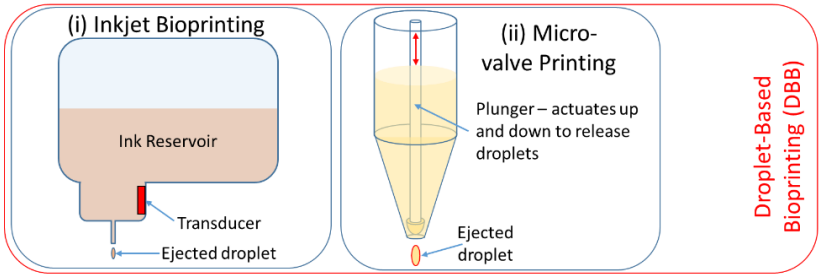

Figure 1-8. Droplet based bioprinting methods: (i) inkjet, where a transducer (piezoelectric, thermal) forces a droplet out of the nozzle. (ii) Microvalve printing where an electromagnetic plunger is actuated up and down to force droplets out of the print head.

1.3.3 Light-Based Bioprinting (LBB)

LBB methods employ light to eject droplets of an ink, propel cells in suspension, or to polymerise an ink. Photo-polymerisation techniques typically employ a photo-initiator which absorbs light and releases radicals which are highly reactive unstable molecules that help polymerize monomers in the ink or crosslink molecules in the ink. The photoinitiators used for photo-polymerisation often have low solubility in water, exhibit cytotoxicity in their stable or activated state, or may require excitation by light in the UV range, which has

limited the use of photo-polymerisation for cell encapsulation/cell printing, settling instead for cell seeding post print. However, photoinitiators have been developed with improved water-solubility, less cytotoxicity, and higher excitation wavelengths, such as Irgacure I2959 and LAP (lithium phenyl-2,4,6-trimethyl- benzoylphosphinate). Both I2959 and LAP have been used to encapsulate cells with a high level of cell viability [107,108], they have also been used as photoinitiators in EBB. LBB photo-polymerisation techniques include 2-photon polymerization (2PP), stereolithography (STL), and digital light processing (DLP)[109].

Other LBB methods include laser-assisted forward transfer (LAFT), laser-induced forward transfer (LIFT), and laser-guidance direct writing (LGDW). They are typically used for cell patterning and may become more popular as the science of scaffold-free TE evolves, but, for the moment, they are the lesser spotted bioprinting technologies. LIFT and LAFT are used interchangeably to refer to the same method of printing. In brief, a "donor" slide is coated with a thin photo-absorbing layer, often gold, this layer is then coated with a bioink, the slide is then placed upside-down above a substrate and a laser is pulsed through the slide and absorbed by the photo-absorbing layer causing extremely local high temperatures. This leads to the formation of a bubble which then collapses causing a droplet in the pico-litre range to be ejected from the bioink [110–112]. LGDW is an even rarer LBB method which propels individual cells in a suspension toward a substrate using light [113–115]. LIFT/LAFT and LGDW are both nozzle-free cell printing techniques and are shown to have some of the highest cell survival rates of all bioprinting techniques and have been utilised with many cell types, yet they are more useful for the growing field of scaffold-free tissue engineering, particularly LIFT since it allows the printing of many cell types by simply changing the donor slide.

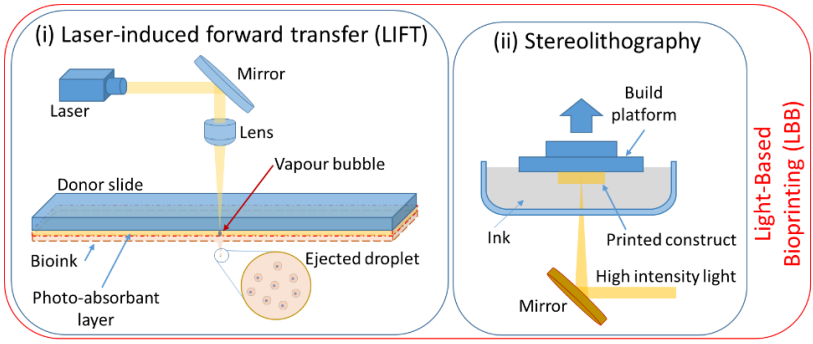

Figure 1-9. Examples of light-based bioprinting methods: (i) LIFT, where a pulse of light from a laser is focused through a donor slide to a photo-absorbent layer causing it to sublimate and produce a vapour bubble which quickly collapses forcing a droplet to be ejected from the bioink layer. (ii) Stereolithography where a beam of high intensity light is directed with aid of a mirror into an ink bath where it polymerises the ink only at the focal point of the light. The build is polymerised onto a build platform which is slowly moved out of the ink bath.

1.3.4 Multi-Modal Bioprinting

Each EBB, DBB, and LBB method has its own advantages and disadvantages, it therefore makes sense that these be incorporated into one bioprinting system to get the best of both, or all worlds. Many bioprinting research groups are now working with multi-modal printers, and several commercial multi-modal bioprinters are available, such as the GeSiM Bioscaffolder 3.2, and the RegenHU. Multi-modal bioprinters typically incorporate different types of EBB methods with DBB methods, such as a pneumatic EBB printhead and a microvalve, or inkjet DBB printhead. Several pneumatic printheads maybe in the same system so that the printer can quickly change between different types of inks. This offers many advantages as it allows the deposition of many different cell types with control over cell count distribution, and allows for the use of inks suited to specific roles, such as a sacrificial ink, cell-carrier ink, and a stiff polymer for mechanical strength. Some multi-modal printers can be procured with a melt-electrowriting (MEW) printhead. MEW is a printing technique pioneered by Paul Dalton at the University of Würzburg which is similar to electrospinning, where electrostatic forces build up in a polymer droplet at the tip of a syringe due to an applied high voltage electric field. The electrostatic forces build up

until they overcome the surface tension of the droplet and a filament leaves the droplet and whips around due to the electric field, stretching the filament into nanofibers, before reaching the cathode. MEW prevents the whipping action, which is difficult to control, through a number of processes, including by having the syringe tip and substrate (the cathode) closer together. MEW creates thicker filaments (>1 μm) than electrospinning but in a controlled way that can be incorporated into printer. MEW printheads in multi-modal printers has led MEW lattices being used to encapsulate cell spheroids with some very promising results at published by Daniel J. Kelly at Trinity College Dublin [116].

1.3.5 Aerosol Jet® Printing

Aerosol Jet® printing (AJP) is not yet considered a bioprinting method but it is the aim of this thesis to demonstrate AJP as one, therefore what follows is a technical introduction of aerosol jet printing which is followed by a more detailed introduction to aerosols, AJP, and the limitations of AJP in Chapter 2. Aerosol Jet® printing (AJP) is a printing technique developed by the company Optomec® (Albuquerque, NM, USA), and first reported in 2007 [117]. AJP typically utilises inks composed of aqueous suspensions of micro-/nano-particles of conductive inorganic material, typically silver, or organic material such as graphene. AJP has seen limited use in depositing biological materials such as DNA, enzymes, and silk fibroin in the context of bio-functionalised surfaces and biosensors, however it has not yet been used to print scaffolds for tissue engineering [10,118–120]. An AJP system can simplified to 3 crucial modules, the mass flow controller (MFC) module which controls the flow of carrier & sheath gas lines, the atomizer which forms the aerosol, seen in Figure 1-10 (a), and the deposition head, seen in Figure 1-10 (b) which aerodynamically focuses the aerosol and directs it to the substrate. The AJP used in this work, the Optomec® AJ300, is calibrated to use nitrogen gas for the atomizer and sheath gas lines, and there is a choice of two different atomizers (ultrasonic and pneumatic). The ultrasonic atomizer forms an aerosol by directing ultrasonic waves from a 1.65 MHz piezoelectric diaphragm

through a water bath into a glass vial containing the ink, the surface of the ink resonates and forms a spout from which aerosol droplets are scattered. The pneumatic atomizer forms an aerosol by feeding an ink into a high velocity flow of nitrogen via a capillary tube, similar to a carburettor. In both cases the aerosol becomes entrained in the flow of the nitrogen carrier gas, however, the pneumatic atomizer requires the use of a virtual impactor which exploits the momentum of the aerosol particles by passing the aerosol through a small vacuum to remove excess gas. However, the virtual impactor can also remove a lot of aerosol particles and adds a layer of complexity that makes repeatability difficult. There is also the risk of aerosol reaching the virtual impactor MFC and affecting its calibration. Thereafter in both atomizers, the entrained aerosol then flows to the deposition head where a coaxial flow of gas (sheath gas) collimates the aerosol flow and prevents the aerosol from making contact with the walls of the nozzle. As the nozzle diameter decreases towards the end of the nozzle (orifice diameter of 100-300 µm), the aerosol accelerates exiting the nozzle at speed until it reaches the print substrate where the aerosol droplets coalesce.

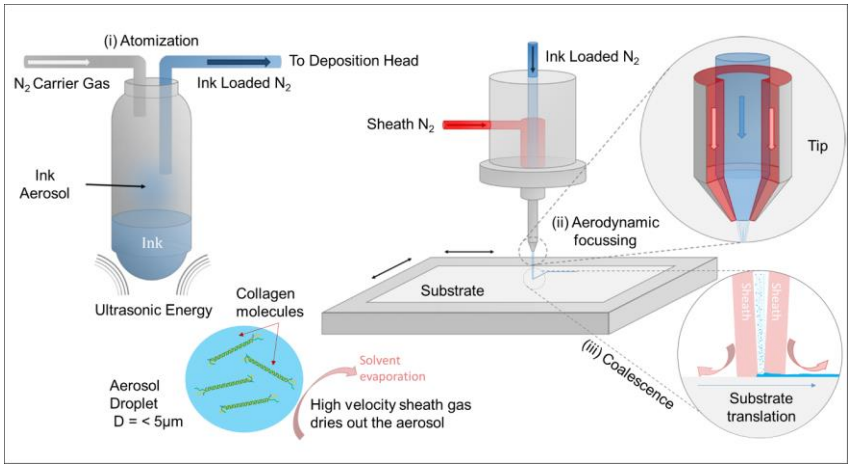

Figure 1-10. A simplified view of an aerosol jet printing illustrating the 3 mains steps of the process when using an ultrasonic atomizer and an illustration of an aerosol droplet of a collagen solution (not to scale) being dried by sheath gas. (i) atomization, (ii) aerodynamic focussing, where the sheath gas surrounds and collimates the ink-laden aerosol from the atomizer, and (iii) collimation, where aerosol droplets impact on the substrate and each other creating a continuous line

on the translating substrate. Parts of illustration were adapted from Smith et al. 2017 [121] *CC 3.0.*

Since the aerosol is separated from the nozzle walls by the sheath gas, the resultant print lines can be as little as 10% of the nozzle diameter, i.e., 10 µm lines can be printed with a 100 µm nozzle. Due to the nitrogen gas in the carrier and sheath gas flows being dry, and the high surface area to volume ratio of the aerosol droplets, much of the solvent in the ink evaporates from the aerosol droplets very quickly, particularly in the deposition head. Cells are highly unlikely to survive this printing process, as even if they survive the mechanical stresses of atomization, they would also have to survive likely dehydration. Therefore AJP should only be considered as a method for bioprinting scaffolds for cell seeding.

1.4 The Cornea

The cornea is a dense collagenous tissue for which an alternative to transplant is in high demand. The cornea is distinguished from other parts of the outer eye by its transparency and curvature, which is different from the sclera. It is surrounded by transitional ring of tissue called the limbus. It serves two main functions, protecting the inner eye, and focussing light into the eye. As light hits the cornea, it is refracted (the cornea is responsible for two thirds of refractive power of the vision system of the eye) through the pupil into the lens where the light is further focused on to the cone cells of the retina.

1.4.1 The Anatomy of the Cornea

In terms of geometry, the cornea is a slightly oblate spheroid cap shell, with a horizontal diameter around 11.5 mm, and a vertical diameter of around 10.6 mm white-to-white [122–124], and a central corneal thickness of around 550 µm which increases with the distance from the centre up to 700-800 µm near the limbus [123,125,126]. The radius of curvature of the anterior and posterior corneal surfaces of an adult human cornea are often reported to be around 7.7 mm, and 6.8 mm, respectively, with a drift from larger radii in infants towards smaller radii in aging adults [127,128]. The cornea is composed of 5 distinct layers, as seen in Figure 1-11: i) the anterior surface is the epithelium, followed by ii) the acellular Bowman's Membrane, iii) the stroma which accounts for the bulk of the cornea, iv) the Descemet's membrane, another acellular layer, and v) the endothelium.

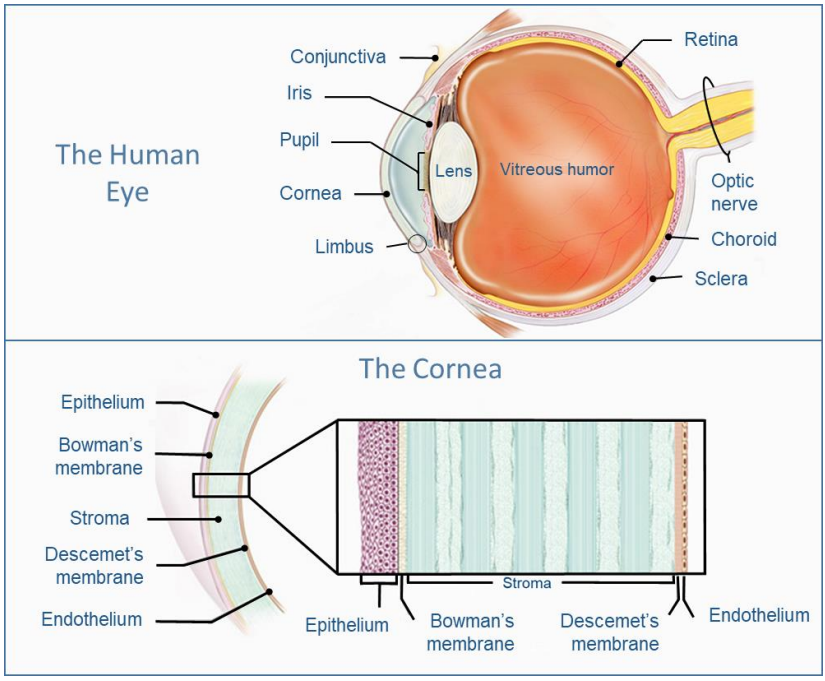

Figure 1-11: Diagram of the human eye and the cornea. The cornea has an increased curvature compared to sclera. Contrasting layers in the corneal stroma depict layers of orthogonally oriented fibrils. Adapted from nei.nih.gov (National Eye Institute, National Institutes of Health)

The corneal epithelium is composed of 4-6 layers of stratified non-keratinized corneal epithelial cells which can be defined into 3 groups (from anterior to posterior): superficial cells, wing cells, and basal cells [129]. These 3 groups comprise the different stages in the life cycle of a corneal epithelial cell. They start off as tall columnar basal cells supplied from stem cells located in the limbal basal epithelium [129]. From there they become polygonal wing cells, before finally becoming superficial cells whose anterior surface are covered in extensive apical microvilli and microplicae which aid in the lubrication of the cornea-eyelid tribo-system [130]. The superficial cells eventually desquamate, and are replaced, completing the life cycle of a corneal epithelial cell, which is about 7-10 days in length [131]. The epithelium is also protected by a mucin-rich tear film which is produced by the conjunctiva, and provides not only lubrication to the cornea-eyelid tribo-system but also protects the cornea from pathogens, and provides oxygen and nutrients (e.g.,

glucose) to the anterior layers of the cornea. The maintenance of the tear film is facilitated by an extensive network of nerves between the basal layer and Bowman's membrane which are very sensitive to mechanical stimuli and trophic signals [132]. Bowman's membrane is a thin acellular layer with a dense collagen meshwork and serves as an anchoring point for many of the anterior-most collagen fibrils of the stroma.

The corneal stroma accounts for up to 90% of the cornea's thickness and is mostly composed of collagen type I, with significant amounts of collagen type V, proteoglycans, and cells (mostly keratocytes). The collagen of the corneal stroma is assembled into fibrils that are much narrower than in other connective tissues in order to maintain transparency, which has been shown to be a function of fibril diameter due to them scattering light [133]. The fibrils are heterotypic with collagen type I interweaved with small amounts of collagen type V (around 10%). This interweaving is believed to regulate the fibril diameter along with other factors, such as the electrostatic repulsion between fibrils, which is generated, in part, by chloride ions forming complexes with fibrils [134]. The corneal fibrils are aligned in parallel into lamellae which are around 200 μm wide and 2 μm thick [135]. The lamellae can span the entire cornea, and overlap orthogonally in the central area, as illustrated in Figure 1-11, with lines depicting the fibrils running parallel to the cross-section and dots representing the fibrils within the lamellae running perpendicular to the cross-section. In the peripheral cornea, the lamellae are arranged annularly circum-cornea, which is believed to support the change in curvature of the cornea from the sclera [136]. At several specific regions of the corneal stroma, the lamellae are interweaved, particularly in the anterior stroma which is denser than the posterior stroma and responsible for much of the cornea's strength. Keratocytes are the main cell type present in the corneal stroma, and are responsible for maintaining the stromal ECM. Keratocytes are joined by much smaller numbers of corneal mesenchymal stem cells in the peripheral cornea [137], dendritic cells, and macrophages, and some Schwann cells surrounding the neural bundles that pass through the corneal stroma [138].

Keratocytes are mostly transparent, apart from their nucleus, due to the presence of “crystallins”, a class of proteins that are believed to reduce the refractive index of the cell membrane and cytoplasm to a value closer to that of the surrounding ECM [139]. Injury, and chronic diseases that recruit other cells or lead to the proliferation of cells other than keratocytes in the cornea can lead to corneal opacities due to the lack, or absence, of crystallins in the cytoplasm.

Descemet’s membrane is a thin dense acellular collagenous layer that is secreted by corneal endothelial cells. It has two distinct regions, an anterior highly ordered banded region formed during foetal development and a more amorphous posterior region formed after birth that grows slowly with age [129]. The corneal endothelium is a monolayer of corneal endothelial cells that are tightly packed into a characteristic hexagonal pattern and have a limited ability to regenerate. The corneal endothelium regulates the ionic balance and hydration of the stroma mostly through numerous Na+/K+ -ATPase ion pumps in the endothelial cell membranes [140]. This makes the corneal endothelium responsible for the electrostatic repulsion between fibrils, and prevents corneal swelling which can result in a corneal oedema causing a corneal opacity. Endothelial cells do not divide and multiply in vivo, hence humans are born with around 3500 corneal endothelial cells per square millimetre which gradually decreases by 0.6% per year with cells spreading to fill gaps left by dead cells [129]. Many degenerative corneal diseases are attributed to a poorly functioning corneal endothelium which may require surgical intervention with a corneal transplant. The cornea also has other components, such as nerves which circle the cornea and are fundamental to the corneal blink reflex, and hence essential in protecting the cornea from trauma and injury.

1.4.1.1 Cornea Immune Privilege

The term “immune-privilege” is reserved for tissues where, due to some anatomical peculiarities such as a lack of blood vessels, there is a reduced immune response to allo-grafted tissue which allows that tissue to survive extended periods of time [141,142]. The cornea is one of the most immune-privileged sites in the human

body due to number of factors and mechanisms such as, its lack of blood and lymphatic vessels, cellular and molecular barriers present in the cornea, and an immunosuppressive intraocular environment [142,143]. The cornea's immune-privilege is thought to have evolved to preserve the refractive power of the cornea, as any distortion to the visual axis through inflammation could render the host functionally blind. As a result, donor corneas do not need to be matched to the recipient like other tissues/organs, and local topical application of immunosuppressive drugs is usually sufficient to prevent graft rejection. This makes the cornea a very attractive tissue for tissue engineering and regenerative medicine (TERM) treatments. The cornea has already had clinical trials for cell therapies [144] and biosynthetic corneas [75].

1.4.1.2 Corneal Optical Properties

As light meets the cornea it can be transmitted into the eye either directly or through refraction, reflected at the refractive interfaces at the anterior and posterior corneal surfaces, absorbed by molecules within the cornea, or scattered in random directions. Many of the clinical tools used to examine patients' eyes in ophthalmology, such as optical coherence tomography (OCT), exploit the scattered, and/or reflected light to investigate the cornea *in vivo*. While the cornea is often treated as a single refractive body, the different layers of the cornea and even the collagen fibrils and surrounding matrix have slightly different refractive indices, however this isn't relevant to the resolution of measurements used in a clinical setting, hence the simplification [145,146]. Although in vivo RI measurements are possible, they only represent the RI of the corneal epithelium, the RI of the corneal stroma has been reported to range from 1.38 in the anterior stroma to 1.37 in the posterior stroma using in vitro measurements [145].

Human corneal transmission has mostly been studied in vitro using excised corneas though this method can be subject to some variation in measurement due to the resultant loss of intraocular pressure which can lead to ripples in the corneal lamellae increasing scattering, or due to swelling during storage [135]. Corneal

transmission has also been studied ex vivo by implanting a photodiode into the anterior chamber of an intact human eye [147,148]. Although reflections from the refractive surfaces of the eye have been used to study the transmission of the human lens in vivo, it is not clear if this technique has been used or is accurate enough to study corneal transmission [149]. Human corneal transmission is >90% for most of the visible spectrum, but begins to drop at wavelengths below 500 nm to a minimum of ~80 % at 400 nm [147,150]. From there the transmission drops sharply to ~0% at 300 nm due to the presence of water, carbohydrates, nucleic acids, certain proteins and their component amino acids which absorb light at wavelengths near or below 300 nm very heavily [151]. This increasingly sharp drop in transmission coincides with the increasing energy of photons of these shorter wavelengths and the hazard they present to the retina [152]. On the other hand, light at wavelengths >700 nm in the near infrared is mostly harmless to the eye at normal exposure level, likely due to their much lower energy. Even the shorter wavelength visible light, 400 nm – 500 nm, is hazardous to the retina [153], hence the proliferation of "blue light glasses" to filter out this light, which we perceive to be blue, from electronic screens. Therefore, the high absorption of the cornea to light at shorter wavelengths contributes to a healthy eye.

1.4.1.3 Cornea mechanical properties

The cornea's mechanical properties are dominated by the properties of the corneal stroma. The precise ordering of the lamellae of the corneal stroma has been shown to have two preferred directions superior-inferior (vertical), and nasal-temporal (horizontal) leading to anisotropic mechanical properties [154]. These preferred directions are thought to arise from the stresses induced by the muscles around the eye, the ocular rectus and the orbicularis [154]. As mentioned earlier, the mechanical properties of the corneal stroma also change along its anterior-posterior axis, from a stiffer anterior stroma to a less stiff posterior stroma, which is thought to arise from increased interweaving in the anterior stroma. Corneal elasticity has been measured and calculated using a number of methods and models including *in vivo* methods, such as the

Orssengo-Pye method which uses intraocular pressure measurements [155], and more traditional material science *in vitro* methods, such as strip extensiometry, and nanoindentation. As a result there is quite a wide range of reported human corneal elastic moduli from 0.075 to 20 MPa [156–159]. Measurements at the higher end of this range tend to be the result of similar methods, often using whole enucleated eyes, and increasing the intraocular pressure while measuring the deflection between two or more fixed points imparted on the corneal surface to calculate circumferential and meridional stresses [159,160]. However, most measurements report an elastic moduli for the corneal stroma between 0.1 and 1.0 MPa, using a number of very different measurement methods [158,161].

1.4.2 Corneal Injury, Pathologies, and Dystrophies

1.4.2.1 Scrapes, scratches, and burns

Due to the fast turnover of the corneal epithelium, it can recover from injury due to mechanical, or chemical injury remarkably quickly [162]. The mucin-rich tear film and the morphology of the superficial epithelial layer can also compensate quickly for small disturbances to the epithelial surface. Deeper wounds that effect the corneal stroma induce a wound-healing response that often results in a corneal opacity in the affected area. The opacity can clear in a number of weeks but in the worse cases can result in the over-expression of wound-healing associated cytokines, chemokines and growth factors, such as transforming growth factor-β, leading to a runaway wound healing response that causes a long-term corneal opacity [130,163]. Upon injury to the corneal stroma, keratocytes become active and more fibroblastic in appearance and behaviour. As the wound-healing response progresses these now corneal fibroblasts can trans-differentiate into myofibroblasts and migrate to the injury site to begin repairing it. The myofibroblasts contain far less crystallins than keratocytes, and hence are less transparent. At the site of injury, myofibroblasts can proliferate and begin producing collagen type I, III, IV & IV, fibronectin and other glycoproteins [164]. The collagens produced don’t possess the fibril arrangement of the

stroma leading to much higher light scattering, this along with the myofibroblasts' lack of crystallins, and other factors leads to the cornea at the site of injury losing transparency. Under normal physiological conditions the new matrix can eventually be remodelled and the myofibroblasts undergo apoptosis leading to the clearing of the corneal opacity [165]. However, in pathological conditions the wound-healing response can lead to corneal fibrosis and a permanent corneal opacity. Injuries deep enough to affect the corneal endothelium.

1.4.2.2 Corneal pathologies and dystrophies

Keratoconus is one of the most common corneal diseases with an occurrence of 1 in every 2,000 of the general population [166]. It is characterized by a thinning of the corneal stroma and a weakening of the cornea's mechanical properties leading to a bulging rounded-cone shape cornea. The root cause or causes of keratoconus remain unknown with multiple hints to a genetic disorder such as its frequent bilaterality, and familial association but no confirmed source gene [167]. Keratoconus may initially be treated with contact lenses, or more recently with the use of photo-crosslinking agents such as riboflavin, but as the disease progresses it may eventually require a corneal transplant [168].

Fuch's endothelial corneal dystrophy (FECD), often referred to as Fuch's dystrophy, affects the cornea through a malfunctioning endothelium. The malfunction of the corneal endothelium leads to a corneal oedema resulting in poor visual acuity, or a corneal opacity. FECD is characterized by endothelial cell loss, a thickening of Descemet's Membrane, and the formation of guttae; small collagenous mounds excreted by the endothelial cells [169]. There are a number of methods by which the effects of Fuch's dystrophy can managed using topical treatments and corrective lenses but in severe cases and cases where it gets progressively worse with age a cornea transplant is the standard treatment.

Keratitis is an infection of the cornea which can be caused by a number of different bacteria (*Staphylococcus* [170]), fungi (*Candida orthopsilosis* [171]), or viruses (herpes simplex virus). Keratitis often

begins from an initial trauma injury, or through the use of non-sterile contact lenses, and in most cases can be treated without a need for surgery. However, if left untreated, keratitis can progress into a corneal opacity (an infectious leukoma), in which case a corneal transplant is the standard treatment. Keratitis is particularly prevalent in countries where there is a lack of adequate hygiene, or medical facilities as it makes preventative measures or effective early treatments difficult to implement. There are many other less prevalent diseases that lead to the need for cornea transplant

1.4.3 Visual Impairment, treatments, and surgical techniques

Any one of the various injuries, pathologies, or dystrophies in the previous section can lead to a corneal opacity causing visual impairment, or blindness in one (unilateral) or both (bilateral) eyes. The WHO's International Classification of Diseases (ICD-11, 2018) defines a person as being blind if they have a visual acuity below 3/60, above this a person still presenting (with corrective lenses) a visual acuity of 6/12 or less is considered visually impaired. Visual impairment is defined in 3 levels mild, moderate, and severe. In 2017 it was estimated by the Vision Loss Expert Group that 36 million people are blind and 216.6 million people suffer from moderate to severe visual impairment [172]. The vast majority of visual impairments globally are caused by untreated refractive errors, and cataracts, while a similar majority of the cases of blindness are caused by cataracts [173]. Both of these can be easily treated but remain so prevalent due to poverty [174]. Poverty remains the most prevalent cause of blindness and visual impairment due to poor access to clean water, hygiene facilities, and primary healthcare facilities, which the WHO is addressing through the SAFE program for trachoma [175]. About 1% of visual impairments, and 4% of the cases of blindness globally are due to corneal opacities for which the standard treatment is a cornea transplant.

A survey carried out between 2012 and 2013 estimated that approximately 185,000 corneal transplants are performed each year in 116 different countries, and that there are 12.7 million people on corneal transplant waiting lists, but only the needs of 1 in 70 are

covered [176]. Corneal transplants are the most common and the oldest transplant performed. As stated earlier, unlike other transplants, donor corneas do not need to be matched to a patient in any way due to its immune-privilege. Donor corneas can also be stored for a long time after they are explanted from a donor, typically in a national eye bank. Using cold storage in media such as Optisol GS a donor cornea can be stored for up to 2 weeks prior to transplantation, whereas in organ culture media at 31-37°C a donor cornea can be stored for up to 48 days prior to transplant [177]. This facilitates a global trade in donor corneas with the United States, Sri Lanka, and Italy being the largest exporters of donor corneas [176]. As a result, corneal transplants are performed in countries where there are no cornea donors, such as Ireland, Greece, and Saudi Arabia. The reasons behind the lack of donors can be due to systemic (countries that have no procurement programme), medical (Ireland ceased accepting native cornea donations in response to a risk of transmission of spongiform encephalopathy), or cultural. Countries that implement a policy of presumed-consent for organ donation (opt-out policy) tend to have higher donor rates. Campaigns have been implemented in some countries that have an opt-in organ donation policy to increase the number of cornea donors. One such campaign in the Brazilian state of Espirito Santo managed to eliminate the corneal transplant waiting list soon after implementation in 2011, but was soon followed by an increase in the waiting list showing the need for continued efforts to increase public awareness of the need for organ donors [178,179]. The standard surgical technique by which a donor cornea is transplanted has been penetrating keratoplasty since the 1950s, however a range of new more targeted surgical techniques, lamellar keratoplasties, are becoming increasingly popular.

1.4.3.1 Penetrating Keratoplasty

A PK involves a resection of full thickness of a patient's cornea, a donor cornea is then implanted with sutures around the periphery of the graft as seen in Figure 1-12. The initial success rate of penetrating keratoplasties is relatively high in developed nations, being 85% after 2 years, but lower in developing countries like India,

where initial success rates are 69% [180]. Their long term success rates at 10, and 15 years after transplantation are much lower at 62% and 55%, respectively; reported in 2006 from a census of corneal transplant recipients in Australia [181]. A more recent study performed in Spain reports data at 1, 5 and 10 years, which are very similar and specifically a 10-year success rate of 65% [182]. The leading cause of graft failure is graft rejection; where the graft is recognised as foreign tissue and the patient's immune system responds to the graft. Immunosuppressive drugs and similar treatments are administered to allo-/xeno-graft recipients to prevent graft rejection, though in the case of a corneal graft these treatments can be tailored to the risks that the patient presents, due to the severe side effects and high mortality of patients on immunosuppressive drug treatment. The second leading cause of corneal graft failure via PK is corneal endothelial cell failure [181]. However, this mode of graft failure can be avoided, where the pathological tissue in the anterior cornea, by performing a partial thickness cornea transplant thereby leaving a healthy host endothelium intact. This is referred to as a lamellar keratoplasty.

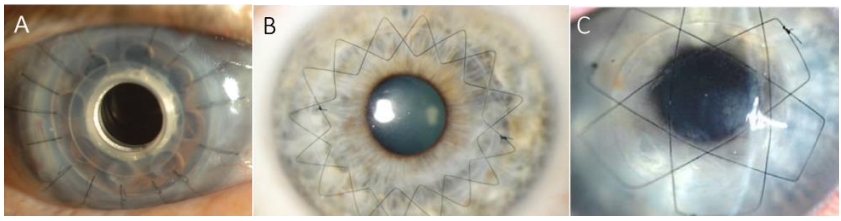

Figure 1-12. Treatments for corneal dystrophies from left to right are a Boston Keratoprosthesis, a PK corneal transplant exhibiting peripheral sutures typically used in corneal transplants, and the biosynthetic stromal substitute implanted using mattress sutures, [171]*© BMJ Publishing Group Ltd. ,* [183] *© 2013 Kang et al., and* [184] *© ARVO Journals 2016. All reprinted with permission respectively.*

1.4.3.2 Emerging Surgical Methods: Lamellar Keratoplasties

Lamellar keratoplasties (LK) are a range of corneal surgical techniques that have become increasingly popular and allow for the selective transplant of parts of the cornea, so that only the pathological layers are resected [185,186]. The most common LKs are deep anterior lamellar keratoplasties (DALK), and Descemet's

membrane endothelial keratoplasties (DMEK). DALK only transplants the anterior layers of the cornea, from the posterior layers of the stroma near Descemet's Membrane (DM) to the epithelium, leaving the host endothelium and DM intact. A DMEK only transplants the endothelium and DM. Both of these particular lamellar keratoplasties show improved graft survival compared to PK; DALK virtually eliminates the risk of failure due to endothelial cell failure, and DMEK has a much reduced rate of graft rejection [186]. One study put the 10 year graft survival rate of DALK surgeries at 99.5% [187]. LK's have also facilitated new treatments that have the potential to address the donor shortage. The split-cornea transplantation has increased the number of patients that may be treated with a single donor cornea, by, as the name suggests, splitting the donor cornea so that one part may be used in a Descemet's membrane endothelial keratoplasty (DMEK) to replace a defective posterior corneal layers, and the other part may be used in a deep anterior lamellar keratoplasty (DALK) to replace a failing anterior layers [188–190]. Each surgery from a single donor cornea can be separated for up to a week [188]. Yet lamellar keratoplasties require specialist equipment, and training, which may not be a priority where there is already a limited supply of ophthalmic surgeons skilled in PK. Hence, lamellar keratoplasties are mostly implemented in developed countries with high quality national healthcare infrastructure.

1.4.3.3 Keratoprostheses

Keratoprostheses, or artificial corneas, have been developed but, rather than addressing the donor shortage, they are mostly used in patients who have experienced the rejection of a transplanted cornea or who are deemed unsuitable for a transplant. The AlphaCor was one of such keratoprosthesis made of a synthetic hydrogel which achieved clinical approval but was discontinued after severe complications, such as corneal melt and corneal vascularization [191]. These complications often arise from keratoprosthesis, as the synthetic materials usually used struggle to integrate with the host tissue, and achieve sufficient oxygen permeability to prevent neovascularisation. The Boston KPro, seen in Figure 1-12, is a widely

used keratoprosthesis; since receiving FDA approval in 1992, it has been continually improved and it has increased the quality of life of many patients. However, the type of Boston Kpro that is in use today requires a donor cornea out of which a central 3mm hole is trephined to make room for a central PMMA button which is then held in place by a rear plate [192]. Hence, keratoprosthesis are not intended to address the donor shortage.

1.4.3.4 The Biosynthetic Cornea

Alternatives to donor corneas are a major topic of research and many animal-derived, and synthetic hydrogels have been investigated along with decellularized xeno-grafts. One of the most promising potential alternatives to a donor cornea has been the biosynthetic stromal substitute (BSS) from the research group of May Griffith [193–195]. The BSS is composed of the same recombinant human collagen type III (RHCIII) produced by FibroGen discussed in the previous section on recombinant collagen. The BSS are produced, on ice, using a double syringe mixing system, where one syringe is loaded with highly concentrated RHCIII 10-18% and the other syringe is loaded with a concentrated MES buffer solution containing a cross-linker EDC. The low temperature, high concentration of buffer, and relatively low pH (~pH 5), is intended to form very small fibrils which absorb less light. The syringe contents are mixed in a closed system in order to prevent bubble formation and remain sterile, and is then deposited into a contact lens mould. The result is an optically clear, dense collagenous construct similar in appearance to a contact lens. The transmission of these constructs has frequently been reported to be >89% between 450 nm and 700 nm and its refractive index was reported to be 1.35 [193]. Although it is not bioengineered, in that it is never cultured before implantation, the BSS is composed of human collagen on which corneal epithelial cells have been shown to proliferate and keratocytes can remodel. The outcome of a 4-year clinical trial of 10 patients suffering from keratoconus or corneal scarring and treated with biosynthetic corneas via DALK, was published in 2014, OCT measurements from which can be seen in Figure 1-13 [75]. It showed that no recipients of the BSS experienced rejection. Topical

immunosuppressive drugs were administered to BSS recipients for the first 6-7 weeks while the sutures remained in place, whereas donor cornea recipients underwent much longer periods of topical immunosuppressive drug treatment. Full epithelium regeneration, and a partial return to corneal sensitivity was observed 1-5 months, and 6-7 months after implantation respectively [196].

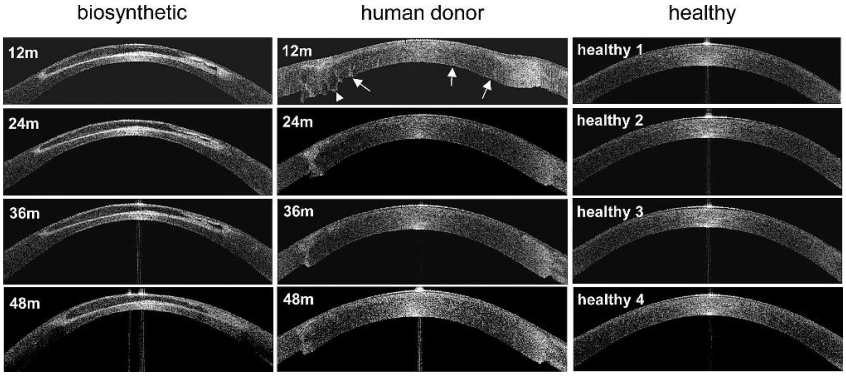

Figure 1-13. Optical Coherence Tomography (OCT) of the anterior cornea at 12, 24, 36, and 48 months post implantation for a BSS implant, a PK-type human donor transplant, and a healthy cornea. The BSS can be seen as the anterior-most clear layer with some changes in appearance between measurements due to different angles of measurement. The human donor transplant appears thicker than the other cases, which is common. Arrows indicate the locations of wound compression due to the presence of sutures [75].

There is limited published data on the mechanical properties of the BSS. One study published in 2008 reporting the tensile strength and elastic modulus of BSS fabricated with 13.7 % w/v RHCIII to be 1.7 MPa and 20 MPa, respectively, whereas BSSs fabricated with 10 % w/v RHCIII that were implanted, were reported to have a tensile strength of 0.3 MPa and elastic modulus of 1.7 MPa [195]. However, it has been stated that the BSS does not have suitable mechanical properties to allow it to be pierced for sutures [197]. Hence the BSS had to be implanted with mattress sutures, rather than peripheral sutures, as is typically done with donor corneas in DALK or PK surgeries. These mattress sutures, in effect, tie down the implant into place rather than stitching it into place, with the sutures anchored in the host peripheral cornea and traversing the implant, as seen in Figure 1-13. This lead to slower epithelium regeneration

and some corneal thinning [198]. BSS recipients were observed to have a significantly thinner central cornea, a steeper corneal curvature, higher astigmatism and more surface irregularities than healthy corneas, or penetrating keratoplasties [75,184]. Further work by some of the authors involved in the BSS stated the importance of shape customisation to minimise post-operative ametropia (refractive errors, long and short sightedness) in relation to the BSS [199]. It is not clear if custom moulds could be used in the manufacturing of the BSS, or if they are being investigated, but it doesn't seem out of the realm of possibility. Of course, another way of producing a patient-specific BSS would be to use the additive manufacturing technology to produce the BSS itself. Given that the BSS is acellular, it must rely on the capability of the cells remaining in the host cornea to populate the implant and remodel it. Bearing in mind that patients eligible for keratoplasty may not have a healthy population of the keratocytes and other corneal cells, the capability of those cells to populate and remodel a biosynthetic implant may be limited. Nevertheless, the BSS would be a great tool in the treatment of corneal visual impairment and blindness. The RHCIII manufacturer FibroGen was meant to be running preclinical trials of the BSS (FG-5200) in order to use them in clinical trials in China since around 2016, however, all references to the FG-5200 have recently been removed from the FibroGen website.

1.5 Cartilage

Cartilage tissue is similar to corneal tissue in that it is highly collagenous, avascular, alymphatic, and has low cell density, however contrary to corneal tissue, cartilage is aneural [200]. Cartilage is also argued to possess some degree of "immune-privilege". Cartilage's avascularity, dense matrix, and some immune-modulatory behaviour in chondrocytes, does allow the use of allogenic transplants with milder immune response [201,202]. There are three major types of human cartilage: articular cartilage found in the articular joints (knee, hip, ankle) and the trachea, fibrous cartilage found in intervertebral discs, and elastic cartilage found in the epiglottis [203]. These cartilage types can be distinguished by the presence and the respective concentrations of different collagens and proteoglycans in their ECM which lead to their respective distinctive appearances and mechanical properties. Articular cartilage provides a load-bearing low-friction surface for the interfaces of bones in articulating joints which often becomes damaged through sporting activities, age-related wear, and degenerative diseases. However, cartilage has limited capacity for regeneration, and hence has become a major tissue of interest for tissue engineering strategies.

1.5.1 Composition and anatomy of articular cartilage

Articular cartilage is mostly composed of collagen and proteoglycans with collagen accounting for 60-70%, and proteoglycans accounting for approximately 30% of the tissue's dry weight [204,205]. The respective ratios of collagen types changes within mammalian articular cartilage with age, though collagen type II always accounts for the vast majority of collagen types. In young articular cartilage collagen type II accounts for at most 80% of collagen, with there being at least 10% of both a FACIT, collagen type IX, and another fibrillar collagen, type XI [204]. These form heterotypic fibrils with collagen types II and XI interweaved to form the fibril, and collagen type IX attached to the outer surface of these fibrils which is believed to enhance inter-fibril interactions. With age, collagen type II concentration increases relative to the other

collagens, accounting for at least 90% of collagen in mature articular cartilage [204]. There are also small amounts of fibrillar collagens type III and V, beaded filament-forming collagen type VI, network-forming collagen type X, and FACITs type XII, and XIV [206].

Of the proteoglycans present in articular cartilage, aggrecan is the most abundant by weight. Aggrecan is comprised of a ~300 kDa core protein with over 100 chondroitin sulphate side chains and, in sometimes, keratan sulphate side chains [200,207]. The sulphate and carboxyl groups on these sulphated glycosaminoglycans (GAGs) lead to a net negative charge in these aggrecan molecules which gives them a high affinity for water [205]. The N-terminus of the aggrecan binds, non-covalently, to hyaluronan to form larger aggregates with a hyaluronan backbone, and aggrecan bottlebrush-like side chains with bristles of chondroitin sulphate and keratan sulphate [200]. The aggrecan molecules attached to the hyaluronan backbone repel each other due to their net negative charge, however in cartilage they are confined by the surrounding collagenous matrix leading to extremely high electrostatic repulsive forces between the sulphated GAGs side chains on aggrecan [200]. These electrostatic repulsive forces are reported to contribute to over 50% of the equilibrium compressive modulus of cartilage [207].

Articular cartilage has five distinct zones, the lamina splendens, superficial zone, the middle zone, the deep zone, and the calcified zone as seen in Figure 1-14 below. The lamina splendens is a thin acellular layer of tightly packed collagen fibrils orientated parallel to the articular surface with ; it is occasionally described as part of the superficial layer [208]. Below the lamina splendens is the superficial zone which is composed of chondrocytes with a flattened shape running parallel to the articular surface, and in collagenous matrix with slightly thinner fibrils with a more radial orientation [208]. Both the lamina splendens and superficial zone have a relatively low concentration of proteoglycans compared to the rest of cartilage, leading to the low staining with Safarin-O seen in Figure 1-14(A). The middle zone accounts for 40-60% of the cartilage thickness and is comprised of spheroidal chondrocytes in a matrix with higher sulphated GAG content and collagen fibrils with a less-ordered

orientation. The deep zone has spherical chondrocytes that tend to align themselves into columns perpendicular to the articular surface, as seen in Figure 1-14(C), in a matrix that contains the thickest collagen fibrils and the highest concentration of proteoglycans [209]. A clear line called the tidemark, visible in the Safarin O and H & E stained sections and the schematic seen in figure 14, roughly corresponds to the boundary between calcified and non-calcified cartilage. The calcified zone is integral to the adhesion of cartilage to subchondral bone. This zone is characterized by a lower cell density, fibrils that are perpendicular to the subchondral bone beneath, and the presence of hypertrophic chondrocytes that secrete collagen type X [210].

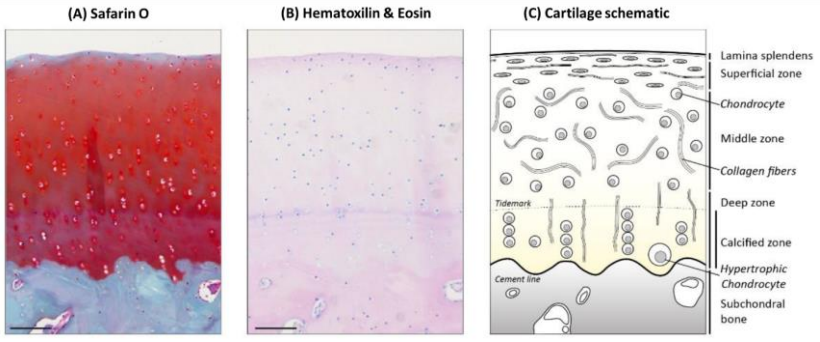

Figure 1-14. Histology sections of adult bovine cartilage stained for (A) sulphated GAG content using Safarin O, (B) collagen and cells using H&E stain, and (C) a schematic of the cartilage zones. © MDPI 2019 [211]

1.5.2 Cartilage injury and pathologies

Cartilage's limited capacity for regeneration has been known for a long time, one 18th century transaction of the Royal Society references observations of Hippocrates and Hildanus (Wilhelm Fabry) in writing that cartilage is more difficult to heal than bone, and that it does not recover from severe injury [212]. We now understand this failure to restore the freedom of movement after injury is at least partly attributed to cartilage's avascular nature. Healing of an injury in articular cartilage requires vascular ingrowth to the affected area, which allows the necessary stem cells to migrate to the area, differentiate, and begin forming matrix. Whilst

this can restore some function, the new matrix produced in the injured site is fibrous cartilage which has significantly different biochemical and biomechanical properties, and hence may only allow limited movement [213]. Treatments such as drilling, abrasion and debridement were used to induce this fibrous cartilage formation by exposing the subchondral bone marrow, and the MSCs therein, to the wound site [214]. More modern arthroscopic abrasion procedures aim to remove inflamed and degenerative tissues and where subchondral bone is exposed, abrade the surface of the bone to induce fibrous cartilage formation [215]. The microfracture (MF) technique is one such technique which is quite commonly used, and uses an arthroscopic awl in place of a drill to create small holes 2-4 mm deep in the subchondral bone without causing tissue necrosis [216].

Cartilage's aneural nature also limits the ability of clinicians to detect degenerative diseases, such as osteoarthritis (OA), in their early stages of development, since they do not cause pain. Osteoarthritis is the most common joint disease worldwide, affecting an estimated 10% of men and 18% of women over the age of 60 [217]. However, OA can also effect young people, particularly post-traumatic OA which arises from an initial mechanical damage to a joint that leads to joint instability and cartilage damage, and represents 12% of OA cases [218]. As OA progresses it leads to inflammation in the joint, the expression of matrix degrading MMPs, narrowing of the joint space and thickening of subchondral bone resulting in a limited range of motion in the joint and joint pain [200]. Many drug and surgical treatments for OA focus on reducing the swelling in the joint, reducing joint pain, and surgical "house-keeping" to remove obstacles such as osteophytes within the joint, and though these do improve the quality of life for the patient they are only tools for managing the disease rather than curing it.

1.5.3 Cartilage mechanical behaviour

The mechanical behaviour of articular cartilage is often represented as a biphasic model with solid components like collagen, proteoglycans, and lipids represented as solid elastic material and

liquid material interstitial fluid represented as an incompressible low viscosity fluid [205]. The majority of methods used to measure the mechanical properties of articular cartilage aim to take account of this biphasic behaviour. A creep test applies a constant load to a tissue section and measures the displacement over time, whereas a relaxation mode test applies constant displacement to a tissue section and measures the load over time. The biphasic model of cartilage can accurately predict the behaviour of cartilage in these tests, hence its use [219]. In both test methods the change in displacement or load over time is assumed to be mostly the result of exudation of the interstitial fluid in the tissue, rather than viscoelastic flow of the solid material. Hence the load, or confinement, is performed with porous material so that the interstitial fluid can flow out of the cartilage [219]. The biphasic theory was further developed into a triphasic theory [220]; the third phase being an ion phase to take account of a "chemical load", i.e. an osmotic effect, however this is likely ignored in most cases because its effects can be neglected when an appropriate media is used for measurements. Studies have been and are still done that measure the instantaneous mechanical behaviour of the tissue and represent it as a single viscoelastic material.

1.5.4 Cartilage tissue engineering

Cartilage's limited capacity for regeneration makes it an ideal tissue for the application of tissue engineering, and indeed tissue engineering in the form of autologous chondrocyte implantation (ACI) was used as early as 1994 [221]. An ACI involves an initial surgery where a biopsy of healthy cartilage is taken, the cartilage is then processed to release the chondrocytes therein, those chondrocytes are then expanded in culture over a number of weeks, and a second surgery allows a suspension of those chondrocytes to be injected into the injured site under a sutured periosteal flap or collagen membrane. However, during in vitro expansion, chondrocytes are known to lower their expression of cartilage matrix proteins and proteoglycans, and de-differentiate into a more fibroblastic state [222]. The first cell therapy product to be approved

by the European Medicines Agency (EMA), ChondroCelect (TiGenix NV, Leuven, Belgium) in 2009, was a form of ACI that employed stringent phenotypic profiling to ensure that the chondrocytes harvested did not de-differentiate during expansion and that they retained their chondrogenic potential [223]. However, ChondroCelect was withdrawn in 2016 for commercial reasons, with the manufacturer, TiGenix, opting instead to proceeding with allogeneic stem cell platforms which were more commercially viable [224]. While the advantages of ACI seem obvious, the clinical studies of ACI versus microfracture treatments have struggled to show a consistent significant advantage of ACI.

Many cartilage tissue engineering strategies aim to form a tissue in vitro prior to implantation by harvesting the autologous chondrocytes and then seeding them onto scaffolds and culturing until a sufficient cell population is achieved. The Chondro-Gide® (Geistlich Pharma, Switzerland) is a bilayer porcine collagen type I and type III membrane which has been used as an acellular implant to aid repair in microfracture surgery [225], and is also used as a scaffold for matrix-induced autologous chondrocyte implant (MACI). MACI is in clinical use and has been shown to lead to statistically significant improvements in patient outcome after 5 years compared to microfracture when treating defects of 3cm² or larger [226]. NeoCart (Histogenics, Waltham, MA, USA) is another similar construct composed of a bovine collagen type I scaffold that is seeded with autogenous chondrocytes and cultured in a bioreactor [227]. The NeoCart successfully completed phase I and II clinical trials, but did not meet the primary endpoint of statistically significant improvement compared to microfracture treatment in a phase III clinical trial (unpublished; ClinicalTrials.gov Identifier: NCT01066702). These results lead to a major collapse in Histogenics' share price, and dissolution of the company leading to the NeoCart's IP and research data being sold to Medavate (Fort Collins, CO, USA). For both the MACI and the NeoCart the product is an autologous chondrocyte-laden thick sheet which the surgeon cuts to the appropriate size during surgery and fixes in places using either sutures, or a collagen/fibrin glue. Both constructs performed

similarly in their clinical trials, and despite statistically significant improvement over microfracture being found in some patient groups in some patients scores, these were not on the level of what might be expected from a tissue engineered/regenerative medicine implant. Although no mechanical testing of these constructs or the scaffolds appears to have been published, it is clear from videos showing their use that they at least do not have sufficient mechanical strength to support their own weight; they appear as a limp wet cloth when held by tweezers. Hence, they may be considered to be far weaker than native cartilage and more similar to the mechanical strength of a collagen sponge. It is difficult to see how such a weak construct could re-capitulate the mechanics of native cartilage, and protect the chondrocytes within from damage. There also remains concerns around the chondrogenic potential of the chondrocytes used considering their in vitro expansion, and the need for 2 surgeries.

Another TE strategy is to use stem cells that can be expanded and differentiated into chondrocytes once a sufficient cell population has been achieved, thereby bypassing the risk of phenotypic changes in the chondrocytes. Mesenchymal stem cells (MSCs), embryonic stem cells, induced-pluripotent stem cells (iPSCs), and chondrogenic stem/progenitor cells (CSPCs) have all been used in cartilage tissue engineering research [228]. CARTISTEM® (Medipost, Republic of Korea) is a hyaluronic acid hydrogel laden with allogeneic MSCs, derived from human umbilical cord blood, the use of which was recently reported in a 7-year follow-up study on patients from a phase I/II clinical trial [229]. 5 mm diameter, 5 mm deep holes were drilled in the patient's cartilage defect site, and the holes were then filled with the CARTISTEM gel. Similar to the MACI studies, CARTISTEM® showed an improvement for large defects when compared to a control group who received microfracture treatment, however the improvement appears more pronounced than that reported for MACI. Despite the MSCs being allogeneic, no cases of rejection were reported in the 7 year study. The MSCs used in CARTISTEM® are harvested non-invasively from the umbilical veins, with informed consent, during neonatal birth, and are

hypoimmunogenic, hence their attractiveness as a source of allogeneic MSCs [230]. However, the authors of the study did point out some of the limitations of the study such as the small sample size (n=7), and that microfracture is not a standard treatment for defects within size range that was treated in the study, particularly in elderly patients.

Biomaterial selection for a cartilage TE scaffold is often reduced to the argument that natural polymers, like collagen, show enhanced bioactivity but are mechanically weaker, whereas synthetic polymers are mechanically stronger but often lack the bioactivity of natural polymers. However, the apparent weak mechanical strength of many natural polymers, like collagen and silk fibroin, is not inherent to the material but a result of our failure to replicate the supramolecular assemblies of these polymers *in vivo*. Chemical modification in the form of crosslinking can improve the mechanical performance of many of these natural polymers but can also impart some cytotoxicity and consume available binding sites for cell adhesion [231]. The advent of additive manufacturing technology could provide a platform for a better replication of these supramolecular assembly processes, or simply, a material processing technique that results in a better replication of some the material's in vivo properties.

1.6 Research Hypothesis and Objectives

1.6.1 General Aim

The field of bioprinting has exploded into a whole industry in recent years which is no longer limited just to printer manufacturers but now also ink manufacturers. Naturally this has coincided with a greater availability of bioprinting technologies and inks, and an explosion in the number of research groups investigating bioprinting. Despite the growth in the field, the number of printing technologies has remained static, although the methods by which these technologies are implemented have improved. Aerosol jet printing could be a welcome addition to the existing bioprinting technologies particularly given its unique capability to process (through printing)

relatively dilute inks into dense, highly concentrated material. However, the atomization process of aerosol jet printing would expose any biomaterial ink to considerably more environmental extremes than any of the existing bioprinting technologies. Hence, this novel investigation would be obliged to include extensive structural characterization of the printed material to evaluate any detrimental effect of AJP on the biomaterial structure and to determine whether AJP remained a feasible method for scaffold fabrication of the biomaterial.

Collagen has been found to be difficult to use with most bioprinting technologies. Hence despite the omnipresence of collagen films, sponges, and gels in tissue engineering, bioprinted collagen scaffolds have only emerged recently and usually in the form of weak collagen type I gels. However, native collagen, particularly the fibrillar collagens, are known to form some of the strongest tissues in mammals such as cartilage, tendon, skin and bone. Should the capability of aerosol jet printing to form dense highly concentrated material be possible to apply to fibrillar collagen with high efficacy, it could possibly overcome some of the limitations of collagen bioprinting. Three different collagens were investigated in this context, recombinant human collagen type III (RHCIII), bovine Achilles' tendon-derived collagen type I, and porcine articular cartilage-derived collagen type II. RHCIII was selected due to it being the most efficient production method of any collagen type with sufficient proline hydroxylation to be comparable to native sources and not due to it specifically being a collagen type III. Composite scaffolds typically made using a biocompatible biodegradable thermoplastic skeleton and cell-laden hydrogel filler had already shown promise in cartilage tissue engineering before the advent of bioprinting [232]. Additive manufacturing introduced a way to easily produce many samples with more controlled and repeatable size and porosity than traditional methods. Additive manufactured composite structures made a relatively early impact in cartilage tissue engineering with the famed Wake Forest Institute, headed by James J Yoo and Anthony Atala, reporting on a scaffold made by combining layers of electrospun polycaprolactone (PCL) with inkjet printed

layers of chondrocyte-laden alginate [233]. The introduction of melt electro-writing (MEW), a printing method similar to electrospinning that produces micron-scale filaments, as a way to print PCL and similar thermoplastic biomaterials really enhanced what could be achieved with these composite AM structures [234,235]. However, MEW is reported to be difficult to integrate with bioprinting methods compared to FDM [236]. The use of thermoplastic biomaterials as a reinforcing agent in cartilage and bone bioprinting research has yielded positive results and strengthened the mechanical properties of the bioprinted constructs. However, many of the thermoplastics being researched have long degradation times and have been selected due to their favourable rheological properties for printing. PCL has a total degradation period of 2-4 years depending on its initial molecular weight [237]. PCL also fails to integrate with host tissue and typically induces an initial mild inflammatory response before being encapsulated in a fibrous capsule and giant cells. Hydrolysis is the main action of degradation in the first year of implantation. Intracellular degradation mostly by macrophages and giant cells begins in the second year [238]. However, given the avascular nature of cartilage the access of macrophages and other immune cells to the scaffold is likely to be reduced, possibly leading to longer degradation and complicating regeneration. Dense collagenous constructs like those that can be evidently produced via aerosol jet printing from this project could be used scaffolds in their own right or as reinforcing agents in cell-laden hydrogels similar to thermoplastics by exploiting the freeform 3D printing possible with concentrated collagen type II inks.

1.6.2 Specific Objectives

1.6.2.1 Specific objective 1

Investigate aerosol jet printing as a method for the production of recombinant human collagen type III, bovine tendon-derived collagen type I and porcine articular cartilage-derived collagen type II scaffolds suitable for tissue engineering and establish methods and protocols for the application of these collagens to aerosol jet printing.

1.6.2.2 Specific Objective 2

Determine the suitability of aerosol jet printed recombinant human collagen type III scaffolds for applications as a tissue engineered corneal substitute

1.6.2.3 Specific Objective 3

Characterize aerosol jet printed bovine tendon-derived collagen type I and porcine articular cartilage-derived collagen type II scaffolds for the purpose of determining suitable applications for them.

1.6.3 Organization of the Thesis

Chapter 2	**The fundamentals of aerosol jet printing collagen and methods development** The development of a method to print and stabilize recombinant human collagen type III (RHCIII) scaffolds via aerosol jet printing (AJP) and with the use of a co-solvent. Extraction and aerosol jet printing of collagen type I and II from animal tissues, including further development of the AJP method for producing collagen scaffolds, and the development of methods to characterize the scaffolds using DSC, FTIR, and nanoindentation
Chapter 3	**High resolution bioprinting of recombinant human collagen type III for corneal tissue engineering** Further development of the method for aerosol jet printing RHCIII scaffolds with characterization of the effect of the shear forces of AJP on RHCIII and mechanical and optical characterization of the scaffolds to determine their suitability for corneal tissue engineering

Chapter 5	**Bioprinting of collagen type I and II via aerosol jet printing for the replication of dense collagenous tissues** Extraction and aerosol jet printing of collagen type I and II from animal tissues with characterization of the effect of the shear stresses of atomization on the collagen solutions, collagen triple helix, and molecular weight, and determination of their mechanical strength, and their structural and swelling properties.
Chapter 6	**Conclusions**

2 The fundamentals of aerosol jet printing collagen and methods development

Parts adapted from:

"High resolution bioprinting of recombinant human collagen type III"; Gibney, Rory; Patterson, Jennifer; Ferraris, Eleonora; Polymers 2021, 13:2973

"Bioprinting of collagen type I and II via aerosol jet printing for the replication of dense collagenous tissues"; Gibney, Rory; Ferraris, Eleonora; Frontiers in Bioengineering and Biotechnology 2021, 9:786945

2.1 Introduction

2.1.1 An Introduction to aerosol jet printing

Aerosols are gases that contain liquid droplets and/or solid particles which are so small and light that they become suspended in the gas. Although the term "aerosol" is meant to refer to the gaseous suspension of "aerosol particles", i.e., liquid or solid particles suspended in a gas, the latter term is often abridged to just aerosols. Aerosols are ubiquitous in nature; the atmosphere is filled with aerosol droplets of water and other liquids, and aerosol particles of sea salt, mineral dust, pollen, spores and microorganisms [239]. There are also many anthropogenic sources of aerosols. Indeed, there is now a greater public awareness of aerosols since the

discovery of the extent of microplastic pollution in air, the impact of airborne particulate matter from the burning of fossil fuels on public health, and of course, since the pandemic caused by the Severe Acute Respiratory Syndrome Coronavirus-2 (SARS-CoV-2) [240,241]. Aerosol particles can be as large 100 µm in diameter, but they tend to be < 5 µm in diameter, or at a size where their mass is so low that the force of gravity can easily be overcome by fluid flow and forces such as the buoyancy and the viscous forces of the gas [242]. However, they may eventually settle out of suspension due to gravity in motionless gas, or impact on surfaces due to the inertia of aerosol particles in a gas flow. Aerosol (liquid) droplets have unique properties, they have a very high surface area to volume ratios which can facilitate a high rate of solvent evaporation/diffusion from the droplet. Aerosol droplets can also reach solute concentrations that are much higher than the saturation concentration of bulk solutions, which can result in a dramatic increases in chemical reaction rates [243,244].

Aerosol jet® printing (AJP) is a printing method that forms an aerosol from an ink and carrier gas, and forces the aerosol to coalesce on a substrate via impaction. AJP was first patented by Optomec® (Albuquerque, NM, USA) in 2006 [245]. It was developed as a way to print electronic components on to virtually any surface [246]. Since the arrival of the first commercially available aerosol jet printer, the Optomec® AJ300, which , AJP has seen use in niche areas of research, and in some commercial applications, such as printed antennas. AJP exploits a pre-existing aerosol observation method, which confines aerosol droplets in a flow with a coaxial annular flow of gas (sheath gas) so that the droplets may be studied [247]. AJP uses this method to collimate an aerosol, where the aerosol particles are ink droplets, into a dense stream, i.e. an aerosol jet®, in which the aerosol droplets are travelling at speeds of up to 100 m/s upon exiting the nozzle [248]. The velocity and subsequent inertia of the droplets in this collimated stream, or aerosol jet, along with the confining effect of the sheath gas allows for the nozzle of the printer to be up to 5 mm away from the substrate, as seen in Figure 2-1, which facilitates the printing onto many different surfaces [249,250].

As a result of the sheath gas the nozzle diameter does not equate to the print resolution, and lines or features can be printed that are 90% smaller than the diameter of the nozzle. This helps prevent nozzle clogging and also removes some of the complications around the fabrication, handling and cleaning of a much smaller nozzle. The sheath gas also facilitates the aforementioned high rate of solvent evaporation from aerosol droplets due to their high surface area to volume ratio and the lack of moisture in the gas. This allows AJP to deposit highly concentrated material that would otherwise require very long drying periods to replicate. The drying effect of AJP is so pronounced that many AJP inks include a small amount humectant (a liquid with a high boiling point and low vapour pressure) as a co-solvent to create a maximum threshold for the amount of evaporation [251]. Although solid aerosol particles can be deposited, under certain conditions, using AJP, this is often less desirable since they are less likely to coalesce upon impaction on the substrate, and they are more likely to diffuse out of the collimated aerosol jet.

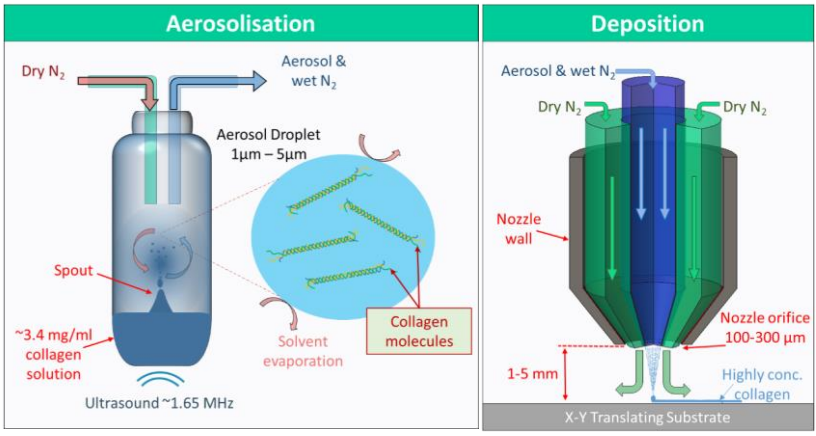

Figure 2-1. ***(a)*** *Aerosolisation begins with 1.65 MHz ultrasonic waves forming a spout in the vial containing the ink, a solution of collagen. Aerosol droplets are dispersed from the spout and become entrained in a nitrogen gas flow towards the deposition head. Solvent evaporation is high due to the high surface area to volume ratio of the aerosol droplets, and the dry nitrogen gas.* ***(b)*** *The aerosol and high humidity N_2 is collimated by a co-axial flow of nitrogen which further dries the aerosol droplets, and separates them from the walls of the nozzle. The aerosol coalesces on a XY translating substrate forming highly concentrated collagen printed lines.*

2.1.2 Aerosol jet printing, why haven't I heard of it?!

AJP has not experienced the "printing-boom" witnessed by other printing technologies in the years since the advent of the first commercial aerosol jet printer, the Optomec® AJ300, and there are several likely explanations for this. One explanation of the slow adoption of AJP is the price; an entry level Optomec® AJ300 seen in Figure 2-2, at around $350,000 for most of its history, is higher than many more familiar and accessible printing technologies such as inkjet and extrusion printing. Another explanation is that aerosol jet printing has a reputation within the printing community for being difficult to use and for suffering from reliability and repeatability issues, which is evident through proportion of AJP papers that focus on AJP process control and optimization [121,248,252,253].

One major disadvantage of the Optomec® AJ300 is that there is no feedback for the amount aerosol generated or for the efficiency of the carrier gas-aerosol mixing. Obviously, the amount of aerosol generated, and the efficiency of the mixing has a major impact on the amount of deposition. This is further complicated by the fact that in the ultrasonic atomizer, the position of the vial can be varied, and the position of the vial has a major impact on the atomization. However, a viewing window in the ultrasonic atomizer allows the user to see the vial during operation to give them some idea of the amount of aerosol generation and the efficiency of the mixing. The recommended procedure from Optomec® to combat possible repeatability issues due to differences in aerosol generation caused by vial positioning is to always position the vial so that the maximum atomization is achieved; the maximum atomization being judged by the user from experience. Other features of the AJ300 can also aid the user in judging aerosol generation and mixing. The process camera is a magnified camera focussed on the substrate directly below the printhead. From watching the process camera feed the user can infer whether the carrier gas is mixing well with the aerosol and giving consistent deposition. The process camera along with pressure feedback from the sheath gas and atomizer gas flows can also be interpreted to judge whether the nozzle is clogging. Nozzle clogging can be common in AJP. The sheath gas encapsulation of the

aerosol flow is not perfect, so aerosol particles can escape the collimated aerosol flow and make contact with the nozzle walls. This can lead to build up on the nozzle walls and eventually a full or partial occlusion. If spotted early the print can be paused, the nozzle cleaned and the print continued, however clogging can also lead to the formation of large (non-aerosol) droplets which can land on the deposited material and re-solubilise it, thereby destroying the print in most-cases. Clearly much of the performance of aerosol jet printing is dependent on the experience and skill of the user.

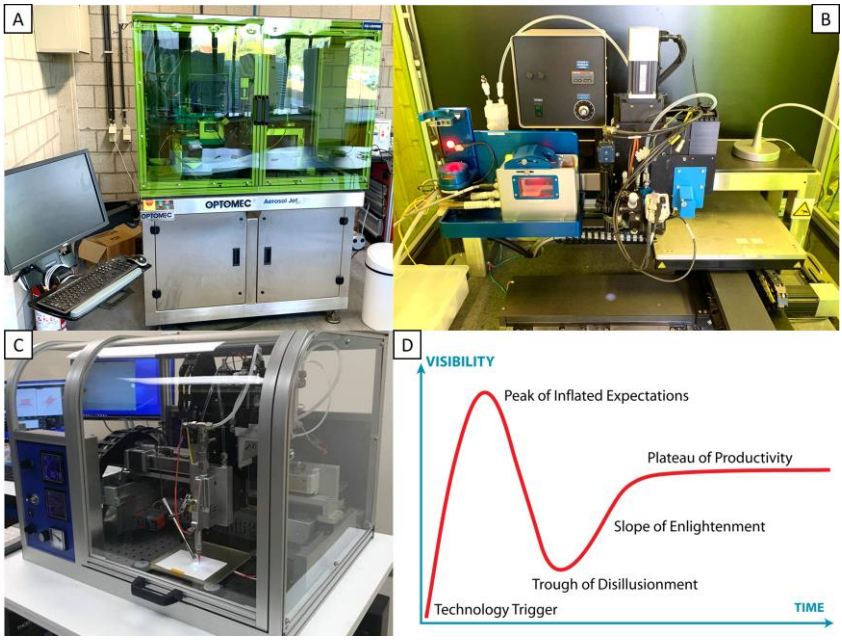

Figure 2-2. (A) The Optomec® AJ300 aerosol jet printer at KU Leuven Campus De Nayer, (B) a view inside the AJ300, (C) the IDS Nanojet ©IDSnm inc. 2021, and (D) the Gartner hype cycle © J. Kemp 2007

A more recent iteration of the Optomec® aerosol jet printer has attempted to lessen the need for extensive user experience. The new ultrasonic atomizer (UA Max) employs a round bottom vial with much thinner glass and has a fixed vial position so that the ultrasound is efficiently transmitted into the vial and to eliminate the variability of the vial positioning. The printer control software includes a better process camera with image processing software capable aiding the user during operation. Unfortunately, these new

features are not backward compatible, and it is not yet clear how effective they are in making aerosol jet printing more user-friendly and less dependent on the experience and skill of the user. There has also been the arrival of a new aerosol jet printer and printer manufacturer, the Nanojet and IDSnm Inc. respectively. The Nanojet, seen in Figure 2-2(C) has slightly different features but the great advantage of a G-code based toolpath programming opening it up to a wealth of existing open-source tooling programs. There also seems to have been somewhat of an increase in the amount of papers investigating aerosol jet printing, and real efforts to address some of the recurrent issues mentioned [254,255]. This suggests that we may be entering the "slope of enlightenment" phase of a Gartner hype cycle graph, as seen in Figure 2-2(D), for this rather bohemian printing technology.

2.1.3 AJP as a bioprinting method for collagen

AJP is particularly intriguing as a printing method for biological materials due to its ability to concentrate a solution (ink) through the process of printing and deposit the resultant concentrated material with feature sizes below the oxygen diffusion limit (frequently reported to be around 100 µm - 200 µm [256,257]). As mentioned in section 1.3.5, AJP has been used to deposit biological materials such as DNA, enzymes, and silk fibroin, with varying degrees of success [10,118–120]. However none of these studies investigated AJP as a bioprinting method, instead they investigated AJP of single layers for cell patterning [10], for biofunctionalization [118,119], and as a fundamental study on AJP of a biodegradable material [120]. A major concern raised in one of these papers was that the ultrasonic atomization in the AJP process caused degradation of their material, DNA [118]. However, another paper concluded that there was no significant decrease in functionality of an enzyme (i.e. no denaturation) which they printed via AJP [119]. Hence, it is not clear-cut whether there is a high risk of degradation when using biological materials with ultrasonic atomization AJP and it is likely dependent on the material. Pneumatic atomization has been shown to be a less-degrading atomization method than ultrasonic atomization, at least

for DNA [118]. However, the pneumatic atomizer has many disadvantages, such as, no cooling, high material losses, poor print quality, and an initial volume of 10 ml to 20 ml is usually required for stable aerosol generation. Hence, ultrasonic atomization is still the preferable atomization method. Also, since collagen is amphiphilic, like many proteins, the pneumatic atomizer is likely to have to overcome problems with foam generation.

Another issue that has to be overcome is the scalability of AJP, particularly in terms of thickness. Most applications of aerosol jet printing require only a small number of layers if not single layers, since there is little need to build thickness for electrical printing. The thickness of aerosol jet printed layers (though often not measured or at least reported in AJP papers) is thought to typically range from 0.1 µm to 2 µm, according to the Optomec® manual. The thickness is largely attributed to the ink "loading", which can be defined as the amount of material suspended or dissolved in the ink that is likely to be left behind upon partial or complete solvent evaporation. Hence, in order to print a thicker structure, as would be necessary for bioprinting, there are two possible solutions, print inks with higher loading, or print a lot more layers. Viscosity is a major inhibitor when it comes to implementing higher loading, particularly when considering a long chain polymer like collagen [258]. Optomec® recommends an ink viscosity range of 1-10 cP for use with the ultrasonic atomizer. Therefore, to make aerosol jet printing a feasible bioprinting technology, it will have to be shown to be possible to print hundreds of layers, and relatively high concentrations of collagen.

As outlined in section 1.2.2.1, through aerosol jet printing a suitable collagen solution will go from solution, into an aerosolized solution, back into a bulk highly concentrated solution (through coalescence on the substrate) until it dries enough to form a solid. It is not clear what form the collagen is likely to take through this process. For most applications of collagen as a gel, the collagen (in solution) is neutralized and incubated in order to induce fibrillogenesis and thereby forming a hydrated network of fibrils. In the course of aerosol jet printing a collagen solution, the solution will

not be neutralized, so the concentrated collagen left on the substrate may never be at a suitable pH to allow the assembly of fibrils. Therefore, the collagen would be likely to remain in a soluble state, which could lead to the dissociation of collagen molecules from the printed structure upon incubation in aqueous media, i.e., scaffold deterioration. Collagen gels or sponges have been made directly from collagen solutions without neutralization, but these usually rely on some other stimulus (e.g. gamma radiation) to induce non-native crosslinking [259]. Hence some method of scaffold stabilization is likely to be necessary to allow the scaffolds to be used in aqueous media without the risk of scaffold deterioration.

2.2 Materials and methods

2.2.1 Materials

Recombinant human collagen type III was originally procured from Fibrogen. However, Fibrogen ceased supplying research activities in 2015. RHCIII with identical properties was then procured from MyBioSource, and later Abcam, after MyBioSource ceased production of RHCIII. The RHCIII was supplied as a ~3.4 mg/ml solution in 0.01 M hydrochloric acid and stored at 4°C. The α-1 chains which assemble into a trimer to make RHCIII had an expected molecular weight of 138.6 kDa based on the UniProt accession P02461 sequence. Bovine Achilles tendon-derived collagen type I and porcine articular cartilage type II were extracted in REMODEL at NUI, Galway. The collagen extraction process is detailed in the proceeding section (section 2.2.2). EDC ([N-(3-Dimethylaminopropyl)-N'-ethylcarbodiimide hydrochloride]), N-hydroxysuccinimide (NHS), ProteoSilver staining kit were purchased from Sigma Aldrich (Leuven, Belgium). All other materials were purchased from VWR, Belgium.

2.2.2 Collagen extractions

Collagen extractions were performed using published protocols with some modifications in REMODEL at the National University of Ireland, Galway [260–262]. Frozen bovine Achilles tendons were

defrosted, fascia were trimmed, and the tendons cut into 1 cm cubes. The cubes of tendon were placed in large beaker of 1XPBS on ice, on a magnetic stirrer at a low speed. After 2 hours the cubes were sieved from the 1XPBS and weighed. The tendon cubes were then frozen and cryo-milled into small pieces. The milled tendon was washed by placing it in a large beaker of 1XPBS at 4°C and leaving it stirring for 2 hours. After 2 hours the suspension was centrifuged at 4000g for 40 min and the supernatant discarded, this step was then repeated two more times. The milled tendon was then re-suspended in 0.5 M acetic acid in a 4°C cold room using an overhead mixer over 48 hours. After the 48 hours, or until the milled tendon appeared adequately suspended, the suspension was removed from the 4°C cold room, and left at room temperature to allow the suspension to slowly reach 15-20°C. Once in this temperature range, pepsin was added to the suspension at a rate of 1 g per 100 g of wet tendon and left for another 2 hours at room temperature before returning it to the 4°C cold room for 72 hours. The suspension was then filtered at room temperature through a 100 µm sieve membrane using a Buckner funnel over a filtering flask attached to low flow vacuum supply. Filtered insoluble pieces of tendon were discarded, and the filtered suspension was returned to the 4°C cold room. Sufficient salt to make the filtered suspension a 0.9 M NaCl solution was gradually added whilst gently stirring with a pipette. The collagen precipitated, forming a mesh of fibrils on top of the suspension. Collagen fibrils were collected with a sieve and centrifuged at 18000g for 20 minutes to remove any remaining solution. The collagen fibrils were weighed and then re-suspended in 1 M acetic acid at 4°C. The collagen solution was centrifuged at 18000g for 20 minutes, and any precipitated material was discarded. The purified collagen solution was put into dialysis tubing and dialyzed against 1 mM acetic acid, with the dialysate changed 5 times. The purity of the dialysed collagen solution was assessed by SDS-PAGE with silver staining, then frozen and lyophilized.

This process was repeated using porcine articular cartilage for the extraction of collagen type II. In brief, slices of cartilage were peeled from the femoral condyles and femoral head of porcine

femurs using a scalpel. Only the white upper zones were resected, cartilage that appeared pinkish or vascularized was avoided and any resected pieces containing such cartilage were discarded. Resected cartilage pieces were immediately placed in 1XPBS on ice. The cartilage was then frozen and cryo-milled. All steps thereafter were identical to the collagen type I extraction. Collagen inks were made by adding the lyophilised collagen type I or type II to a suitable amount of cold 0.01 M hydrochloric acid and stirring at 4°C for at least 48 hours.

2.2.3 AJP print program development and sample production

The recommended procedure for generating toolpaths or print programs for the Optomec® AJ300 was to use AutoCAD with a plugin called "VMTools", however, this plugin only seemed to work on Windows XP operating systems. The programs the plugin generated also tended to be very computationally heavy, regularly causing the system crash even with single layered samples, and the program often changed the scalar value by which the input units (mm) were multiplied in order to calculate the machine units (steps of stepper motor) leading to a sample of the wrong dimensions. A toolpath generator was developed in MATLAB to generate more efficient code and facilitate the encoding of prints with hundreds of layers in a single print program. The MATLAB program would take a user input circle diameter, track spacing (print line width), and an angle of rotation. Each even-numbered layer was printed perpendicular to the preceding layer, and each odd-numbered layer (apart from layer 1) was rotated by "the angle of rotation" to the preceding layer, as seen in Figure 2-2. This system of rotating the print pattern between layers was implemented to minimize the overlap of peaks and troughs with repeated layers so that samples would possess relatively smooth surfaces. This program was used to print test samples of 1-5 mm in diameter and 48 – 768 layers. Samples were printed onto 10 mm diameter circular glass cover slips. Cover slips were cleaned before printing using isopropanol.

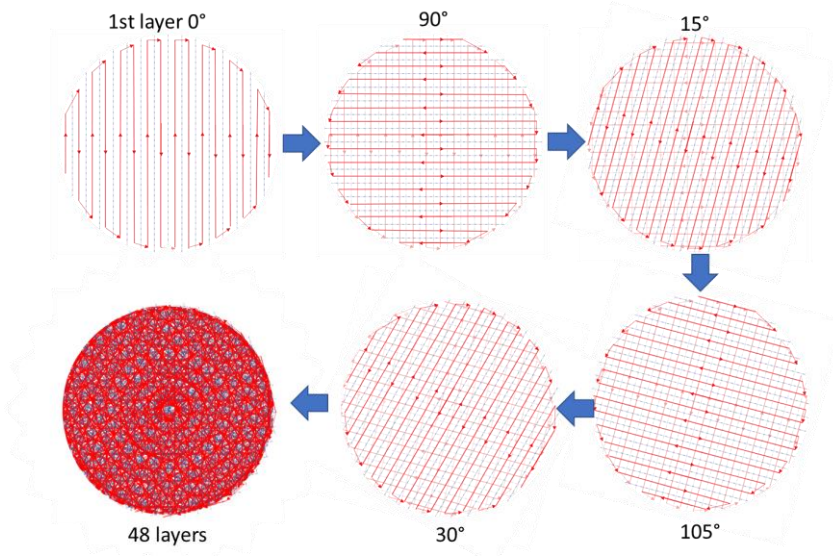

Figure 2-3. The scheme of the print program with even-numbered layers (2nd, 4th, ..) at 90° to the previous layer and odd-number layers rotated by the "angle of rotation" (typically 15°) to the previous odd-numbered layer. Each layer is a rectilinear raster of the same circle, as layers overlay some particular areas of overlap lead to superficial patterns.

The samples used in the experiments outlined in this chapter were printed using different printing parameters since the experiments were carried out at different times while efforts were being made to increase sample production rates. The major print parameters were the number of layers, the track spacing, the nozzle diameter, the atomizer and sheath gas flow rates, and the print speed. The values for these print parameters used for all samples used in each experiment within this chapter are outlined in Table 2-1 below. The production rate was improved by gradually increasing the print speed and flow rates, however, with each increment issues typically arose that need to be resolved. *Pooling*, where adjacent print lines coalesced into a larger print line was the most common issue often arising at corners as print speeds and flow rates increased. The larger volume to surface area ratio in these pools leads to slower drying. At times the proceeding layer would add to the pool and a pool would gradually grow through a print. Larger pools were also at risk of being blown across the sample by sheath

gas leading to major disruption of the sample. Hence, for every attempt at increasing print speeds and flow rates, sets of samples with a relatively small number of layers would be printed and inspected under a microscope to determine whether pooling was occurring. Pooling was also often detected during a print from observing the process camera. Other issues that often arose were condensation in tubing and droplets entering the tubing in the atomizer. These were addressed by close observation and regular purging of the tubing during prints.

Experiment	No. of Layers	Track spacing	Nozzle diameter	Atomizer flow rate	Sheath flow rate	Print speed
Scaffold stabilization	30	100 µm	300 µm	20 ml/min	16 ml/min	5 mm/s
DSC	192	30 µm	100 µm	30 ml/min	35 ml/min	10 mm/s
FTIR	576	60 µm	100 µm	40 ml/min	60 ml/min	11.5 mm/s
Nanoindentation	576	60 µm	100 µm	50 ml/min	50 ml/min	12.5 mm/s

Table 2-1. Summary of the print parameters used for all samples used in each experiment in this chapter

2.2.4 AJP scaffold stabilization

Preliminary experiments showed that the AJP collagen was soluble in 1XPBS, so much so that all early samples dissociated into solution in the 1XPBS, with only a slight residue of collagen left behind on the substrates. This was also the case when EDC : NHS crosslinking ([N-(3-Dimethylaminopropyl)-N'-ethylcarbodiimide hydrochloride] : N-hydroxysuccinimide crosslinking) was employed using a method in an aqueous buffer similar to Liu et al. 2008 where the same recombinant human collagen type III was also used [193]. The use of ethanol as a co-solvent is not uncommon for EDC crosslinking. Ethanol use is often implemented in EDC crosslinking to prevent hydrolysis of the EDC in solution and thereby increase the crosslinking efficiency, and for its apparent ability to preserve porosity [263]. In a paper investigating the influence of different

ethanol/water co-solvent concentrations on the efficiency of EDC : NHS crosslinking of collagen type I, it was noted that at high ethanol concentrations only the surface of the collagen gel was crosslinked [264]. The crosslinking was determined to be limited to the collagen gel surface due to a decrease in solvent absorption with increasing ethanol concentration. The use of ethanol as a co-solvent was investigated for AJP-deposited RHCIII since the low ethanol absorption of collagen shown in that study could prevent sample dissolution. The potential drawback was that if the bulk of the sample did not absorb the crosslinking solution, it would remain in a soluble state and be lost during sample washing post-crosslinking. The pH of the crosslinking solution was also determined to be of interest since the hydrochloric acid that leaches from the AJP RHCIII needed to be neutralised but the optimal pH of EDC : NHS crosslinking, pH ~5.5, was also considered [193]. A lower temperature was also expected to further slow absorption and prevent collagen denaturation. Hence an experiment was set up where ethanol concentration, pH and temperature were varied between two levels. A simple grading system was employed to evaluate sample performance during crosslinking was developed. Control samples using protocols in pure aqueous buffer, and pure ethanol were included to illustrate the subsequent dissolution of the sample, which was observed in preliminary tests.

In order to make the buffer first a 0.01 M solution of MES was made. A 10 M solution of sodium hydroxide was used to adjust the pH of the buffer to either 5.5 or 8.5. The buffers were then added, in suitable amounts, slowly to ethanol while stirring, resulting in 4 different solutions, 40% ethanol pH 5.5, 40% ethanol pH 8.5, 70% ethanol pH 5.5, and 70% ethanol pH 8.5. A 0.4 mg/ml EDC, 0.24 mg/ml NHS solution was formed with each of the 4 buffers.

The complete printing conditions of the 22 aerosol jet printed samples used in the experiment were included in table 2-1 above, briefly, these were 4 mm samples consisting of 30 layers with 100 µm track spacing printed at 5 mm/s. These parameters are quite different to those used for other work in this thesis, though this is just as a result of the increases in print velocity that were made after

the work on scaffold stabilization was completed. 40 µl of each solution was pipetted onto 2 samples each either at room temperature or on ice. A small volume was used so that the solution could be limited to the coverslip. The wellplates containing the samples were then left at room temperature or in a fridge at 4°C for 24 hours. The crosslinking solution was then removed, and the samples were washed once in cold PBS and twice in cold ddH_2O for 15 minutes. Control samples using the same EDC concentration in 100% ethanol at 4°C and 20°C, and in 0.625 M MES adjusted to pH 5.5 at 37°C

Condition		
pH	5.5	8.5
Ethanol %	40%	70%
Temperature	4°C	20°C

Table 2-2: Conditions used to investigate the influence

2.2.4.1 Crosslinking/stabilization *performance*

Typical methods for assessing crosslinking performance such as testing crosslinking efficiency with a ninhydrin assay, or measuring changes in swelling behaviour, were of no use in assessing whether the printed material was re-solubilized during crosslinking. Samples could not be removed from their substrate intact before crosslinking hence changes in weight could not be used. However, in early experiments clear signs of re-solubilization could be determined visually. Hence a quality assessment system was devised where samples were observed under an optical microscope before and after crosslinking to determine whether re-solubilization has occurred. Samples were rated from 1 to 10 based on how closely they resembled the microscope images taken pre-crosslinking. Samples were rated 10 if no difference could be discerned, and 1 if the sample had completely dissolved.

2.2.5 Differential Scanning Calorimetry (DSC)

DSC was employed to determine the melting temperature of aerosol jet printed RHCIII in contrast to acidic and neutralized non-printed control samples in an effort to gain a better understanding of

whether any fibrils assembled in the printed samples. Control samples were made from a stock RHCIII solution and a RHCIII solution that had been neutralized with 1 M NaOH. The control samples were made by pipetting 10 µl of the respective solutions into aluminium crucibles under a fume hood, and allowing time for some evaporation before adding another 10 µl. This was repeated until a total of 150 µl of RHCIII had been pipetted into the crucible and the crucibles were left to dry overnight. The neutralized samples were then washed twice in PBS and three times in ddH_2O to remove any salts remaining from the neutralization and again left to dry overnight under the fume hood. Printed samples consisted of 7 mm diameter samples with 192 layers, printed using the program outlined in section 2.2.2. The printed samples were crosslinked at 4°C in a co-solvent of 7 parts ethanol to 3 part MES buffer at pH 8.5 with 40 µg/ml EDC and 24 µg/ml NHS, then washed in 1XPBS three times, and twice in ddH_2O before placing them in a crucible and leaving them to dry overnight under a fume hood. In all cases the empty crucibles with lids were weighed beforehand and again after the samples placed within them had dried. A TA Instruments Q2000 DSC (access provided by Prof. Carola Corcionne at the Università del Salento, Lecce, Italy) was run from 15°C up to 250°C at a heating rate of 10°C/min.

2.2.6 Attenuated Total Reflectance Fourier-Transform Infrared (ATR-FTIR)

FT-IR has been used to distinguish different structural conformations (beta sheet, triple helix, and random coil) within collagen and to distinguish the different types of collagen, heat-denatured collagen, UV irradiated collagen, and gelatin [265–269]. Some of these papers focus on different areas of the spectrum in order to carry out their analysis, most focus on the Amide I and amide II bands while others combine one of these with an interpretation of the amide III band and the amide A band. The hydrolysis or denaturation of collagen is reportedly characterized by a narrowing of the amide I band and a decrease in its intensity. A shift in the amide II band maximum intensity from around 1543 cm^{-1}

to 1521 cm^{-1}, is reported to be indicative of a transition from an ordered helical conformation to a random coil conformation [267]. A decrease in the amide III band intensity, and a broadening of the amide A band has also been used to characterize hydrolysis of collagen.

Positive control samples were collagen films made by repeatedly pipetting 5 µl onto a cover slip in a well plate under a fume hood and letting it dry (10 times; 50 µl total) and leaving it to dry overnight. Negative controls were obtained by first pipetting some collagen into an Eppendorf and heating the Eppendorf up to 70°C for 10 minutes. A collagen film was then formed from the now denatured collagen in the same way as the positive control. Printed samples were 4 mm diameter samples with 576 layers printed with the same program developed in 3.2.1. Samples and controls were stored in a well plate at 4°C until required. Samples were measured using Varian 620-IR spectrometer scanning in the range 400 – 4000 cm^{-1}.

2.2.7 Nanoindentation

Preliminary nanoindentation tests were carried out on a recently procured Optics11 Chiaro ferrule-topped nanoindenter. This nanoindenter is composed of a spherical tip on a cantilever of known stiffness. Fabry-Pérot interferometry is employed to measure the deflection of the tip of the cantilever from an optical fibre at the tip of the ferrule body. A piezoelectric motor precisely moves the tip for indentations in accordance with a user-defined indentation profile (z-displacement against time). The indentation depth (d_i) can then be obtained by subtracting the cantilever deflection (d_c) from the displacement of the piezoelectric motor (d_p) [270]:

$$d_i = d_p - d_c \tag{2-1}$$

The load applied during the indentation (P) is calculated using the known stiffness of the cantilever (k) and the deflection of the cantilever in equation (2-2) [270]:

$$P = k \times d_c \tag{2-2}$$

This results in a graph of the load against the indentation or the piezo displacement which can be analysed using one of two indentation models in the Optics11 nanoindentation software, the Hertzian model or the Oliver-Pharr model. The Hertz model analyses the loading curve of the graph and assumes fully elastic contact, whereas the Oliver-Pharr model analyses a portion of the unloading curve and assumes elastic plastic contact [271–273]. However, the Hertz model is generally recommended for viscoelastic materials and most biomaterials by Optics11 [274]. Given a material with unknown Poisson's Ratio the Optics11 software, assuming a Hertzian model, calculates the effective elastic modulus (E_{eff}) of the material using the load (P), indentation depth (d_i), and the radius of the indenter tip (r) in the equation 2-3 below:

$$E_{eff} = \frac{3P}{4\sqrt{r.d_i^3}} \tag{2-3}$$

The relationship of the effective elastic modulus to the elastic modulus of the sample material in a Hertzian model is defined as:

$$\frac{1}{E_{eff}} = \frac{1-v^2}{E} + \frac{1-v'^2}{E'} \tag{2-4}$$

Where, E and v are the elastic modulus and Poisson's ratio of the sample material respectively, and E' and v' are the same values for the indenter respectively. The elastic modulus of the sample can be calculated once the Poisson's ratio of the sample material is known, and assuming that the elastic modulus of the indenter is far greater than the elastic modulus of the sample material (i.e., E' >> E), resulting in equation (2-5) below:

$$E = \frac{3(1-v^2)P}{4\sqrt{r.d_i^3}} \quad OR \quad E = (1-v^2)E_{eff} \tag{2-5}$$

Since most materials have a Poisson's ratio in a limited range of values, typically 0.3-0.5, we can expect the elastic modulus of the

samples material to be between 75% and 90% of the effective elastic modulus.

Before performing any indentations, the Optics11 Chiaro nanoindenter needs to be calibrated for the measurement medium, and the "calibration factor". These adjust the interferometer to the refractive index of the measurement medium (which was 1XPBS for all measurements carried out in this thesis), and performs an indentation on a very hard material, typically a glass slide, to ensure compliance between the interferometer signal and the piezo displacement when the tip is in contact with a much stiffer material, i.e., the graph of displacement of the piezo motor, and the cantilever deflection are superimposed upon each other.

Tests were carried out on aerosol jet printed collagen type I and II to determine whether a lower concentration of crosslinking agent, or no crosslinking agent could be used without creating a much weaker construct. The tests were also used to determine an efficient method for carrying out nanoindentation to measure the elastic moduli of the bulk material rather than investigating spatial variations in the elastic moduli within a sample. Samples were left to equilibrate at room temperature for 1 hour before measurements. Measurements were performed in a small petri dish filled with 1XPBS. Samples were transferred from PBS in wellplates, still on their glass cover slip substrates, to the petri dish immediately before each sample measurement. A fine-tipped tweezers was used to apply pressure to the substrate around the sample to ensure full contact between the underside of the substrate and the petri dish and to fix it in position.

Six 4.5 mm diameter samples with 576 layers printed from a 6 mg/ml collagen type II solution and six similar samples printed from a 3 mg/ml collagen type I solution were used. The collagen type II samples were crosslinked in 0.04 mg/ml EDC, 0.024 mg/ml NHS using a co-solvent of 3 parts ethanol to 2 parts 1XPBS adjusted to pH 8.5 with 10 M sodium hydroxide. The collagen type I samples were not crosslinked but stabilized by neutralizing them in the same ethanol-1XPBS co-solvent without EDC or NHS. 45 indentations were

performed in 1XPBS on each sample in these two sample sets in a 3 x 15 matrix with 200 µm spacing in each direction; this eccentric matrix shape was chosen to investigate for variations in stiffness across the sample from inside the rim of the sample to the centre. The collagen type I samples were indented with a probe of stiffness 0.49 N/m and tip radius 58 µm, whereas the collagen type II samples were indented with a probe of stiffness 58.68 N/m and tip radius 26.5 µm, since they appeared outside of the ideal stiffness range of the 0.49 N/m probe upon initial measurement. The 4 sample sets, summarized in table 2-3, were left in their respective stabilizing solutions at 4°C for 18 hours, then washed 3 times in 1XPBS and stored in 1XPBS.

Subsequently, another 2 more sample sets were printed from 3 mg/ml collagen type I and 6 mg/ml collagen type II using the same print program for 4.5 mm samples with 576 layers. Both sample sets were stabilized by incubating them at 4°C in the same co-solvent consisting of 3 parts ethanol to 2 parts 1XPBS at pH 8.5 with no crosslinking agent for 18 hours. The samples were then washed in 1XPBS three times and stored in 1XPBS. A 5X5 matrix of 25 indentations with 200 µm was performed on all samples in 1XPBS using a probe of stiffness 0.49 N/m and tip radius 58 µm.

Ink (Solution)	**3 mg/ml Col-I**	**6 mg/ml Col-II**	**3 mg/ml Col-I**	**6 mg/ml Col-II**
No. of samples	6	6	9	9
Crosslinker	N/A	EDC : NHS	N/A	N/A
No. of indentations	45	45	25	25

Table 2-3 Properties of each sample set measured and the number of indentations made in preliminary nanoindentation

2.3 Results

2.3.1 Collagen extractions

The yield of the extractions in both cases was around 4 % yield of collagen per gram of wet tissue. SDS-PAGE was performed on the extracted collagens to check for purity. In both cases the gels only resolved molecular weights consistent with their respective collagens.

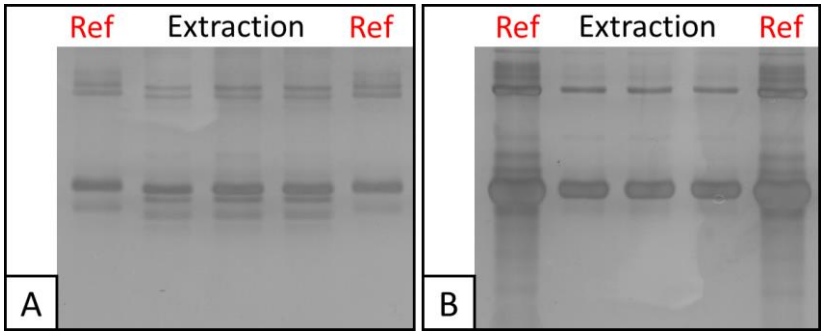

Figure 2-4. SDS-PAGE gels of extracted (A) collagen type I, and (B) collagen type II, where "Ref" lanes denote the reference collagen type I and II used as controls on their respective gels, and extraction denotes the three central lanes where the extracted collagens were loaded.

2.3.2 AJP print program

The system of rotating the print toolpath between layers and pairs of layers lead to smoother samples relative to preliminary experiments with toolpaths with no rotation or just rotations of 90° between layers. The MATLAB-generated toolpaths were compiled and executed by the AJ300 without any errors in most cases. An error of "line of zero length" was encountered when the diameter of the sample was a multiple of the track spacing, as it led to two consecutive commands with the same co-ordinates, however this always occurred between the command that moved the printhead close to the first point in a layer before deposition was initiated and the command that printed a line to that point. This was resolved by ensuring that the first command was 1 µm to the right of the first point in the layer. The samples were not perfectly smooth as seen in

Figure 2-2. Superficial patterns were observed on the surface and appeared to occur due to repeating overlaps of the print patterns.

As stated in section 2.1.2, the lack of a system of feedback for the user on the Optomec AJ300 other than observation of the deposition camera feed makes it difficult to investigate the process. However, observations were made in increasing the rate of production. A smaller nozzle diameter generally led to drier printing which can be attributed to greater proportion of the aerosol being exposed to the drying effect of the sheath gas. Drier printing facilitated faster printing speeds, and avoiding pooling. Due to changes in the rate of atomization and the humidity inside the printer, printing would be drier at the start of a print, and would gradually get wetter. This was later attributed to shear-thinning/thixotropic behaviour of the collagen solutions, shown in Chapter 4, which would cause a drop in viscosity leading to increased atomization. Although humidity was never directly measured in the tubing, the build-up of condensation inside the tubing could be used to indicate the level of humidity therein. Heavy condensation would indicate saturated tubing where little or no evaporation was occurring, hence wetter printing. Slight adjustments, such as lowering the atomizer flow and increasing the sheath flow could mitigate these effects to some degree. Otherwise, the addition of fresh collagen solution would counteract the thixotropic behaviour, and purging the tubing would lower the humidity.

The glass coverslip substrates were found to possess poor wettability for the extracted collagens in particular. This poor wettability manifested itself in the form of patches within a sample where little or no collagen adhered to the substrate, and was often only apparent by observation under a microscope after completion of the print. To enhance the wettability of the glass coverslips for the extracted collagens they were washed in 20% nitric acid for 12 hours on a shaker plate at low speed. The use of concentrated, 6 mg/ml collagen solutions lead to a more frequent occurrence of the high aspect ratio structures occasionally seen when printing less concentrated solutions. These structures grew vertically from the substrate while the printhead was stationary during deposition

typically when a relatively low flow of aerosol was used with a sheath flow around double or triple the aerosol flow. Whilst the deposition of these structures was typically very difficult to control with less concentrated solutions, with the 6 mg/ml collagen type II they could be controlled somewhat and resulted in hollow structures.

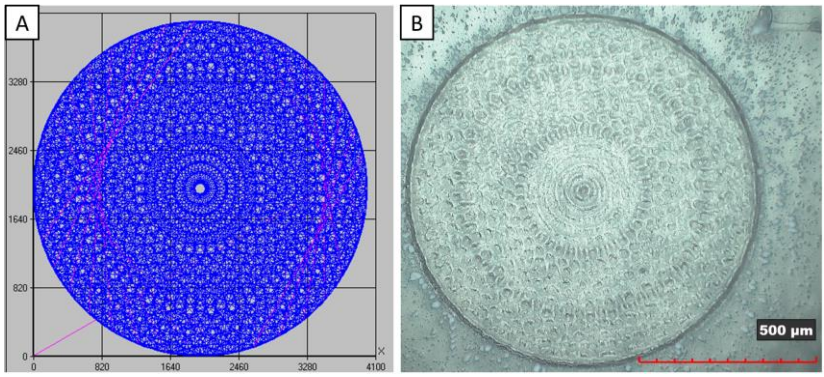

Figure 2-5. (A) A print preview of a MATLAB-generated print program with units in steps of the stepper motor (1 mm = 4000 steps) and (B) the resultant 1 mm diameter sample after printing showing similar superficial patterning.

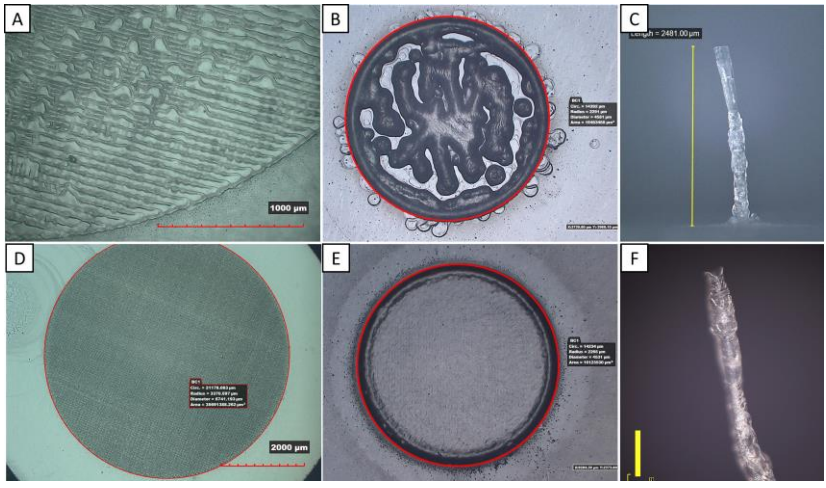

Figure 2-6. Image of aerosol jet printed collagen: (A) an example of pooling in a printed sample, (B) a failed collagen type II sample affected by hydrophobic interactions with the print substrate, (C) and (F) high aspect ratio structures printed with concentrated collagen type II solutions both around 100 µm in diameter (F; scale bar 250 µm), (D) an early RHCIII sample with 30 layers, (E) a more recent 576 layer collagen type II sample.

2.3.3 AJP scaffold stabilisation

Examples of samples ratings can be seen in Figure 2-3, and a table of the ratings is in table 2. The samples crosslinked in 70% ethanol clearly performed better than those at other ethanol concentrations. Despite the high ethanol concentration clear signs of dissolution could be seen in 40% ethanol pH 5.5 samples compared to 40% ethanol pH 8.5 samples. Some difference was also seen between the different pH in 70% samples. As expected, the 100% ethanol samples resulted in only the surface being crosslinked and neutralised, and the bulk was washed out in the post-crosslinking washing steps. Differences due to temperature were less obvious. Despite the limitations of the study in terms of sample number and the arbitrary rating system, this did provide clear evidence of what were the major factors influencing sample dissolution ethanol concentration and pH.

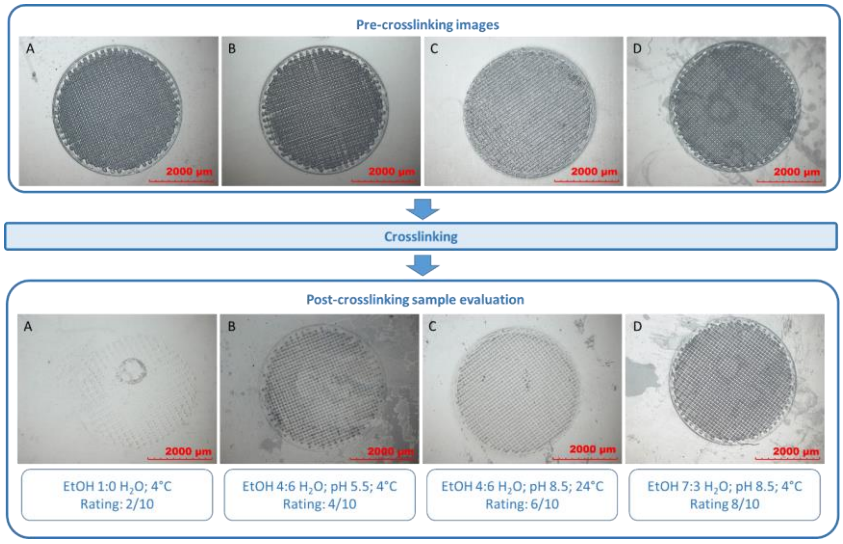

Figure 2-7. Images of samples A to D before and after crosslinking with the crosslinking conditions and sample rating below the post-crosslinking images of the samples. Sample A retained many superficial features, but the bulk of the samples appeared to have disappeared, most likely much collagen remained soluble and was removed during washing steps. Similarly, for sample B and C there seemed to have been significant sample loss, more so for B. D appeared largely unchanged, however on closer inspection there were signs of some sample dissolution in the troughs of the print pattern.

Ethanol % v/v	pH			
	5.5		8.5	
	Temperature		Temperature	
	4°C	20°C	4°C	20°C
40%	3	6	7	6
	4	5	8	8
70%	7	8	8	7
	8	8	9	9
	Controls			
	pH not applicable		pH 5.5	
	4°C	20°C	37°C	
100%	2	2	1	
	2	4	1	

Table 2-4 Table of the crosslinking performance ratings with samples rated 1(dissolved completely) to 10 (no signs of dissolution).

2.3.4 DSC

The thermograms for acidic and neutral controls, and 2 printed samples are seen in Figure 2-5 below. One printed sample could not be reliably measured due to it detaching from the crucible. IN all cases, likely due to the low mass of the samples, very small denaturation peaks were obtained. The acidic non-printed controls and printed samples performed similarly with peaks centred on 210°C and 215°C respectively. The neutral non-printed controls resolved melting peaks at a higher temperature, as expected, at 235°C.

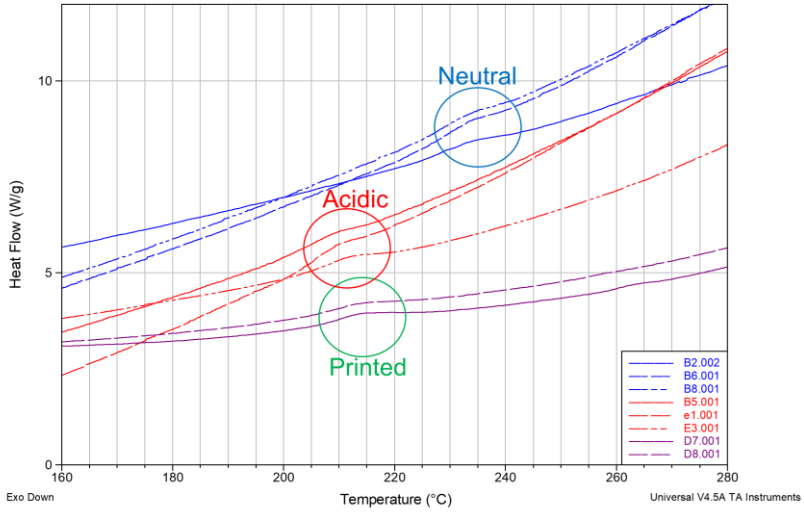

Figure 2-8. DSC thermograms of aerosol jet printed RHCIII with acidic (non-fibrillar) and neutral (fibrillar) non-printed controls.

2.3.5 FTIR

Positive controls and printed samples performed similarly for collagen type I and RHCIII as seen in Figure 2-10. The collagen type II positive control spectra resolved no amide I band and resembled more the spectra of a chitosan than a collagen [275]. All negative controls showed attenuated amide I bands as expected though not to the same degree, and a slight narrowing of the band was observed in collagen type I and II. The amide I band of the collagen type I and II negative controls also exhibited a shift in their maxima, as expected. All printed samples and positive controls except collagen type II had an amide I band maximum intensity at 1630 cm^{-1} indicative of beta sheet conformation, and shoulders 1639 cm^{-1} and 1658 cm^{-1} which are likely to be attributed to peaks for the collagen triple helix at 1637 cm^{-1}, and the widely reported peak for α- and triple helices at 1660 cm^{-1} [269]. The amide II and III bands of the negative controls also exhibited much less intense peaks, or no peaks at all relative to the printed samples and positive controls.

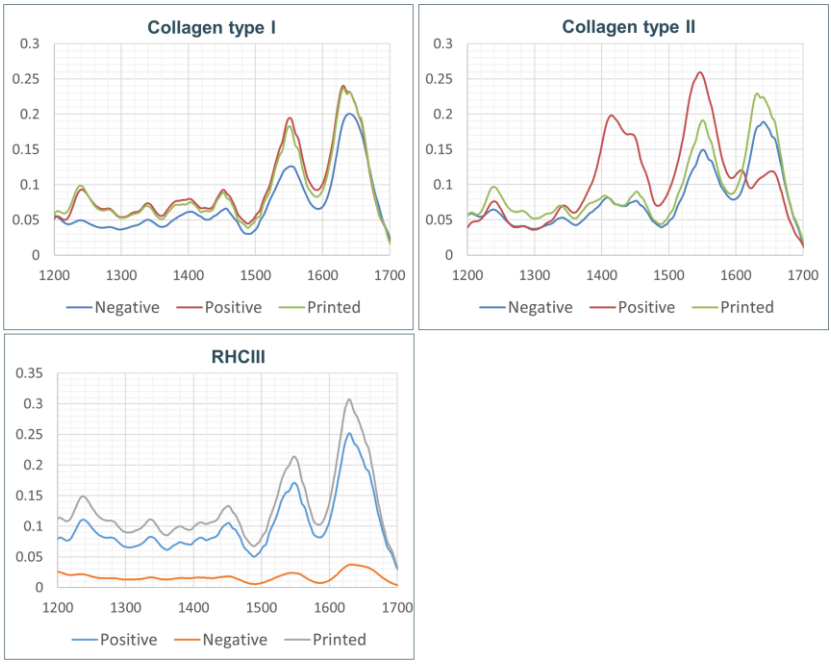

Figure 2-9. The average spectra negative controls, positive controls, and printed samples for collagen type I and II, and RHCIII. (Positive controls), B (negative controls), and C (printed samples), highlighting the changes in the amide I (1600-1700), II (1500-1580), and III (1230-1260) peaks of the collagen FTIR spectra due to denaturation.

2.3.6 Nanoindentation

Initial attempts at measuring aerosol jet printed collagen type I and II samples had been hampered by the samples detaching from the substrate, likely for similar reasons as the hydrophobic interactions seen in Figure 2-5. Nitric acid substrate cleaning method used to improve printing also facilitated nanoindentation as the more samples remained attached after stabilization and swelling. However, a few samples still partially detached from their substrate which even if not evident by the naked eye, was evident in the load-v-indentation graph seen immediately after the indentation.

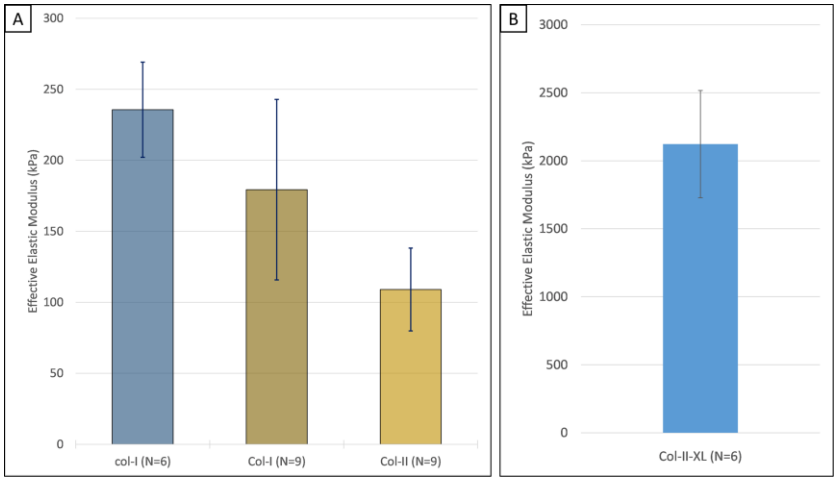

Figure 2-10. The average effective elastic moduli measured for (A) the non-crosslinked sample sets col-I (N=6), and col-II (N=6) where 45 indentations were made in a 3X15 matrix, on each sample and Col-I (N=9) sample set where 25 indentations were made in a 5x5 matrix on each sample, and (B) EDC:NHS crosslinked collagen type II sample set.

2.4 Discussion

This chapter comprises the first studies performed on aerosol jet printing of each collagen used in this PhD, and in each case was the first known example of aerosol jet printing collagen. AJP was not intended for building 3-dimensional structures, hence it was very challenging to apply this method to produce scaffolds for tissue engineering. Gradual increments in printing speeds and deposition rates, which can be seen in the differences between parameters of the different sample sets in table 2-1, had to be made for this method to be considered feasible for printing scaffolds. The most challenging aspect of the AJP collagen production was the lack of any tangible numerical value that could represent the sample quality or the operation of the printer, hence the use of the arbitrary sample quality rating system for the scaffold stabilization study. This challenge is not unique to aerosol jet printing of collagen and was highlighted in Section 2.1.2

Aerosol jet printing of collagen scaffolds posed other difficult challenges, such as the stability of the printed material. The stability of the printed material was shown to be majorly influenced by

hydration (i.e., ethanol concentration) and pH of the buffer used in crosslinking the samples. By adjusting the hydration and pH of the buffer to make it unsuitable for collagen dissolution, it was possible to preserve the printed structure of the scaffolds. Once the aerosol jet printed collagen is stable in the co-solvent buffer, the crosslinking serves to further stabilize the structure of the samples and increase their mechanical properties. It was clear that the aerosol jet printed collagen remains soluble and should be handled with care to prevent hydration of the material and deformation due to re-solubilization. The stabilization study formed a basic understanding of how aerosol jet printed collagen should be treated and this understanding facilitated the development of a neutralizing buffer used to stabilize AJP collagen constructs without using a crosslinking agent.

DSC enhanced the understanding gained from the stabilization study by illustrating that the crosslinked aerosol jet printed RHCIII constructs possessed a melting temperature more similar to acidic samples than neutralised samples. The melting peaks were higher than expected, but the only reported DSC studies of RHCIII were performed on solutions or swollen hydrogel samples in sealed pans, which was not possible at MTM [193]. The peaks, though small, were the only peaks after the loss of water, and were repeated amongst all replicates. It was understood from the DSC experiments that the aerosol jet printed RHCIII probably had very few typical fibrils, and that the transition from liquid to solid was driven more by the drying effect of AJP rather than any fibrillogenesis as a result of a combination of the evaporation and increased temperature. The results obtained in this DSC study performed at the Universitá del Salento, Lecce, were much more conclusive than similar studies performed using the TA Instruments Q2000 at MTM. Similar studies at MTM had produced very noisy results with no clear repetition amongst replicates, this was likely a result of low mass of the samples, the relative age of the Q2000 at MTM compared to the much newer Q2000 in Lecce, and having the ability to prepare and measure the samples directly afterward. Repeatable results could possibly have been achieved at MTM with more massive samples, however, this would be very time consuming and there remained the

risk that inconsistent results would be obtained, hence, no further replica DSC studies were performed at MTM.

FTIR showed that the scaffolds themselves were mostly composed of intact collagen type I and II and RHCIII based on the relative performance of the scaffolds compared to their non-printed positive controls and negative controls. However, the peak at 1630 cm^{-1}, indicative of beta sheet conformations, dominated the amide I band throughout the samples of different collagens, and it was difficult to discern any information on the collagen structure from the shoulders at wavenumbers related to triple helix conformations. While FTIR was found to be useful initially, often the only difference discerned between positive and negative controls was attenuation of the amide I, II, and III bands, however it was found that this could also be influenced by the pressure with which the crystal of the ATR-FTIR was applied. It is also possible that the differences observed in the relative intensities at least to some extent were influenced by the method of film preparation, since the collagen in the printed films are likely to be formed at a higher concentration [276]. One of the most heavily cited papers on FTIR spectroscopy of proteins is M. Jackson & H.H. Mantsch's 1995 paper, entitled "*The use and misuse of FTIR spectroscopy in the determination of protein structure*", which details how experience is key to the correct use of FTIR spectroscopy of proteins, particularly for large proteins [277]. Other methods for the preparation of collagen methods may have improved the signal but ultimately FTIR could only be used to detect relative changes in structure, hence the importance of good controls. However, the method used to produce positive controls did expose the collagen to risk of denaturation as the collagen film was left at room temperature to dry. The thermal stability of the collagen increases as it dries, but before the film reaches a stable level of hydration some collagen therein could potentially become denatured, hence dispersions of collagen fibrils are often used to form films for FTIR rather than collagen solutions but these would not have been suitable controls for the AJP collagens [278,279]. While there were many examples in the literature where FTIR was employed to elucidate a lot of structural information on collagen

samples it would likely require far more experience to be able to attribute the peaks to a particular structure with any degree of confidence. Hence, circular dichroism which resolves a unique collagen spectrum due to the chiral properties of collagen triple helices was determined to be the more useful tool for future investigations of the test hypothesis for these FTIR studies.

The nanoindentation study demonstrated the capability of the Optics 11 nanoindenter to measure the mechanical properties of the aerosol jet printed collagen samples. More conventional mechanical testing methods were not applicable to aerosol jet printed collagen samples due to the size limitation. The relatively flat and stiff nature of the AJP collagen samples measured was beneficial to the Chiaro nanoindenter which often struggled to perform repeatable measurements on rougher weaker samples. Non-printed collagen samples were considered as controls, however, these were very difficult to produce with sufficient integrity for a measurement using the 3.4 mg/ml RHCIII. While this material was used by May Griffith and colleagues to produce stiff collagen hydrogels all papers omitted the method by which the 3.4 mg/ml RHCIII solution was concentrated to 137 mg/ml in order to form these hydrogels [193,195]. The manufacturers stated that lyophilization of the material was not recommended. While some attempts were made to concentrate the material using vacuum centrifuge, the resultant material was very difficult to manipulate and free from their Eppendorf containers. Given the expense of the material, and the limited amount available, there was a reluctance to experiment further in trying to produce non-printed controls. When the more plentiful supplies of collagen type I and II were obtained, methods were developed to produce control collagen films for FTIR and other studies, however, without a suitable spin-coater these were subject to the coffee ring effect [280]. This coffee ring topography made them unsuitable for a nanoindentation study.

Each individual indentation was closely monitored to look for signs of a poor quality measurements, such as the load increasing too early which would indicate that the sample was adhering to the probe and likely detached from the substrate. If 2 or 3 poor

indentations were made consecutively the measurement was stopped and re-set at a different location on the sample to avoid locations where the sample had detached. If the poor quality indentation was a one-off and was clearly a poor measurement the data from that indentation was omitted from the average and standard deviation calculations. This study also demonstrated how stiff the aerosol jet printed collagen constructs were, which was already evident from handling the samples. The stiffness of the EDC:NHS crosslinked collagen type II samples was particularly evident, and these samples were later measured to have an average swelling ratio of 2.8 ± 0.6. The 3x15 matrix of indentations did not reveal any clear spatial variations in the sample stiffness between the rim of the sample and the centre. Hence, square matrices were used thereafter since it was easier to locate a suitably smooth area that was stably attached to the substrate for 5x5 matrices than for 3x15 matrices.

2.5 Conclusion

The work outlined in this chapter demonstrated how aerosol jet printing could be used to print dense stiff collagen scaffolds. The MATLAB program generated programs that were compiled far quicker than the conventional programs generated by VMTools and rarely crashed the system. The rate of production of the aerosol jet printed collagen scaffolds was increased to the point where clinical dimensions of a corneal stromal substitute, or cartilage defect were deemed feasible. The aerosol jet printed collagen was shown to be soluble in aqueous media, and ethanol was shown to be effective as a co-solvent to slow the hydration of the collagen allowing it to be neutralized and crosslinked by the alkaline buffer part of the co-solvent without sample dissociation. Some of the characterization methods outlined, FTIR and DSC, were not employed any further for the for the reasons outlined in the discussion, but new methods in the proceeding chapters would add to the understanding of aerosol jet printed collagen. Nanoindentation proved to be an effective method for measuring the mechanical properties of the aerosol jet printed collagen and would go on to be used throughout the project.

3 High resolution bioprinting of recombinant human collagen type III for corneal tissue engineering

Adapted from:

"High resolution bioprinting of recombinant human collagen type III"; Gibney, Rory; Patterson, Jennifer; Ferraris, Eleonora; Polymers 2021, 13:2973

3.1 Abstract

The development of commercial collagen inks for extrusion-based bioprinting has increased the amount of research on pure collagen bioprinting, i.e., collagen inks not mixed with gelatin, alginate, or other more common biomaterial inks. New printing techniques have also improved the resolution achievable with pure collagen bioprinting. However, the resultant collagen constructs still appear too weak to replicate dense collagenous tissues, such as the cornea. This work aims to demonstrate the first reported case of bioprinted recombinant collagen films with suitable optical and mechanical properties for corneal tissue engineering. The printing technology used, aerosol jet® printing (AJP), is a high-resolution printing method normally used to deposit conductive inks for electronic printing. In this work, AJP was employed to deposit recombinant human collagen type III (RHCIII) in overlapping continuous lines of 60 µm to form thin layers. Layers were repeated

up to 764 times to result in a construct that was considered a few hundred microns thick when swollen. Samples were subsequently neutralised and crosslinked using EDC:NHS crosslinking. Nanoindentation and absorbance measurements were conducted, and the results show that the AJP-deposited RHCIII samples possess suitable mechanical and optical properties for corneal tissue engineering: an average effective elastic modulus of 506 ± 173 kPa and transparency ≥87% at all visible wavelengths. Circular dichroism showed that there was some loss of helicity of the collagen due to aerosolization. SDS-PAGE and pepsin digestion were used to show that while some collagen is degraded due to aerosolization, it remains an inaccessible substrate for pepsin cleavage.

3.2 Introduction

The cornea's immune-privilege, avascularity, low cell density and small size eliminates or attenuates many of the major challenges to tissue engineering strategies, e.g. vascularisation of an TE implant [143]. The most likely strategy for the application of TE or bioprinting in the treatment of corneal visual impairments is the fabrication of a stromal substitute, similar to the BSS (biosynthetic stromal substitute by M. Griffith et al. [198]); though it is acellular, is normally considered a TE device since it is made of 'living material'. Such a stromal substitute should have suitable optical, geometrical and mechanical properties to be considered. It should also have sufficient glucose and oxygen permeability to sustain its population of cells and prevent neovascularisation. A suitable stromal substitute should allow nerve growth from the limbus through and over the cornea upon implantation to restore the blink reflex. A healthy corneal epithelium is essential to the function cornea-eyelid tribosystem, hence a TE stromal substitute should also support the culture of a confluent layer of corneal epithelial cells pre-implantation, or regenerate of the corneal epithelium post-implantation. Due to the cornea's immune-privilege, it is also feasible to use allogeneic stem cells to culture a healthy population of cells in the cornea pre-implantation with a lower risk of complications .

In terms of geometry, as mentioned in the introductory chapter, the cornea is a slightly oblate hollow spheroid cap with a central cornea thickness of 550µm and anterior surface radius of curvature of 7.7 mm [126,127]. Corneal transplants via DALK usually measure 7-10 mm in diameter and 500-550 µm in thickness, though this varies between donor and patient requirements [281,282]. Transmission of visible light should be >80%, with higher absorbance at wavelengths <400 nm being beneficial in preventing UV damage to the retina (though UV protection could be achieved using lenses) [147,150]. An elastic modulus similar to that of the corneal stroma (0.1 - 1 MPa [158,161]) should be suitable for a corneal substitute. A major engineering challenge of a TE or bioprinted corneal substitute is the surface roughness of the construct. The typical method for producing the printer toolpaths, "slicing", is likely to exacerbate these problems and much of the mechanics of the structure would be dependent on the bonds between layers, which are typically the weakest part of a 3D printed structure. Laser-ablated porcine corneas, which are rougher than the untreated corneas due to ablation, have been reported to have a surface roughness of 150-250 nm RMS [283]. This level of roughness would be very difficult to achieve with any printing method without some form of post-print processing. However, the corneal epithelium, should it be cultured or restored on implantation, is capable of compensating for some level of roughness. A rougher anterior surface can also be compensated for, after implantation, using contact lenses. This method was applied to patients who received May Griffith's RHCIII biosynthetic corneas in their 4-year clinical trial [75].

There are a number of corneal stromal substitutes similar to the biosynthetic cornea, which have been researched through the *in vitro* culture of corneal cell types, and *in vivo* implantation in animal models. One corneal stromal substitute that went through a phase II clinical trial in high risk patients was also from the group of May Griffith, and differed from the BSS by the addition of 2-methacryloyloxyethyl phosphorylcholine (MPC) as a reinforcing agent [284]. However, the efficacy of this study and a number of other studies involving the RHCIII-MPC stromal substitutes has been

a topic of controversy surrounding May Griffith. An image duplication and apparent clerical errors lead to one RHCIII-MPC paper being corrected twice, and a letter to the editor [285–289]. The BSS and RHCIII-MPC corneal substitute are the only known TE alternatives to transplant that have gone to clinical trial.

Corneal stroma substitutes have been bioprinted using extrusion-based bioprinting methods with limited success. In one study the construct only supported itself for one day when keratocytes were present [290]. Another attempt printed a scaled-up version of the cornea with a larger diameter using a micro-extrusion bioprinter programmed to deposit material more like a drop-on-demand printer with no continuous lines, and survived for up to 7 days in culture when the experiment was ended [291]. In both cases keratocytes were deposited with high cell viability, however, the materials applied at their respective concentrations in both inks could not be expected to reach the desired mechanical and optical properties of a stromal substitute. The print resolution in both cases was ≥ 200µm which inevitably led to the anterior surface of the construct appearing quite rough. Most EBB methods struggle to achieve print-lines below 200µm, which is problematic for print resolution and surface roughness. Higher print resolution is possible, though it usually depends on the EBB system being used, the material being extruded, and whether cells are present in the ink. Silk fibroin, which has similar properties to collagen, has been printed with print lines of 5µm in diameter at high concentrations 28-30% w/v, though it is not clear if the silk fibroin printed with this method would have sufficient optical properties for a bioprinted cornea [292]. Different EBB systems also offer different levels of control in terms of extrusion parameters (e.g., extrusion pressure, print speed, nozzle diameter and shape, etc.) and environmental factors (active cooling and/or heating of nozzle and of substrate), which have a major influence over ink rheology. For example, nozzles can clog due to inconsistencies in the ink (a folded protein or undissolved particle), due to the build-up of dehydrated material at the nozzle, or, when working with thermo-responsive materials, due to different temperatures within the nozzle. Generally, EBB cell

printing requires much larger nozzles to avoid clogging, and to reduce the shear forces imparted on the cells as they flow through the nozzle. However, cell seeding can be performed in vitro post print, and the work of May Griffith and others has also shown how an acellular scaffold can recruit keratocytes upon implantation [75].

To date there is one example of a light-based bioprinting method being used to print a corneal substitute. Mahdavi et al. used methacrylated gelatin, and the photoinitiator Eosin Y, to encapsulate keratocytes in a stromal substitute using digital light processing (DLP) [293]. The constructs appear cornea-shaped and were robust enough to be held with a tweezers out of solution. The constructs were stable for up to 28 days in culture, however, unfortunately, the constructs did not exhibit high transmissibility [293]. DLP has been used to print methacrylated silk fibroin, which could potentially be applied to corneal bioprinting but the mechanical properties of the resultant gel would need to be improved [109]. At the time of writing this piece there were no example of 2-photon polymerisation (2PP) corneal substitutes, however given its resolution, it has potential for great impact in bioprinted corneal substitutes albeit with very long print times. The LBB methods, stereolithography, DLP, and 2PP, all have potential for bioprinting corneal substitutes and could potentially achieve higher print resolution and lower surface roughness than EBB methods but may struggle with transmissibility at certain wavelengths due to the use of highly absorbing photoinitiators and photoabsorbers.

The dense collagen constructs achieved in the Chapter 2 using aerosol jet printing hold potential to address some of the issues raised in the previous examples bioprinted corneal substitutes, regarding their mechanical and optical properties. Assuming that the collagen content of the scaffolds is very high due to the amount of drying that occurs through AJP, the mechanical properties should be very high in comparison to more conventional bioprinting techniques. The fact that the printed collagen is not neutralized, and the phase change is likely to be more a result of drying means that the formation of light-scattering fibrils should be impeded and the transmissibility high relative to a conventional collagen hydrogel.

Similarly, the RHCIII gels of the BSS are formed in conditions where atypical fibrils would be expected to form; a relatively low pH 5.5, a mid-range ionic strength, a low temperature, and with EDC : NHS crosslinking carried out in tandem [194]. Under these conditions, sparse narrow collagen fibrils were formed which scattered less light and allowed the RHCIII gel to be highly transparent [21].

3.3 Materials & Methods

3.3.1 Materials

3.4 mg/ml recombinant human collagen type III (produced by yeast; pichia pastoris) solutions in 0.01 M hydrochloric were procured from MyBioSource (San Diego, CA, USA), and later Abcam (Abcam (Netherlands) B.V.) after the production of RHCIII was ceased at MyBioSource. The α-1 chains which assemble into a trimer to make RHCIII had an expected molecular weight of 138.6 kDa based on the UniProt accession P02461 sequence. This particular recombinant collagen was selected as the most viable commercial recombinant collagen for this application at the time of procurement. One other recombinant collagen available at that time (recombinant human collagen type I produced in tobacco plants; Collplant®) was less preferred due to the low concentration at which it was supplied (1 mg/ml), the higher cost, and its limited use reported in literature at that time. EDC [N-(3-Dimethylaminopropyl)-N'-ethylcarbodiimide hydrochloride], hexamethyldisiloxane (HMDS), and the ProteoSilver staining kit were purchased from Sigma Aldrich (Leuven, Belgium) and N-hydroxysuccinimide (NHS) was purchased from Fluka (Buch's, Switzerland). All other materials were purchased from VWR Belgium.

3.3.2 Production of AJP RHCIII samples

3.3.2.1 Aerosol jet printing pf RHCIII samples

The Optomec® AJ300 was used to print two sets of circular samples: twelve 4.5 mm diameter samples (B1-B12) and eight 7 mm diameter samples (A1-A8). In all cases unaltered stock 3.4 mg/ml RHCIII was employed as ink for printing. The number of layers and

print time for each set of samples were 764 layers in 4 hours and 384 layers in 8-9 hours, respectively. The 7 mm samples were intended to fully cover the well of a 96 well plate for transmission measurements. The sample diameter was reduced to 4.5 mm for samples that were not to proceed to transmission measurements in order to achieve thicker samples in a shorter print time. The toolpath generator developed in Chapter 2 was used for all toolpaths. The program rotated each even-numbered layer by 90° relative to the preceding layer, whereas each odd-numbered layer was rotated by 15°, since this led to samples that appeared to possess a smooth and flat topography. All samples were printed using a nozzle with an orifice diameter of 100 µm, a print speed of 11.5 mm/s, sheath flow of 60 cc/min, atomiser flow of 40 cc/min, and atomizer power of 90% with slight variations in atomizer power and flows to account for low or high atomisation. It was known from experience that printing with these parameter values, and with this many layers lead to growth of the sample diameter of about 0.5 mm. Hence, the programmed diameters were 4 mm and 6.5 mm, for the 4.5 mm and 7 mm samples, respectively.

Diameter	No. of Layers	Track spacing (µm)	Nozzle diameter (µm)	Atomizer flow rate (ml/min)	Sheath flow rate (ml/min)	Print speed (mm/s)
4.5 mm	764	60	100	40	60	11.5
7 mm	384	60	100	40	60	12.5

Table 3-1. Summary table of all sample parameters

All 4.5 mm samples were measured after printing to confirm that this was a precise and repeatable deviation that could be incorporated into the toolpath program generator. For all samples, 850 µl were pipetted into the vial at the beginning of a print and this volume was topped up as needed, every 1-1.5 hours of printing. Once the samples were printed, they were kept dry at 4°C until the entire sample set was printed, then they were observed under a microscope before proceeding to crosslinking.

3.3.2.2 Crosslinking of aerosol jet printed RHCIII

EDC : NHS crosslinking was performed in a co-solvent made of 2 parts; an aqueous 0.01 M 2-(N-morpholino)ethanesulfonic acid (MES buffer) solution and 3 parts ethanol. The aqueous content of the co-solvent was slightly increased from that selected in Chapter 2 to make it more suitable for the thicker samples and since no difference could be observed between crosslinked samples in a similar smaller experiment on the crosslinking performance. The pH of the MES buffer was adjusted to pH 8-9 using 1 M NaOH. The MES buffer was then added slowly to the ethanol to prevent precipitation of the MES, and the solution was left mixing for ~1 hour. The pH was checked at this point and further adjustment of the pH (to pH 8-9) was performed if necessary. EDC and NHS were then dissolved in the reaction buffer at a 1:1 molar ratio; final concentration 40 µg/ml EDC, 24 µg/ml NHS. 1ml of the crosslinking solution was carefully pipetted into each well in a 24 wellplate containing the samples, on ice. The wellplate was then stored at 4°C for 18 hours. After 18 hours, the crosslinking solution was removed from the wells and the samples were rinsed twice in ultrapure water, and stored in 1X PBS @ 4°C.

3.3.3 Optical Characterization

The optical properties of the 7 mm samples were measured using a plate reader. The samples were swollen in 1X PBS, detached from their substrate and placed in a flat-bottomed 96 well plate with 200µl of 1X PBS. The samples were made slightly wider than the wells to ensure full well coverage. A corneal scalpel and tweezers were used to ensure the sample was flat and completely covering the bottom of the well. The absorbance was measured with wells containing only 1X PBS as blanks. The absorbance was measured between 390 nm and 700 nm and converted to % transmission, using the Beer-Lambert law equation for transmission:

$$Transmission = 10^{-Absorbance} \quad (3\text{-}1)$$

The refractive index was measured using an Atago 7000X . The samples were swollen in 1X PBS, then placed on the prism of the refractometer; each measurement was repeated three times.

3.3.4 Physical characterization

3.3.4.1 Nano-indentation

The mechanical properties of the AJP samples were characterized using a Chiaro nanoindenter (Optics11). This system and its sister system, the Piuma, are emerging tools for measuring the mechanical properties of hydrogels, and for mechanobiology [294–296]. Both are comprised of a spherical indenter on a cantilever of known stiffness, the deflection of which is measured by interferometry via a ferrule-topped optical fiber [270]. A piezoelectric actuator displaces the probe by a user-defined distance and speed (the indentation profile in Figure 3(a)) leading to deflection of the cantilever. The deflection is then used to calculate the load, and the stiffness thereafter. While these systems are mostly used to measure local variations in stiffness, they are also used to measure the bulk modulus of hydrogels [297–299]. This form of micro/nano-indentation has provided results consistent with tensile and compressive test results [300]. For these measurements a probe with a cantilever stiffness of 5.2 N/m and a 50 µm diameter spherical indenter was selected. 25 indentations were performed on each sample in a 5X5 matrix with 200 µm spacing between indentations in both directions. The indentation profile, seen in Figure 4-2(a), went to a maximum of 12 µm at an indentation rate of ~1.7 µm/s. An 8 µm offset was included for all measurements to ensure that the probe was not in contact with the sample surface upon beginning the indentation. The effective elastic modulus was calculated by the Chiaro software using the slope of the loading curve according to a Hertz model. Only samples that remained attached to their substrate could be measured accurately. All measurements were taken in PBS with samples that had been equilibrated in PBS overnight.

3.3.4.2 Scanning electron microscopy (SEM)

Sample preparation was performed according to a protocol that was a modified version of that reported by Raub et al. [301]. Briefly, samples were fixed in 4% glutaraldehyde in 1X PBS for 1 hour at room temperature, then washed 3 times in PBS for 7 minutes, and 2 times in ddH_2O for 7 minutes. Samples were then dehydrated in increasing concentrations of ethanol in ddH_2O (30%, 50%, 70%, 90%, and 100% v/v) for 10 minutes each and twice in 100% ethanol. The samples were further dehydrated in increasing concentrations of HMDS in ethanol (33%, 50%, 66%, and 100% v/v) for 15 minutes each, and twice in 100%. Samples were then torn apart with tweezers if possible, or cut, and left to dry on aluminium foil under a fume hood overnight. The dried samples were mounted on SEM stubs using carbon tape, and sputter-coated with platinum to a thickness of 5 nm. The samples were imaged at 5 kV using the SEM at KU Leuven Campus De Nayer (VEGA-3, TESCAN, Czechia)

3.3.4.3 Swelling ratio

Both the swelling ratio and water content of the scaffolds were calculated to represent the swelling properties of the scaffold, and for use in comparisons to the native cornea for which water content is frequently reported. In order to measure the swelling ratio and water content, six of the 4.5 mm AJP RHCIII samples were incubated in 1X PBS at 4°C overnight. The wet samples were turned over quickly on a filter paper to remove the excess water and then weighed. The samples were then rinsed twice in ultrapure water and frozen. The frozen samples were lyophiliized and weighed to measure the dry weight. The swelling ratio was calculated using equation 2 and the water content was calculated using equation 3; both below:

$$\text{Swelling ratio} = \frac{wet\ weight - dry\ weight}{dry\ weight} \tag{3-2}$$

$$\text{Water content} = \frac{Wet\ weight - dry\ weight}{wet\ weight} \times 100\% \tag{3-3}$$

3.3.5 Viscosity

Viscosity measurements were made using a Lovis 2000 Rolling-Ball Viscometer (Anton Parr, Graz, Austria). Measurements were made at 20°C, 25°C, 30°C, 35°C, and 40°C. A standard size capillary tube was filled carefully with 600µl of stock 3.4 mg/ml RHCIII in 0.01 M hydrochloric acid using a syringe and a filling adapter while avoiding the formation of bubbles. A ball dispenser was employed to drop a 1.8mm inert gold ball into the capillary tube. The tube was checked for bubbles before being sealed and fixed into the viscometer. The viscometer performs a measurement by measuring the time for the ball to fall through the liquid several times in opposing directions, then data from these runs is used to calculate the Lovis Dynamic Viscosity, µ.

3.3.6 SDS-PAGE

Samples were taken from the printer during operation in two different printer set-ups designed to indicate whether any detected degradation was the result of ultrasonic atomisation, or solely due to the exposure of the RHCIII to 1.65 MHz ultrasound. To measure degradation as a result of ultrasonic atomisation, the printing apparatus was set up similar as if to print but without deposition. Aliquots of 850 µl RHCIII solution were pipetted into a vial and subjected to aerosolization for up to 2 hours, at the minimum atomizer power that generated sufficient aerosol for printing (90%). The sheath flow was set at 100 cc/min to simulate the pressure in the atomiser during printing (0.4-0.5 bar). To measure degradation as a result of exposure to 1.65 MHz ultrasound alone, a small amount of RHCIII solution (150 µl), which was too low to result in atomisation, was pipetted into a vial. The vial was closed tightly with a cap to prevent evaporation and placed in the atomizer at 90% power for up to 2 hours. In each case, samples were taken from the vial at 20, 60, and 120 minutes. For comparison, printed samples, 4.5mm in diameter and 75 layers thick, were analysed by re-solubilising them in ~100µl 0.01 M HCl and diluting them appropriately. Samples were also subjected to a pepsin digestion (0.2 mg/ml pepsin at room temperature for 1.5 hours) to remove

any non-helical collagen. SDS-PAGE was performed using a Mini Gel Tank, the Invitrogen NuPAGE® Electophoresis System (ThermoFisher Scientific) under reducing conditions in order to reduce the disulphide bonds in the C-termini of the alpha-1 chains. A ProteoSilver silver staining kit (Sigma Aldrich) was used to visualise the proteins on the gels.

3.3.7 CD Spectroscopy

The CD spectra of untreated RHCIII (control) and RHCIII that had been treated with aerosolization for 120 minutes, similar to the sample treatment for SDS-PAGE, were measured using a Jasco J-1500-150ST CD spectrometer. The spectra were measured between 190 nm and 260 nm, with a scan speed of 50 nm/min and wavelength interval of 0.5 nm. Rectangular quartz cuvettes with a 1 mm path length were first measured with 0.01 M hydrochloric acid to obtain the background spectra which was subtracted from the results. The treated RHCIII sample and the control were each diluted to 0.3 mg/ml for the measurements, using 0.01 M HCl.

3.4 Results

3.4.1 AJP RHCIII sample production

All samples were observed under a microscope after sample production and their diameter measured optically. The 4.5 mm samples had an average diameter of 4.54 mm with a standard deviation (SD) of 0.03 mm, and the 7 mm samples had an average diameter of 7.06 mm with a standard deviation of 0.04 mm. Samples were on average 0.55 mm ± 0.035 mm (± SD) larger than their programmed diameters (4 mm and 6.5 mm), but as mentioned previously this was expected. Print lines were difficult to resolve due to the transparency of the material and flatness of the printed lines but some print lines, 60 µm wide, could be resolved in the centre of samples, as seen in Figure 4-1(b). The samples were labelled A(x) (7 mm sample) or B(x) (4.5 mm sample) with ‘x’ denoting the sequence of their print.

3.4.2 Optical Characterization

The samples appeared highly transparent to the eye, as seen in Figure 4-1(a), and this was confirmed in the transmission results which measured an average transmission of 87.5 % ± 6 % (± the S) for the 7 mm samples over all visible wavelengths measured. Samples transmitted less light at wavelengths below 450 nm, as seen in Figure 4-1(d). Two samples, A5 and A6, exhibited lower transmission spectra than the other samples, and which was noticeable upon close inspection by eye. It was likely caused by increased presence of fibrils in the samples due to hydration of the sample during crosslinking. The average refractive index (RI) of the samples was 1.3463 ± 0.0223

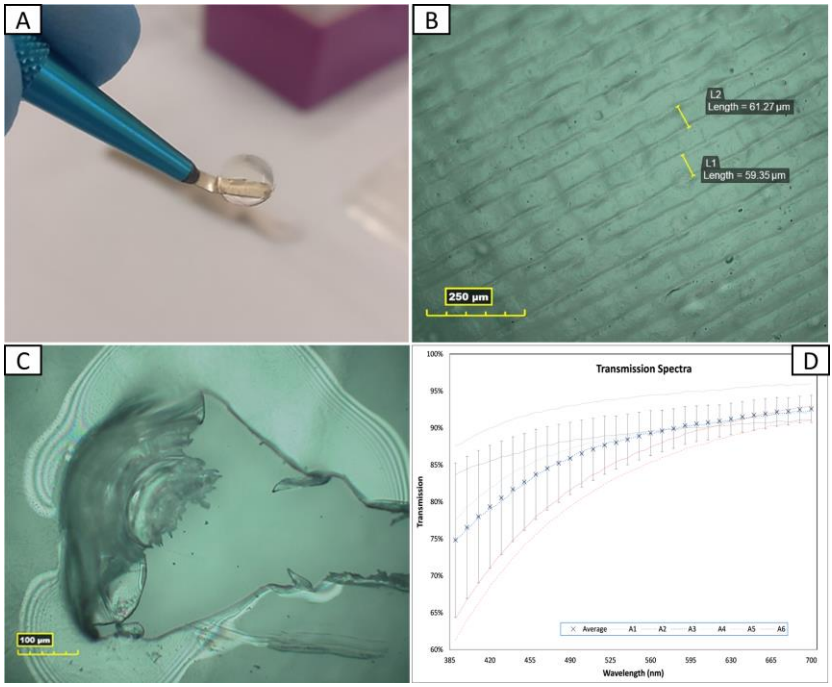

Figure 3-1. (A) A crosslinked 7 mm sample swollen in PBS held on a corneal scalpel; (B) print lines ~60 µm in width in the centre of a 7 mm sample imaged under microscope after printing; (C) a failed sample in which a hole was torn to exhibit the birefringence seen in the samples. (D) The transmission spectra of each of the 7 mm samples measured, cross points with error bars represent the average transmission and standard deviation at 10 nm interval.

3.4.3 Physical characterization

3.4.3.1 Nano-indentation

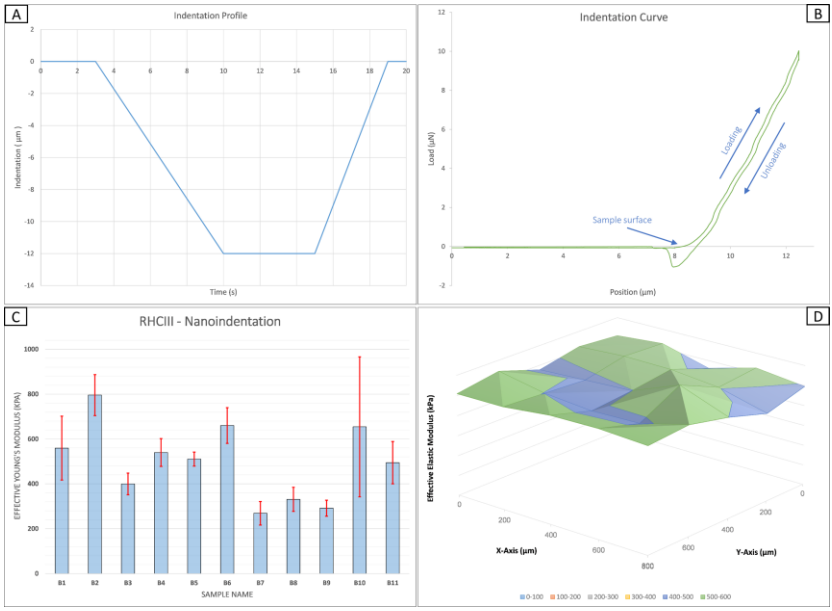

Figure 3-2. (a) The indentation profile used in the study which included an 8 μm off-set, so the sample was indented 4 μm. (b) The indentation curve illustrates the offset, with the load only increasing after the probe has moved 8 μm. The loading slope of the loading curve is used to calculate the elastic modulus. (c) The average effective E of each sample from 25 indentations with error bars representing the standard deviation. (d) An effective E map of sample B5

The load-indentation curve shown in Figure 3-2(b) was typical of the indentations performed, indicating quite an elastic response with low hyteresis observed in the unloading curve. The negative load at the end of the unloading curve was likely due to the probe tip sticking to the sample surface briefly. The average effective elastic modulus found for the 11 samples measured was 506 ± 173 kPa (± the standard deviation). A twelfth sample could not be measured since the sample had detached from its substrate. The effective elastic modulus of each sample can be seen in Figure 3(c). Local variations of the effective elastic modulus tended to be relatively small, as in Figure 3(d), though some very stiff indentations lead to higher standard deviations in some samples, particularly in sample B10 which recorded one outlier indentation measuring an effective

elastic modulus of 2.2 MPa. The effective elastic modulus was reported, since poisson's ratio was unknown for the material.

3.4.3.2 Swelling ratio

The mean wet weight of the 4.5 mm samples was 4.9 ± 0.7 mg, the mean dry weight after lyophilisation was 0.66 ± 0.16 mg. The mean swelling ratio was calculated as 6.8 ± 1.6 (± standard deviation).

3.4.3.3 SEM

Whilst no pores could be resolved on the top or bottom surfaces of the samples, clearly defined distinct layers could be seen at the edges where samples were torn apart, as seen in Figure 3-3. These layers continued across the entire span of the samples, from what could be seen at the cross-sections, and hence were deemed to be the printed layers. The thickness of the layers was too thin to be accurately measured in SEM. Fibrous structures seen at tear edges could not be clearly resolved and would require TEM or AFM to determine any D-banded patterns, if present.

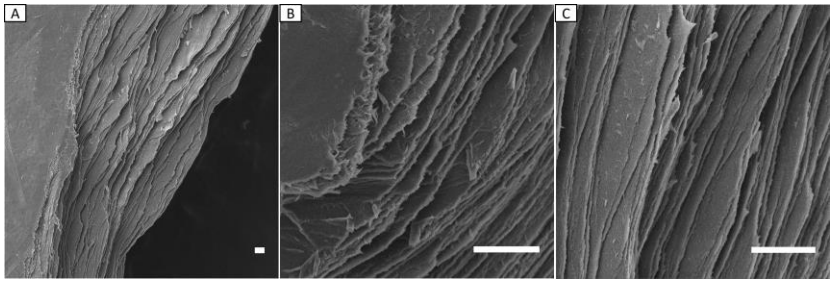

Figure 3-3. SEM images of 4.5 mm AJP RHCIII samples at the edges where they were torn apart, illustrating the distinct layers from the printing process. All scale bars represent 10 µm.

3.4.4 Viscosity

A viscosity of 18.2 mPa.s was measured for RHCIII at 20°C, which is above the recommended viscosity range of the Optomec® ultrasonic atomizer: ≤ 5 mPa.s. However, this did not prevent aerosolization. In this soluble form, the viscosity of the RHCIII decreased with increase in temperature as expected. The viscosities

for 25°C, 30°C, and 35°C were 15.9, 12.2, and 3.0 mPa.s, respectively. A value could not be resolved at 40°C as the viscosity was too low.

3.4.5 CD Spectroscopy

Typical collagen CD spectra were measured for both sonicated and untreated control RHCIII samples with a minimum ellipticity peak centred at 198 nm and a maximum ellipticity centred at 221 nm. However, a significant drop in peak intensities for the 2 hour treated sample indicates denaturation of the collagen due to the exposure to ultrasonic atomization. There was also a red-shift in the cross-over point from 214.7 nm to 215.6 nm, likely due to contributions from randomly coiled collagen and collagen degradants which would contribute a negative ellipticity at these wavelengths [302].

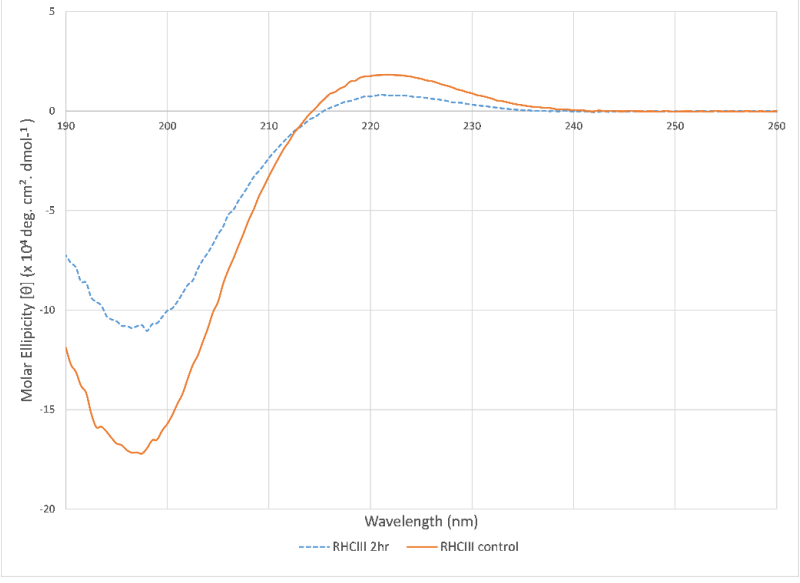

Figure 3-4. CD spectra of untreated RHCIII and 2-hour sonicated RHCIII showing the characteristic collagen CD ellipticity with a positive peak centred on 221 nm and a negative peak centred on 197 nm.

3.4.6 SDS-PAGE

SDS-PAGE analysis showed that some RHCIII was gradually degraded from the exposure to ultrasonic atomization, but a clear α-

1 band remained at the expected molecular weight of ~130-140 kDa. β-bands at the top of the gel showed that not all disulphide bonds were reduced. It appeared that this degradation was the result of the shear stresses involved in atomisation rather than the exposure to 1.65 MHz ultrasound alone, since no degradation could be seen in the samples that were not atomized, Figure 3-5 (b) and (d).

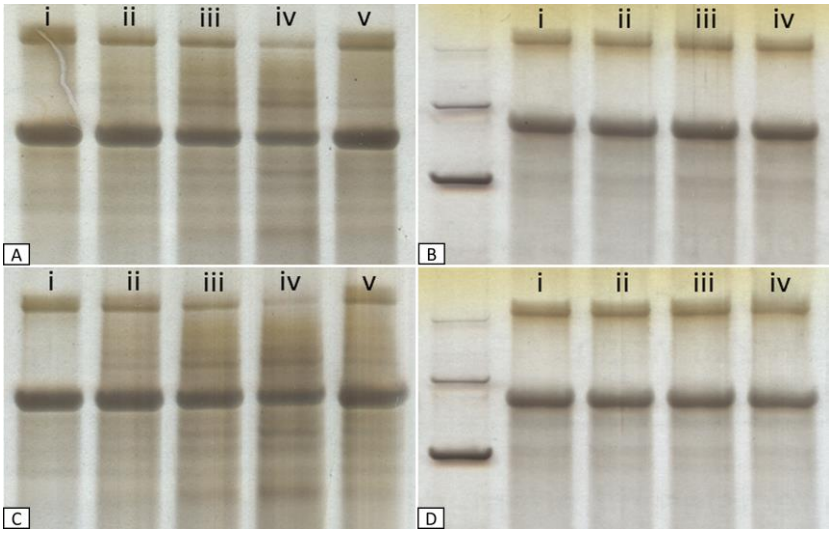

Figure 3-5. SDS-PAGE gels of ultrasonically atomized RHCIII, (a, c), and non-atomized RHCIII that was exposed to 1.65 MHz ultrasound, (b, d). Samples in gels (c, d) were digested with pepsin, whereas samples in (a, b) were their non-digested controls. All lanes marked (i)-(iv) correspond to 0, 20, 60, and 120 minutes. Lanes marked (v) were re-solubilized printed samples. Molecular weight standards in the left-most lane of (b) and (d) mark 250, 150, and a high intensity band at 100 kDa.

Printed samples which were re-solubilised did not exhibit any evidence of an additional mode of degradation due to deposition. Lanes resolved for the printed samples appeared similar to those for 20 and 60 minutes samples which corresponded to the approximate print time of these printed samples, ~40 minutes. The degraded collagen showed no preferential molecular weight, though bands did seem to be emerging around 100 kDa and 80 kDa, after 120 minutes of aerosolization; lane iv Figure 3-5 (a) and (c). The pepsin digested samples in Figure 3-5 (c) and (d) appeared very similar to their non-digested counterparts. Although there did seem to be slightly increased non-specific staining in (c), the same level of band

depletion with time was seen. The pepsin digestion did not deplete the staining of the α-1 bands nor the emerging bands at 100 and 80 kDa suggesting that the degraded collagen remained in some conformation that made it inaccessible as a substrate for cleavage, i.e., a triple helix conformation.

3.5 Discussion

This work was published in the first research article on aerosol jet printing of collagen and the first research article on 3D printed recombinant human collagen; only collagen-like and collagen-based recombinant proteins have been printed previously [303]. Sample printing went through a series of phases through Chapter 2 to the present chapter to achieve AJP RHCIII samples of this size and number of layers within a print time that allowed multiple samples to be printed in one day. In this context, these samples are near the limit of what can be achieved with RHCIII on the Optomec® AJ300 AJP system used in this study, and near-constant observation was required to monitor the amount of aerosol generated and the deposition, and to make changes to the flow rates when necessary. The high flow rates used lead to a high relative pressure in the deposition head (0.4 – 0.5 bar), compared to normal operating conditions for AJP (0 – 0.2 bar). It appeared that this, along with the high print speed, was likely a major contributing factor to the increased sample diameter as the resultant excessive jet could often be seen to push some material over the edge of the deposited area during turns. Nevertheless, it has been shown here that this "non-programmed deposition" is precise and repeatable, and hence can be incorporated into the MATLAB® toolpath generator. A more concentrated ink may allow quicker sample production with less need for high flows and print speeds, however a more concentrated RHCIII solution would likely be too viscous to atomize. Along with the high print fidelity measured, very little contraction due to crosslinking was observed both sample sets, likely due to the relatively low EDC concentration and the density of the material.

It is known from Chapter 2 that the AJP process, more specifically ultrasonic atomization, leads to some denaturation and degradation

of the RHCIII. However, this happens gradually, and fresh RHCIII was added to the vial during a print run every hour as the RHCIII was consumed, therefore, the amount of degraded/denatured collagen is not likely to reach the levels seen in the 2 hour treatment SDS-PAGE and CD spectra measurements. The fact that the degradation and denaturation of the RHCIII occurs gradually, means that the construct will not be homogenous and that the layers around the hour mark, before the RHCIII is replenished, will contain more denatured/degraded RHCIII than the preceding layers, and the first layers will contain little to no denatured/degraded RHCIII. However, the results indicate that there should be no single layer in any of the samples where degraded RHCIII is in the majority, and intact RHCIII accounts for the bulk of material at all times in this study. It was a concern that the RHCIII and any fragments in random coil formations may absorb more light, but the transmission study has shown that this AJP RHCIII, which contains some degraded/denatured collagen, is highly transmissible. It is not clear if the inclusion of degraded RHCIII will have any impact on the response of corneal cells to the potential scaffold. In cartilage, the presence of denatured and degraded collagen in culture media has been shown to upregulate the expression of matrix metalloproteinases (MMPs) in chondrocytes [304,305]. If these results would be replicated for fragmented collagen in the scaffold material with corneal cells, it could lead to faster remodelling, or deterioration of the construct.

The birefringence exhibited by samples, seen in Figure 4-1(c), suggests that the RHCIII is in liquid crystal conformations within the AJP constructs, though further work with cross-polarized microscopy of sample sections to confirm this was not possible at SBE or MTM at KU Leuven. This could reveal similarities between the AJP-deposited RHCIII and the liquid crystal collagen type I films produced by Giraud-Guille, who performed many investigations into the liquid crystallinity of highly concentrated collagen type I films, made from solutions that had been sonicated in a cooled ultrasonic bath (20 kHz, 50 W) prior to being concentrated and forming films [306–309]. It was concluded in those studies that the presence of the

fragmented collagen facilitated a quicker formation of liquid crystalline collagen.

The optical characterization results show that AJP-deposited RHCIII, at least in optical characteristics, is a suitable candidate for a bioprinted cornea, with >80% light at all visible wavelengths transmitted in every sample, similar to the native cornea [151]. Thicker fibrils are likely to be the cause of the higher absorbance in samples A5 and A6. The RI measurement was similarly skewed by one sample with a much higher RI than the other samples. Nevertheless, even the least transparent samples were still within the range of what is considered acceptable for a corneal substitute, and high blue light absorption in the cornea is necessary to protect the retina [152,153]. Despite the efforts to limit fibrillogenesis, thicker light-scattering fibrils could form when the AJP-deposited RHCIII is hydrated for neutralization and crosslinking, particularly if the pH becomes acidic. The basis for the co-solvent used as a crosslinking buffer for the EDC : NHS crosslinking was the work carried out in chapter 2. This crosslinking buffer was determined to best preserve sample morphology and lead to little or no signs of dissolution of the AJP-deposited RHCIII. Ethanol was employed as a co-solvent to slow the hydration of the AJP-deposited RHCIII, based on observations reported of collagen's poor absorption of ethanol [264]. The pH of the crosslinking buffer was adjusted compensate for the small amount of acid that leached out of the AJP RHCIII upon re-hydration. PBS was purposely excluded from the crosslinking buffer since phosphate ions are known to have a major influence on collagen precipitation (which would impair the transparency of the material) [60]. However, the storage in PBS after crosslinking could still affect the AJP RHCIII if it is not completely neutralized in the crosslinking, and hence could be substituted for a phosphate-free buffer, such as citrate buffer, adjusted to a similar pH. Thicker samples would be expected to absorb more, though predicting how much more is challenging as it depends on how much of the incident light for the measurements carried out here was absorbed and how much was scattered. Should the absorbance measurement largely be the result of the AJP RHCIII absorbing the incident light then a

relatively linear relationship between thickness and transmission could be anticipated according to the Beer-Lambert law. If however, light scattered at the interfaces of the on either side of the sample is a major contributor to the absorbance measurement then thickness could have less of an impact on the absorbance.

It is difficult to propose any particular fibril assembly for the arrangement of collagen molecules in the AJP-deposited RHCIII, but there is evidence in the SEM images, that the collagen retains distinct printed layers after crosslinking and, hence does not experience major re-solubilisation during neutralisation and crosslinking which would be necessary for native-type fibrils to form. Therefore, any fibrils that form are most likely to be atypical very skinny fibrils that assemble within a printed layer. Each printed layer was composed of overlapping printed lines 60 µm in width, as seen in Figure 4-1(b), but these were lost in the sample preparation for SEM. The dense collagenous nature of these layers, and the fact that their estimated thickness (~330 nm on average measured using optical coherence tomography at the University of Antwerp [310]) is within the range of reported corneal stroma lamellae thickness (0.2-2.5 µm [311]), could be considered to be biomimesis of the lamellae of the corneal stroma. This could be enhanced by printing 200 µm wide strips, instead of whole layers, traversing and circumnavigating the centre of the sample for closer mimesis of the corneal lamellae structure [135]. Transmission electron microscopy could reveal the fibril arrangement of collagen in the AJP RHCIII scaffolds, however, this would most likely require a collaborative effort with experienced microscopy scientists to develop a suitable sample preparation method for resolving such structures. Cross-polarization microscopy would also be highly useful in this regard.

The swelling ratio measurements show that the constructs absorb aqueous media well, which could be advantageous for cell culture but may be a concern for dimensional accuracy should this translate into volumetric swelling. However, this was anticipated. As stated earlier, layers are expected to be ~330 nm thick when swollen. The transparency of the material made any accurate swollen geometrical measurements unfeasible with the available

equipment, however samples were observed to swell mostly vertically, with no major changes apparent in the sample diameter. The water content calculated for the samples, 86.7%, is between that normally found for the native cornea, ~78%, and that reported for the RHCIII biosynthetic corneas of May Griffith, ~90% [312,313]. This could potentially change with cell culture, or with remodelling upon implantation, and the subsequent deposition of proteoglycans, new collagen and other matrix material.

The elastic moduli measured for the aerosol jet printed RHCIII samples was far higher than previously reported elastic moduli results for pure printed collagen found in the literature. The highest reported elastic moduli for printed collagen found were compressive moduli of around 110 kPa for glutaraldehyde-crosslinked bovine collagen type I [314], 47.2 ± 14.2 kPa for EDC-crosslinked porcine-hide collagen, and 21.5 ± 1.4 kPa for porcine-tendon collagen type I, though higher elastic moduli have been reported for constructs made with collagen hybrid inks [315,316]. The aerosol jet printed RHCIII samples outperformed previous reported attempts of cornea printing both in terms of mechanical and optical properties [290,291,317]. However, moulded collagen hydrogels for the cornea have been reported with higher elastic moduli than the aerosol jet printed RHCIII samples, though their optical properties were very similar [75,318]. Corneal elasticity has been measured using a number of methods including *in vivo* methods, such as the Orssengo-Pye method [155], and *in vitro* methods, such as membrane pressure, strip extensiometry, and nanoindentation, resulting in quite a wide range of reported human corneal Young's Moduli from 0.075 to 20 MPa [156–159] . The elastic moduli of each of the AJP RHCIII samples fits well within this range and fits within the range of the reported elastic moduli for the human anterior cornea stroma, measured using nanoindentation (range: 59 – 765 kPa, average: 281 ± 214 kPa). Larger samples would be required to further investigate the mechanical properties of the AJP RHCIII with more established methods for the characterization of mechanical properties, such as tensile testing. However, a more revealing test of the suitability of AJP RHCIII's mechanical properties would likely be a test of the

suturability of the samples. Suturability has been shown to be a limitation of the moulded RHCIII corneal substitute [184], and from what can be told from the nanoindentation results and the handling of the AJP RHCIII samples, they appear to have suitable flexibility to allow it to be pierced with a needle. However, it was not possible to have a suturability test performed on the AJP RHCIII samples over the course of this project.

In order to progress this printing method towards producing a clinically relevant scaffold for corneal applications more studies on the average thickness of the printed layers and the effect of increasing thickness on the transparency would be required. The only accurate method of measuring the sample thickness found in this work was the OCT at the University of Antwerp. However, this was a surgical tool used in corneal surgeries at UZ Antwerp with limited availability. A more local source or another method could facilitate more comprehensive studies on the thickness of the scaffolds and how this affects transparency. There would also be a need to perform comprehensive characterization of the commercial RHCIII since it is a novel material for medical devices. The method of aerosol jet printing would facilitate the printing of curved cornea-shaped scaffolds. A 5-axis motor control system would have to be added to the AJ300, or a new AJP printer, to allow perpendicular printing in all locations. Sacrificial support material in the form of cellulose nanocrystal suspensions (which can be printed easily with AJP and can be made dissociate in water) could be employed to achieve the curved shape, possibly starting from an already curved substrate to circumvent long periods of printing support material. Considering these points a new design of AJP printer with these attributes and suited to printing higher volumes of material would be highly beneficial to future investigations of AJP bioprinting.

3.6 Conclusion

Aerosol jet-printed recombinant human collagen type III exhibits higher print resolution, print fidelity and mechanical strength than any pure collagen bioprinting previously reported. This work demonstrates that aerosol jet printing offers a way of processing

pure collagen solutions into dense stiff material with high fidelity to a prescribed geometry and with properties suitable for replicating native dense collagenous tissue like the cornea.

4 Bioprinting of collagen type I and II via aerosol jet printing for the replication of dense collagenous tissues

Adapted from:

"Bioprinting of collagen type I and II via aerosol jet printing for the replication of dense collagenous tissues"; Gibney, Rory; Ferraris, Eleonora; Frontiers in Bioengineering and Biotechnology 2021, 9:786945

4.1 Abstract

Collagen has grown increasingly present in bioprinting, however collagen bioprinting has mostly been limited to the extrusion printing of collagen type I to form weak collagen hydrogels. While these weak collagen hydrogels have their applications, synthetic polymers are often required to reinforce gel-laden constructs that aim to replicate dense collagenous tissues found in vivo. In this study, aerosol jet printing (AJP) was used to print and process collagen type I and II into dense constructs with a greater capacity to replicate the dense collagenous ECM found in connective tissues. Collagen type I and II was isolated from animal tissues to form solutions for printing. Collagen type I and II constructs were printed with 576 layers and measured to have average effective elastic moduli of 241.3 ± 94.3 and 196.6 ± 86.0 kPa (±SD), respectively, without any chemical modification. Collagen type II solutions were measured to be less

viscous than type I and both collagen type I and II exhibited a drop in viscosity due to AJP. Circular dichroism and SDS-PAGE showed collagen type I to be more vulnerable to structural changes due to the stresses of the aerosol formation step of aerosol jet printing while the collagen type II triple helix was largely unaffected. SEM illustrated that distinct layers remained in the aerosol jet print constructs. The results show that aerosol jet printing should be considered an effective way to process collagen type I and II into stiff dense constructs with suitable mechanical properties for the replication of dense collagenous connective tissues.

4.2 Introduction

Bioprinting has been facilitated by a number of additive manufacturing technologies. These are typically either extrusion-based, droplet based, or light based. Extrusion based methods usually extrude a hydrogel or hydrogel precursor through a nozzle via pneumatic or mechanical means [319]. Droplet, or jet-based methods, similar to conventional inkjet printing, generally use less viscous inks and eject droplets of the ink from a reservoir through a nozzle onto a substrate, facilitated by a stimulus in the printhead such as heat or piezoelectric actuation [320,321]. The most common light based additive manufacturing methods used in bioprinting are vat polymerization methods which contain the ink in a transparent vat and use light to polymerize monomers within the ink via a photoinitiator [322]. All these technologies execute code which contains the geometry of a virtual 3-dimensional object in 2-dimensional slices, or layers, which are executed consecutively to build the physical 3D object. Naturally, this relies on some form of phase transition from a fluid to some form of a solid, often a hydrogel. This phase transition can be an inherent feature of the material, like the self-assembly of collagen molecules into fibrils, or it can be the result of chemical modification of the material, such as the photocrosslinking of collagen methacrylamide [323]. Most examples of collagen printing are extrusion methods that rely on collagen fibrillogenesis. However, the slow solution-to-gel transition of collagen fibrillogenesis allows time for a deposited print line to flow and spread away from its deposited position, which results in

poor print resolution, and can make multiple layers difficult to achieve [324]. Innovative methods have managed to circumvent these limitations such as microvalve printing multiple thin layers of collagen with a nebulized alkaline solution providing a coating between layers to raise the pH and allow fibrillogenesis [325]. For extrusion printing, it was found that at a high enough concentration and suitable pH the viscosity of a collagen solution can make it feasible to print multiple over-lying layers at room temperature with an incubation step at 37°C post-print rather than between layers [326]. This understanding of the ideal rheology of a collagen solution for printing has been complemented by new extrusion printing techniques. Printing methods, such as the FRESH method, have further improved the accuracy and resolution of collagen printing [327–330]. However, the mechanical properties of printed collagen constructs remains limited when compared to the dense collagenous tissues from which the collagen is typically sourced and the replication of which is a often attempted. This can be attributed to the low range of collagen concentrations that are suitable for most printing techniques, generally < 2% w/v [326]. Whereas, collagen concentration in native dense collagenous tissues is often much higher ranging from > 10% in cartilage, to > 14% in the cornea [146,331]. At higher concentrations collagen becomes too viscous for extrusion or droplet methods, and likely too turbid for light based methods. Some chemical crosslinking techniques can greatly improve the mechanical properties of a printed scaffold, but this can also result in cytotoxicity, and/or the consumption of motifs that are involved in integrin-mediated cell binding [84,231].

Published research on collagen printing, thus far, has focused almost exclusively on animal-derived collagen type I, likely due to its commercial availability, particularly with the arrival of commercial collagen type I inks for extrusion bioprinting. However other fibrillar collagens such as collagen type II could prove useful particularly in cartilage tissue engineering. Collagen type II doesn't have the same commercial availability as collagen type I, and collagen type II is also associated with the induction of arthritis in rats, however this association is related to the intravenous administration of soluble

(monomeric) collagen type II, and can be treated prophylactically [332–334]. Collagen type II has been shown to improve attachment of mesenchymal stem cells (MSCs), and induce and maintain MSC chondrogenesis when used in TE scaffolds [335,336]. Collagen type II has also been shown to perform similar to, or to outperform the more preferred collagen type I in comparative chondrogenic studies [337–339]. While commercial collagen type II might be less common, the extraction of collagen type II is very similar to that of collagen type I with the only major difference being the starting tissue, which is typically articular cartilage in place of the tendon, bone or skin that is typically used for the extraction of collagen type I. Therefore by investigating the bioprinting of collagen type II some of the advantages of collagen type I as a substrate for cell culture could be exploited with a different set of material properties for more bioprinting options.

Furthermore most published research on collagen printing has been performed using one printing technique, extrusion printing. Continuing from the previous chapter on aerosol jet printing of recombinant human collagen type III, here the same novel collagen printing technique was applied to bovine Achilles tendon-derived collagen type I and porcine articular cartilage-derived collagen type II. While recombinant collagens still possess many advantages over animal derived collagens their high cost and apparent limited commercial feasibility is still a major hurdle. A number of bovine and porcine collagen type I medical devices have received FDA approval devices such as Collagraft™(Collagen Corp., USA) and Bio-Gide (Geistlich Pharma AAG, Switzerland). The only known RHCIII medical device, the Fibrogen FG-5200 corneal stroma substitute, appears to have stalled in its pre-clinical phase. Hence further investigation with animal derived collagens was deemed necessary and also allowed for more controlled experimentation with collagen concentration, since the RHCIII used in the previous chapter could not be lyophilised. No chemical crosslinking was performed on the printed collagen scaffolds in an effort to avoid the possible risk of cytotoxicity due to residual crosslinking agent and/or the consumption of motifs that are involved in integrin-mediated cell binding further down the line

[84,231]. Further characterization of the effect of ultrasonic atomization on the collagen structure and solution viscosity was performed to determine the mechanism of degradation.

In the ultrasonic atomizer of the Optomec® AJ300 ultrasonic waves are transmitted by a piezoelectric diaphragm operating at 1.65 MHz with the power supplied to the transducer ranging from a few watts up to a maximum of around 40 W. The waves travel through a water bath, then the walls of the borosilicate glass vial and into the ink producing a small fountain or spout within the vial. Atomization is believed to be the result of droplets being sheared off of Faraday waves that are superposed on the surface of this spout/fountain, similar to a common commercial nebulizer, the mist maker [340]. Hence, there is an additional physical stress, a shear stress, of atomization on top of the stresses of exposure to ultrasound. Ultrasound is defined as sound waves with a frequency above 20 kHz [341]. These sound waves force the movement of molecules which could lead to denaturation or degradation through mechanical stress, or through the heat that the movement generates. Whilst no research papers on ultrasonic atomization of collagen solutions could be found, there are 2 papers from the 1950's on audible range sonic fragmentation of collagen, and a number of papers from one research group, that of Marie Giraud-Guille (*Université Pierre-et-Marie-Curie*, now part of the Sorbonne), who found that ultrasound could be used to achieve liquid crystalline collagen conformations [306–308,342,343]. In the Giraud-Guille papers collagen solutions were sonicated in a 20 kHz, 50W ultrasonic bath which was cooled with ice. They found that the ultrasound over time forced supramolecular aggregates to dissociate but also fragmented some collagen molecules into shorter triple helices, and that these two effects combined lowered the viscosity of the solution [344]. They proposed that the drop in viscosity and the presence of fragmented collagen increased the rate of liquid crystal formation in their apparatus for making liquid crystalline collagen films. However, they also showed that the thermal stability of the fragmented collagen was significantly lower, and therefore decided to limit the duration of sonication to 20 minutes in order to lower

the risk of collagen denaturation [308]. The fact that this sonic fragmentation of collagen was also characterized for 9 kHz sonic waves suggests that this fragmentation effect may be found at many sonic frequencies [342]. Nevertheless the signs that the triple helix remains intact are encouraging, plus the drying effect of AJP could allow the collagen solutions to achieve concentrations necessary for liquid crystalline collagen conformations which are thought to be involved in the assembly of dense collagenous tissues such as cartilage and bone [345].

4.3 Materials and methods

4.3.1 Ink preparation

Inks were made using the same bovine Achilles tendon-derived collagen type I and porcine articular cartilage-derived collagen type II that were extracted at NUI, Galway using the protocol described in Chapter 2. Collagen inks were made by adding the lyophilised collagen type I or type II to a suitable amount of cold 0.01 M hydrochloric acid, or 1 M acetic acid and stirring at 4°C for at least 48 hours. It was found to be necessary to tear up the lyophilized collagen type I before adding the solvent in order to achieve a consistent solution, otherwise pieces of undissolved collagen type I could often be seen even after 72 hours stirring. Collagen type II readily formed solutions in comparison.

4.3.2 Aerosol jet printing of collagen type I and II

All printing was performed using the Optomec® AJ300 aerosol jet printer at Campus De Nayer. Six sets of samples were printed from 3 different inks, 3 mg/ml collagen type I, and 3 mg/ml & 6 mg/ml collagen type II, and 2 different print programs (A and B). Collagen type II solutions were clearly less viscous that type I solutions, hence the use of 6 mg/ml collagen type II while no higher concentrations of collagen type I could be printed in preliminary experiments. Both print program A and B consisted 576 layers of rectilinear rasters (or serpentine infill) of a circle, where each even-numbered layer was rotated 90° relative to the pattern of the previous layer, and each

odd-numbered layer was rotated by 15° relative to the last odd-numbered layer as in the previous chapters. The programs were inherently different and were executed with different parameters, summarized in Table 4-1. Program A was for a 4 mm sample and the spacing between parallel print lines was 60 µm. Program A was executed with a 100 µm nozzle, 50 ml/min atomizer flow, 50 ml/min sheath flow, and a print speed of around 12.5 mm/s which typically resulted in print lines of 60-65 µm in width leading to continuous films as layers. Program B was for a 5 mm sample and the spacing between parallel print lines was 90 µm. Program B was executed with a 150 µm nozzle, 50 ml/min atomizer flow, 100 ml/min sheath flow, and a print speed of around 17.5 mm/s, which typically resulted in print lines of 60-70 µm, leading to more of a lattice structure.

Table 4-1. Parameters set for print programs A and B

Parameter	Program A	Program B
Sample diameter	4.5 mm	5.25 mm
Track spacing	60 µm	90 µm
Atomizer flow	50 ml/min	50 ml/min
Sheath flow	50 ml/min	100 ml/min
Print velocity	12.5 mm/s	17.5 mm/s
Exp. Print line width	60 - 65 µm	60 - 70 µm
Exp. print pressure	0.4 - 0.6 bar	0.1 - 0.2 bar

All samples were printed onto glass cover slips that had been washed for 12 hours in 20% nitric acid. In all cases print parameters were varied slightly during printing to account for changes in aerosol production, and the volume of ink in the vial was replenished with every hour of printing. This particular regime was selected as the print time and aerosol flow were similar for both samples despite the discrepancy in size. It was also desired to increase the sample surface area improve the likely outcome of cell-seeding and maximise the possible cell number. Hence, program B was developed to compare to program A, which had typically been typically employed for printing collagen. Once printed, the samples were stored in a well plate at 4°C to await processing.

4.3.3 Post print processing of aerosol jet printed collagen type I and II

Since all samples were printed from an acidic collagen solution, the samples possessed an inherent acidity and upon incubation in aqueous media residual solvent in the printed material would leach out leading to a low pH and re-solubilization of the material. Hence a neutralizing buffer was used, similar to the co-solvent used in Chapters 2 and 4, which employed ethanol to slow the hydration of the printed material to allow time for any leachate to be neutralized, thereby preventing re-solubilization of the printed material. The neutralizing buffer consisted of 3 parts ethanol and 2 parts 1XPBS. Prior to mixing of the two parts of the neutralizing buffer, the pH of the PBS was adjusted to pH 8-9 with 1 M NaOH. Thereafter the ethanol was slowly added to the PBS while stirring, and left stirring for approximately 1 hour. The pH was checked again at this point and adjusted as necessary to pH 8-9 with 1 M NaOH. The buffer was then stored at 4°C for around 1 hour. Once cold, 1 ml of the neutralizing buffer was pipetted onto the samples in a well plate on ice, and incubated for at least 12 hours at 4°C.

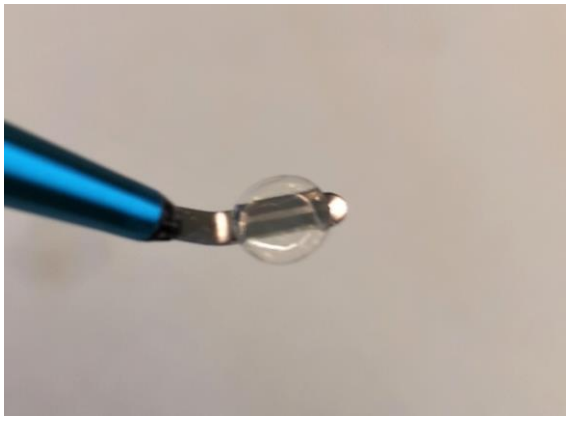

Figure 4-1 A 6 mg/ml collagen type II 5.25 mm diameter sample after being removed from its print substrate post neutralization.

The neutralizing buffer was then removed, and the samples were washed in PBS 3 times for 15 minutes and stored in PBS at 4°C thereafter. At this point the samples could be removed from their print substrate as a dense swollen hydrogel, as seen in Figure 4-1.

4.3.4 Viscosity

Fresh solutions of 3 mg/ml collagen type I, 3 mg/ml of collagen type II, and 6 mg/ml collagen type II in 10 mM hydrochloric acid were made by stirring at a low speed at 4°C for at least 48 hours. Sonicated samples were treated by pipetting 850 ul into the vial and sonicating for 5 minutes, this was repeated 3-4 times so that there was 3-4 ml of solution for viscosity and density measurements. The samples were tested on a Lovis 2000 M rolling ball viscosity meter and density meter. In each measurement the solutions, at close to room temperature, were loaded into the 1.8 mm capillary tube already containing a gold ball, using a syringe. The capillary was checked for bubbles then sealed and loaded into the viscosity meter. The density meter was also loaded with a sample for the viscosity measurement. Measurements were performed at 20°C with a measuring angle of 70°.

4.3.5 SDS-PAGE

SDS-PAGE was employed to characterize any degradation of collagen type I or II from ultrasonic aerosolization. Collagen type I and II solutions at 3 mg/ml in 0.01 M hydrochloric acid were treated with 20, 60, or 120 minutes of ultrasonic aerosolization. These samples and their respective untreated controls of either collagen solution were diluted to 0.3 mg/ml in order to run the SDS-PAGE. The gels were subsequently stained using ProteoSilver stain kit from Sigma Aldrich.

4.3.6 Circular Dichroism

CD spectroscopy is particularly effective at detecting changes in collagen structure given the unique spectra resulting from the collagen triple helix with a minimum peak around 198 nm and maximum peak around 221 nm. The presence of randomly coiled denatured collagen should lead attenuation and broadening of the peak around 198 nm, and attenuation or removal of the peak around 221 nm [302,346]. Hence, CD was used to characterize any unravelling of the collagen triple helix due to exposure to ultrasonic

atomization, or ultrasound alone. For the samples that were exposed to ultrasonic atomization, the set up was similar to a print but with a closed vial to prevent evaporation. Samples that were exposed to ultrasound alone were in a similar set up but with a much smaller starting volume, 150 µl, in the vial which was insufficient to generate the spout needed for atomization. In each case samples were taken at 20, 60, and 120 minutes. Samples were diluted to 0.15 mg/ml with 0.01 M HCl for the CD measurements. Sample CD spectra were collected between 260 nm and 185 nm using a Jasco J-1500 CD spectrophotometer with samples in quartz cuvettes with a 1 mm path length. The spectra of the samples were accumulations of 3 measurments between 260 nm and 185 nm with a scan speed of 20 nm/min, and 1 nm bandwidth. The spectra of 0.01 M hydrochloric acid was automatically substracted from the spectra by the CD software as background. The ratio of positive to negative (Rpn) peak was calculated to represent any drop in the intensities of characterisitic collagen positive peak at 221 nm, and negative peak at 198 nm, relative to the control. This ratio, Rpn, has often been used as a numerical representation of the changes in collagen CD spectra in response to a denaturing reagent or force [347–349]. The spectra in mdeg v wavelength were converted to ellipticity using equation (4-1) below [346]:

$$Ellipticity\ [\theta] = \frac{(mdeg \times MRW)}{(pathlength \times concentration)} \qquad (4\text{-}1)$$

Where MRW is the mean residual weight, the pathlength is in mm and the concentration is in mg/ml. The MRW was calculated for collagen type I by dividing the molecular weight found by SDS-PAGE by the number of amino acid residues in the triple helical domain of the bovine collagen type I α-1 chain, 1014 residues (UniProt: P02453). No porcine collagen type II α-1 chain was described by UniProt, hence the number of residues in the triple helical domain of bovine collagen type II α-1 (1014 residues, UniProt P02459) was used with the SDS-PAGE result to calculate the MRW.

4.3.7 Nanoindentation

The mechanical properties of the AJP samples were characterized using a Chiaro nanoindenter (Optics11). This ferrule-top nanoindenter and its sister system, the Piuma, have emerged in recent years as useful tools tools for measuring the mechanical properties of hydrogels, and for mechanobiology [294–296]. Both systems employ a spherical indenter on a cantilever of known stiffness, which is mounted on a ferrule-topped optical fiber [270]. A piezoelectric actuator displaces this assembly, or probe, by a user-defined distance and speed leading to the indenter making contact with the sample and deflection of the cantilever to which it is attached. Interferometry is used to measure the deflection of the cantilever. The deflection is then used to calculate the load, and the stiffness thereafter using a Hertzian (for visco-/elastic material) or Oliver-Pharr (for elastoplastic material) contact model [350]. While these systems are mostly used to measure local variations in stiffness, they are also used to measure the bulk modulus of hydrogels [297–299]. This form of micro/nano-indentation has provided results consistent with tensile and compressive test results [300]. For these measurements a probe with a cantilever stiffness of 0.57 N/m and a 52.5 µm radius spherical indenter was selected. 25 indentations were performed on each sample in a 5X5 matrix with 200 µm spacing between indentations in both directions. The indentation profile went to a maximum of 10 µm at an indentation rate of 1.4 µm/s. This indentation included a 4 µm offset from the sample surface to ensure that the probe was not in contact with the material before beginning the indentation.

4.3.8 Swelling Ratio

Samples were swollen overnight in 1XPBS then blotted on filter paper before weighing for the wet weight. For dry weight measurements, samples were dehydrated in increasing concentrations of ethanol (30%, 50%, 70%, 90% and twice in 100% v/v in ddH_2O) for 10 minutes each, and left on aluminium foil to dry overnight.

4.3.9 Scanning Electron Microscopy (SEM)

SEM was employed to characterize the layered structure that resulted from the use of AJP. Samples were prepared using a protocol reported by Raub et al. with some modifications [301]. Briefly, samples were fixed in 4% glutaraldehyde in 1X PBS for 1 hour at room temperature, then washed 3 times in PBS for 7 minutes, and 2 times in ddH_2O for 7 minutes. Samples were then dehydrated in increasing concentrations of ethanol in ddH_2O (30%, 50%, 70%, 90%, and 100% v/v) for 10 minutes each and twice in 100% ethanol. The samples were further dehydrated in increasing concentrations of HMDS in ethanol (33%, 50%, 66%, and 100% v/v) for 15 minutes each, and twice in 100%. Samples were then torn apart with tweezers and left to dry on aluminium foil under a fume hood overnight. The dried samples were mounted on SEM stubs using carbon tape, and sputter-coated with platinum to a thickness of 5 nm. The samples were imaged at 5 kV.

4.3.10 Statistical Analysis

Statistical analysis was performed on the nanoindentation and swelling ratio result to discern statistically significant differences between sample groups. In both cases a three-way (collagen type, concentration, and print program) ANOVA was performed with two levels. The values were considered significant if their p values were < 0.05.

4.4 Results

4.4.1 AJP of collagen type I and II

In observing samples printed with program A under the microscope all print lines were seen to overlap, i.e., the print lines of underlying layers could not be observed. Gaps were observed between printed lines in the top layer of samples printed with program B, and print lines of underlying could be observed.

4.4.1.1 Post print processing

All samples printed with program A performed as expected for the post-print processing with no signs of dissolution, and clear signs of enhanced structural integrity when handled. However, samples printed with program B appeared thinner, by eye, than those of program A, and some samples appeared to have performed better than others with some samples showing signs of dissolution. However, sample group B still showed signs of structural integrity when handled.

4.4.2 Viscosity

During the treatment with the ultrasonic atomizer all samples generated aerosol soon after initiation of the ultrasound. However, the 3 mg/ml solutions of both collagen type I and type II reached a sufficient rate of aerosol generation for printing almost immediately, whereas the 6 mg/ml collagen type II solution only reached sufficient aerosol generation after around 3 minutes of the treatment, and the amount of aerosol generated remained low relative to the other solutions. The viscosity of all three solutions dropped as a result of the ultrasonic aerosolization as seen in Figure 4-2. The most viscous solution, 3 mg/ml collagen type I exhibited the greatest change in viscosity. The 6 mg/ml collagen type II ink also exhibited a large drop in viscosity whereas 3 mg/ml collagen type II ink measured a relatively small decrease in viscosity.

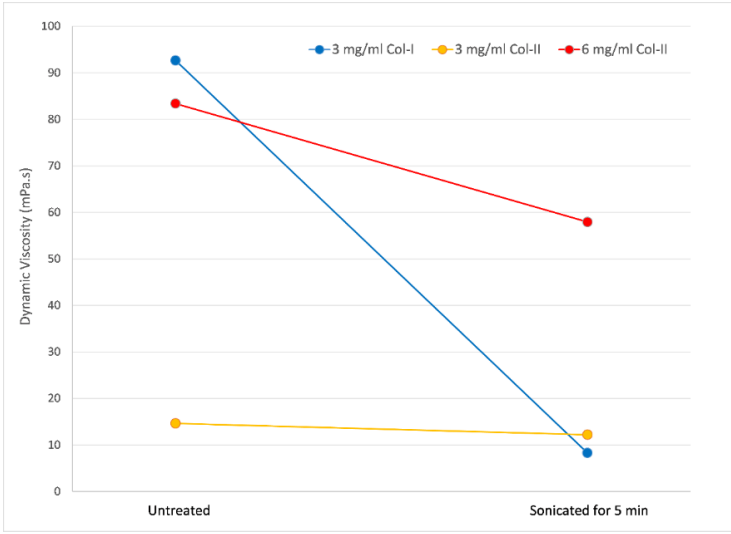

Figure 4-2. The dynamic viscosity of untreated collagen solutions and the same solutions after a 5-minute treatment with ultrasonic atomization in an aerosol jet printer.

4.4.3 SDS-PAGE

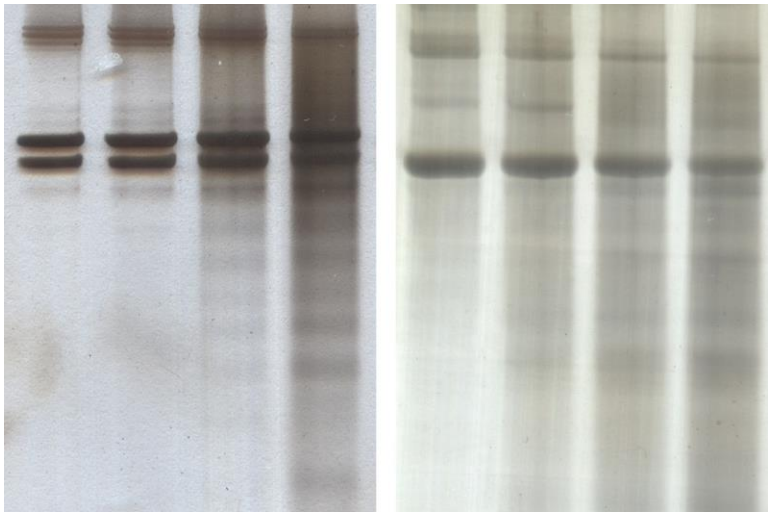

Figure 4-3. Silver stained SDS-PAGE gels for detecting degradation of collagen of collagen type I (a) and collagen type II (b) from exposure to ultrasonic atomization. In each case the lanes are in order of (left to right) 0, 20, 60, and 120 minutes of exposure.

SDS-PAGE revealed that both collagen type I and type II were gradually degraded by ultrasonic atomization as seen in Figure 4-3. The degraded chains did not appear to show any preferential molecular weight, instead a distribution of what could be confused with non-specific staining spread over the lane. The α and β bands became slightly less intense in both cases after 120 minutes, and the distribution of degraded α and β chains became increasingly intense in the 60- and 120-minute treatment lanes.

4.4.4 CD spectroscopy

Typical collagen CD spectra with minima at 198 nm and maxima at 221 nm were measured for all samples, as seen in Figure 4-4 A-D. However, in some cases the sample treatment caused a drop in the intensity of these peaks. Collagen type I was shown to be vulnerable to denaturation as a result of exposure to ultrasonic radiation with a drop in the peak intensities resulting change in Rpn from an untreated control of 0.16, to 0.12 after 2 hours of ultrasonic radiation. However, there was no significant red-shift of the crossover point and no clear shift of the 198 nm and 221 nm peaks. Ultrasonic atomization of collagen type I lead to clearer signs of denaturation with a drop in Rpn from 0.16 to 0.08 after 2 hours of atomization, and a gradual red-shift in the cross-over point from 213.6 nm to 214.9 nm.

Collagen type II showed far less signs of denaturation due to ultrasonic exposure and atomization. The spectra from samples that were exposed to ultrasonic radiation alone were virtually superimposed on each other and resulted in no significant changes in Rpn. Ultrasonic atomization did lead to gradual decreases in the peak intensities at each time point. The Rpn decreased from an untreated control value of 0.14 to 0.13 after 2 hours of ultrasonic atomization. There was no significant shift in the crossover point.

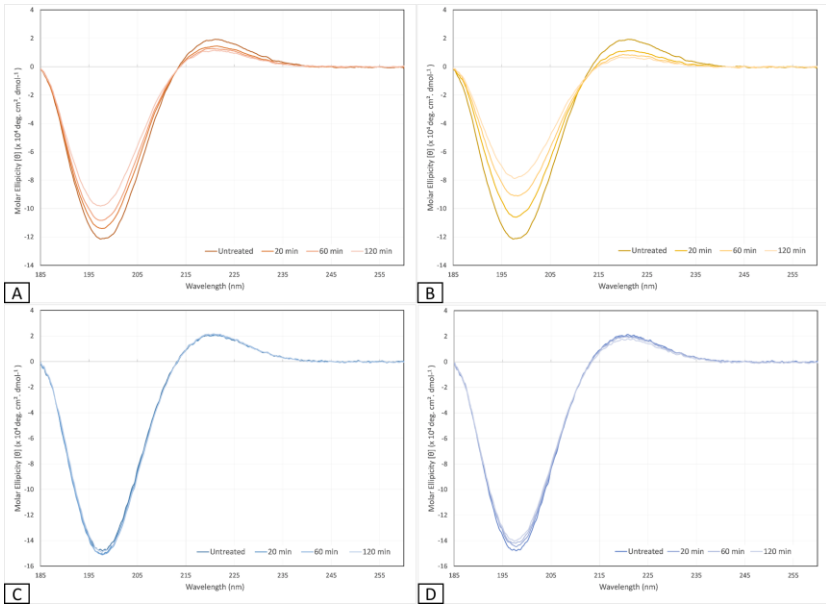

Figure 4-4. CD spectra of (a)collagen type I sonicated non-atomized, (b) collagen type I ultrasonically atomized, (c) collagen type II sonicated non-atomized, and (d) collagen type II ultrasonically atomized.

4.4.5 Aerosol jet printing of collagen type I and II

During printing in both cases the print pressure stayed within the expected ranges; 0.4 – 0.6 bar for program A and 0.1 – 0.2 bar for program B. In observing samples printed with program A under the microscope post-print all print lines were seen to overlap, i.e., the print lines of underlying layers could not be observed. Gaps were observed between printed lines in the top layer of samples printed with program B when observed under the microscope post-print, and print lines of underlying could be observed.

4.4.6 Post print processing of aerosol jet printed collagen type I and II

All samples printed with program A performed as expected for the post-print processing with no signs of dissolution, and clear signs of enhanced structural integrity when handled. However, samples printed with program B appeared thinner, by eye, than those of program A, and some samples appeared to have performed better

than others with some samples showing signs of dissolution. However, sample group B still showed signs of structural integrity when handled.

4.4.7 Nanoindentation

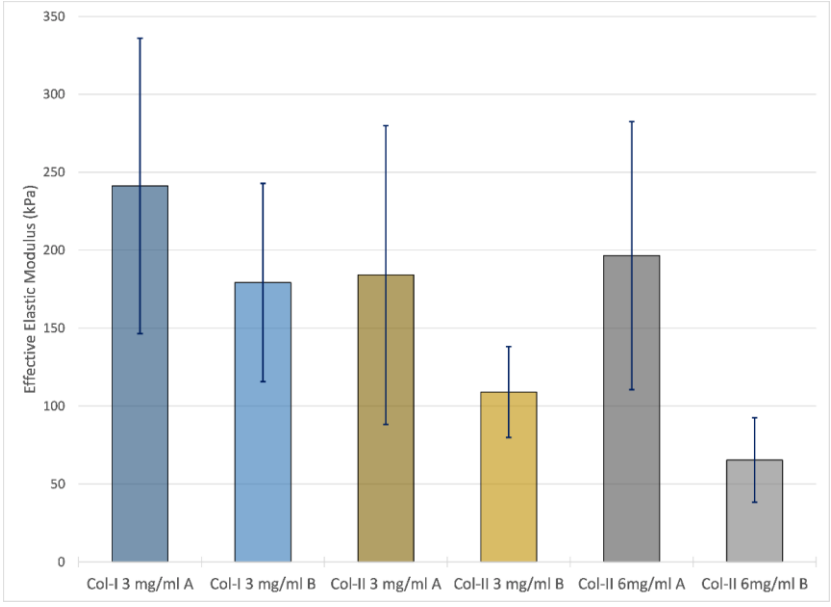

Figure 4-5. The average elastic modulus of each sample group measured by nanoindentation using a Hertzian model. Error bars represent the standard deviation of each sample group.

As seen in the nanoindentation results in Figure 4-5, collagen type I printed with program A resulted in the highest average effective elastic modulus, 241.3 kPa ± 94.3 kPa (± SD), while the 6 mg/ml collagen type II samples printed with program B resulted in the lowest average effective elastic modulus with 65.4 kPa ± 27.1 kPa (± SD). The print program and the collagen type were found to be statistically significant factors in relation to the mechanical properties ($p < 0.05$). Collagen type I samples were stiffer than those made with collagen type II, and samples printed with program A were stiffer than those printed with program B.

4.4.8 Swelling ratio

Samples printed with program B had on average had a higher and more variable swelling ratio as seen in Figure 4-6. The program was found to be the only statistically significant factor in relation to the swelling ratio ($p < 0.05$).

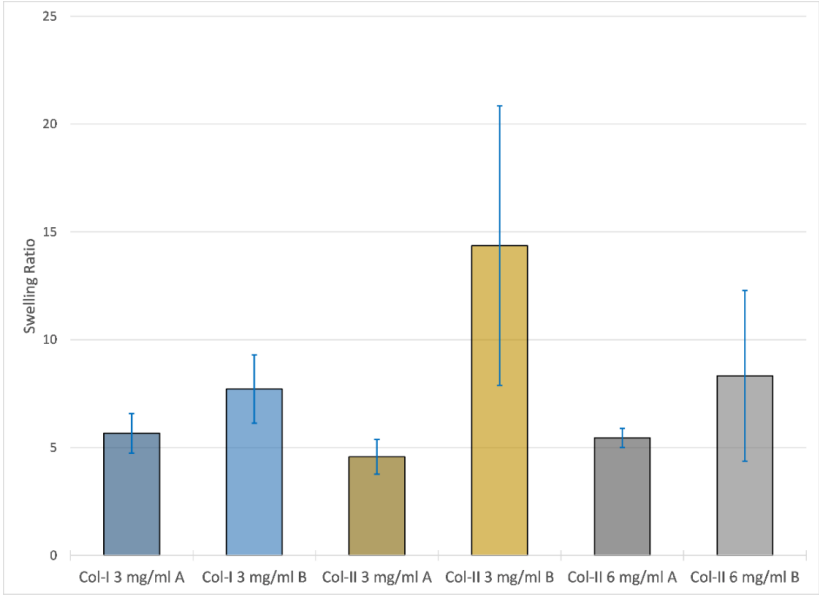

Figure 4-6. The average swelling ratio of each sample group with error bars representing the standard deviation within each group.

4.4.9 SEM

Distinct layers could be resolved in all samples as seen in Figure 4-7. Whilst in program A samples these layers continued throughout the samples, in samples printed with program B the layers were not always continuous across the section. Most of the samples possessed a very smooth surface topography, however some samples printed with program B had dimples that appeared to continue through several layers.

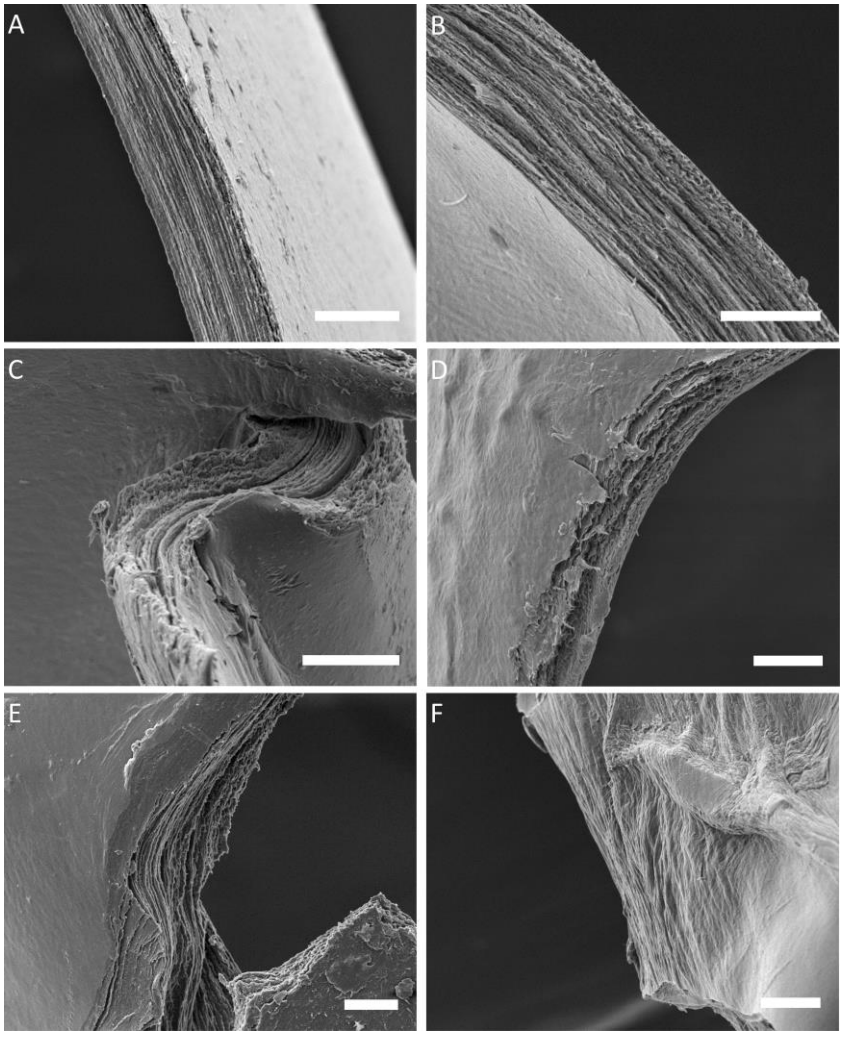

Figure 4-7. SEM images of cross-sections from sample groups, (A) col-I 3 mg/ml A, (B) col-I 3 mg/ml B, (C) col-II 3 mg/ml A, (D) col-II 3 mg/ml B, (E) col-II 6 mg/ml A, and (F) col-II 6 mg/ml B. All scale bars measure 20 µm.

4.5 Discussion

This work was published in the first research article on the aerosol jet printed collagen type I, and likewise collagen type II. Aerosol jet printing of collagen type I and type II again proved to be very similar to aerosol jet printing of recombinant human collagen type III. Print program A was similar to the program used in to print

RHCIII in chapters 2 and 3, however here it was printed with higher atomizer flow and higher print velocity in an effort to improve the print time. Print program B was developed to increase the surface area of samples and investigate porous prints, but this was also an effort to improve the print time. By increasing the distance between print lines, the print speed could be increased with a lower risk of pooling. Pooling is more likely to occur at corners since the amount of material printed in a given area increases at corners. However, it is likely that some of the significant differences observed between program A and program B samples here, are the result of a less than optimal neutralization process for the program B samples, so this should be kept in mind when considering these differences. It was apparent upon removal of the neutralization buffer that the program B samples had some signs of dissolution. They also appeared far thinner than program A samples which could be due to dissociation of some collagen during incubation in the neutralizing buffer or could be an effect of the printing pattern. It appears likely that the neutralization buffer requires refinement for samples with increased porosity like the program B samples. A higher ethanol concentration in the neutralization buffer could further slow the absorption of the buffer and prevent dissociation of the molecular collagen from the printed material.

The drop in viscosity of the collagen solutions from exposure to ultrasound has been previously reported (albeit for a much lower frequency of ultrasound, 20 kHz) [308,344]. The viscosity measurements were performed twice 2 days apart without any change, so the drop does not seem to be transient at least on that time scale. The drop in viscosity is thought to be the result of an initial break up of supramolecular aggregates remaining in solution, followed by a gradual degradation of the collagen as seen in the SDS-PAGE. The shear stress of atomization may also exacerbate this effect of the ultrasound, particularly for collagen type I given the increased unfolding observed for atomized samples versus the non-atomized samples in the CD measurements. The viscosity of the 6 mg/ml collagen type II was considerably higher than the other samples after the atomization treatment, and as noted, there was

less atomization occurring for this solution compared to the others. However, the viscosity of the 6 mg/ml would be expected to continue to drop as the atomization time increases. A 6 mg/ml collagen type II solution that was atomized for one hour has been measured to have a dynamic viscosity of 7 mPa.s. Another explanation for the increased viscosity drops observed for collagen type I solutions compared to collagen type II solutions would be the increased vulnerability of the collagen type I to degradation and unfolding via observed in CD and SDS-PAGE.

The degradation and denaturation revealed by SDS-PAGE and CD spectroscopy, particularly for aerosol jet printing of collagen type I, could have advantages. As stated in the discussion of the previous chapter, studies have found that the presence of denatured and degraded collagen in culture media upregulates the expression of collagenase matrix metalloproteinases (MMPs) in chondrocytes [304,305]. While excessive upregulation of these MMPs could degrade an AJP collagen scaffold, their expression is also a sign of chondrogenesis. Klatt et al. 2009 found this MMP upregulation to be dose-dependent by supplementing the culture media with different concentrations of fragmented collagen. The mechanism of interaction for chondrocytes on AJP collagen would likely be quite different since much of the degraded or denatured collagen would be expected to remain in the AJP collagen scaffold. Hence this upregulation of MMPs could be dependent on the degradation rate of the AJP collagen scaffolds which for samples printed with program A has been observed to be quite slow. However, this should be considered in any future chondrogenic cell culture experiments on AJP collagen, which is discussed in the appendix section 6.3.

It is not clear whether the differences observed between collagen type I and II CD spectra in response to ultrasonic exposure and ultrasonic atomization hold any implications beyond this particular application. The shear forces involved in ultrasonic atomization are likely to be the denaturing factor since ultrasound alone had a less of an impact on the spectra with increasing treatment. There are a number of caveats that must be considered before directly comparing the performance of the two collagen

types. The fact that the collagens tested were from different species and from single batches (extractions), thereby makes the findings potentially subject to special variations and batch-to-batch variations. These results were also for monomeric collagen in solution; hence it is difficult to translate any of the findings to assembled collagen fibrils in the ECM. However, even considering these caveats, the fact that ultrasound had no clear impact on collagen type II CD spectra and did on collagen type I spectra is interesting, and at the very least indicates that collagen type II would be more suitable for aerosol jet printing in general. Nevertheless, this does not rule out collagen type I's suitability for aerosol jet printing, since a large proportion of the collagen must remain in a triple helix conformation for the average signal to still retain the collagen triple helix minimum and maximum peaks. Similar to the discussion in the previous chapter, transmission electron microscopy could be used to try to resolve any fibrillar structures that might be present in the AJP collagen. While atomic force microscopy has been used to resolve fibrillar structures, it may struggle to resolve the atypical fibrils expected to be in present in AJP collagen.

All aerosol jet printed collagen samples possessed remarkable stiffness for bioprinted collagen constructs that have not been covalently crosslinked. The only significant difference between the sample groups, regarding stiffness, was the print program. However, as stated earlier, the differences observed between the samples printed with the program A or B may have more to do with the neutralization of the construct that any intrinsic properties imparted by the print program. Any significant re-solubilization like that seen in some program B samples would disrupt the layered structure of the printing and thereby change the constructs mechanical behaviour. The average effective elastic moduli of the program A samples were 241.3 ± 94.3 kPa, 185.1 ± 95.8 kPa, and 196.6 ± 86.0 kPa (all ± SD) for 3 mg/ml collagen type I samples, and 3 mg/ml and 6 mg/ml collagen type II samples respectively. The highest reported mechanical characterization results for printed collagen found were compressive moduli of around 110 kPa for glutaraldehyde-crosslinked bovine collagen type I, 47.2 ± 14.2 kPa for EDC-

crosslinked porcine-hide collagen, and 21.5 ± 1.4 kPa for porcine-tendon collagen type I without any modification [314–316]. The elastic moduli of the aerosol jet printed collagen constructs printed with program A obtained by nanoindentation were all significantly higher. Furthermore, in separate work where EDC and NHS were added to the neutralizing buffer (40 µg/ml EDC, 24 µg/ml NHS) to crosslink aerosol jet printed 6 mg/ml collagen type II (program A, 576 layers), nanoindentation revealed an average effective elastic modulus of 2.1 ± 0.4 MPa (see supplementary material). These results were compared to results reported on the nanoindentation of dense collagenous tissues. Using a similar Optics11 nanoindenter human ear, septal, and alar cartilage were found to have effective elastic moduli of 1.14 ± 0.71 MPa, 2.65 ± 1.78 MPa, and 1.26 ±0.51 MPa respectively [351]. Similarly, the stroma of human donor corneas were measured to have an average effective elastic modulus of around 75 kPa [156]. This places aerosol jet printed collagen within reach of replicating the mechanical properties of dense collagenous tissues. Chemical crosslinking could be used to enhance the stiffness of the constructs for closer replication of the stiffest cartilage, whereas different print programs and a deeper understanding of the post-print neutralization could be employed for a closer replication of the weaker collagenous tissues.

For swelling ratio, the only significant difference between sample groups regarding swelling ratio was the print program. Samples printed with program A had a more consistent swelling ratio between and within sample groups whereas program B samples varied a lot between and within sample groups. This could be taken as further evidence of re-solubilization as this would allow collagen to dissociate creating regions within samples with lower density and a higher capacity to absorb water. Evidence of continuous layers traversing entire samples was observed in all program A samples in SEM. However, program B samples possessed regions that appeared amorphous or had very faint signs of layering which were interpreted as signs of dissolution. Some program B samples also possessed a strange topography with potholes or dimples which was also interpreted as signs of dissolution probably starting at a region

where multiple layers were accessible at the surface, like a pore. Nevertheless, the observation of distinct layers in most samples is promising for many applications. We have previously estimated similar layers of RHCIII to be ~330 nm thick, this would likely increase for the 6 mg/ml collagen type II printing since thickness is usually related to the in concentration in aerosol jet printing. Alternating layers of different material could be used to induce certain behaviours in cells, and layers of conductive material could be printed within a collagen construct for electro-stimulation.

4.6 Conclusion

It was shown in this work that aerosol jet printing could be used to generate stiff collagen constructs with hundreds of layers and that were suitable for tissue engineering. While some collagen type I was shown to be denatured by the aerosol jet printing process, the effect was gradual. Hence the denaturation would be mitigated somewhat by the addition of fresh collagen to vial with every hour of printing, as is practice during sample production. Collagen type II was shown to be particularly useful for aerosol jet printing due to its lower viscosity, which allowed a greater concentration range to be printed, and its relative invulnerability to the stresses of the AJP process. While the resolution of this printing process limited scale of the constructs, this was achieved using an aerosol jet printer intended for printing small electrical components with just a few layers. The scalability of this method could potentially be improved by designing an aerosol jet printer with the intention to print biomaterials for biofabrication and perhaps combining this with other bioprinting methods. Moreover, the combination of AJP's capability to print high resolution structures with conductive inks and it's demonstrated capability to print collagen will likely be advantageous to the field of electrically stimulated cell culture where inkjet printers have been used to print far more dilute collagen solutions with far fewer layers over conductive material [352]. The field of bioprinting can only be enhanced with the addition of alternative printing methods and materials, like aerosol jet printing and collagen type II.

5 Concluding remarks and where the future lies for aerosol jet printing collagen

Parts adapted from:

> "Bioprinting of collagen type I and II via aerosol jet printing for the replication of dense collagenous tissues"; Gibney, Rory; Ferraris, Eleonora; Frontiers in Bioengineering and Biotechnology 2021, 9:786945

This work has established aerosol jet printing as a feasible method for producing 3D printed collagen scaffolds. The scale of these scaffolds is limited, but the suggested applications may not require much of an increase in scalability. Optical coherence tomography measurements carried out by our collaborators at the University of Antwerp measured the average thickness of ten 4.5 mm diameter 288 layer AJP RHCIII samples swollen in 1XPBS to be 93 µm ± 36 µm. Hence, for an average sample thickness of 500 µm (i.e., suitable thickness for a corneal stroma substitute) around 1500 layers would be required. Therefore, using the fastest print speeds reliably achieved in this work, a sample with suitable dimensions for a corneal stroma substitute (7 mm wide, 1500 layers) would require at least 12.5 hours to print. While this would be difficult to achieve, it is possible. As highlighted in Chapter 2, the printer used for these studies, the Optomec® AJ300, was intended to print electrical connections and components of limited size. Aerosol jet printers have been developed with multiple atomizers and print-heads to

facilitate the production of multiple samples simultaneously. The print speed could be increased somewhat by optimizing an aerosol jet printer for collagen and similar biopolymer inks. Wider nozzles that print in higher resolution might be considered a solution, however these were found to require slower print speeds to prevent pooling, likely due to a higher moisture content in the aerosol as a result of there being a greater volume of aerosol not in contact with the sheath gas. Hence, nozzles with oblong or oval orifices have been developed for the Optomec aerosol jet printers to increase the perimeter-to-area ratio of the nozzle, relative to a nozzle with a circular orifice, and thereby increasing the amount of aerosol in contact with the sheath gas. However, these oblong nozzles require a considerable investment not just in the nozzles themselves, but also in a new deposition head capable of receiving them.

The higher flow rates used with the 150 µm nozzle in Chapter 5 were the maximum of what could be used reliably with this particular aerosol jet printer when printing collagen. Condensation in the tubing and large droplets of collagen making their way into the tubing made it necessary to limit the collective flow (i.e. aerosol flow + sheath flow) to just below the maximum sheath flow in order to allow the flow to be reversed through the tubing (changing flow from atomizer-to-nozzle to nozzle-to-atomizer by shutting off the aerosol flow and increasing the sheath flow). A higher maximum sheath flow and atomizer flow could possibly allow higher print speeds to be used with the 150 µm nozzle, closer to those used with the 100 µm nozzle. The printing of the high aspect ratio structures shown in Chapter 2 could be facilitated by a motion controller that allows programming of the Z-axis, and with the addition of a better process camera. A concentrated collagen ink like the 6 mg/ml collagen type II ink used here could be enhanced with the addition of other biomaterials to increase the loading of the ink and thereby increase the growth rate of these high aspect ratio structures. Printing experiments were carried out on inks consisting of 3 mg/ml collagen type I and 1.5 mg/ml cellulose nanocrystals to test whether such the addition of CNCs would render the ink too viscous for printing, however, the ink aerosolized similarly to a control 6 mg/ml

collagen type II ink and dramatically increased the growth rate of the high aspect ratio structures. These structures are not new to aerosol jet printing and one group has focussed on creating these structures via aerosol jet printing using highly-loaded (~40% w/v) silver nanoparticles inks [251,353]. They have been able to print macro-scale pillar arrays and lattices which could be highly beneficial to tissue engineering if replicated with collagen or similar biomaterials. Moreover, the combination of AJP's capability to print high resolution structures with conductive inks and it's demonstrated capability to print collagen will likely be advantageous to the field of electrically stimulated cell culture where inkjet printers have been used to print far more dilute collagen solutions with far fewer layers over conductive material [352]. Furthermore, AJP collagen could be advantageous to the field of biosensors, where collagen's piezoelectric properties have been exploited as a power source though it is yet to be seen whether AJP collagen possesses the same piezoelectric properties [354]. The ability of AJP to produce strong thin collagen films could be exploited to form a robust biocompatible substrates or matrices for other types of biosensors such as a glucose-sensing or hydrogen peroxide-sensing silver nanoparticle-based sensors [355–357]. The ability of aerosol jet printing to deposit on rough surfaces could also be exploited using collagen to form a biocompatible coating on medical devices. This could potentially form tougher, more controlled coatings than are typically achieved with spraying techniques. Should it prove possible to print stable material without the need for the neutralizing buffer used here, for instance by printing in ammonia vapour then it could even be in the realm of possibility to see an aerosol jet printing collagen handheld pen for use in wound dressing, perhaps even with silver nanoparticles present as an antibacterial treatment [358].

The scale and nature of the aerosol jet printed collagen scaffolds caused issues in attempting to characterize the AJP collagen throughout this project. Sample masses, typically measuring ≤ 1mg, were too low for a reliable study using the differential scanning calorimeter (DSC) available in MTM, and similarly the low mass caused repeatability issues in attempts at ninhydrin and TNBSA

(2,4,6-trinitrobenzene sulfonic acid) crosslinking efficiency assays. DSC studies were even more challenging because the collagen appeared to remain in soluble form, based on results in Chapter 2, meaning it had higher entropy than if it had formed fibrils and thereby leading a low signal for the phase transition at the denaturation temperature [259]. For both the DSC and the attempted assays, attributing the issues experienced to the low sample mass holds with the typically recommended sample mass for collagen samples using the particular type of calorimeter and these particular assays [37]. However, given the collagen characterization performed via CD spectroscopy and SDS-PAGE presented in Chapters 3 and 4, DSC may no longer be necessary at least for collagen characterization. A more interesting use of resources would likely be spent on cross-polarization microscopy of single print layers or thin sections of samples to determine whether the AJP collagen is in liquid crystalline conformations. Likewise, optimising the crosslinking efficiency was determined to be less of a priority when it became clear that samples were dissolving in the reaction buffer, before the co-solvent buffer was devised. Equally now a study on the crosslinking efficiency may not be as interesting as further studies to determine the solubility of the AJP collagen in the co-solvent buffer/neutralizing buffer given the reappearance of suspected solubility issues for the more porous program B samples Chapter 4. The current co-solvent buffer could be improved, or other buffers could possibly be found that would allow cells to be printed alongside aerosol jet printed material without the obvious risk of them dying due to the presence of ethanol in the neutralizing buffer post-print. Coagulation, or fiber formation buffers containing high concentrations of polyethylene glycol (5-40% w/v) in a phosphate buffer have been used to induce the formation of collagen fibers from extruded collagen solutions on contact, and could potentially be used to neutralize AJP collagen with a lower risk to any cells that might be deposited alongside it [260,359,360]. Although PEG is not cytotoxic, the osmotic pressure that the PEG is there to generate could still pose a major risk to any cells present. For improving the mechanical properties, rather than chemical crosslinking, another consideration could again be the addition of other stiffer material to

increase loading and to form composites, or even interpenetrating networks [361]. As stated earlier, preliminary experiments combining collagen type I solutions with cellulose nanocrystals proved fruitful with the CNCs increasing the loading making high aspect ratio structures quicker. Indeed, aerosol jet printing lends itself to the inclusion of such non-soluble components, or dispersants compared to other printing techniques since the ink is constantly agitated during printing which should prevent the formation of aggregates.

As stated in Chapter 2, there have been a number of papers published in recent years focussed on further developing the understanding of the AJP process and on enhancing aerosol jet printers themselves. The most impactful of these papers have been authored by Ethan Secor and colleagues at Sandia National Laboratories (Albuquerque, New Mexico, USA), which is where the aerosol jet printing technique was first developed, and where both Optomec and IDS Nanojet first started [248,254,255,362]. They have recently published patents on a recirculating ink cartridge, an in-line mixing printhead for multi-material printing, and an optical measurement system for monitoring aerosol generation in the atomizer [363–365]. These devices could really improve aerosol jet printers, and the pace at which this work has come out of Sandia National Laboratories instils confidence in the idea that further enhancements will soon be developed by Sandia. A measurement of thickness during printing would be highly useful to AJP collagen, particularly for corneal applications, and could be possible using a modern CMOS (complementary metal oxide semiconductor) chip to look at the light reflected from the substrate-AJP collagen interface and the AJP collagen-air interface and calculate the thickness using Fresnel equations as an update to the work of Shedd and Newell in 1998 [366]. This would give the user useful feedback during printing, but the final thickness of the scaffold would likely be heavily dependent upon the conditions during sample stabilization. However, the patented recirculating ink cartridge and optical measurement system developed by Sandia National Laboratories

would go a long way towards giving the user feedback on the rate of deposition and towards keeping that rate of deposition consistent.

A major emphasis was placed on characterizing the collagen that was printed given the obvious environmental extremes that would be experienced through aerosol jet printing. It is now known that aerosol jet printing of collagen imparts a varied detrimental effect on the collagen structure depending on the collagen type. A further step to take in this regard would be to perform a similar analysis as that in Chapter 4 on commercial sources of collagen type I since it is the most common commercially available collagen. The more extensive CD spectroscopy study performed on the animal derived collagens in Chapter 3 was not possible with recombinant collagen type III due to a combination of material limitations and further issues in finding a supplier since the last supplier used, Abcam, discontinued the product shortly after the last order. Indeed, while aerosol jet printing was demonstrated to be a feasible production method for RHCIII scaffolds, it is naturally dependent upon the availability of RHCIII and hence its commercial feasibility. The price of RHCIII saw a sharp increase from when it was synthesized by the patent-holder, Fibrogen, at $315 per 100 mg, to when licensed antibody and protein suppliers started producing RHCIII, like MyBiosource at $1415 per 100 mg, and Abcam at $3290 per 100 mg. Therefore, it seems the exorbitant cost of RHCIII since Fibrogen ceased supply could be caused by the licensed suppliers passing on high licensing fees to consumers along with the high production costs. There is also the concerning case of the Fibrogen FG-5200 RHCIII corneal substitute appearing to stall in the pre-clinical phase, meaning there is no RHCIII medical device approved for use in humans. However, collagen type II is clearly the most suited collagen to aerosol jet printing from those tested, and though it has been treated with scepticism in the past, that may change since there is a growing database of evidence illustrating its superior performance compared to collagen type I in cartilage tissue engineering [339].

Overall, it can be said from this work that aerosol jet printing is a collagen bioprinting method capable of producing dense stiff collagen scaffolds with elastic moduli >2 MPa. While there are many

disadvantages to this method as a bioprinting method, the continuing development of the aerosol jet printing method and equipment, particularly at Sandia National Laboratories, could address many of these disadvantages, and make aerosol jet printing a more attractive bioprinting method.

6 Appendices

6.1 Nanoindentation – Load-v-indentation graphs

During each nanoindentation experiment the load-v-indentation graphs were inspected after each indentation to look for signs of any inaccuracies. These inaccuracies were most likely to be the result of the sample being partially detached, meaning that the movement of the indenter is not indenting the material but pushing out media from gap between the sample and the substrate. Other causes are a false surface detection, where the nanoindenter detects some debris on top of the sample as the sample surface, or where a bubble is caught between the cantilever and the ferrule body, though these issues were more likely to be spotted in set-up and hence were far less likely to occur during a measurement.

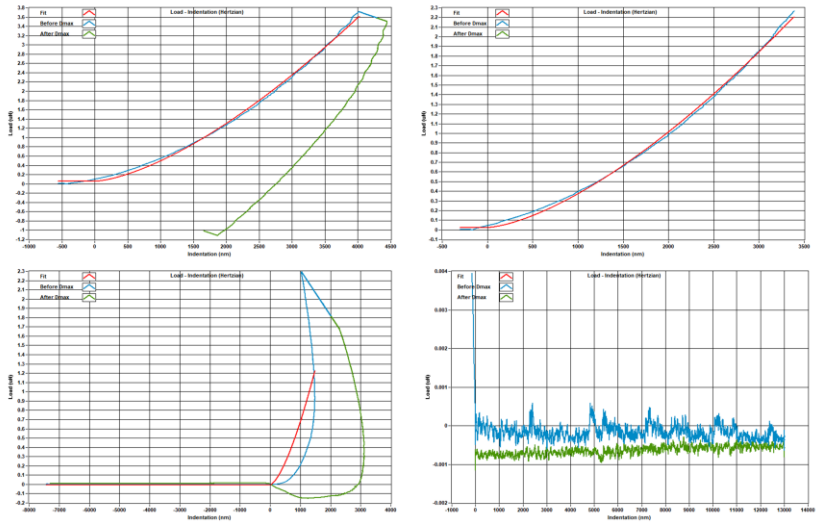

Figure 6-1. Examples of inaccurate, or bad indentations.(top right) No clear off-set, hence sample may have been in contact with tip due to buoyancy of sample and substrate detachment, (top left) incomplete indentation possibly caused by an interferometer error, (bottom left) poor model fit, low load and the decrease in indentation with increasing load indicates movement of the sample in the z-direction due, (bottom right) the extremely low load and lack of typical loading and unloading indicates that the indenter has not made contact with any surface.

If inaccurate or bad indentation were immediately followed by another bad indentation, the measurement would be stopped and restarted in another position on the sample, where there might be better adhesion. Similarly, if a bad indentation was later followed by a bad indentation at a point adjacent to the first bad indentation the measurement would be stopped and started at another location. This was developed as a habit since it was found that it would be likely for a whole side or portion of the matrix of indentations would be bad indentations due to poor substrate adhesion.

6.2 Glycerol as a stabilizing agent

This experiment was performed to investigate whether glycerol could be used as a stabilizing agent for collagen type I during ultrasonic atomization. However, the investigation was suspended upon discovering that glycerol appeared to enhance degradation in some cases rather than prevent it. Nevertheless, the experiment was instrumental in deciding to compare ultrasonically atomized solutions and non-atomized sonicated solutions.

After finding that collagen type I was degraded by ultrasonic atomization in initial experiments, it was still unclear whether this was due to mechanical or thermal stress. The stabilizing effect of glycerol and other glycols on collagen is well documented, however, this is usually in respect to collagen type I's thermal stability [69,70]. Glycerol was explored as a stabilizing agent with two different solvents, 0.01 M HCl, and 1 M acetic acid. Samples were taken similar to the SDS-PAGE samples for ultrasonic atomization in this chapter, at 0, 20, 60, and 120 min.

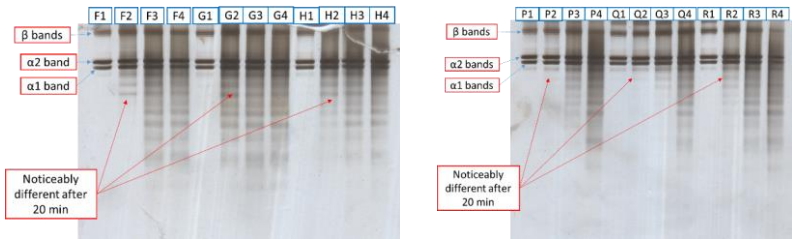

*Figure 6-2 (**a**) Collagen type I in 1 M acetic acid with 0 M glycerol (F1-F4), 1 M glycerol (G1-G4), or 2 M glycerol (H1-H4). (**b**) Collagen type I in 0.01 M HCl with 0 M*

glycerol (P1-P4), 1 M glycerol (Q1-Q4), or 2 M glycerol (R1-R4). The samples for each condition are labelled 1 to 4 representing their period of sonication, i.e., 1 = 0 min, 2 = 20 min, 3 = 60 min, and 4 = 120 min.

As seen in the results above the addition of glycerol actually seemed to enhance the degrading effect of the ultrasonic atomization. The use of acetic acid as a solvent also seemed to enhance the degradation compared to hydrochloric acid. It was noticed during the atomization that the inks containing glycerol appeared less viscous, but they also seemed to possess a lower surface tension. The apparent lower surface tension and viscosity allowed the ink that coalesced on the walls of the vial during atomization to quickly fall back down to the bottom of the vial where it would be atomized again, which was not typical behaviour. Typically, the collagen ink that coalesced on the walls of the vials would have to build up into large droplets before their fluid properties would allow them to spread and fall back down. These results suggested that the degradation was a result of the atomization rather than the exposure to ultrasound, and that the addition of glycerol enhanced the degradation because of the effect it had on the fluid properties of the ink and how that increased how often the ink experienced atomization. However, this was all based on observation of the ink during atomization and no viscosity study was performed at that time because the equipment was not available, and it was not within the scope of the project.

6.3 Preliminary Cell Culture on Aersol Jet Printed Collagen Type I and II

Preliminary cell culture was carried out on aerosol jet printed collagen type I and II scaffolds using human periosteum-derived cell in suspension plates at SBE in Gasthuisberg, however a number of issues prevented these experiments from generating any conclusive evidence. These issues were largely to do with sterility of the AJP collagen, physical manipulation of the AJP collagen scaffolds during culture, the cell population.

Contamination (the growth of mould on the scaffolds) was observed in a large number of samples after a prolonged storage (~3

months) of the AJP collagen in PBS at 4°C. The scaffolds had been washed in 70% ethanol before storage, but not in a biosafety cabinet. Hence, thereafter scaffolds were put through the full sterilization procedure used for cell culture, before placing the scaffolds in a sterile well-plate with sterile PBS and wrapping with parafilm for storage at 4°C. 70% ethanol was used to sterilize the AJP collagen scaffolds, however, a number of contamination events occurred during culture in preliminary experiments. The time allowed for incubation of the AJP collagen in the 70% ethanol was longer than that typically used in the lab, however, as pointed out in chapter 2, collagen does not readily absorb ethanol. Hence, the contamination could be attributed to an unsuitable sterilization method. Peracetic acid sterilization has been shown to be an effective sterilization method for collagen scaffolds with little impact on scaffolds [367]. However, the efficacy of any sterilization method should be considered device dependent, and therefore for a sterilization study would be recommended for future work.

It was originally thought that detaching the scaffolds from their substrates would be beneficial to the culture study since it could allow for cell seeding on both sides of the scaffold, however during culture of the AJP collagen scaffolds with hPdCs this caused a lot of issues. With the scaffolds now free to float around the wells and almost completely transparent, it was very difficult not to remove them when changing media. The use of the vacuum line with Pasteur pipettes was quickly abandoned after a number of scaffolds were sucked into the pipette. Even careful use of the manual micro-pipettes still led to damage of the scaffolds, since it was very difficult to locate the samples in the well and hence it was very difficult to avoid the scaffolds. For future cell culture study it would be recommended that the scaffolds be printed onto functionalized substrates to facilitate better adhesion of the scaffolds to the substrates throughout cell culture, and this would also be beneficial to nanoindentation.

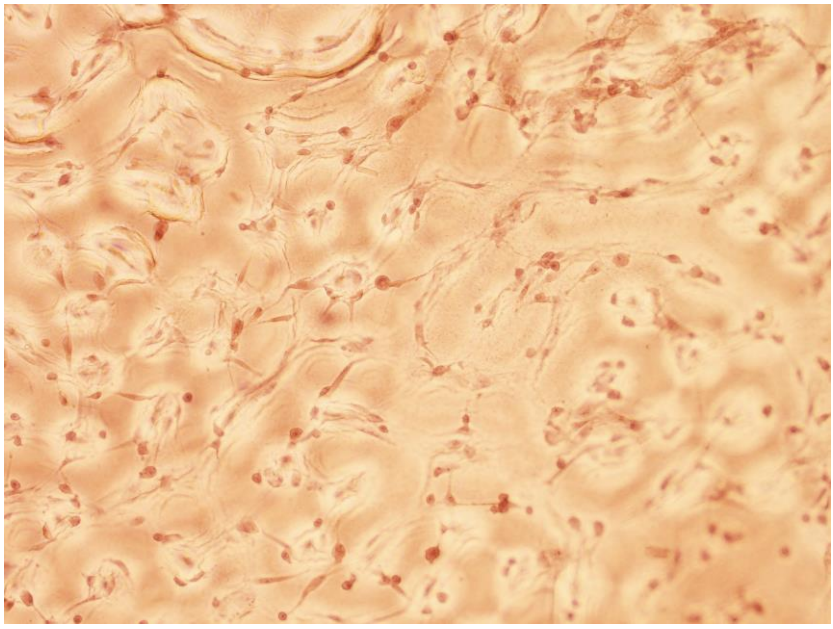

Figure 6-3. A H&E stained collagen type II 5.25 mm sample after 3 days of culture with 50,000 hPCs

An initial culture study with a mix of 4 mm and 5.25 mm collagen type I and II samples had to be terminated after contamination was observed in the batch of cells (surplus cells from a postdoc's study were used). Thereafter, all scaffolds were 5.25 mm collagen type I and II scaffolds identical to those in Chapter 4. The structural issues observed during neutralization and nanoindenation in these wider samples also arose during cell culture leading to some scaffold deterioration. However, this was not observed in the 4 mm samples which were incubated in culture medium for up to 4 weeks. This further suggests that the neutralization needs to be optimised for these wider samples. The 5.25 mm samples that remained at the time points of the study were very difficult to remove intact for embedding, and hence some that appeared thin were stained in the plate with hematoxylin & eosin imaged under the microscope, the result of which can be seen in Figure 6-3.

Unfortunately time constraints within the project did not allow for these observations to lead to a better study. Indeed, this study itself was rushed and bypassed steps normally taken in culturing a

new material, such as seeding optimization and sterilization procedure optimization, in the interest of time. Any future cell culture study using similar AJP collagen scaffolds will require time to be taken to optimize these procedures for this material before any investigation is done.

6.4 MATLAB® Code

6.4.1 Multi-layered circular sample toolpath generator

```
%%%
```

```
filename = input('Please give a name for the prg file: ', 's');

%% Write positions to prg file
% The resolution of the Optomec system (this should not be altered)
x_res = 4000;
y_res = 4000;

% Create new file
% file = fopen([folder '\' filename '.prg'],'w');
file = fopen([filename '.prg'],'w');

% Write header of the file
fprintf(file, '! ********************************\r\n');
fprintf(file, '! FID1 0,0\r\n');
fprintf(file, '! FID  END\r\n');
fprintf(file, '! Generated by: Simple Optomec file generator\r\n');
fprintf(file, '! Axes: XYZTR=XY---\r\n');
fprintf(file, '! Resolution: %i,%i,-,-,-\r\n', x_res, y_res);
fprintf(file, '! %s.prg\r\n', filename);
fprintf(file, '! ********************************\r\n');
fprintf(file, '\r\n');

while a2 < 360
% Calculate the hatch points
[ x_hatch, y_hatch ] = CircHatch_v1( D, x0, y0, ...
   tr_sp, deg2rad(a2));

    % Write hatch path;
    fprintf(file, '! %d layer \r\n',a2);
    writepos2prg_v1([x_hatch;y_hatch], file, x_res, y_res);

   a3 = a2 + 90;

   % Orthognal layer
   [ x_hatch, y_hatch ] = CircHatch_v1( D, x0, y0, ...
   tr_sp, deg2rad(a3));
   % Write hatch path
   fprintf(file, '! %d Orthogonal LAYER \r\n',a3);
   writepos2prg_v1([x_hatch;y_hatch], file, x_res, y_res);
```

```
    a2 = a2 + alpha;

end

% Stop program
fprintf(file, 'MSEG XY,7761,2076\r\n');
fprintf(file, 'STOP\r\n');

% Close file
fclose(file);

%% End message
disp('File creation finished!');
```

6.4.1.1 Write positions to file function

```
function [ output_args ] = writepos2prg_v1( A, file, x_res, y_res )
%UNTITLED2 Summary of this function goes here
%   Detailed explanation goes here

% Go to point fast travel
fprintf(file, 'ptp/e XY,%i,%i\r\n', round(A(1,1)*x_res),
round(A(2,1)*y_res));
% Open the shutter
fprintf(file, 'OUT0.0=1\r\n');
fprintf(file, 'wait 20\r\n');

% Write positions
fprintf(file, 'MSEG XY,%i,%i\r\n', round((A(1,1)*x_res)-5),
round((A(2,1)*y_res)-5));
for i = 2:length(A)
    fprintf(file, 'line XY,%d,%d\r\n', round(A(1,i)*x_res),
round(A(2,i)*y_res));
end

% End segmentation
fprintf(file, 'ENDS XY\r\n');
fprintf(file, 'till (^X_AST.#MOVE) & (^Y_AST.#MOVE)\r\n');
fprintf(file, 'OUT0.0=0\r\n');
fprintf(file, '\r\n');
```

```
end
```

6.4.1.2 Raster function

```
function [ x, y ] = CircHatch_v1( D, x0, y0, tr_sp, alpha)
   % Outside radius
   R_c = (D/2);

   % Determine the number of raster lines
   n = round((R_c*2)/tr_sp);
% Establish an array of zeros for vertices
% 2 vertices per line
   x = zeros(n*2,1);
   y = zeros(n*2,1);

   % Starting point for the hatch
   i = 1;
   y_sign = 1;
   x(i) = (n/2)*tr_sp;
   y(i) = sqrt(R_c^2-(x(i)^2));
   count = 2;

   i = i+1;
   x(i) = x(i-1);
   % Determine the direction of the line
   if count >= 2
      y_sign = -y_sign;
      count = 1;
   else
      count = count+1;
   end
   y(i) = y_sign * sqrt(R_c^2-(x(i)^2));

   while x(i)-tr_sp >= -R_c
%    for i = 3:2:n*2
      i = i+1;
      x(i) = x(i-2)-tr_sp;

      if count >= 2
         y_sign = -y_sign;
```

```
            count = 1;
        else
            count = count+1;
        end
        y(i) = y_sign * sqrt(R_c^2-(x(i)^2));

        i = i+1;
        x(i) = x(i-1);

        if count >= 2
            y_sign = -y_sign;
            count = 1;
        else
            count = count+1;
        end
        y(i) = y_sign * sqrt(R_c^2-(x(i)^2));
    end

    % Rotate hatch with rotation matrix
    A = [cos(alpha) , sin(alpha);...
      -sin(alpha) , cos(alpha)];

    B = A*[x';y'];
    x = B(1,:);
    y = B(2,:);

    % Move hatch
    x = x0+x;
    y = y0+
end
```

Bibliography

1. Langer, R.; Vacanti, J.P. Tissue Engineering. *Science (80-.).* **1993**, *260*, 920–926, doi:10.1205/0960308041614927.
2. George, J.H.S. Engineering of Fibrous Scaffolds for use in Regenerative Medicine, Imperial College London, 2009.
3. O'Brien, F.J. Biomaterials & scaffolds for tissue engineering. *Mater. Today* **2011**, *14*, 88–95, doi:10.1016/S1369-7021(11)70058-X.
4. Squillaro, T.; Peluso, G.; Galderisi, U. Clinical trials with mesenchymal stem cells: An update. *Cell Transplant.* **2016**, *25*, 829–848, doi:10.3727/096368915X689622.
5. Caplan, A.I. Mesenchymal stem cells: Time to change the name! *Stem Cells Transl. Med.* **2017**, *6*, 1445–1451, doi:10.1002/sctm.17-0051.
6. Lenza, R.F.S.; Vasconcelos, W.L.; Jones, J.R.; Hench, L.L. Surface-modified 3D scaffolds for tissue engineering. *J. Mater. Sci. Mater. Med.* **2002**, *13*, 837–842, doi:10.1023/A:1016592127407.
7. Frantz, C.; Stewart, K.M.; Weaver, V.M. The extracellular matrix at a glance. *J. Cell Sci.* **2010**, *123*, 4195–4200, doi:10.1242/jcs.023820.
8. Järveläinen, H.; Sainio, A.; Koulu, M.; Wight, T.N.; Penttinen, R. Extracellular Matrix Molecules: Potential Targets in Pharmacotherapy. *Pharmalogical Rev.* **2009**, *61*, 198–223, doi:10.1124/pr.109.001289.provided.
9. Fukuda, J.; Sakai, Y.; Nakazawa, K. Novel hepatocyte culture system developed using microfabrication and collagen/polyethylene glycol microcontact printing. *Biomaterials* **2006**, *27*, 1061–1070, doi:10.1016/j.biomaterials.2005.07.031.
10. De Silva, M.N.; Paulsen, J.; Renn, M.J.; Odde, D.J. Two-Step cell patterning on planar and complex curved surfaces by precision spraying of polymers. *Biotechnol. Bioeng.* **2006**, *93*, 919–927, doi:10.1002/bit.
11. Rammelt, S.; Illert, T.; Bierbaum, S.; Scharnweber, D.; Zwipp, H.; Schneiders, W. Coating of titanium implants with collagen, RGD peptide and chondroitin sulfate. *Biomaterials* **2006**, *27*, 5561–5571, doi:10.1016/j.biomaterials.2006.06.034.
12. Rye, C.; Wise, R.; Jurukovski, V.; Jean, D.; Choi, J.; Avissar, Y. *Biology*; 2017; ISBN 9781938168093.
13. Ferrara, N.; Gerber, H.P.; LeCouter, J. The biology of VEGF and its receptors. *Nat. Med.* **2003**, *9*, 669–676, doi:10.1038/nm0603-669.
14. Steward, A.J.; Kelly, D.J. Mechanical regulation of mesenchymal stem cell differentiation. *J. Anat.* **2015**, *227*, 717–731,

doi:10.1111/joa.12243.
15. Yamada, M.; Tanemura, K.; Okada, S.; Iwanami, A.; Nakamura, M.; Mizuno, H.; Ozawa, M.; Ohyama-Goto, R.; Kitamura, N.; Kawano, M.; et al. Electrical Stimulation Modulates Fate Determination of Differentiating Embryonic Stem Cells. *Stem Cells* **2007**, *25*, 562–570, doi:10.1634/stemcells.2006-0011.
16. Chan, Y.C.; Ting, S.; Lee, Y.K.; Ng, K.M.; Zhang, J.; Chen, Z.; Siu, C.W.; Oh, S.K.W.; Tse, H.F. Electrical stimulation promotes maturation of cardiomyocytes derived from human embryonic stem cells. *J. Cardiovasc. Transl. Res.* **2013**, *6*, 989–999, doi:10.1007/s12265-013-9510-z.
17. Costa, P.F.; Vaquette, C.; Baldwin, J.; Chhaya, M.; Gomes, M.E.; Reis, R.L.; Theodoropoulos, C.; Hutmacher, D.W. Biofabrication of customized bone grafts by combination of additive manufacturing and bioreactor knowhow. *Biofabrication* **2014**, *6*, 035006, doi:10.1088/1758-5082/6/3/035006.
18. Williams, D.F. On the nature of biomaterials. *Biomaterials* **2009**, *30*, 5897–5909, doi:10.1016/j.biomaterials.2009.07.027.
19. Burdick, J.A.; Mauck, R.L. *Biomaterials for Tissue Engineering Applications*; Springer-Verlag/Wien: Wien, 2011; ISBN 9783709103845.
20. Fidler, A.L.; Boudko, S.P.; Rokas, A.; Hudson, B.G. The triple helix of collagens - An ancient protein structure that enabled animal multicellularity and tissue evolution. *J. Cell Sci.* **2018**, *131*, doi:10.1242/jcs.203950.
21. Karsdal, M.A. Introduction. In *Biochemistry of Collagens, Laminins and Elastin: Structure, Function and Biomarkers*; Karsdal, M.A., Ed.; Elsevier Inc., 2016; pp. xix–xxxiv ISBN 9780128098998.
22. Exposito, J.Y.; Cluzel, C.; Garrone, R.; Lethias, C. Evolution of collagens. *Anat. Rec.* **2002**, *268*, 302–316, doi:10.1002/ar.10162.
23. Ignat'eva, N.Y.; Danilov, N.A.; Averkiev, S. V.; Obrezkova, M. V.; Lunin, V. V.; Sobol', E.N. Determination of hydroxyproline in tissues and the evaluation of the collagen content of the tissues. *J. Anal. Chem.* **2007**, *62*, 51–57, doi:10.1134/S106193480701011X.
24. Ricard-Blum, S. The Collagen Family. *Cold Spring Harb. Perspect. Biol.* **2011**, *3*, 1–19, doi:10.1101/cshperspect.a004978.
25. Xiao, J.; Sun, X.; Madhan, B.; Brodsky, B.; Baum, J. NMR studies demonstrate a unique AAB composition and chain register for a heterotrimeric type IV collagen model peptide containing a natural interruption site. *J. Biol. Chem.* **2015**, *290*, 24201–24209, doi:10.1074/jbc.M115.654871.
26. Bornstein, P.; Sage, H. Structurally Distinct Collagen Types. *Annu Rev Biochem* **1980**, *49*, 957–1003.

27. Fratzl, P. *Collagen: Structure and mechanics*; 2008; ISBN 9780387739052.
28. Sorushanova, A.; Delgado, L.M.; Wu, Z.; Shologu, N.; Kshirsagar, A.; Raghunath, R.; Mullen, A.M.; Bayon, Y.; Pandit, A.; Raghunath, M.; et al. The Collagen Suprafamily: From Biosynthesis to Advanced Biomaterial Development. *Adv. Mater.* **2018**, *1801651*, 1–39, doi:10.1002/adma.201801651.
29. Gordon, M.K.; Hahn, R.A. Collagens. *Cell Tissue Res.* **2010**, *339*, 247–257, doi:10.1007/s00441-009-0844-4.
30. Shaw, L.M.; Olsen, B.R. FACIT collagens: diverse molecular bridges in extracellular matrices. *Trends Biochem. Sci.* **1991**, *16*, 191–194.
31. Hulmes, D.J.S. Collagen diversity, synthesis and assembly. In *Collagen: Structure and Mechanics*; 2008; pp. 15–47 ISBN 9780387739052.
32. Lees, J.F.; Tasab, M.; Bulleid, N.J. Identification of the molecular recognition sequence which determines the type-specific assembly of procollagen. *EMBO J.* **1997**, *16*, 908–916, doi:10.1093/emboj/16.5.908.
33. Koide, T.; Nagata, K. Collagen biosynthesis. In *Topics in Current Chemistry*; 2005; Vol. 247, pp. 85–114 ISBN 3540232729.
34. Olsen, D.R.; Leigh, S.D.; Chang, R.; McMullin, H.; Ong, W.; Tai, E.; Chisholm, G.; Birk, D.E.; Berg, R.A.; Hitzeman, R.A.; et al. Production of Human Type I Collagen in Yeast Reveals Unexpected New Insights into the Molecular Assembly of Collagen Trimers. *J. Biol. Chem.* **2001**, *276*, 24038–24043, doi:10.1074/jbc.M101613200.
35. Rutschmann, C.; Baumann, S.; Cabalzar, J.; Luther, K.B.; Hennet, T. Recombinant expression of hydroxylated human collagen in Escherichia coli. *Appl. Microbiol. Biotechnol.* **2014**, *98*, 4445–4455, doi:10.1007/s00253-013-5447-z.
36. Myllyharju, J.; Kivirikko, K.I. Collagens, modifying enzymes and their mutations in humans, flies and worms. *Trends Genet.* **2004**, *20*, 33–43, doi:10.1016/j.tig.2003.11.004.
37. Capella-Monsonís, H.; Coentro, J.Q.; Graceffa, V.; Wu, Z.; Zeugolis, D.I. An experimental toolbox for characterization of mammalian collagen type I in biological specimens. *Nat. Protoc.* **2018**, *13*, 507–529, doi:10.1038/nprot.2017.117.
38. Weis, M.A.; Hudson, D.M.; Kim, L.; Scott, M.; Wu, J.J.; Eyre, D.R. Location of 3-Hydroxyproline residues in collagen types I, II, III, and V/XI implies a role in fibril supramolecular assembly. *J. Biol. Chem.* **2010**, *285*, 2580–2590, doi:10.1074/jbc.M109.068726.
39. Hudson, D.M.; Eyre, D.R. Collagen prolyl 3-hydroxylation: A major role for a minor post-translational modification? *Connect. Tissue Res.* **2013**, *54*, 245–251, doi:10.3109/03008207.2013.800867.

40. Cabral, W.A.; Perdivara, I.; Weis, M.A.; Terajima, M.; Blissett, A.R.; Chang, W.; Perosky, J.E.; Makareeva, E.N.; Mertz, E.L.; Leikin, S.; et al. Abnormal Type I Collagen Post-translational Modification and Crosslinking in a Cyclophilin B KO Mouse Model of Recessive Osteogenesis Imperfecta. *PLoS Genet.* **2014**, *10*, doi:10.1371/journal.pgen.1004465.
41. Makareeva, E.; Leikin, S. Procollagen triple helix assembly: An unconventional chaperone-assisted polding paradigm. *PLoS One* **2007**, *2*, doi:10.1371/journal.pone.0001029.
42. Nagai, N.; Hosokawa, M.; Itohara, S.; Adachi, E.; Matsushita, T.; Hosokawa, N.; Nagata, K. Embryonic lethality of molecular chaperone Hsp47 knockout mice is associated with defects in collagen biosynthesis. *J. Cell Biol.* **2000**, *150*, 1499–1505, doi:10.1083/jcb.150.6.1499.
43. Canty, E.G.; Kadler, K.E. Procollagen trafficking, processing and fibrillogenesis. *J. Cell Sci.* **2005**, *118*, 1341–1353, doi:10.1242/jcs.01731.
44. Romanic, A.M.; Adachi, E.; Kadler, K.E.; Hojima, Y.; Prockop, D.J. Copolymerization of pNcollagen III and Collagen I. *J. Biol. Chem.* **1991**, *266*, 12703–12709.
45. Kadler, K.E.; Holmes, D.F.; Trotter, J.A.; Chapman, J.A. Collagen fibril formation. *Biochem. J.* **1996**, *316*, 1–11, doi:10.1042/bj3160001.
46. Trelstad, R.L.; Hayashi, K.; Gross, J. Collagen fibrillogenesis: intermediate aggregates and suprafibrillar order. *Proc. Natl. Acad. Sci.* **1976**, *73*, 4027–4031, doi:10.1073/pnas.73.11.4027.
47. Orgel, J.P.R.O.; Irving, T.C.; Miller, A.; Wess, T.J. Microfibrillar structure of type I collagen in situ. *Proc. Natl. Acad. Sci. U. S. A.* **2006**, *103*, 9001–9005, doi:10.1073/pnas.0502718103.
48. Eyre, D.R.; Weis, M.A.; Hudson, D.M.; Wu, J.J.; Kim, L. A novel 3-hydroxyproline (3Hyp)-rich motif marks the triple-helical C terminus of tendon type I collagen. *J. Biol. Chem.* **2011**, *286*, 7732–7736, doi:10.1074/jbc.C110.195768.
49. Canty, E.G.; Lu, Y.; Meadows, R.S.; Shaw, M.K.; Holmes, D.F.; Kadler, K.E. Coalignment of plasma membrane channels and protrusions (fibropositors) specifies the parallelism of tendon. *J. Cell Biol.* **2004**, *165*, 553–563, doi:10.1083/jcb.200312071.
50. Kadler, K.E.; Hill, A.; Canty-Laird, E.G. Collagen fibrillogenesis: fibronectin, integrins, and minor collagens as organizers and nucleators. *Curr. Opin. Cell Biol.* **2008**, *20*, 495–501, doi:10.1016/j.ceb.2008.06.008.
51. Wenstrup, R.J.; Florer, J.B.; Brunskill, E.W.; Bell, S.M.; Chervoneva, I.; Birk, D.E. Type V collagen controls the initiation of collagen fibril assembly. *J. Biol. Chem.* **2004**, *279*, 53331–53337,

doi:10.1074/jbc.M409622200.
52. Fernandes, R.J.; Weis, M.A.; Scott, M.A.; Seegmiller, R.E.; Eyre, D.R. Collagen XI chain misassembly in cartilage of the chondrodysplasia (cho) mouse. *Matrix Biol.* **2007**, *26*, 597–603, doi:10.1016/j.matbio.2007.06.007.
53. Canelón, S.P.; Wallace, J.M. β-Aminopropionitrile-induced reduction in enzymatic crosslinking causes in vitro changes in collagen morphology and molecular composition. *PLoS One* **2016**, *11*, 1–13, doi:10.1371/journal.pone.0166392.
54. Li, Y.; Asadi, A.; Monroe, M.R.; Douglas, E.P. pH effects on collagen fibrillogenesis in vitro: Electrostatic interactions and phosphate binding. *Mater. Sci. Eng. C* **2009**, *29*, 1643–1649, doi:10.1016/j.msec.2009.01.001.
55. Gobeaux, F.; Mosser, G.; Anglo, A.; Panine, P.; Davidson, P.; Giraud-Guille, M.M.; Belamie, E. Fibrillogenesis in Dense Collagen Solutions: A Physicochemical Study. *J. Mol. Biol.* **2008**, *376*, 1509–1522, doi:10.1016/j.jmb.2007.12.047.
56. Highberger, J.H. The iso-electric point of collagen. *J. Am. Chem. Soc.* **1939**, *61*, 2302–2303, doi:10.1021/ja01422a025.
57. Hattori, S.; Adachi, E.; Ebihara, T.; Shirai, T.; Someki, I.; Irie, S. Alkali-Treated the Ligand Collagen Activity Retained the Triple Helical Conformation and the Ligand Activity for the Cell Adhesion via α2β1 Integrin. *J. Biochem.* **1999**, *125*, 676–684, doi:10.1093/oxfordjournals.jbchem.a022336.
58. Xie, J.; Bao, M.; Bruekers, S.M.C.; Huck, W.T.S. Collagen Gels with Different Fibrillar Microarchitectures Elicit Different Cellular Responses. *ACS Appl. Mater. Interfaces* **2017**, *9*, 19630–19637, doi:10.1021/acsami.7b03883.
59. Harris, J.R.; Soliakov, A.; Lewis, R.J. In vitro fibrillogenesis of collagen type I in varying ionic and pH conditions. *Micron* **2013**, *49*, 60–68, doi:10.1016/j.micron.2013.03.004.
60. Mertz, E.L.; Leikin, S. Interactions of inorganic phosphate and sulfate anions with collagen. *Biochemistry* **2004**, *43*, 14901–14912, doi:10.1021/bi048788b.
61. Muyonga, J.H.; Cole, C.G.B.; Duodu, K.G. Characterisation of acid soluble collagen from skins of young and adult Nile perch (Lates niloticus). *Food Chem.* **2004**, *85*, 81–89, doi:10.1016/j.foodchem.2003.06.006.
62. Chinitz, J.L.; Yokoyama, T.; Bower, R.; Swartz, C. Self-sealing prosthesis for arteriovenous fistula in man. *Trans. Am. Soc. Artif. Intern. Organs* **1972**, *18*, 452–455.
63. Charriere, G.; Bejot, M.; Schnitzler, L.; Ville, G.; Hartmann, D.J. Reactions to a bovine collagen implant: Clinical and immunologic

study in 705 patients. *J. Am. Acad. Dermatol.* **1989**, *21*, 1203–1208, doi:10.1016/S0190-9622(89)70330-3.
64. Chou, D.B.; Frismantas, V.; Milton, Y.; David, R.; Pop-Damkov, P.; Ferguson, D.; MacDonald, A.; Vargel Bölükbaşı, Ö.; Joyce, C.E.; Moreira Teixeira, L.S.; et al. On-chip recapitulation of clinical bone marrow toxicities and patient-specific pathophysiology. *Nat. Biomed. Eng.* **2020**, *4*, 394–406, doi:10.1038/s41551-019-0495-z.
65. Andrée, B.; Ichanti, H.; Kalies, S.; Heisterkamp, A.; Strauß, S.; Vogt, P.M.; Haverich, A.; Hilfiker, A. Formation of three-dimensional tubular endothelial cell networks under defined serum-free cell culture conditions in human collagen hydrogels. *Sci. Rep.* **2019**, *9*, 1–11, doi:10.1038/s41598-019-41985-6.
66. Vuorela, A.; Myllyharju, J.; Nissi, R.; Pihlajaniemi, T.; Kivirikko, K.I. Assembly of human prolyl 4-hydroxylase and type III collagen in the yeast Pichia pastoris: formation of a stable enzyme tetramer requires coexpression with collagen and assembly of a stable collagen requires coexpression with prolyl 4-hydroxylase. *EMBO J.* **1997**, *16*, 6702–6712, doi:10.1093/emboj/16.22.6702.
67. Stein, H.; Wilensky, M.; Tsafrir, Y.; Rosenthal, M.; Amir, R.; Avraham, T.; Ofir, K.; Dgany, O.; Yayon, A.; Shoseyov, O. Production of bioactive, post-translationally modified, heterotrimeric, human recombinant type-I collagen in transgenic tobacco. *Biomacromolecules* **2009**, *10*, 2640–2645, doi:10.1021/bm900571b.
68. Rohrbach, M.; Giunta, C. Recessive osteogenesis imperfecta: Clinical, radiological, and molecular findings. *Am. J. Med. Genet. Part C Semin. Med. Genet.* **2012**, *160 C*, 175–189, doi:10.1002/ajmg.c.31334.
69. Hart, G.J.; Russell, A.E.; Cooper, D.R. The effects of certain glycols, substituted glycols and related organic solvents on the thermal stability of soluble collagen. *Biochem. J.* **1971**, *125*, 599–604, doi:10.1042/bj1250599.
70. Penkova, R.; Goshev, I.; Gorinstein, S.; Nedkov, P. Stabilizing effect of glycerol on collagen type I isolated from different species. *Food Chem.* **1999**, *66*, 483–487, doi:10.1016/S0308-8146(99)00097-7.
71. Kivirikki, K.I.; Pihlajaniemi, T. Synthesis fo human procollagens and collagens in recombinant DNA systems 1997, 1–91.
72. Vuorela, A.; Myllyharju, J.; Pihlajaniemi, T.; Kivirikko, K.I. Coexpression with collagen markedly increases the half-life of the recombinant human prolyl 4-hydroxylase tetramer in the yeast Pichia pastoris. *Matrix Biol.* **1999**, *18*, 519–522, doi:10.1016/S0945-053X(99)00040-2.
73. Myllyharju, J.; Nokelainen, M.; Vuorela, A.; Kivirikko, K.I. Expression of recombinant human type I-III collagens in the yeast Pichia

pastoris. *Biochem. Soc. Trans.* **2000**, *28*, 353–357, doi:10.1042/bst0280353.
74. Nokelainen, M.; Tu, H.; Vuorela, A.; Notbohm, H.; Kivirikko, K.I.; Myllyharju, J. High-level production of human type I collagen in the yeast Pichia pastoris. *Yeast* **2001**, *18*, 797–806, doi:10.1002/yea.730.
75. Fagerholm, P.; Lagali, N.S.; Ong, J.A.; Merrett, K.; Jackson, W.B.; Polarek, J.W.; Suuronen, E.J.; Liu, Y.; Brunette, I.; Griffith, M. Stable corneal regeneration four years after implantation of a cell-free recombinant human collagen scaffold. *Biomaterials* **2014**, *35*, 2420–2427, doi:10.1016/j.biomaterials.2013.11.079.
76. Farkash, U.; Avisar, E.; Volk, I.; Slevin, O.; Shohat, N.; El Haj, M.; Dolev, E.; Ashraf, E.; Luria, S. First clinical experience with a new injectable recombinant human collagen scaffold combined with autologous platelet-rich plasma for the treatment of lateral epicondylar tendinopathy (tennis elbow). *J. Shoulder Elb. Surg.* **2019**, *28*, 503–509, doi:10.1016/j.jse.2018.09.007.
77. Iacopi, E.; Banchellini, E.; Riitano, N.; Abbruzzese, L.; Goretti, C.; Piaggesi, A. Pilot trial of plant-derived recombinant type I human collagen in healing post-surgical diabetic foot wounds. *Diabet. Foot J.* **2020**, *23*, 30–36.
78. Browne, S.; Zeugolis, D.I.; Pandit, A. Collagen: Finding a Solution for the Source. *Tissue Eng. Part A* **2013**, *19*, 1491–1494, doi:10.1089/ten.tea.2012.0721.
79. Tal, Y. Collplant Biotechnologies press release 18-02-2021 2021.
80. Eyre, D.R.; Paz, M.A.; Gallop, P.M. Cross-linking in collagen and elastin. *Annu. Rev. Biochem.* **1983**, *VOL. 53*, 717–748, doi:10.1146/annurev.biochem.53.1.717.
81. Gautieri, A.; Passini, F.S.; Silván, U.; Guizar-Sicairos, M.; Carimati, G.; Volpi, P.; Moretti, M.; Schoenhuber, H.; Redaelli, A.; Berli, M.; et al. Advanced glycation end-products: Mechanics of aged collagen from molecule to tissue. *Matrix Biol.* **2017**, *59*, 95–108, doi:10.1016/j.matbio.2016.09.001.
82. Sanami, M.; Sweeney, I.; Shtein, Z.; Meirovich, S.; Sorushanova, A.; Mullen, A.M.; Miraftab, M.; Shoseyov, O.; O'Dowd, C.; Pandit, A.; et al. The influence of poly(ethylene glycol) ether tetrasuccinimidyl glutarate on the structural, physical, and biological properties of collagen fibers. *J. Biomed. Mater. Res. - Part B Appl. Biomater.* **2016**, *104*, 914–922, doi:10.1002/jbm.b.33445.
83. Grabarek, Z.; Gergely, J. Zero-Length Crosslinking Procedure with the Use of Active Esters. *Anal. Biochem.* **1990**, *185*, 131–135, doi:10.1016/0003-2697(90)90267-D.
84. van Luyn, M.J.A.; van Wachem, P.B.; Damink, L.H.H.O.; Dijkstra, P.J.;

Feijen, J.; Nieuwenhuis, P. Secondary cytotoxicity of cross-linked dermal sheep collagens during repeated exposure to human fibroblasts. *Biomaterials* **1992**, *13*, 1017–1024, doi:10.1016/0142-9612(92)90153-F.

85. Gough, J.E.; Scotchford, C.A.; Downes, S. Cytotoxicity of glutaraldehyde crosslinked collagen/poly(vinyl alcohol) films is by the mechanism of apoptosis. *J. Biomed. Mater. Res.* **2002**, *61*, 121–130, doi:10.1002/jbm.10145.
86. Sallent, I.; Capella-Monsonís, H.; Zeugolis, D.I. Chapter 3 - Production and Characterization of Chemically Cross-linked Collagen Scaffolds. In *Collagen: Methods and Protocols*; Sagi, I., Afratis, N.A., Eds.; Springer Science & Business Media, 2019; Vol. 1944, pp. 23–38 ISBN 9781493990955.
87. ThermoFisher: EDC/NHS reaction scheme Available online: https://www.thermofisher.com/be/en/home/life-science/protein-biology/protein-biology-learning-center/protein-biology-resource-library/pierce-protein-methods/carbodiimide-crosslinker-chemistry.html.
88. Geggel, H.S.; Friend, J.; Thoft, R.A. Collagen gel for ocular surface. *Investig. Ophthalmol. Vis. Sci.* **1985**, *26*, 901–905.
89. Fritz, M.; Belcher, A.M.; Radmachert, M.; Walterst, D.A.; Hansmat, P.K.; Stuckyt, G.D.; Morse, D.E.; Mann, S. Flat pearls from biofabrication of organized composites on inorganic substrates. *Nature* **1994**, *371*, 49–51.
90. Schröder, H.C.; Wang, X.; Tremel, W.; Ushijima, H.; Müller, W.E.G. Biofabrication of biosilica-glass by living organisms. *Nat. Prod. Rep.* **2008**, *25*, 455–474, doi:10.1039/b612515h.
91. Wu, L.Q.; Payne, G.F. Biofabrication: Using biological materials and biocatalysts to construct nanostructured assemblies. *Trends Biotechnol.* **2004**, *22*, 593–599, doi:10.1016/j.tibtech.2004.09.008.
92. Groll, J.; Boland, T.; Blunk, T.; Burdick, J.A.; Cho, D.W.; Dalton, P.D.; Derby, B.; Forgacs, G.; Li, Q.; Mironov, V.A.; et al. Biofabrication : reappraising the definition of an evolving field. *Biofabrication* **2016**, *8*.
93. Moroni, L.; Boland, T.; Burdick, J.A.; De Maria, C.; Derby, B.; Forgacs, G.; Groll, J.; Li, Q.; Malda, J.; Mironov, V.A.; et al. Biofabrication: A Guide to Technology and Terminology. *Trends Biotechnol.* **2018**, *36*, 384–402, doi:10.1016/j.tibtech.2017.10.015.
94. Mironov, V.; Reis, N.; Derby, B. Bioprinting : A Beginning. *Tissue Eng.* **2006**, *12*.
95. Guillemot, F.; Mironov, V.; Nakamura, M. Bioprinting is coming of age: Report from the International Conference on Bioprinting and Biofabrication in Bordeaux (3B'09). *Biofabrication* **2010**, *2*,

doi:10.1088/1758-5082/2/1/010201.
96. Groll, J.; Burdick, J.A.; Cho, D.; Derby, B.; Gelinsky, M.; Heilshorn, S.C.; Jüngst, T.; Malda, J.; Mironov, V.A.; Nakayama, K.; et al. A definition of bioinks and their distinction from biomaterial inks. *Biofabrication* **2019**, *11*, doi:10.1088/1758-5090/aaec52.
97. Klebe, R.J. Cytoscribing: A method for micropositioning cells and the construction of two- and three-dimensional synthetic tissues. *Exp. Cell Res.* **1988**, *179*, 362–373, doi:10.1016/0014-4827(88)90275-3.
98. Wilson, W.C.; Boland, T. Cell and organ printing 1: Protein and cell printers. *Anat. Rec. - Part A Discov. Mol. Cell. Evol. Biol.* **2003**, *272*, 491–496, doi:10.1002/ar.a.10057.
99. Sun, W.; Starly, B.; Daly, A.C.; Burdick, J.A.; Groll, J.; Skeldon, G.; Shu, W.; Sakai, Y.; Shinohara, M.; Nishikawa, M.; et al. The bioprinting roadmap. *Biofabrication* **2020**, *12*, doi:10.1088/1758-5090/ab5158.
100. Foty, R. A simple hanging drop cell culture protocol for generation of 3D spheroids. *J. Vis. Exp.* **2011**, 2–6, doi:10.3791/2720.
101. Wu, Z.; Su, X.; Xu, Y.; Kong, B.; Sun, W.; Mi, S. Bioprinting three-dimensional cell-laden tissue constructs with controllable degradation. *Sci. Rep.* **2016**, *6*, doi:10.1038/srep24474.
102. Ahlfeld, T.; Cidonio, G.; Kilian, D.; Duin, S.; Akkineni, A.R.; Dawson, J.I.; Yang, S.; Lode, A.; Oreffo, R.O.C.; Gelinsky, M. Development of a clay based bioink for 3D cell printing for skeletal application. *Biofabrication* **2017**, *9*, doi:10.1088/1758-5090/aa7e96.
103. Mandrycky, C.; Wang, Z.; Kim, K.; Kim, D.H. 3D bioprinting for engineering complex tissues. *Biotechnol. Adv.* **2016**, *34*, 422–434, doi:10.1016/j.biotechadv.2015.12.011.
104. Pepper, M.E.; Seshadri, V.; Burg, T.C.; Burg, K.J.L.; Groff, R.E. Characterizing the effects of cell settling on bioprinter output. *Biofabrication* **2012**, *4*, doi:10.1088/1758-5082/4/1/011001.
105. Inzana, J.A.; Olvera, D.; Fuller, S.M.; Kelly, J.P.; Graeve, O.A.; Schwarz, E.M.; Kates, S.L.; Awad, H.A. 3D printing of composite calcium phosphate and collagen scaffolds for bone regeneration. *Biomaterials* **2014**, *35*, 4026–4034, doi:10.1016/j.biomaterials.2014.01.064.
106. Tse, C.C.W.; Smith, P.J. Inkjet Printing for Biomedical Applications. In *Cell-Based Microarrays: Methods and Protocols*; Ertl, P., Rothbauer, M., Eds.; Springer New York: New York, NY, 2018; pp. 107–117 ISBN 978-1-4939-7792-5.
107. Fairbanks, B.D.; Schwartz, M.P.; Bowman, C.N.; Anseth, K.S. Photoinitiated polymerization of PEG-diacrylate with lithium phenyl-2,4,6-trimethylbenzoylphosphinate: polymerization rate and cytocompatibility. *Biomaterials* **2009**, *30*, 6702–6707,

doi:10.1016/j.biomaterials.2009.08.055.
108. Lin, H.; Zhang, D.; Alexander, P.G.; Yang, G.; Tan, J.; Cheng, A.W.M.; Tuan, R.S. Application of visible light-based projection stereolithography for live cell-scaffold fabrication with designed architecture. *Biomaterials* **2013**, *34*, 331–339, doi:10.1016/j.biomaterials.2012.09.048.
109. Kim, S.H.; Yeon, Y.K.; Lee, J.M.; Chao, J.R.; Lee, Y.J.; Seo, Y.B.; Sultan, M.T.; Lee, O.J.; Lee, J.S.; Yoon, S. Il; et al. Precisely printable and biocompatible silk fibroin bioink for digital light processing 3D printing. *Nat. Commun.* **2018**, *9*, doi:10.1038/s41467-018-03759-y.
110. Koch, L.; Deiwick, A.; Franke, A.; Schwanke, K.; Haverich, A.; Zweigerdt, R.; Chichkov, B. Laser bioprinting of human induced pluripotent stem cells — the effect of printing and biomaterials on cell survival , pluripotency, and differentiation. *Biofabrication* **2018**, *10*, 035005, doi:10.1088/1758-5090/aab981.
111. Koch, L.; Deiwick, A.; Schlie, S.; Michael, S.; Gruene, M.; Coger, V.; Zychlinski, D.; Schambach, A.; Reimers, K.; Vogt, P.M.; et al. Skin tissue generation by laser cell printing. *Biotechnol. Bioeng.* **2012**, *109*, 1855–1863, doi:10.1002/bit.24455.
112. Sorkio, A.; Koch, L.; Koivusalo, L.; Deiwick, A.; Miettinen, S.; Chichkov, B.; Skottman, H. Human stem cell based corneal tissue mimicking structures using laser-assisted 3D bioprinting and functional bioinks. *Biomaterials* **2018**, *171*, 57–71, doi:10.1016/j.biomaterials.2018.04.034.
113. Odde, D.J.; Renn, M.J. Laser-guided direct writing for applications in biotechnology. *Trends Biotechnol.* **1999**, *17*, 385–389, doi:10.1016/S0167-7799(99)01355-4.
114. Odde, D.J.; Renn, M.J. Laser-guided direct writing of living cells. *Biotechnol. Bioeng.* **2000**, *67*, 312–318, doi:10.1002/(SICI)1097-0290(20000205)67:3<312::AID-BIT7>3.0.CO;2-F.
115. Nahmias, Y.; Odde, D.J. Micropatterning of living cells by laser-guided direct writing: Application to fabrication of hepatic-endothelial sinusoid-like structures. *Nat. Protoc.* **2006**, *1*, 2288–2296, doi:10.1038/nprot.2006.386.
116. Daly, A.C.; Kelly, D.J. Biofabrication of spatially organised tissues by directing the growth of cellular spheroids within 3D printed polymeric microchambers. *Biomaterials* **2019**, *197*, 194–206, doi:10.1016/j.biomaterials.2018.12.028.
117. Mette, A.; Richter, P.L.; Horteis, M.; Glunz, S.W. Metal Aerosol Jet Printing for Solar Cell Metallization. *Prog. Photovoltaics Res. Appl.* **2007**, *15*, 621–627, doi:10.1002/pip.
118. Grunwald, I.; Groth, E.; Wirth, I.; Schumacher, J.; Maiwald, M.; Zoellmer, V.; Busse, M. Surface biofunctionalization and production

of miniaturized sensor structures using aerosol printing technologies. *Biofabrication* **2010**, *2*, 014106, doi:10.1088/1758-5082/2/1/014106.
119. Williams, N.X.; Watson, N.; Joh, D.Y.; Chilkoti, A.; Franklin, A.D. Aerosol jet printing of biological inks by ultrasonic delivery. *Biofabrication* **2019**, *12*, 025004, doi:10.1016/j.procbio.2006.09.007.
120. Xiao, Y.; Kalaitzidou, K.; Yao, D.; Yeo, W.H.; Harris, T.A.L. Challenges and Advances in Aerosol Jet Printing of Regenerated Silk Fibroin Solutions. *Adv. Mater. Interfaces* **2020**, *7*, 1902005, doi:10.1002/admi.201902005.
121. Smith, M.; Choi, Y.S.; Boughey, C.; Kar-narayan, S. Controlling and assessing the quality of aerosol jet printed features for large area and flexible electronics. *Flex. Print. Electron.* **2017**, *2*, 015004.
122. Khng, C.; Osher, R.H. Evaluation of the relationship between corneal diameter and lens diameter. *J. Cataract Refract. Surg.* **2008**, *34*, 475–479, doi:10.1016/j.jcrs.2007.10.043.
123. Gonzalez-Andrades, M.; Argüeso, P.; Gipson, I. Corneal Anatomy. **2019**, 3–12, doi:10.1007/978-3-030-01304-2_1.
124. Gharaee, H.; Abrishami, M.; Shafiee, M.; Ehsaei, A. White-to-white corneal diameter: Normal values in healthy Iranian population obtained with the Orbscan II. *Int. J. Ophthalmol.* **2014**, *7*, 309–312, doi:10.3980/j.issn.2222-3959.2014.02.20.
125. Doughty, M.J.; Jonuscheit, S. An assessment of regional differences in corneal thickness in normal human eyes, using the Orbscan II or ultrasound pachymetry. *Optometry* **2007**, *78*, 181–190, doi:10.1016/j.optm.2006.08.018.
126. Luo, L.; Liu, Z.; Chen, J.; Xiao, Q.; Zhang, M.; Chen, L.; Jiang, A. Normal human keratocyte density and corneal thickness by confocal microscopy in vivo. *Chinese Ophthalmic Res.* **2004**, *22*, 512–515.
127. Kohlhaas, M.; Boehm, A.G.; Spoerl, E.; Pürsten, A.; Grein, H.J.; Pillunat, L.E. Effect of central corneal thickness, corneal curvature, and axial length on applanation tonometry. *Arch. Ophthalmol.* **2006**, *124*, 471–476, doi:10.1001/archopht.124.4.471.
128. Vojniković, B.; Gabrić, N.; Dekaris, I.; Jurić, B. Curvature analyses of the corneal front and back surface. *Coll. Antropol.* **2013**, *37*, 93–96.
129. Delmonte, D.W.; Kim, T. Anatomy and physiology of the cornea. *J Cataract Refract Surg* **2011**, *37*, 588–598, doi:10.1016/j.jcrs.2010.12.037.
130. Farjo, A.A.; Brumm, M. V.; Soong, H.K. Corneal Anatomy, Physiology, and Wound Healing. In *Ophthalmology*; 2018; pp. 163–168.
131. Hanna, C.; Bicknell, D.S.; O'brien, J.E. Cell Turnover in the Adult

Human Eye. *Arch. Ophthalmol.* **1961**, *65*, 695–698, doi:10.1001/archopht.1961.01840020697016.
132. Schimmelpfennig, B. Nerve structures in human central corneal epithelium. *Graefe's Arch. Clin. Exp. Ophthalmol.* **1982**, *218*, 14–20, doi:10.1007/BF02134093.
133. Hart, R.W.; Farrell, R.A. Light scattering in the cornea. *J. Opt. Soc. Am.* **1969**, *59*, 766–774, doi:10.1364/JOSA.59.000766.
134. Meek, K.M. Corneal collagen-its role in maintaining corneal shape and transparency. *Biophys. Rev.* **2009**, *1*, 83–93, doi:10.1007/s12551-009-0011-x.
135. Meek, K.M.; Knupp, C. Corneal structure and transparency. *Prog. Retin. Eye Res.* **2015**, *49*, 1–16, doi:10.1016/j.preteyeres.2015.07.001.
136. Boote, C.; Hayes, S.; Young, R.D.; Kamma-Lorger, C.S.; Hocking, P.M.; Elsheikh, A.; Inglehearn, C.F.; Ali, M.; Meek, K.M. Ultrastructural changes in the retinopathy, globe enlarged (rge) chick cornea. *J. Struct. Biol.* **2009**, *166*, 195–204, doi:10.1016/j.jsb.2009.01.009.
137. Branch, M.J.; Hashmani, K.; Dhillon, P.; Jones, D.R.E.; Dua, H.S.; Hopkinson, A. Mesenchymal stem cells in the human corneal limbal stroma. *Investig. Ophthalmol. Vis. Sci.* **2012**, *53*, 5109–5116, doi:10.1167/iovs.11-8673.
138. Müller, L.J.; Pels, L.; De Wolf, A.; Kliffen, M.; Vrensen, G.F.J.M. Ultrastructural analysis of human corneal nerves. *Investig. Ophthalmol. Vis. Sci.* **1996**, *37*.
139. Jester, J. V.; Petroll, W.M.; Cavanagh, H.D. Corneal stromal wound healing in refractive surgery: The role of myofibroblasts. *Prog. Retin. Eye Res.* **1999**, *18*, 311–356, doi:10.1016/S1350-9462(98)00021-4.
140. Stiemke, M.M.; Edelhauser, H.F.; Geroski, D.H. The developing corneal endothelium: Correlation of morphology, hydration and na/k ATPase pump site density. *Curr. Eye Res.* **1991**, *10*, 145–156, doi:10.3109/02713689109001742.
141. Barker, C.F.; Billingham, R.E. Immunologically privileged sites. *Adv. Immunol.* **1978**, *25*, 1–54, doi:10.1002/9780470719985.ch6.
142. Streilein, J.W. Ocular immune privilege: Therapeutic opportunities from an experiment of nature. *Nat. Rev. Immunol.* **2003**, *3*, 879–889, doi:10.1038/nri1224.
143. Hori, J.; Yamaguchi, T.; Keino, H.; Hamrah, P.; Maruyama, K. Immune privilege in corneal transplantation. *Prog. Retin. Eye Res.* **2019**, *71*, 100758, doi:10.1016/j.preteyeres.2012.08.002.
144. Kinoshita, S.; Koizumi, N.; Ueno, M.; Okumura, N.; Imai, K.; Tanaka, H.; Yamamoto, Y.; Nakamura, T.; Inatomi, T.; Bush, J.; et al. Injection of Cultured Cells with a ROCK Inhibitor for Bullous Keratopathy. *N.*

Engl. J. Med. **2018**, *378*, 995–1003, doi:10.1056/NEJMoa1712770.
145. Patel, S.; Marshall, J.; Fitzke, F.W. Refractive index of the human corneal epithelium and stroma. *J. Refract. Surg.* **1995**, *11*, 100–105, doi:10.3928/1081-597x-19950301-09.
146. Leonard, D.W.; Meek, K.M. Refractive indices of the collagen fibrils and extrafibrillar material of the corneal stroma. *Biophys. J.* **1997**, *72*, 1382–1387, doi:10.1016/S0006-3495(97)78784-8.
147. Beems, E.M.; Van Best, J.A. Light transmission of the cornea in whole human eyes. *Exp. Eye Res.* **1990**, *50*, 393–395, doi:10.1016/0014-4835(90)90140-P.
148. van Best, J.A.; Bollemeijer, J.G.; Sterk, C.C. Corneal transmission in whole human eyes. *Exp. Eye Res.* **1988**, *46*, 765–768, doi:10.1016/S0014-4835(88)80062-9.
149. SAID, F.S.; WEALE, R.A. The variation with age of the spectral transmissivity of the living human crystalline lens. *Gerontologia* **1959**, *3*, 213–231, doi:10.1159/000210900.
150. Boettner, E.A.; Wolter, J.R. Transmission of the Ocular Media. *Invest. Ophthalmol. Vis. Sci.* **1962**, *1*, 776–783.
151. Freegard, T.J. The physical basis of transparency of the normal cornea. *Eye* **1997**, *11*, 465–471, doi:10.1038/eye.1997.127.
152. Young, R.W. Solar radiation and age-related macular degeneration. *Surv. Ophthalmol.* **1988**, *32*, 252–269, doi:10.1016/0039-6257(88)90174-9.
153. Wu, J.; Seregard, S.; Spångberg, B.; Oskarsson, M.; Chen, E. Blue light induced apoptosis in rat retina. *Eye* **1999**, *13*, 577–583, doi:10.1038/eye.1999.142.
154. Boote, C.; Dennis, S.; Huang, Y.; Quantock, A.J.; Meek, K.M. Lamellar orientation in human cornea in relation to mechanical properties. *J. Struct. Biol.* **2005**, *149*, 1–6, doi:10.1016/j.jsb.2004.08.009.
155. Orssengo, G.J.; Pye, D.C. Determination of the true intraocular pressure and modulus of elasticity of the human cornea in vivo. *Bull. Math. Biol.* **1999**, *61*, 551–572, doi:10.1006/bulm.1999.0102.
156. Shavkuta, B.S.; Gerasimov, M.Y.; Minaev, N. V.; Kuznetsova, D.S.; Dudenkova, V. V.; Mushkova, I.A.; Malyugin, B.E.; Kotova, S.L.; Timashev, P.S.; Kostenev, S. V.; et al. Highly effective 525 nm femtosecond laser crosslinking of collagen and strengthening of a human donor cornea. *Laser Phys. Lett.* **2018**, *15*, 015602, doi:10.1088/1612-202X/aa963b.
157. Hamilton, K.E.; Pye, D.C. Young's modulus in normal corneas and the effect on applanation tonometry. *Optom. Vis. Sci.* **2008**, *85*, 445–450, doi:10.1097/OPX.0b013e3181783a70.
158. Cartwright, N.E.K.; Tyrer, J.R.; Marshall, J. Age-related differences in the elasticity of the human cornea. *Investig. Ophthalmol. Vis. Sci.*

2011, *52*, 4324–4329, doi:10.1167/iovs.09-4798.
159. Hjortdal, J. Regional elastic performance of the human cornea. *J. Biomech.* **1996**, *29*, 931–942, doi:10.1016/0021-9290(95)00152-2.
160. Jue, B.; Maurice, D.M. The mechanical properties of the rabbit and human cornea. *J. Biomech.* **1986**, *19*, 847–853, doi:10.1016/0021-9290(86)90135-1.
161. Dias, J.M.; Ziebarth, N.M. Anterior and posterior corneal stroma elasticity assessed using nanoindentation. *Exp. Eye Res.* **2013**, *115*, 41–46, doi:10.1016/j.exer.2013.06.004.
162. Matsuda, M.; Ubels, J.L.; Edelhauser, H.F. A larger corneal epithelial wound closes at a faster rate. *Investig. Ophthalmol. Vis. Sci.* **1985**, *26*, 897–900.
163. Tandon, A.; Tovey, J.C.K.; Sharma, A.; Gupta, R.; Mohan, R.R. Role of Transforming Growth Factor Beta in Corneal Function, Biology and Pathology. *Curr. Mol. Med.* **2012**, *10*, 565–578, doi:10.2174/156652410792231286.
164. Barrientez, B.; Nicholas, S.E.; Whelchel, A.; Sharif, R.; Hjortdal, J.; Karamichos, D. Corneal injury: Clinical and molecular aspects. *Exp. Eye Res.* **2019**, *186*, 1–13, doi:10.1016/j.exer.2019.107709.
165. Chaurasia, S.; Lim, R.; Lakshminarayanan, R.; Mohan, R. Nanomedicine Approaches for Corneal Diseases. *J. Funct. Biomater.* **2015**, *6*, 277–298, doi:10.3390/jfb6020277.
166. Rabinowitz, Y.S. Keratoconus. *Surv. Ophthalmol.* **1998**, *42*, 297–319, doi:10.1016/S0039-6257(97)00119-7.
167. Rabinowitz, Y.S. The genetics of keratoconus. *Ophthalmol. Clin. North Am.* **2003**, *16*, 607–620, doi:10.1016/S0896-1549(03)00099-3.
168. Brown, S.E.; Simmasalam, R.; Antonova, N.; Gadaria, N.; Asbell, P.A. Progression in keratoconus and the effect of corneal cross-linking on progression. *Eye Contact Lens* **2014**, *40*, 331–338, doi:10.1097/ICL.0000000000000085.
169. Elhalis, H.; Azizi, B.; Jurkunas, U. V. Fuchs endothelial corneal dystrophy. *Ocul. Surf.* **2010**, *8*, 173–184, doi:10.1016/S1542-0124(12)70232-X.
170. Bourcier, T.; Thomas, F.; Borderie, V.; Chaumeil, C.; Laroche, L. Bacterial keratitis: Predisposing factors, clinical and microbiological review of 300 cases. *Br. J. Ophthalmol.* **2003**, *87*, 834–838, doi:10.1136/bjo.87.7.834.
171. Wessel, J.M.; Bachmann, B.O.; Meiller, R.; Kruse, F.E. Fungal interface keratitis by Candida orthopsilosis following deep anterior lamellar keratoplasty. *BMJ Case Rep.* **2013**, 1–4, doi:10.1136/bcr-2012-008361.
172. Bourne, R.R.A.; Flaxman, S.R.; Braithwaite, T.; Cicinelli, M. V; Das, A.; Jonas, J.B.; Keeffe, J.; Kempen, J.H.; Leasher, J.; Limburg, H.; et al.

Magnitude, temporal trends, and projections of the global prevalence of blindness and distance and near vision impairment: a systematic review and meta-analysis. *Lancet Glob Heal.* **2017**, *5*, 888–897, doi:10.1016/S2214-109X(17)30293-0.
173. WHO Global Data on Visual Impairment. *Glob. Data Vis. Impair. 2010* **2010**, 17.
174. Kuper, H.; Polack, S.; Eusebio, C.; Mathenge, W.; Wadud, Z.; Foster, A. A Case-Control Study to Assess the Relationship between Poverty and Visual Impairment from Cataract in Kenya, the Philippines, and Bangladesh. *PLoS Med.* **2008**, *5*, e244, doi:10.1371/journal.pmed.0050244.
175. Whitcher, J.P.; Srinivasan, M.; Upadhyay, M.P. Corneal blindness : a global perspective. *Bull. World Heal. Organ.* **2001**, *79*, 214–221.
176. Gain, P.; Jullienne, R.; He, Z.; Aldossary, M.; Acquart, S.; Cognasse, F.; Thuret, G. Global survey of corneal transplantation and eye banking. *JAMA Ophthalmol.* **2016**, *134*, 167–173, doi:10.1001/jamaophthalmol.2015.4776.
177. Jeng, B.H. Preserving the cornea: Corneal storage media. *Curr. Opin. Ophthalmol.* **2006**, *17*, 332–337, doi:10.1097/01.icu.0000233950.63853.88.
178. Rocon, P.C.; Ribeiro, L.P.; Scárdua, R.F.; De Almeida, A. V; Gomes, L.M.; Azeredo, H.C.; Piras, C.; Paro, F.M. Main Causes of Nonfulfillment of Corneal Donation in Five Hospitals of a Brazilian State. *Transplant. Proc.* **2013**, *45*, 1038–1042, doi:10.1016/j.transproceed.2013.02.008.
179. Freitas, L.; Rocon, P.; de Almeida, A.; Erlacher, R.; Paro, F.; Santo, E.; Pró-Vidas Transplantes, A. Corneal donor profile and evolution of corneal donation in a Brazilian state where the number of individuals on the waiting list reached zero but increased again. *Transplant. Proc.* **2018**, *50*, 509–512, doi:10.1016/j.transproceed.2017.12.053.
180. Wright, B.; Griffith, M.; Merrett, K.; Connon Editors, C.J. Corneal Regenerative Medicine Methods and Protocols Methods in Molecular Biology 1014.
181. Williams, K.A.; Esterman, A.J.; Bartlett, C.; Holland, H.; Hornsby, N.B.; Coster, D.J. How effective is penetrating corneal transplantation? Factors influencing long-term outcome in multivariate analysis. *Transplantation* **2006**, *81*, 896–901, doi:10.1097/01.tp.0000185197.37824.35.
182. Barraquer, R.I.; Pareja-Aricò, L.; Gómez-Benlloch, A.; Michael, R. Risk factors for graft failure after penetrating keratoplasty. *Medicine (Baltimore).* **2019**, *98*, 1–8, doi:10.1097/MD.0000000000015274.
183. Kang, J.J.; Allemann, N.; Vajaranant, T.; de la Cruz, J.; Cortina, M.S.

Anterior segment optical coherence tomography for the quantitative evaluation of the anterior segment following Boston keratoprosthesis. *PLoS One* **2013**, *8*, doi:10.1371/journal.pone.0070673.
184. Ong, J.A.; Auvinet, E.; Forget, K.J.; Lagali, N.; Fagerholm, P.; Griffith, M.; Meunier, J.; Brunette, I. 3D corneal shape after implantation of a biosynthetic corneal stromal substitute. *Investig. Ophthalmol. Vis. Sci.* **2016**, *57*, 2355–2365, doi:10.1167/iovs.15-18271.
185. Shimmura, S.; Tsubota, K. Deep anterior lamellar keratoplasty. *Curr. Opin. Ophthalmol.* **2006**, *17*, 349–355, doi:10.1097/01.icu.0000233953.09595.91.
186. Hos, D.; Matthaei, M.; Bock, F.; Maruyama, K.; Notara, M.; Clahsen, T.; Hou, Y.; Le, V.N.H.; Salabarria, A.C.; Horstmann, J.; et al. Immune reactions after modern lamellar (DALK, DSAEK, DMEK) versus conventional penetrating corneal transplantation. *Prog. Retin. Eye Res.* 2019, *73*, 100768.
187. Sarnicola, V.; Toro, P.; Sarnicola, C.; Sarnicola, E.; Ruggiero, A. Long-term graft survival in deep anterior lamellar keratoplasty. *Cornea* **2012**, *31*, 621–626, doi:10.1097/ICO.0b013e31823d0412.
188. Heindl, L.M.; Riss, S.; Adler, W.; Bucher, F.; Hos, D.; Cursiefen, C. Split cornea transplantation: relationship between storage time of split donor tissue and outcome. *Ophthalmology* **2013**, *120*, 899–907, doi:10.1016/j.ophtha.2012.11.012.
189. Heindl, L.M.; Cursiefen, C. One cornea, two patients: A potential new strategy for tackling donor shortage? *Expert Rev. Ophthalmol.* **2011**, *6*, 273–276, doi:10.1586/eop.11.30.
190. Heindl, L.M.; Riss, S.; Bachmann, B.O.; Laaser, K.; Kruse, F.E.; Cursiefen, C. Split cornea transplantation for 2 recipients: A new strategy to reduce corneal tissue cost and shortage. *Ophthalmology* **2011**, *118*, 294–301, doi:10.1016/j.ophtha.2010.05.025.
191. Jirásková, N.; Rozsival, P.; Burova, M.; Kalfertova, M. AlphaCor artificial cornea: Clinical outcome. *Eye* **2011**, *25*, 1138–1146, doi:10.1038/eye.2011.122.
192. Gomaa, A.; Comyn, O.; Liu, C. Keratoprostheses in clinical practice - a review. *Clin. Exp. Ophthalmol.* **2010**, *38*, 211–224, doi:10.1111/j.1442-9071.2010.02231.x.
193. Liu, W.; Merrett, K.; Griffith, M.; Fagerholm, P.; Dravida, S.; Heyne, B.; Scaiano, J.C.; Watsky, M.A.; Shinozaki, N.; Lagali, N.; et al. Recombinant human collagen for tissue engineered corneal substitutes. *Biomaterials* **2008**, *29*, 1147–1158, doi:10.1016/j.biomaterials.2007.11.011.
194. Liu, Y.; Gan, L.; Carlsson, D.J.; Fagerholm, P.; Lagali, N.; Watsky, M.A.; Munger, R.; Hodge, W.G.; Priest, D.; Griffith, M. A simple,

cross-linked collagen tissue substitute for corneal implantation. *Investig. Ophthalmol. Vis. Sci.* **2006**, *47*, 1869–1875, doi:10.1167/iovs.05-1339.
195. Merrett, K.; Fagerholm, P.; McLaughlin, C.R.; Dravida, S.; Lagali, N.; Shinozaki, N.; Watsky, M.A.; Munger, R.; Kato, Y.; Li, F.; et al. Tissue-engineered recombinant human collagen-based corneal substitutes for implantation: Performance of type I versus type III collagen. *Investig. Ophthalmol. Vis. Sci.* **2008**, *49*, 3887–3894, doi:10.1167/iovs.07-1348.
196. Fagerholm, P.; Lagali, N.S.; Carlsson, D.J.; Merrett, K.; Griffith, M. Corneal Regeneration Following Implantation of a Biomimetic Tissue-Engineered Substitute. *Clin. Transl. Sci.* **2009**, *2*, 162–164, doi:10.1111/j.1752-8062.2008.00083.x.
197. Kozak Ljunggren, M.; Elizondo, R.A.; Edin, E.; Olsen, D.; Merrett, K.; Lee, C.-J.; Salerud, O.; Polarek, J.; Fagerholm, P.; Griffith, M. Effect of Surgical Technique on Corneal Implant Performance. *Transl. Vis. Sci. Technol.* **2014**, *3*, doi:10.1167/tvst.3.2.6.
198. Fagerholm, P.; Lagali, N.S.; Merrett, K.; Jackson, W.B.; Munger, R.; Liu, Y.; Polarek, J.W.; Söderqvist, M.; Griffith, M. A biosynthetic alternative to human donor tissue for inducing corneal regeneration: 24-Month follow-up of a phase 1 clinical study. *Sci. Transl. Med.* **2010**, *2*, 46–61, doi:10.1126/scitranslmed.3001022.
199. Durr, G.M.; Auvinet, E.; Ong, J.; Meunier, J.; Brunette, I. Corneal shape, volume, and interocular symmetry: Parameters to optimize the design of biosynthetic corneal substitutes. *Investig. Ophthalmol. Vis. Sci.* **2015**, *56*, 4275–4282, doi:10.1167/iovs.15-16710.
200. Krishnan, Y.; Grodzinsky, A.J. Cartilage diseases. *Matrix Biol.* **2018**, *71–72*, 51–69, doi:10.1016/j.matbio.2018.05.005.
201. Fujihara, Y.; Takato, T.; Hoshi, K. Immunological response to tissue-engineered cartilage derived from auricular chondrocytes and a PLLA scaffold in transgenic mice. *Biomaterials* **2010**, *31*, 1227–1234, doi:10.1016/j.biomaterials.2009.10.053.
202. Arzi, B.; Duraine, G.D.; Lee, C.A.; Huey, D.J.; Borjesson, D.L.; Murphy, B.G.; Hu, J.C.Y.; Baumgarth, N.; Athanasiou, K.A. Cartilage immunoprivilege depends on donor source and lesion location. *Acta Biomater.* **2015**, *23*, 72–81, doi:10.1016/j.actbio.2015.05.025.
203. Wachsmuth, L.; Söder, S.; Fan, Z.; Finger, F.; Aigner, T. Immunolocalization of matrix proteins in different human cartilage subtypes. *Histol. Histopathol.* **2006**, *21*, 477–485, doi:10.14670/HH-21.477.
204. Eyre, D. Collagen of articular cartilage. *Arthritis Res.* **2002**, *4*, 30–35, doi:10.1186/ar380.
205. Mansour, J.M. Biomechanics of cartilage. In *Kinesiology: The*

Mechanics and Pathomechanics of Human Movement; Oatis, C.A., Ed.; Lippincott Williams & Wilkins: Baltimore, 2013; pp. 69–83 ISBN 9781469837574.
206. Alford, J.W.; Cole, B.J. Cartilage restoration, part 1: Basic science, historical perspective, patient evaluation, and treatment options. *Am. J. Sports Med.* **2005**, *33*, 295–306, doi:10.1177/0363546504273510.
207. Ng, L.; Grodzinsky, A.J.; Patwari, P.; Sandy, J.; Plaas, A.; Ortiz, C. Individual cartilage aggrecan macromolecules and their constituent glycosaminoglycans visualized via atomic force microscopy. *J. Struct. Biol.* **2003**, *143*, 242–257, doi:10.1016/j.jsb.2003.08.006.
208. Teshima, R.; Otsuka, T.; Takasu, N.; Yamagata, N.; Yamamoto, K. Structure of the superficial layer of articular cartilage. *J. Bone Jt. Surg.* **1995**, *77-B*, 460–464.
209. Buckwalter, J.A.; Mankin, H.J.; Grodzinsky, A.J. Articular cartilage and osteoarthritis. *AAOS Instr. Course Lect.* 2005, *54*, 466–480.
210. Kronenberg, H.M. Developmental regulation of the growth plate. *Nature* **2003**, *423*.
211. Thielen, N.G.M.; van der Kraan, P.M.; van Caam, A.P.M. TGFb/BMP signaling pathway in cartilage homeostasis. *Cells* **2019**, *8*, 969.
212. Hunter, W. VI. On the structure and diseases of articular cartilages. *Philos. Trans. R. Soc.* **1743**, *45*, 514–521, doi:10.1098/rstl.1742.0079.
213. Curl, W.W.; Krome, J.; Gordon, E.S.; Rushing, J.; Smith, B.P.; Poehling, G.G. Cartilage injuries: A review of 31,516 knee arthroscopies. *Arthroscopy* **1997**, *13*, 456–460, doi:10.1016/S0749-8063(97)90124-9.
214. Insall, J. The Pridie debridement operation of osteoartritis of the knee. *Clin. Orthop. Relat. Res.* **1974**, *101*, 61–67.
215. Johnson, L.L. Arthroscopic abrasion arthroplasty: A review. *Clin. Orthop. Relat. Res.* **2001**, doi:10.1097/00003086-200110001-00028.
216. Steadman, J.R.; Rodkey, W.G.; Rodrigo, J.J. Microfracture: Surgical Technique and Rehabilitation to Treat Chondral Defects. *Clin. Orthop. Relat. Res.* **2001**, 362–369.
217. Woolf, A.D.; Pfleger, B. Burden of major musculoskeletal conditions. *Bull. World Heal. Organ.* **2003**, *81*, 646–656, doi:10.2143/EJCS.11.0.2029488.
218. Brown, T.D.; Johnston, R.C.; Saltzman, C.L.; Marsh, J.L.; Buckwalter, J.A. Posttraumatic osteoarthritis: A first estimate of incidence, prevalence, and burden of disease. *J. Orthop. Trauma* **2006**, *20*, 739–744, doi:10.1097/01.bot.0000246468.80635.ef.
219. Mow, V.C.; Kuei, S.C.; Lai, W.M.; Armstrong, C.G. Biphasic creep and stress relaxation of articular cartilage in compression: Theory and

experiments. *J. Biomech. Eng.* **1980**, *102*, 73–84, doi:10.1115/1.3138202.
220. Lai, W.M.; Hou, J.S.; Mow, V.C. A triphasic theory for the swelling and deformation behaviors of articular cartilage. *J. Biomech. Eng.* **1991**, *113*, 245–258, doi:10.1115/1.2894880.
221. Brittberg, M.; Lindahl, A.; Nilsson, A.; Ohlsson, C.; Isaksson, O.; Peterson, L. Treatment of deep cartilage defects in the knee with autologous chondrocyte transplantation. *New English J. Med.* **1994**, *331*, 889–895, doi:10.1056/NEJM199410063311401.
222. Darling, E.M.; Athanasiou, K.A. Rapid phenotypic changes in passaged articular chondrocyte subpopulations. *J. Orthop. Res.* **2005**, *23*, 425–432, doi:10.1016/j.orthres.2004.08.008.
223. Saris, D.B.F.; Vanlauwe, J.; Victor, J.; Almqvist, K.F.; Verdonk, R.; Bellemans, J.; Luyten, F.P. Treatment of Symptomatic Cartilage Defects of the Knee: Characterized Chondrocyte Implantation Results in Better Clinical Outcome at 36 Months in a Randomized Trial Compared to Microfracture. *Am. J. Sports Med.* **2009**, *37*, 10S-19S, doi:10.1177/0363546509350694.
224. Abou-El-Enein, M.; Elsanhoury, A.; Reinke, P. Overcoming Challenges Facing Advanced Therapies in the EU Market. *Cell Stem Cell* **2016**, *19*, 293–297, doi:10.1016/j.stem.2016.08.012.
225. Volz, M.; Schaumburger, J.; Frick, H.; Grifka, J.; Anders, S. A randomized controlled trial demonstrating sustained benefit of Autologous Matrix-Induced Chondrogenesis over microfracture at five years. *Int. Orthop.* **2017**, *41*, 797–804, doi:10.1007/s00264-016-3391-0.
226. Brittberg, M.; Recker, D.; Ilgenfritz, J.; Saris, D.B.F. Matrix-Applied Characterized Autologous Cultured Chondrocytes Versus Microfracture: Five-Year Follow-up of a Prospective Randomized Trial. *Am. J. Sports Med.* **2018**, *46*, 1343–1351, doi:10.1177/0363546518756976.
227. Crawford, D.C.; Deberardino, T.M.; Williams, R.J. NeoCart, an autologous cartilage tissue implant, compared with microfracture for treatment of distal femoral cartilage lesions. *J. Bone Jt. Surg.* **2012**, *94*, 979–989.
228. Medvedeva, E. V.; Grebenik, E.A.; Gornostaeva, S.N.; Telpuhov, V.I.; Lychagin, A. V.; Timashev, P.S.; Chagin, A.S. Repair of damaged articular cartilage: Current approaches and future directions. *Int. J. Mol. Sci.* **2018**, *19*, doi:10.3390/ijms19082366.
229. Lim, H.C.; Park, Y.B.; Ha, C.W.; Cole, B.J.; Lee, B.K.; Jeong, H.J.; Kim, M.K.; Bin, S. Il; Choi, C.H.; Choi, C.H.; et al. Allogeneic Umbilical Cord Blood–Derived Mesenchymal Stem Cell Implantation Versus Microfracture for Large, Full-Thickness Cartilage Defects in Older

Patients: A Multicenter Randomized Clinical Trial and Extended 5-Year Clinical Follow-up. *Orthop. J. Sport. Med.* **2021**, *9*, 1–15, doi:10.1177/2325967120973052.
230. Park, Y.-B.; Ha, C.-W.; Lee, C.-H.; Yoon, Y.C.; Park, Y.-G. Cartilage Regeneration in Osteoarthritic Patients by a Composite of Allogeneic Umbilical Cord Blood-Derived Mesenchymal Stem Cells and Hyaluronate Hydrogel: Results from a Clinical Trial for Safety and Proof-of-Concept with 7 Years of Extended Follow-Up. *Stem Cells Transl. Med.* **2017**, *6*, 613–621, doi:10.5966/sctm.2016-0157.
231. Bax, D. V.; Davidenko, N.; Hamaia, S.W.; Farndale, R.W.; Best, S.M.; Cameron, R.E. Impact of UV- and carbodiimide-based crosslinking on the integrin-binding properties of collagen-based materials. *Acta Biomater.* **2019**, *100*, 280–291, doi:10.1016/j.actbio.2019.09.046.
232. Moutos, F.T.; Freed, L.E.; Guilak, F. A biomimetic three-dimensional woven composite scaffold for functional tissue engineering of cartilage. *Nat. Mater.* **2007**, *6*, 162–167, doi:10.1038/nmat1822.
233. Xu, T.; Binder, K.W.; Albanna, M.Z.; Dice, D.; Zhao, W.; Yoo, J.J.; Atala, A. Hybrid printing of mechanically and biologically improved constructs for cartilage tissue engineering applications. *Biofabrication* **2013**, *5*, doi:10.1088/1758-5082/5/1/015001.
234. Brown, T.D.; Dalton, P.D.; Hutmacher, D.W. Direct writing by way of melt electrospinning. *Adv. Mater.* **2011**, *23*, 5651–5657, doi:10.1002/adma.201103482.
235. Visser, J.; Melchels, F.P.W.; Jeon, J.E.; Van Bussel, E.M.; Kimpton, L.S.; Byrne, H.M.; Dhert, W.J.A.; Dalton, P.D.; Hutmacher, D.W.; Malda, J. Reinforcement of hydrogels using three-dimensionally printed microfibres. *Nat. Commun.* **2015**, *6*, 1–10, doi:10.1038/ncomms7933.
236. Schipani, R.; Scheurer, S.; Florentin, R.; Critchley, S.E.; Kelly, D.J. Reinforcing interpenetrating network hydrogels with 3D printed polymer networks to engineer cartilage mimetic composites. *Biofabrication* **2020**, *12*, doi:10.1088/1758-5090/ab8708.
237. Woodruff, M.A.; Hutmacher, D.W. The return of a forgotten polymer - Polycaprolactone in the 21st century. *Prog. Polym. Sci.* **2010**, *35*, 1217–1256, doi:10.1016/j.progpolymsci.2010.04.002.
238. Woodward, S.C.; Brewer, P.S.; Moatamed, F.; Schindler, A.; Pitt, C.G. The intracellular degradation of poly(ε-caprolactone). *J. Biomed. Mater. Res.* **1985**, *19*, 437–444, doi:10.1002/jbm.820190408.
239. Boucher, O.; Randall, D.; Artaxo, P.; Bretherton, C.; Feingold, G.; Forster, P.; Kerminen, V.-M.; Kondo, Y.; Liao, H.; Lohmann, U.; et al. Clouds and aerosols. In *Climate Change 2013 the Physical Science Basis: Working Group I Contribution to the Fifth Assessment Report of the Intergovernmental Panel on Climate Change*; Cambridge

University Press: Cambridge, 2013; Vol. 9781107057, pp. 571–658 ISBN 9781107415324.
240. Evangeliou, N.; Grythe, H.; Klimont, Z.; Heyes, C.; Eckhardt, S.; Lopez-Aparicio, S.; Stohl, A. Atmospheric transport is a major pathway of microplastics to remote regions. *Nat. Commun.* **2020**, *11*, doi:10.1038/s41467-020-17201-9.
241. Vohra, K.; Vodonos, A.; Schwartz, J.; Marais, E.A.; Sulprizio, M.P.; Mickley, L.J. Global mortality from outdoor fine particle pollution generated by fossil fuel combustion: Results from GEOS-Chem. *Environ. Res.* **2021**, *195*, 110754, doi:10.1016/j.envres.2021.110754.
242. Lazaridis, M.; Colbeck, I. 1. Introduction. In *Aerosol Science: Technology and Applications*; Colbeck, I., Lazaridis, M., Eds.; John Wiley & Sons Ltd.: Chichester, UK, 2014; Vol. 9781119977, pp. 1–14 ISBN 9781118682555.
243. Bzdek, B.R.; Reid, J.P.; Cotterell, M.I. Open questions on the physical properties of aerosols. *Commun. Chem.* **2020**, *3*, 105, doi:10.1038/s42004-020-00342-9.
244. Yan, X.; Bain, R.M.; Cooks, R.G. Organic Reactions in Microdroplets: Reaction Acceleration Revealed by Mass Spectrometry. *Angew. Chemie - Int. Ed.* **2016**, *55*, 12960–12972, doi:10.1002/anie.201602270.
245. Renn, M.J.; King, B.H.; Essien, M.; Hunter, L.J. Apparatuses and method for maskless mesoscale material deposition 2006.
246. Optomec - Aerosol Jet Technology webpage Available online: https://optomec.com/printed-electronics/aerosol-jet-technology/ (accessed on Jun 7, 2021).
247. May, K.R.; Clifford, R. The impaction of aerosol particles on cylinders, spheres, ribbons and discs. *Ann. Occup. Hyg.* **1967**, *10*, 83–95, doi:10.1093/annhyg/10.2.83.
248. Tafoya, R.R.; Secor, E.B. Understanding and mitigating process drift in aerosol jet printing. *Flex. Print. Electron.* **2020**, *5*, doi:10.1088/2058-8585/ab6e74.
249. Salary, R.; Lombardi, J.P.; Tootooni, M.; Donovan, R.; Rao, P.; Borgesen, P.; Poliks, M.D. Computational Fluid Dynamics Modeling and Online Monitoring of Aerosol Jet Printing Process. *J. Manuf. Sci. Eng.* **2017**, *139*, 021015, doi:10.1115/1.4034591.
250. Secor, E.B. Principles of aerosol jet printing. *Flex. Print. Electron.* **2018**, *3*, 035002, doi:10.1088/2058-8585/aace28.
251. Saleh, M.S.; Hu, C.; Panat, R. Three-dimensional microarchitected materials and devices using nanoparticle assembly by pointwise spatial printing. *Sci. Adv.* **2017**, *3*, doi:10.1126/sciadv.1601986.
252. Mahajan, A.; Frisbie, C.D.; Francis, L.F. Optimization of aerosol jet printing for high-resolution, high-aspect ratio silver lines. *ACS Appl.*

Mater. Interfaces **2013**, *5*, 4856–4864, doi:10.1021/am400606y.
253. Binder, S.; Glatthaar, M.; Rädlein, E. Analytical investigation of aerosol jet printing. *Aerosol Sci. Technol.* 2014, *48*, 924–929.
254. Secor, E.B. Light scattering measurements to support real-time monitoring and closed-loop control of aerosol jet printing. *Addit. Manuf.* **2021**, *44*, 102028, doi:10.1016/j.addma.2021.102028.
255. Secor, E.B. Guided ink and process design for aerosol jet printing based on annular drying effects. *Flex. Print. Electron* **2018**, *3*, 035007, doi:10.1088/2058-8585/aadffd.
256. Jain, R.K.; Au, P.; Tam, J.; Duda, D.G.; Fukumura, D. Engineering vascularized tissue. *Nat. Biotechnol.* **2005**, *23*, 821–823, doi:10.1038/nbt0705-821.
257. Gershlak, J.R.; Hernandez, S.; Fontana, G.; Perreault, L.R.; Hansen, K.J.; Larson, S.A.; Binder, B.Y.K.; Dolivo, D.M.; Yang, T.; Dominko, T.; et al. Crossing kingdoms: Using decellularized plants as perfusable tissue engineering scaffolds. *Biomaterials* **2017**, *125*, 13–22, doi:10.1016/j.biomaterials.2017.02.011.
258. Dunstan, A.E.; Thole, F.B. CLXXV. - The Relation between Viscosity and Chemical Constitution. Part IV. Viscosity and Hydration in Solution. *J. Chem. Soc. Trans.* **1909**, *95*, 1556–1561.
259. Koshimizu, N.; Bessho, M.; Suzuki, S.; Yuguchi, Y.; Kitamura, S.; Hara, M. Gamma-Crosslinked Collagen Gel without Fibrils: Analysis of Structure and Heat Stability. *Biosci. Biotechnol. Biochem.* **2014**, *73*, 1915–1921, doi:10.1271/bbb.80771.
260. Zeugolis, D.I.; Paul, R.G.; Attenburrow, G. Extruded collagen-polyethylene glycol fibers for tissue engineering applications. *J. Biomed. Mater. Res. - Part B Appl. Biomater.* **2008**, *85*, 343–352, doi:10.1002/jbm.b.30952.
261. Delgado, L.M.; Shologu, N.; Fuller, K.; Zeugolis, D.I. Acetic acid and pepsin result in high yield, high purity and low macrophage response collagen for biomedical applications. *Biomed. Mater.* **2017**, *12*, doi:10.1088/1748-605X/aa838d.
262. Sorushanova, A.; Skoufos, I.; Tzora, A.; Mullen, A.M.; Zeugolis, D.I. The influence of animal species, gender and tissue on the structural, biophysical, biochemical and biological properties of collagen sponges. *J. Mater. Sci. Mater. Med.* **2021**, *32*, doi:10.1007/s10856-020-06485-4.
263. Buttafoco, L.; Engbers-Buijtenhuijs, P.; Root, A.A.; Dijkstra, P.J.; Daamen, W.F.; Van Kuppeveit, T.H.; Vermes, I.; Feijen, J. First steps towards tissue engineering of small-diameter blood vessels: preparation of flat scaffolds of collagen and elastin by means of freeze drying. *J. Biomed. Mater. Res. - Part B Appl. Biomater.* **2006**, *77*, 357–368, doi:10.1002/jbm.b.30444.

264. Nam, K.; Kimura, T.; Kishida, A. Controlling coupling reaction of EDC and NHS for preparation of collagen gels using ethanol/water co-solvents. *Macromol. Biosci.* **2008**, *8*, 32–37, doi:10.1002/mabi.200700206.
265. Rabotyagova, O.S.; Cebe, P.; Kaplan, D.L. Collagen structural hierarchy and susceptibility to degradation by ultraviolet radiation. *Mater. Sci. Eng. C* **2008**, *28*, 1420–1429, doi:10.1016/j.msec.2008.03.012.
266. Muyonga, J.H.; Cole, C.G.B.; Duodu, K.G. Fourier transform infrared (FTIR) spectroscopic study of acid soluble collagen and gelatin from skins and bones of young and adult Nile perch (Lates niloticus). *Food Chem.* **2004**, *86*, 325–332, doi:10.1016/j.foodchem.2003.09.038.
267. W. Fries; Lee, G. Basic thermoanalytical studies of insoluble collagen matrices. *Biomaterials* **1996**, *17*, 2289–2294, doi:10.1016/0142-9612(96)00047-6.
268. De Campos Vidal, B.; Mello, M.L.S.; Luiza, M.; Mello, S. Collagen type I amide I band infrared spectroscopy. *Micron* **2011**, *42*, 283–289, doi:10.1016/j.micron.2010.09.010.
269. Belbachir, K.; Noreen, R.; Gouspillou, G.; Petibois, C. Collagen types analysis and differentiation by FTIR spectroscopy. *Anal. Bioanal. Chem.* **2009**, *395*, 829–837, doi:10.1007/s00216-009-3019-y.
270. Chavan, D.; Van De Watering, T.C.; Gruca, G.; Rector, J.H.; Heeck, K.; Slaman, M.; Iannuzzi, D. Ferrule-top nanoindenter: An optomechanical fiber sensor for nanoindentation. *Rev. Sci. Instrum.* **2012**, *83*, doi:10.1063/1.4766959.
271. Hertz, H. *Miscellaneous Papers*; Lenard, P., Jones, D.E., Schott, G.A., Eds.; Macmillan & Co. Ltd.: London, 1896;
272. Oliver, W.C.; Pharr, G.M. An improved technique for determining hardness and elastic modulus using load and displacement sensing indentation experiments. *J. Mater. Res.* **1992**, *7*, 1564–1583.
273. Oliver, W.C.; Pharr, G.M. Measurement of hardness and elastic modulus by instrumented indentation: Advances in understanding and refinements to methodology. *J. Mater. Res.* **2004**, *19*, 3–20, doi:10.1557/jmr.2004.19.1.3.
274. Pathak, S.; Kalidindi, S.R.; Klemenz, C.; Orlovskaya, N. Analyzing indentation stress-strain response of LaGaO3 single crystals using spherical indenters. *J. Eur. Ceram. Soc.* **2008**, *28*, 2213–2220, doi:10.1016/j.jeurceramsoc.2008.02.009.
275. Fernandes, L.L.; Resende, C.X.; Tavares, D.S.; Soares, G.A.; Castro, L.O.; Granjeiro, J.M. Cytocompatibility of chitosan and collagen-chitosan scaffolds for tissue engineering. *Polimeros* **2011**, *21*, 1–6, doi:10.1590/S0104-14282011005000008.
276. Manning, M.C. Use of infrared spectroscopy to monitor protein

structure and stability. *Expert Rev. Proteomics* **2005**, *2*, 731–743, doi:10.1586/14789450.2.5.731.
277. Jackson, M.; Mantsch, H.H. The use and misuse of FTIR spectroscopy in the determination of protein structure. *Crit. Rev. Biochem. Mol. Biol.* **1995**, *30*, 95–120, doi:10.3109/10409239509085140.
278. Zeugolis, D.I.; Raghunath, M. The physiological relevance of wet versus dry differential scanning calorimetry for biomaterial evaluation: A technical note. *Polym. Int.* **2010**, *59*, 1403–1407, doi:10.1002/pi.2882.
279. Friess, W.; Lee, G. Basic thermoanalytical studies of insoluble collagen matrices. *Biomaterials* **1996**, *17*, 2289–2294, doi:10.1016/0142-9612(96)00047-6.
280. Deegan, R.D.; Bakajin, O.; Dupont, T.F.; Huber, G.; Nagel, S.R.; Witten, T.A. Capillary flow as the cause of ring stains from dried liquid drops. *Nature* **1997**, *389*, 827–829.
281. Seitz, B.; Langenbucher, A.; Küchle, M.; Naumann, G.O.H. Impact of Graft Diameter on Corneal Power and the Regularity of Postkeratoplasty Astigmatism before and after Suture Removal. *Ophthalmology* **2003**, *110*, 2162–2167, doi:10.1016/S0161-6420(03)00659-6.
282. Li, C.; Zhao, G.Q.; Che, C.Y.; Lin, J.; Li, N.; Jia, W.Y.; Zhang, Q.Q.; Jiang, N.; Hu, L.T. Effect of corneal graft diameter on therapeutic penetrating keratoplasty for fungal keratitis. *Int. J. Ophthalmol.* **2012**, *5*, 698–703, doi:10.3980/j.issn.2222-3959.2012.06.09.
283. Lombardo, M.; De Santo, M.P.; Lombardo, G.; Barberi, R.; Serrao, S. Roughness of excimer laser ablated corneas with and without smoothing measured with atomic force microscopy. *J. Refract. Surg.* **2005**, *21*, 469–475, doi:10.3928/1081-597X-20050901-08.
284. Buznyk, O.; Pasyechnikova, N.; Islam, M.M.; Iakymenko, S.; Fagerholm, P.; Griffith, M. Bioengineered Corneas Grafted as Alternatives to Human Donor Corneas in Three High-Risk Patients. *Clin. Transl. Sci.* **2015**, *8*, 558–562, doi:10.1111/cts.12293.
285. Jangamreddy, J.R.; Haagdorens, M.K.C.; Mirazul Islam, M.; Lewis, P.; Samanta, A.; Fagerholm, P.; Liszka, A.; Ljunggren, M.K.; Buznyk, O.; Alarcon, E.I.; et al. Short peptide analogs as alternatives to collagen in pro-regenerative corneal implants. *Acta Biomater.* **2018**, *69*, 120–130, doi:10.1016/j.actbio.2018.01.011.
286. Jangamreddy, J.R.; Haagdorens, M.K.C.; Islam, M.M.; Lewis, P.; Samanta, A.; Fagerholm, P.; Liszka, A.; Ljunggren, M.K.; Buznyk, O.; Alarcon, E.I.; et al. Corrigendum to “Short peptide analogs as alternatives to collagen in pro-regenerative corneal implants” [Acta Biomater. 69 (2018) 120–130]. *Acta Biomater.* **2019**, *88*, 556–557,

doi:10.1016/j.actbio.2019.01.046.
287. Jangamreddy, J.R.; Haagdorens, M.K.C.; Islam, M.M.; Lewis, P.; Samanta, A.; Fagerholm, P.; Liszka, A.; Ljunggren, M.K.; Buznyk, O.; Alarcon, E.I.; et al. Corrigendum to “Short peptide analogs as alternatives to collagen in pro-regenerative corneal implants” [Acta Biomaterialia 69 (2018) 120–130]. *Acta Biomater.* **2018**, *81*, 330–331, doi:10.1016/j.actbio.2018.10.009.
288. Phopase, J. Comment on “Short peptide analogs as alternatives to collagen in pro-regenerative corneal implants” by Jangamreddy JR et al. *Acta Biomater.* **2019**, *97*, 691, doi:10.1016/j.actbio.2019.06.004.
289. Griffith, M. Response to Letter to Editor “Comment on ‘Short peptide analogs as alternatives to collagen in pro-regenerative corneal implants’ by Jangamreddy JR et al.” *Acta Biomater.* **2019**, *97*, 692–693, doi:10.1016/j.actbio.2019.06.006.
290. Isaacson, A.; Swioklo, S.; Connon, C.J. 3D bioprinting of a corneal stroma equivalent. *Exp. Eye Res.* **2018**, *173*, 188–193, doi:10.1016/j.exer.2018.05.010.
291. Duarte Campos, D.F.; Rohde, M.; Ross, M.; Anvari, P.; Blaeser, A.; Vogt, M.; Panfil, C.; Yam, G.H.-F.; Mehta, J.S.; Fischer, H.; et al. Corneal bioprinting utilizing collagen-based bioinks and primary human keratocytes. *J. Biomed. Mater. Res. - Part A* **2019**, 1–9, doi:10.1002/jbm.a.36702.
292. Ghosh, S.; Parker, S.T.; Wang, X.; Kaplan, D.L.; Lewis, J.A. Direct-write assembly of microperiodic silk fibroin scaffolds for tissue engineering applications. *Adv. Funct. Mater.* **2008**, *18*, 1883–1889, doi:10.1002/adfm.200800040.
293. Mahdavi, S.S.; Abdekhodaie, M.J.; Kumar, H.; Mashayekhan, S.; Baradaran-Rafii, A.; Kim, K. Stereolithography 3D Bioprinting Method for Fabrication of Human Corneal Stroma Equivalent. *Ann. Biomed. Eng.* **2020**, *48*, 1955–1970, doi:10.1007/s10439-020-02537-6.
294. Dobre, O.; Oliva, M.A.G.; Ciccone, G.; Trujillo, S.; Rodrigo-Navarro, A.; Venters, D.C.; Llopis-Hernandez, V.; Vassalli, M.; Gonzalez-Garcia, C.; Dalby, M.J.; et al. A Hydrogel Platform that Incorporates Laminin Isoforms for Efficient Presentation of Growth Factors – Neural Growth and Osteogenesis. *Adv. Funct. Mater.* **2021**, *31*, doi:10.1002/adfm.202010225.
295. Xie, S.A.; Zhang, T.; Wang, J.; Zhao, F.; Zhang, Y.P.; Yao, W.J.; Hur, S.S.; Yeh, Y.T.; Pang, W.; Zheng, L.S.; et al. Matrix stiffness determines the phenotype of vascular smooth muscle cell in vitro and in vivo: Role of DNA methyltransferase 1. *Biomaterials* **2018**, *155*, 203–216, doi:10.1016/j.biomaterials.2017.11.033.

296. Emig, R.; Knodt, W.; Krussig, M.J.; Zgierski-Johnston, C.M.; Gorka, O.; Groß, O.; Kohl, P.; Ravens, U.; Peyronnet, R. Piezo1 Channels Contribute to the Regulation of Human Atrial Fibroblast Mechanical Properties and Matrix Stiffness Sensing. *Cells* **2021**, *10*, 1–20, doi:10.3390/cells10030663.
297. Giobbe, G.G.; Crowley, C.; Luni, C.; Campinoti, S.; Khedr, M.; Kretzschmar, K.; De Santis, M.M.; Zambaiti, E.; Michielin, F.; Meran, L.; et al. Extracellular matrix hydrogel derived from decellularized tissues enables endodermal organoid culture. *Nat. Commun.* **2019**, *10*, doi:10.1038/s41467-019-13605-4.
298. Mattei, G.; Cacopardo, L.; Ahluwalia, A. Engineering gels with time-evolving viscoelasticity. *Materials (Basel).* **2020**, *13*, 1–14, doi:10.3390/ma13020438.
299. Yue, L.; Wang, S.; Wulf, V.; Willner, I. Stiffness-switchable DNA-based constitutional dynamic network hydrogels for self-healing and matrix-guided controlled chemical processes. *Nat. Commun.* **2019**, *10*, 1–10, doi:10.1038/s41467-019-12697-2.
300. Ye, D.; Chang, C.; Zhang, L. High-strength and tough cellulose hydrogels chemically dual cross-linked by using low- and high-molecular-weight cross-linkers. *Biomacromolecules* **2019**, *20*, 1989–1995, doi:10.1021/acs.biomac.9b00204.
301. Raub, C.B.; Suresh, V.; Krasieva, T.; Lyubovitsky, J.; Mih, J.D.; Putnam, A.J.; Tromberg, B.J.; George, S.C. Noninvasive assessment of collagen gel microstructure and mechanics using multiphoton microscopy. *Biophys. J.* **2007**, *92*, 2212–2222, doi:10.1529/BIOPHYSJ.106.097998.
302. Wallace, B.A. The role of circular dichroism spectroscopy in the era of integrative structural biology. *Curr. Opin. Struct. Biol.* **2019**, *58*, 191–196, doi:10.1016/j.sbi.2019.04.001.
303. Tytgat, L.; Markovic, M.; Qazi, T.H.; Vagenende, M.; Bray, F.; Martins, J.C.; Rolando, C.; Thienpont, H.; Ottevaere, H.; Ovsianikov, A.; et al. Photo-crosslinkable recombinant collagen mimics for tissue engineering applications. *J. Mater. Chem. B* **2019**, *7*, 3100–3108, doi:10.1039/c8tb03308k.
304. Klatt, A.R.; Paul-Klausch, B.; Klinger, C.; Kühn, C.; Renno, J.H.; Banerjee, M.; Malchau, G.; Wielckens, K. A critical role for collagen II in cartilage matrix degradation: Collagen II induces pro-inflammatory cytokines and MMPS in primary human chondrocytes. *J. Orthop. Res.* **2009**, *27*, 65–70, doi:10.1002/jor.20716.
305. Fichter, M.; Körner, U.; Schömburg, J.; Jennings, L.; Cole, A.A.; Mollenhauer, J. Collagen degradation products modulate matrix metalloproteinase expression in cultured articular chondrocytes. *J. Orthop. Res.* **2006**, *24*, 63–70, doi:10.1002/jor.20001.

306. Giraud-Guille, M.-M. Liquid crystalline phases of sonicated type I collagen. *Biol. Cell* **1989**, *67*, 97–101, doi:10.1111/j.1768-322x.1989.tb03014.x.
307. Giraud-Guille, M.M. Liquid crystallinity in condensed type I collagen solutions: A clue to the packing of collagen in extracellular matrices. *J. Mol. Biol.* **1992**, *224*, 861–873, doi:10.1016/0022-2836(92)90567-4.
308. Giraud-Guille, M.M.; Besseau, L.; Herbage, D.; Gounon, P. Optimization of collagen liquid crystalline assemblies: Influence of sonic fragmentation. *J. Struct. Biol.* **1994**, *113*, 99–106, doi:1047-8477/94.
309. Giraud-Guille, M.-M.; Belamie, E.; Mosser, G.; Helary, C.; Gobeaux, F.; Vigier, S. Liquid crystalline properties of type I collagen: Perspectives in tissue morphogenesis. *Comptes Rendus Chim.* **2008**, *11*, 245–252, doi:10.1016/j.crci.2007.05.005.
310. Gibney, R.; Matthyssen, S.; Patterson, J.; Zakaria, N.; Ferraris, E. High Resolution 3D Printing of Recombinant Human Collagen Type III for Corneal Tissue Engineering. In Proceedings of the Annual Meeting of the International Society for Biofabrication, Oct 28-31, 2018; Würzburg, Germany, 2018.
311. Komai, Y.; Ushiki, T. The three-dimensional organization of collagen fibrils in the human cornea and sclera. *Investig. Ophthalmol. Vis. Sci.* **1991**, *32*, 2244–2258.
312. Geroski, D.H.; Matsuda, M.; Yee, R.W.; Edelhauser, H.F. Pump Function of the Human Corneal Endothelium: Effects of Age and Cornea Guttata. *Ophthalmology* **1985**, *92*, 759–763, doi:10.1016/S0161-6420(85)33973-8.
313. Hayes, S.; Lewis, P.; Islam, M.M.; Doutch, J.; Sorensen, T.; White, T.; Griffith, M.; Meek, K.M. The structural and optical properties of type III human collagen biosynthetic corneal substitutes. *Acta Biomater.* **2015**, *25*, 121–130, doi:10.1016/J.ACTBIO.2015.07.009.
314. Lee, A.; Hudson, A.R.; Shiwarski, D.J.; Tashman, J.W.; Hinton, T.J.; Yerneni, S.; Bliley, J.M.; Campbell, P.G.; Feinberg, A.W. Supplementary Material: 3D bioprinting of collagen to rebuild components of the human heart. *Science (80-.).* **2019**, *365*, 482–487, doi:10.1126/science.aav9051.
315. Lode, A.; Myer, M.; Brüggemeier, S.; Paul, B.; Baltzer, H.; Schröpfer, M.; Winkelmann, C.; Sonntag, F.; Gelinsky, M. Additive manufacturing of collagen scaffolds by three-dimensional plotting of highly viscous dispersions. *Biofabrication* **2016**, *8*, 015015, doi:10.1088/1758-5090/8/1/015015.
316. Osidak, E.O.; Karalkin, P.A.; Osidak, M.S.; Parfenov, V.A.; Sivogrivov, D.E.; Pereira, F.D.A.S.; Gryadunova, A.A.; Koudan, E. V.; Khesuani,

Y.D.; Kasyanov, V.A.; et al. Viscoll collagen solution as a novel bioink for direct 3D bioprinting. *J. Mater. Sci. Mater. Med.* **2019**, *30*, 31, doi:10.1007/s10856-019-6233-y.
317. Kim, H.; Jang, J.; Park, J.; Lee, K.-P.; Lee, S.; Lee, D.-M.; Kim, K.H.; Kim, H.K.; Cho, D.-W. Shear-induced alignment of collagen fibrils using 3D cell printing for corneal stroma tissue engineering. *Biofabrication* **2019**, *11*, 035017, doi:10.1088/1758-5090/ab1a8b.
318. Zhang, J.; Sisley, A.M.G.; Anderson, A.J.; Taberner, A.J.; McGhee, C.N.J.; Patel, D. V. Characterization of a novel collagen scaffold for corneal tissue engineering. *Tissue Eng. - Part C Methods* **2016**, *22*, 165–172, doi:10.1089/ten.tec.2015.0304.
319. Ozbolat, I.T.; Hospodiuk, M. Current advances and future perspectives in extrusion-based bioprinting. *Biomaterials* **2016**, *76*, 321–343, doi:10.1016/j.biomaterials.2015.10.076.
320. Saunders, R.E.; Derby, B. Inkjet printing biomaterials for tissue engineering: Bioprinting. *Int. Mater. Rev.* **2014**, *59*, 430–448, doi:10.1179/1743280414Y.0000000040.
321. Gudapati, H.; Ozbolat, I.T. The Role of Concentration on Drop Formation and Breakup of Collagen, Fibrinogen, and Thrombin Solutions during Inkjet Bioprinting. *Langmuir* **2020**, *36*, 15373–15385, doi:10.1021/acs.langmuir.0c02926.
322. Ng, W.L.; Lee, J.M.; Zhou, M.; Chen, Y.W.; Lee, K.X.A.; Yeong, W.Y.; Shen, Y.F. Vat polymerization-based bioprinting - process, materials, applications and regulatory challenges. *Biofabrication* **2020**, *12*, doi:10.1088/1758-5090/ab6034.
323. Drzewiecki, K.E.; Malavade, J.N.; Ahmed, I.; Lowe, C.J.; Shreiber, D.I. A thermoreversible, photocrosslinkable collagen bio-ink for free-form fabrication of scaffolds for regenerative medicine. *Technology* **2017**, *05*, 185–195, doi:10.1142/s2339547817500091.
324. Murphy, S. V.; Skardal, A.; Atala, A. Evaluation of hydrogels for bio-printing applications. *J. Biomed. Mater. Res. - Part A* **2013**, *101 A*, 272–284, doi:10.1002/jbm.a.34326.
325. Lee, W.; Debasitis, J.C.; Lee, V.K.; Lee, J.H.; Fischer, K.; Edminster, K.; Park, J.K.; Yoo, S.S. Multi-layered culture of human skin fibroblasts and keratinocytes through three-dimensional freeform fabrication. *Biomaterials* **2009**, *30*, 1587–1595, doi:10.1016/j.biomaterials.2008.12.009.
326. Diamantides, N.; Wang, L.; Pruiksma, T.; Siemiatkoski, J.; Dugopolski, C.; Shortkroff, S.; Kennedy, S.; Bonassar, L.J. Correlating rheological properties and printability of collagen bioinks: The effects of riboflavin photocrosslinking and pH. *Biofabrication* **2017**, *9*, doi:10.1088/1758-5090/aa780f.
327. Park, J.Y.; Choi, J.C.; Shim, J.H.; Lee, J.S.; Park, H.; Kim, S.W.; Doh, J.;

Cho, D.W. A comparative study on collagen type i and hyaluronic acid dependent cell behavior for osteochondral tissue bioprinting. *Biofabrication* **2014**, *6*, doi:10.1088/1758-5082/6/3/035004.
328. Yoon, H.; Lee, J.S.; Yim, H.; Kim, G.; Chun, W. Development of cell-laden 3D scaffolds for efficient engineered skin substitutes by collagen gelation. *RSC Adv.* **2016**, *6*, 21439–21447, doi:10.1039/c5ra19532b.
329. Lee, A.; Hudson, A.R.; Shiwarski, D.J.; Tashman, J.W.; Hinton, T.J.; Yerneni, S.; Bliley, J.M.; Campbell, P.G.; Feinberg, A.W. 3D bioprinting of collagen to rebuild components of the human heart. *Science* **2019**, *365*, 482–487, doi:10.1126/science.aav9051.
330. Lee, J.M.; Suen, S.K.Q.; Ng, W.L.; Ma, W.C.; Yeong, W.Y. Bioprinting of Collagen: Considerations, Potentials, and Applications. *Macromol. Biosci.* **2021**, *21*, 1–18, doi:10.1002/mabi.202000280.
331. Fox, A.J.S.; Bedi, A.; Rodeo, S.A. The Basic Science of Articular Cartilage: Structure, Composition, and Function. *Sports Health* **2009**, *1*, 461–468, doi:10.1177/1941738109350438.
332. Morgan, K.; Clague, R.B.; Evans, H.B.; Firth, S.A.; Wallace, J.E.; Holt, P.J. Native type II collagen-induced arthritis in the rat. I. Incidence and humoral response to collagen. *Ann. Rheum. Dis.* **1980**, *39*, 285–290.
333. Nagler-Anderson, C.; Bober, L.A.; Robinson, M.E.; Siskind, G.W.; Thorbecke, G.J. Suppression of type II collagen-induced arthritis by intragastric administration of soluble type II collagen. *Proc. Natl. Acad. Sci. U. S. A.* **1986**, *83*, 7443–7446, doi:10.1073/pnas.83.19.7443.
334. Mikulowska, A.; Metz, C.N.; Bucala, R.; Holmdahl, R. Macrophage migration inhibitory factor is involved in the pathogenesis of collagen type II-induced arthritis in mice. *J. Immunol.* **1997**, *158*, 5514–5517.
335. Bosnakovski, D.; Mizuno, M.; Kim, G.; Takagi, S.; Okumura, M.; Fujinaga, T. Chondrogenic differentiations of bovine bone marrow mesenchymal stem cells in different hydrogels: Influence of collagen type II ECM on MSC chondrogenesis. *Biotechnol. Bioeng.* **2006**, *93*, 1152–1163, doi:10.1002/bit.
336. Ragetly, G.; Griffon, D.J.; Chung, Y.S. The effect of type II collagen coating of chitosan fibrous scaffolds on mesenchymal stem cell adhesion and chondrogenesis. *Acta Biomater.* **2010**, *6*, 3988–3997, doi:10.1016/j.actbio.2010.05.016.
337. Freyria, A.; Ph, D.; Ronzie, M.; Ph, D.; Cortial, D.; Ph, D.; Galois, L.; Ph, D. Comparative Phenotypic Analysis of Articular Chondrocytes Cultured within Type I or Type II Collagen Scaffolds. **2009**, *15*.
338. Rutgers, M.; Saris, D.B.; Vonk, L.A.; Van Rijen, M.H.; Akrum, V.;

Langeveld, D.; Van Boxtel, A.; Dhert, W.J.; Creemers, L.B. Effect of collagen type I or type II on chondrogenesis by cultured human articular chondrocytes. *Tissue Eng. - Part A* **2013**, *19*, 59–65, doi:10.1089/ten.tea.2011.0416.

339. Wu, Z.; Korntner, S.; Mullen, A.; Zeugolis, D. Collagen type II: From biosynthesis to advanced biomaterials for cartilage engineering. *Biomater. Biosyst.* **2021**, *4*, 100030, doi:10.1016/j.bbiosy.2021.100030.
340. Kooij, S.; Astefanei, A.; Corthals, G.L.; Bonn, D. Size distributions of droplets produced by ultrasonic nebulizers. *Sci. Rep.* **2019**, *9*, 1–8, doi:10.1038/s41598-019-42599-8.
341. Shung, K.K. *Diagnostic Ultrasound: Imaging and Blood Flow Measurements*; 2nd ed.; Taylor & Francis: Boca Raton, 2015; ISBN 9781466582651.
342. Nishihara, T.; Doty, P. The Sonic Fragmentation of Collagen Macromolecules. *Proc. Natl. Acad. Sci. U. S. A.* **1958**, *44*, 411–417.
343. Hodge, A.J.; Schmitt, F.O. Interaction Properties of Sonically Fragmented Collagen Macromolecules. *Proc. Natl. Acad. Sci.* **1958**, *44*, 418–424, doi:10.1073/pnas.44.5.418.
344. Giraud-Guille, M.-M.M.; Besseau, L.; Chopin, C.; Durand, P.; Herbage, D. Structural aspects of fish skin collagen which forms ordered arrays via liquid crystalline states. *Biomaterials* **2000**, *21*, 899–906, doi:10.1016/S0142-9612(99)00244-6.
345. Giraud-Guille, M.-M.; Besseau, L.; Martin, R. Liquid crystalline assemblies of collagen in bone and in vitro systems. *J. Biomech.* **2003**, *36*, 1571–1579, doi:10.1016/S0021-9290(03)00134-9.
346. Greenfield, N.J. Using circular dichroism spectra to estimate protein secondary structure. *Nat. Protoc.* **2007**, *1*, 2876–2890, doi:10.1038/nprot.2006.202.
347. Feng, Y.; Melacini, G.; Taulane, J.P.; Goodman, M. Acetyl-terminated and template-assembled collagen-based polypeptides composed of Gly-Pro-Hyp sequences. 2. Synthesis and conformational analysis by circular dichroism, ultraviolet absorbance, and optical rotation. *J. Am. Chem. Soc.* **1996**, *118*, 10351–10358, doi:10.1021/ja961260c.
348. Feng, Y.; Melacini, G.; Taulane, J.P.; Goodman, M. Collagen-based structures containing the peptoid residue N-Isobutylglycine (Nleu): Synthesis and biophysical studies of Gly-Nleu-Pro sequences by circular dichroism and optical rotation. *Biochemistry* **1997**, *36*, 859–872, doi:10.1021/bi962980z.
349. Freudenberg, U.; Behrens, S.H.; Welzel, P.B.; Müller, M.; Grimmer, M.; Salchert, K.; Taeger, T.; Schmidt, K.; Pompe, W.; Werner, C. Electrostatic interactions modulate the conformation of collagen I. *Biophys. J.* **2007**, *92*, 2108–2119, doi:10.1529/biophysj.106.094284.

350. Mattei, G.; Breel, E.J. Measuring micro-mechanical properties of (bio)materials by nanoindentation. *Opt. B.V. [White Pap.* **2017**.
351. Bos, E.J.; Pluemeekers, M.; Helder, M.; Kuzmin, N.; van der Laan, K.; Groot, M.L.; van Osch, G.; van Zuijlen, P. Structural and mechanical comparison of human ear, alar, and septal cartilage. *Plast. Reconstr. Surg. - Glob. Open* **2018**, *6*, 1–9, doi:10.1097/GOX.0000000000001610.
352. Weng, B.; Liu, X.; Shepherd, R.; Wallace, G.G. Inkjet printed polypyrrole/collagen scaffold: A combination of spatial control and electrical stimulation of PC12 cells. *Synth. Met.* **2012**, *162*, 1375–1380, doi:10.1016/j.synthmet.2012.05.022.
353. Saleh, M.S.; Hamidvishkasougheh, M.; Zbib, H.; Panat, R. Polycrystalline micropillars by a novel 3-D printing method and their behavior under compressive loads. *Scr. Mater.* **2018**, *149*, 144–149, doi:10.1016/j.scriptamat.2018.02.027.
354. Vivekananthan, V.; Alluri, N.R.; Purusothaman, Y.; Chandrasekhar, A.; Selvarajan, S.; Kim, S. Biocompatible Collagen Nano fibrils: An Approach for Sustainable Energy Harvesting and Battery-Free Humidity Sensor Applications. *ACS Appl. Mater. Interfaces* **2018**, *10*, 18650–18656, doi:10.1021/acsami.8b02915.
355. Song, Y.; Cui, K.; Wang, L.; Chen, S. The electrodeposition of Ag nanoparticles on a type I collagen-modified glassy carbon electrode and their applications as a hydrogen peroxide sensor. *Nanotechnology* **2009**, *20*, 105501, doi:10.1088/0957-4484/20/10/105501.
356. Ngeontae, W.; Janrungroatsakul, W.; Maneewattanapinyo, P.; Ekgasit, S.; Aeungmaitrepirom, W.; Tuntulani, T. Novel potentiometric approach in glucose biosensor using silver nanoparticles as redox marker. *Sensors Actuators B Chem.* **2009**, *137*, 320–326, doi:10.1016/J.SNB.2008.11.003.
357. Ravichandran, R.; Martinez, J.G.; Jager, E.W.H.; Phopase, J.; Turner, A.P.F. Type I Collagen-Derived Injectable Conductive Hydrogel Scaffolds as Glucose Sensors. *ACS Appl. Mater. Interfacesmaterials* **2018**, *10*, 16244–16249, doi:10.1021/acsami.8b04091.
358. Ge, L.; Xu, Y.; Li, X.; Yuan, L.; Tan, H.; Li, D.; Mu, C. Fabrication of Antibacterial Collagen-Based Composite Wound Dressing. *ACS Sustain. Chem. Eng.* **2018**, *6*, 9153–9166, doi:10.1021/acssuschemeng.8b01482.
359. Cavallaro, J.F.; Kemp, P.D.; Kraus, K.H. Collagen Fabrics as Biomaterials. *Biotechnol. Bioeng.* **1994**, *43*, 781–791, doi:10.1002/bit.260430813.
360. Zeugolis, D.I.; Paul, R.G.; Attenburrow, G. Factors influencing the properties of reconstituted collagen fibers prior to self-assembly:

Animal species and collagen extraction method. *J. Biomed. Mater. Res. - Part A* **2008**, *86*, 892–904, doi:10.1002/jbm.a.31694.
361. Yang, J.; Han, C.; Xu, F.; Sun, R. Simple approach to reinforce hydrogels with cellulose nanocrystals †. *Nanoscale* **2014**, *6*, 5934–5943, doi:10.1039/c4nr01214c.
362. Tafoya, R.R.; Secor, E.B. Understanding effects of printhead geometry in aerosol jet printing. *Flex. Print. Electron.* **2020**, *5*, doi:10.1088/2058-8585/aba2bb.
363. Secor, E.B. Recirculating Ink Cartridge for Aerosol Jet Printing 2021.
364. Secor, E.B. In-Line Mixing Printhead for Multimaterial Aerosol Jet Printing 2022.
365. Secor, E.B.; Cook, A.W.; Kaehr, B.J.; Tafoya, R.R. Optical Measurement System for Real-Time Process Monitoring of Aerosol Jet Printing 2022.
366. Shedd, T.A.; Newell, T.A. Automated optical liquid film thickness measurement method. *Rev. Sci. Instrum.* **1998**, *69*, 4205–4213.
367. Delgado, L.M.; Pandit, A.; Zeugolis, D.I. Influence of sterilisation methods on collagen-based devices stability and properties. *Expert Rev. Med. Devices* **2014**, *11*, 305–314, doi:10.1586/17434440.2014.900436.

7 Curriculum Vitae

Rory Gibney
rory.gibney2@mail.dcu.ie

Research Experience

- **KU Leuven**, Leuven, Belgium
  PhD Candidate, January 2016 – June 2022
- **Dublin City University**, Dublin, Ireland
  Postdoctoral Researcher, September 2021 – Present
- **Curam (REMODEL), NUI Galway**, Ireland
  Visiting Researcher, October 2018 – April 2019
- **University of Leeds**, Leeds, UK
  Early Stage Researcher, January 2015 – January 2016
- **Dublin City University**, Dublin, Ireland
  Research Assistant, February 2014 – January 2015

Education

- Bachelor of Engineering in Biomedical Engineering
  Dublin City University

List of Publications

Papers

- *"High resolution bioprinting of recombinant human collagen type III";* **Gibney, R**, Patterson, J, Ferraris, E; Polymers 2021, 13:2973
- *"Bioprinting of collagen type I and II via aerosol jet printing for the replication of dense collagenous tissues*"; **Gibney, R**; Ferraris, E; Frontiers in Bioengineering and Biotechnology 2021, 9:786945

Conference Papers

- *"The human cornea as a model tissue for additive biomanufacturing: a review"; **Gibney, R**; Matthyssen, S; Patterson, J.; Ferraris, E; Zakaria, N;* Procedia CIRP Vol. 65, 2017, Pages 56-63 [Abstract, oral, paper, & session co-chair].

Book Chapters

- *"Biomimetic Materials"* In: Mishra M. (Eds.), Encyclopedia of Biomedical Polymers and Polymeric Biomaterials, Concise Edition, New York, USA: Taylor and Francis, 2017; *Leonidakis, K, Soultan, A, Piluso, S, Van den Broeck, L, Meiga, T, Gibney, R, Patterson* J; DOI: 10.1081/E-EBPPC
- *"Introduction to Tissue Engineering"* & *"Biofabrication of Corneal Substitutes",* in Arras, P. & Luengo, D. (Eds.) *Teaching and Subjects on Bio-medical Engineering: Approaches* funded by BIOART Erasmus+ programme; peer-reviewed by Springer Nature, published by Acco cv, Leuven 2021; **Gibney, R;** Ferraris, E

Abstracts

- Gibney, R; Matthyssen, S; Ferraris, E; Patterson, J; Zakaria, N; "*Additive manufacturing of recombinant human collagen type III (RHC III) films for corneal tissue engineering applications"*, BSTE Belgian Symposium on Tissue Engineering [Abstract & oral presentation], 4th-5th May 2017, Leuven. Belgium.
- Gibney, R; Matthyssen, S; Patterson, J; Zakaria, N; Ferraris, E; *"High resolution printing of collagen"*, [abstract & oral presentation] EORS (European Orthopaedic research Society) 26th Annual Meeting. Galway, Ireland, 25-28 September 2018.
- Gibney, R; Matthyssen, S; Patterson, J; Zakaria, N; Ferraris, E;

"High Resolution 3D Printing of Recombinant Human Collagen Type III for Corneal Tissue Engineering"; [accepted abstract & poster] Annual Meeting of the International Society for Biofabrication 28-31 October 2018, Wurzburg, Germany.

- Gibney, R; Matthyssen, S; Patterson, J; Zakaria, N; Ferraris, E; *"Aerosol Jet Printing as a Novel Method for 3D Bioprinting of Recombinant Human Collagen Type III for Corneal Tissue Engineering",* [abstract & poster]. The 5th Annual Matrix Biology Ireland meeting 21-22 November 2018.

FACULTY OF ENGINEERING TECHNOLOGY
DEPARTMENT OF MECHANICAL ENGINEERING &
DEPARTMENT OF MATERIALS ENGINEERING

Maakprocessen en -Systemen (MaPS), Campus De Nayer
Jan Pieter de Nayerlaan 5
2860 Sint-Katelijne-Waver
BELGIUM.

mech.kuleuven.be/en/maps